

Design and development of hybrid cathode structures for aqueous zinc ion battery systems

by

Kamalambika Muthukumar

B.Tech., CSIR- Central Electrochemical Research Institute, 2017

AN ABSTRACT OF A DISSERTATION

submitted in partial fulfillment of the requirements for the degree

DOCTOR OF PHILOSOPHY

Department of Chemistry  
College of Arts and Sciences

KANSAS STATE UNIVERSITY  
Manhattan, Kansas

2022

## Abstract

Renewable energy generation is forecast to rise rapidly, increasing almost 60% from 2020 to 2026 (International Energy Agency's 2021 report). This is the driving force for developing better and safer large-scale energy storage systems. Despite the lithium-ion batteries (LIB) dominating the global energy market due to their higher specific capacity and energy density, the poor safety feature of LIBs owing to their usage of flammable organic electrolytes is a significant concern for their application in large-scale electrical energy storage (EES) systems. Aqueous zinc ion battery (AZIB) systems are particularly attractive as a promising candidate for large-scale EES systems due to their high theoretical gravimetric capacity (820 mAh/g) and volumetric capacity (5855 mAh/cm<sup>3</sup>), low redox potential (-0.76V) of the zinc metal anodes. In addition to that, AZIB is a safer and more cost-effective alternative to the LIB systems because of the use of aqueous electrolytes with higher safety feature and higher ionic conductivity (1 S cm<sup>-1</sup>). Despite the advantages, AZIB possesses complications associated with the larger ionic radii of the hydrated Zn<sup>2+</sup> ions (4.3 Å) and higher electrostatic attraction of the divalent Zn<sup>2+</sup> ion with the cathode structures leading to severe capacity fading and poor cycling stability. This thesis focuses on the impact of defect engineering, interlayer expansion, and the addition of conductive carbon in optimizing the electrochemical Zn<sup>2+</sup> storage properties of the classical layered cathode structures such as V<sub>2</sub>O<sub>5</sub>, MoS<sub>2</sub>.

In the first study, we report the preparation of a set of hybrid materials consisting of Molybdenum disulfide (MoS<sub>2</sub>) nanopatches on reduced graphene oxide (rGO) nanosheets by applying the microwave specific heating of graphene oxide (GO) and molecular molybdenum precursors followed by thermal annealing in 3% H<sub>2</sub> and 97% Ar. The microwave process converts GO to ordered rGO nanosheets that are sandwiched between uniform thin layers of amorphous

Molybdenum trisulfide ( $\text{MoS}_3$ ). The subsequent thermal annealing converts the intermediate layers into  $\text{MoS}_2$  nanopatches with two-dimensional layered structures whose defect density is tunable by controlling the annealing temperature at 250, 325, and 600 °C, respectively. The Zn-ion storage properties strongly depend on the defects in the  $\text{MoS}_2$  adlayer. The highly defective  $\text{MoS}_2/\text{rGO}$  hybrid prepared by annealing at 250 °C shows the highest initial Zn-ion storage capacity ( $\sim 300 \text{ mAh g}_{\text{MoS}_x}^{-1}$ ) and close to 100% coulombic efficiency, which is dominated by pseudocapacitive surface reactions at the edges or defects in the  $\text{MoS}_2$  nanopatches. This study validates that defect engineering is critical in improving Zn-ion storage.

In the second approach, the synthesis of hybrid materials consisting of Vanadium pentoxide ( $\text{V}_2\text{O}_5$ ) nanoribbons (NRs) and rGO nanosheets by divalent metal cation mediated coprecipitation is adopted toward high-performance cathodes for AZIB. The divalent metal ions  $\text{M}^{2+}$  (including  $\text{Zn}^{2+}$  and  $\text{Mn}^{2+}$ ) effectively neutralize the negative charges on the surface of microwave exfoliated  $\text{V}_2\text{O}_5$  NRs and GO nanosheets to form a strongly bound assembly. The hybrids are further annealed in the  $\text{N}_2$  atmosphere to convert the GO into rGO to improve the electrical conductivity. When only  $\text{Zn}^{2+}$  ions are used during coprecipitation, the Zn- $\text{V}_2\text{O}_5$  NR/rGO hybrid shows a high reversible specific capacity of  $\sim 386 \text{ mAh g}^{-1}$  at  $0.50 \text{ A g}^{-1}$  suffers from poor stability. This is improved by mixing some  $\text{Mn}^{2+}$  with the  $\text{Zn}^{2+}$  ions during coprecipitation. The (Mn+Zn)- $\text{V}_2\text{O}_5$  NR/rGO hybrid shows a slightly lower specific capacity of  $\sim 289 \text{ mAh g}^{-1}$  at  $0.5 \text{ A g}^{-1}$  but with improved long-cycling stability and rate-performance due to the stronger binding of  $\text{Mn}^{2+}$  ions with the  $\text{V}_2\text{O}_5$  host which serve as stable pillars to support the expanded  $\text{V}_2\text{O}_5$  layers. This study ratifies the importance of morphology control in improving the ionic and electronic conductivity of the hybrid cathode structures and preventing structural collapse upon repeated intercalation/deintercalation cycles.

Design and development of hybrid cathode structures for aqueous zinc ion battery systems

by

Kamalambika Muthukumar

B.Tech., CSIR-Central Electrochemical Research Institute, 2017

A DISSERTATION

submitted in partial fulfillment of the requirements for the degree

DOCTOR OF PHILOSOPHY

Department of Chemistry  
College of Arts and Sciences

KANSAS STATE UNIVERSITY  
Manhattan, Kansas

2022

Approved by:  
Major Professor  
Dr. Jun Li

# **Copyright**

© Kamalambika Muthukumar 2022

## Abstract

Renewable energy generation is forecast to rise rapidly, increasing almost 60% from 2020 to 2026 (International Energy Agency's 2021 report). This is the driving force for developing better and safer large-scale energy storage systems. Despite the lithium-ion batteries (LIB) dominating the global energy market due to their higher specific capacity and energy density, the poor safety feature of LIBs owing to their usage of flammable organic electrolytes is a significant concern for their application in large-scale electrical energy storage (EES) systems. Aqueous zinc ion battery (AZIB) systems are particularly attractive as a promising candidate for large-scale EES systems due to their high theoretical gravimetric capacity (820 mAh/g) and volumetric capacity (5855 mAh/cm<sup>3</sup>), low redox potential (-0.76V) of the zinc metal anodes. In addition to that, AZIB is a safer and more cost-effective alternative to the LIB systems because of the use of aqueous electrolytes with higher safety feature and higher ionic conductivity (1 S cm<sup>-1</sup>). Despite the advantages, AZIB possesses complications associated with the larger ionic radii of the hydrated Zn<sup>2+</sup> ions (4.3 Å) and higher electrostatic attraction of the divalent Zn<sup>2+</sup> ion with the cathode structures leading to severe capacity fading and poor cycling stability. This thesis focuses on the impact of defect engineering, interlayer expansion, and the addition of conductive carbon in optimizing the electrochemical Zn<sup>2+</sup> storage properties of the classical layered cathode structures such as V<sub>2</sub>O<sub>5</sub>, MoS<sub>2</sub>.

In the first study, we report the preparation of a set of hybrid materials consisting of Molybdenum disulfide (MoS<sub>2</sub>) nanopatches on reduced graphene oxide (rGO) nanosheets by applying the microwave specific heating of graphene oxide (GO) and molecular molybdenum precursors followed by thermal annealing in 3% H<sub>2</sub> and 97% Ar. The microwave process converts GO to ordered rGO nanosheets that are sandwiched between uniform thin layers of amorphous

Molybdenum trisulfide ( $\text{MoS}_3$ ). The subsequent thermal annealing converts the intermediate layers into  $\text{MoS}_2$  nanopatches with two-dimensional layered structures whose defect density is tunable by controlling the annealing temperature at 250, 325, and 600 °C, respectively. The Zn-ion storage properties strongly depend on the defects in the  $\text{MoS}_2$  adlayer. The highly defective  $\text{MoS}_2/\text{rGO}$  hybrid prepared by annealing at 250 °C shows the highest initial Zn-ion storage capacity ( $\sim 300 \text{ mAh g}_{\text{MoS}_x}^{-1}$ ) and close to 100% coulombic efficiency, which is dominated by pseudocapacitive surface reactions at the edges or defects in the  $\text{MoS}_2$  nanopatches. This study validates that defect engineering is critical in improving Zn-ion storage.

In the second approach, the synthesis of hybrid materials consisting of Vanadium pentoxide ( $\text{V}_2\text{O}_5$ ) nanoribbons (NRs) and rGO nanosheets by divalent metal cation mediated coprecipitation is adopted toward high-performance cathodes for AZIB. The divalent metal ions  $\text{M}^{2+}$  (including  $\text{Zn}^{2+}$  and  $\text{Mn}^{2+}$ ) effectively neutralize the negative charges on the surface of microwave exfoliated  $\text{V}_2\text{O}_5$  NRs and GO nanosheets to form a strongly bound assembly. The hybrids are further annealed in the  $\text{N}_2$  atmosphere to convert the GO into rGO to improve the electrical conductivity. When only  $\text{Zn}^{2+}$  ions are used during coprecipitation, the  $\text{Zn-V}_2\text{O}_5$  NR/rGO hybrid shows a high reversible specific capacity of  $\sim 386 \text{ mAh g}^{-1}$  at  $0.50 \text{ A g}^{-1}$  suffers from poor stability. This is improved by mixing some  $\text{Mn}^{2+}$  with the  $\text{Zn}^{2+}$  ions during coprecipitation. The  $(\text{Mn}+\text{Zn})\text{-V}_2\text{O}_5$  NR/rGO hybrid shows a slightly lower specific capacity of  $\sim 289 \text{ mAh g}^{-1}$  at  $0.5 \text{ A g}^{-1}$  but with improved long-cycling stability and rate-performance due to the stronger binding of  $\text{Mn}^{2+}$  ions with the  $\text{V}_2\text{O}_5$  host which serve as stable pillars to support the expanded  $\text{V}_2\text{O}_5$  layers. This study ratifies the importance of morphology control in improving the ionic and electronic conductivity of the hybrid cathode structures and preventing structural collapse upon repeated intercalation/deintercalation cycles.

# Table of Contents

List of Figures .....	xi
List of Tables .....	xix
Acknowledgements .....	xx
Dedication .....	xxi
Preface .....	xxii
Chapter 1 - Introduction .....	1
1.1. Motivation .....	1
1.2. Electrical Energy Storage Systems .....	1
1.3. Working Principle of Electrochemical Energy Storage .....	3
1.4. Commercialized EES Systems .....	4
1.4. Challenges with Commercialized Battery Energy Storage (BES) Systems .....	6
1.5. Aqueous Zinc Ion Batteries (AZIB) .....	7
1.6. Energy Storage Mechanisms in AZIB .....	9
1.6.1. Reversible Zn <sup>2+</sup> Insertion and Extraction Mechanism .....	9
1.6.2. Co-insertion of Zn <sup>2+</sup> and H <sup>+</sup> ions: .....	10
1.6.3. Chemical Conversion Reaction: .....	11
1.7. Categories of Cathode Materials .....	11
1.7.1. Layered Manganese Based Oxides .....	13
1.7.2. Layered Vanadium Based Oxides .....	14
1.7.3. Layered Transition Metal Dichalcogenides .....	15
1.8. Overview of Challenges with AZIB .....	16
1.9. Design Strategies and Structural Engineering in AZIB Cathodes .....	17
1.9.1. Interlayer Intercalation Strategy .....	17
1.9.2. Defect Engineering .....	19
1.9.3. Composite Engineering .....	20
1.9.4. Nanostructure Engineering and Morphology Control: .....	21
1.10. Summary: .....	22
Chapter 2 - Synthesis and Electrochemical Characterization of Cathode Materials for AZIB ....	25
2.1. Introduction to Microwave Assisted Synthesis Process .....	25

2.2. Microwave Synthesis Vs. Conventional Hydrothermal Synthesis .....	26
2.2.1. Synthesis of Two Dimensional MoS <sub>2</sub> /rGO hybrid <sup>103</sup> .....	27
2.2.2. Synthesis of V <sub>2</sub> O <sub>5</sub> Nanoribbons:.....	29
2.3. Electrochemical Characterization .....	29
2.3.1. Preparation of Electrode.....	30
2.3.2. Coin Cell Assembly .....	30
2.3.3. Electrochemical Characterization .....	31
2.3.3.1. Galvanostatic Charge Discharge Process.....	31
2.3.3.2. Cyclic Voltammetry.....	32
Chapter 3 - Tuning Defects in the MoS <sub>2</sub> /Reduced Graphene Oxide 2D Hybrid Materials for Optimizing Battery Performance .....	34
3.1. Introduction.....	34
3.2. Experimental .....	37
3.2.1. Materials .....	37
3.2.2. Preparation of MoS <sub>2</sub> /rGO hybrid .....	37
3.2.3. Material Characterization.....	38
3.2.4. Electrochemical Characterization .....	39
3.3. Results and Discussion .....	41
3.3.1. Synthesis design.....	41
3.3.2. Structure Characterization.....	43
3.3.4. Materials Composition Analyses: .....	49
3.3.5. Electrochemical Evaluation of Energy Storage: .....	54
3.4. Conclusion .....	60
Chapter 4 - Coprecipitation Synthesis of V <sub>2</sub> O <sub>5</sub> Nanoribbons on Reduced Graphene Oxide Nanosheets through Divalent Transition Metal Cations for High-Capacity and Stable Aqueous Zinc Ion Batteries .....	62
4.1. Introduction.....	62
4.2. Experimental Methods.....	66
4.2.1. Chemicals and Materials:.....	66
4.2.2. Material Characterization:.....	67
4.2.3. Electrochemical Characterization: .....	67

4.2.4. Synthesis of V <sub>2</sub> O <sub>5</sub> Nanoribbons:.....	68
4.2.5. Preparation of V <sub>2</sub> O <sub>5</sub> NR/rGO hybrids by coprecipitation:.....	69
4.3. Results and discussion: .....	70
4.3.1. Synthesis Design:.....	70
4.3.2. Morphological Characterization: .....	72
4.3.3. Structural Characterization: .....	75
4.3.4. XPS Analysis:.....	78
4.3.5. Thermogravimetric Analysis: .....	81
4.3.6. Electrochemical Characterization: .....	82
4.4. Conclusion .....	87
Chapter 5 - Promoting Electrocatalytic Conversion of Lithium Polysulfides to Suppress Polysulfide Shuttle Effect in Li-S Batteries (Current Work).....	89
5.1. Introduction:.....	89
5.2. Polysulfide Shuttle Effect:.....	90
5.3. Strategies to Suppress the Polysulfide Shuttle Effect:.....	92
5.4. Experimental Methods:.....	94
5.4.1. Synthesis of MoS <sub>2</sub> /rGO Electrocatalysts: .....	94
5.4.2. Preparation of Lithium Polysulfide Solutions: .....	95
5.4.3. Lithium Polysulfide Adsorption Tests:.....	95
5.4.3. Symmetric Cell Measurements: .....	96
5.5. Results and Discussion: .....	96
5.5.1. Physical Anchoring of LiPSs on the Surface of MoS <sub>2</sub> /rGO:.....	97
5.5.2. Electrochemical Characterization: .....	99
5.6. Conclusion .....	101
Chapter 6 - Summary .....	103
Chapter 7 - Future Projects .....	106
References.....	109
Appendix A - Supplementary Information for Chapter 3.....	123
Appendix B - Supplementary Information for Chapter 4.....	143
Appendix C - Supplementary information for Chapter 5 .....	155

## List of Figures

- Figure 1.1. Ragone plot comparing the gravimetric energy density and gravimetric power density of various commercial electrical energy storage systems and aqueous zinc ion battery<sup>2</sup> (the AZIB data was collected from current research publication<sup>4</sup>). Adapted with permission from Jia, X.; Liu, C.; Neale, Z. G.; Yang, J.; Cao, G., Active Materials for Aqueous Zinc Ion Batteries: Synthesis, Crystal Structure, Morphology, and Electrochemistry. *Chemical Reviews* **2020**, *120* (15), 7795-7866. Copyright © 2020, American Chemical Society. .... 4
- Figure 1.2. Representative schematic of aqueous zinc ion batteries showing the three integral components of AZIB- Zinc metal anode, aqueous electrolyte, and cathode<sup>3</sup>. Adapted with permission from Zeng, X.; Hao, J.; Wang, Z.; Mao, J.; Guo, Z., Recent progress and perspectives on aqueous Zn-based rechargeable batteries with mild aqueous electrolytes. *Energy Storage Materials* **2019**, *20*, 410-437. Copyright © 2019 Elsevier B.V. .... 8
- Figure 1.3. Comparison of specific capacities and average operating voltages of cathode materials for neutral aqueous ZIBs<sup>1</sup>. Adapted with permission from Liu, H.; Wang, J.-G.; You, Z.; Wei, C.; Kang, F.; Wei, B., Rechargeable aqueous zinc-ion batteries: Mechanism, design strategies and future perspectives. *Materials Today* **2021**, *42*, 73-98. Copyright © 2020 Elsevier Ltd. .... 11
- Figure 1.4. Schematic flowchart illustrating the design strategies adapted in the different approaches in this thesis dissertation. .... 22
- Figure 2.1. Schematic representation of AZIB Coin cell and the components. .... 30
- Figure 3.1. Schematic illustration of the two-step synthesis of MoS<sub>2</sub>/rGO hybrid materials by microwave-heating of ATM and GO precursors in THF followed by thermal annealing the intermediate MoS<sub>3</sub>/rGO powder at varied temperature in 3%H<sub>2</sub>/97%Ar in a tube furnace. Reproduced from Muthukumar, K.; Leban, L.; Sekar, A.; Elangovan, A.; Sarkar, N.; Li, J., Tuning the defects in MoS<sub>2</sub>/reduced graphene oxide 2D hybrid materials for optimizing battery performance. *Sustainable Energy & Fuels* **2021**, *5* (16), 4002-4014 with permission from the Royal Society of Chemistry .... 41

Figure 3.2. (a) Powder XRD spectra of MoS<sub>2</sub>/rGO prepared by annealing at 600 °C (MoS<sub>2</sub>/rGO-600), 325 °C (MoS<sub>2</sub>/rGO-325) and 250 °C (MoS<sub>2</sub>/rGO-250) in comparison to a bulk MoS<sub>2</sub> powder. (b) The full scale and (c) the expanded region of Raman spectra of MoS<sub>2</sub>/rGO-600 and the bulk MoS<sub>2</sub> powder. Reproduced from Muthukumar, K.; Leban, L.; Sekar, A.; Elangovan, A.; Sarkar, N.; Li, J., Tuning the defects in MoS<sub>2</sub>/reduced graphene oxide 2D hybrid materials for optimizing battery performance. *Sustainable Energy & Fuels* **2021**, 5 (16), 4002-4014 with permission from the Royal Society of Chemistry ..... 43

Figure 3.3. Characterization of the MoS<sub>2</sub>/rGO hybrid material annealed at 600 °C (i.e. MoS<sub>2</sub>/rGO-600) by FESEM at (a) a lower and (b) a higher magnification, by TEM at (c) a lower and (d) a higher magnification, and (e) by the selected area electron diffraction (SAED) from the frame in (d). The red-colored indices at the top portion in panel (e) indicate the isolated hexagonal 2D electron diffraction spots from the monocrystalline rGO nanosheets while the black indices at the bottom indicate the continuous rings of 2D powder electron diffraction from the MoS<sub>2</sub> adlayers. (f) Schematic illustration of the hybrid structure of MoS<sub>2</sub> nanopatches with random rotational orientations on the rGO nanosheet. Reproduced from Muthukumar, K.; Leban, L.; Sekar, A.; Elangovan, A.; Sarkar, N.; Li, J., Tuning the defects in MoS<sub>2</sub>/reduced graphene oxide 2D hybrid materials for optimizing battery performance. *Sustainable Energy & Fuels* **2021**, 5 (16), 4002-4014 with permission from the Royal Society of Chemistry..... 47

Figure 3.4. The Mo 3d and S 2p XPS spectra of (a,b) MoS<sub>2</sub>/rGO-600, (c,d) MoS<sub>2</sub>/rGO-325), (e,f) MoS<sub>2</sub>/rGO-250, (g,h) MoS<sub>3</sub>/rGO-intermediate product. The inset of panel (b) shows the schematic structure of the hexagonal MoS<sub>2</sub> nanopatches. The inset of panel (h) shows the schematic structure of MoS<sub>3</sub> chain. Reproduced from Muthukumar, K.; Leban, L.; Sekar, A.; Elangovan, A.; Sarkar, N.; Li, J., Tuning the defects in MoS<sub>2</sub>/reduced graphene oxide 2D hybrid materials for optimizing battery performance. *Sustainable Energy & Fuels* **2021**, 5 (16), 4002-4014 with permission from the Royal Society of Chemistry ..... 50

Figure 3.5. (a) The rate-performance tests of the LIB half-cell with the MoS<sub>2</sub>/rGO-600 cathode vs. a Li disk anode at 100, 150, 300, 600 mA cell current in the cell voltage window of 0.50 – 3.0 V. (b) The galvanostatic charge/discharge curves in the initial 10 cycles at 145 mA g<sup>-1</sup>

(~C/4 rate) in (a). (c) The galvanostatic charge/discharge curves of LIB half-cells made of MoS<sub>2</sub>/rGO-600 at 145 mA g<sup>-1</sup> (blue), MoS<sub>2</sub>/rGO-325 at 97 mA g<sup>-1</sup> (black), MoS<sub>2</sub>/rGO-250 at 160 mA g<sup>-1</sup> (red) and MoS<sub>3</sub>/rGO intermediate material at 87 mA g<sup>-1</sup> (green) in the 10<sup>th</sup> cycle at 100 mA current rate. Be noted that all measurements in panels (b) and (c) were done at 100 μA cell current but are translated into different current densities due to variation of mass loading on each electrode. Reproduced from Muthukumar, K.; Leban, L.; Sekar, A.; Elangovan, A.; Sarkar, N.; Li, J., Tuning the defects in MoS<sub>2</sub>/reduced graphene oxide 2D hybrid materials for optimizing battery performance. *Sustainable Energy & Fuels* **2021**, 5 (16), 4002-4014 with permission from the Royal Society of Chemistry ..... 55

Figure 3.6. (a) Rate performance of MoS<sub>2</sub>/rGO-250 in a Zn-ion battery half-cell at 100, 200, 300 and 400 mA cell currents, which are converted to corresponding current densities for ease of comparison among different cells. (b) CV curves of MoS<sub>2</sub>/rGO-250 at various scan rates in the cell voltage window of 0.25 – 1.30 V (vs. Zn<sup>2+</sup>/Zn). (c) Galvanostatic charge-discharge curves in the 2<sup>nd</sup> cycle of Zn-ion battery half-cells at 78 mA g<sup>-1</sup> with MoS<sub>2</sub>/rGO-600, MoS<sub>2</sub>/rGO-325 and MoS<sub>2</sub>/rGO-250 cathode, respectively. (d) Long-term stability of a Zn-ion half-cell with the MoS<sub>2</sub>/rGO-250 cathode at the charge/discharge current density of 311 mA g<sup>-1</sup>. Reproduced from Muthukumar, K.; Leban, L.; Sekar, A.; Elangovan, A.; Sarkar, N.; Li, J., Tuning the defects in MoS<sub>2</sub>/reduced graphene oxide 2D hybrid materials for optimizing battery performance. *Sustainable Energy & Fuels* **2021**, 5 (16), 4002-4014 with permission from the Royal Society of Chemistry ..... 58

Figure 4.1. Schematic illustration of synthesis by coprecipitated V<sub>2</sub>O<sub>5</sub> NR/rGO hybrid. 1: V<sub>2</sub>O<sub>5</sub> NRs and Graphene Oxide (GO) precursors are dispersed in water to form stable suspensions by ultrasonication; 2: The mixed V<sub>2</sub>O<sub>5</sub> and GO precursors remain as a homogeneous suspension due to electrostatic repulsion; 3: Zinc acetate or Manganese acetate solutions are added dropwise to coprecipitate the negatively charged V<sub>2</sub>O<sub>5</sub> NRs and GO nanosheets into a gel-like precipitate which is collected and dried by heating for approximately 6 hours at 70°C on a hotplate; and 4: The dried V<sub>2</sub>O<sub>5</sub> NR/GO is further annealed in a tube furnace at 300°C for 2 hours in N<sub>2</sub> atmosphere to convert GO to rGO and form the hybrid material of V<sub>2</sub>O<sub>5</sub> NR/rGO..... 71

Figure 4.2. TEM images of (a) bare rGO and (b) as-exfoliated  $V_2O_5$  NRs. (c) The selected area electron diffraction (SAED) pattern of the  $V_2O_5$  NR red-circled in panel (b) and the (hk0) index according to orthorhombic  $\alpha$ - $V_2O_5$  crystal structure (based on standard pattern of JCPDS:41-1426) with the (001) plane perpendicular to the electron beam. (d) Illustration of the crystal orientation of the  $V_2O_5$  NRs. TEM images of the coprecipitated hybrid materials of  $V_2O_5$  NRs on rGO nanosheets in form of (e) Zn- $V_2O_5$  NR/rGO and (f) (Mn+Zn)- $V_2O_5$  NR/rGO. .... 73

Figure 4.3. FESEM images at low to higher magnifications of (a-c)  $V_2O_5$  NR, (d-f) Zn- $V_2O_5$  NR/rGO, and (g-i) (Mn+Zn)- $V_2O_5$  NR/rGO. .... 74

Figure 4.4. (a) Raman spectra and (b) powder XRD spectra of Zn- $V_2O_5$  NR/rGO (blue), (Mn+Zn)- $V_2O_5$  NR/rGO (green)) in comparison to the control samples of  $V_2O_5$  NR (red) and bulk  $V_2O_5$  powder (black). The bottom part of panel (b) is the standard pattern of orthorhombic  $\alpha$ - $V_2O_5$  crystal (JCPDS:41-1426). .... 76

Figure 4.5. The high-resolution XPS spectra of V 2p (510-528 eV) and O1s (528-534 eV) from (a)  $V_2O_5$  NR, (b) Zn- $V_2O_5$  NR/rGO and (c) (Mn+Zn)- $V_2O_5$  NR/rGO. The Zn2p spectra of (d) Zn- $V_2O_5$  NR/rGO and (e) (Mn+Zn)- $V_2O_5$  NR/rGO. (f) The Mn2p spectra of (Mn+Zn)- $V_2O_5$  NR/rGO. .... 79

Figure 4.6. Galvanostatic charge-discharge characterization of the aqueous ZIBs in the potential window of 0.20 – 1.80 V. (a) The rate-performance plots measured sequentially at different current densities (i.e.,  $0.5 \text{ A g}^{-1}$ ,  $1.0 \text{ A g}^{-1}$ ,  $2.0 \text{ A g}^{-1}$ ,  $4.0 \text{ A g}^{-1}$  and  $6.0 \text{ A g}^{-1}$ ) for (a) Zn- $V_2O_5$  NR/rGO cathode and (b) (Mn+Zn)- $V_2O_5$  NR/rGO cathode. Long-cycle tests of the aqueous ZIBs at the fixed current density of  $4.0 \text{ A g}^{-1}$  with (c) Zn- $V_2O_5$  NR/rGO cathode and (d) (Mn+Zn)- $V_2O_5$  NR/rGO cathode. The current densities are calculated based on the total mass of M- $V_2O_5$  NR/rGO materials while the specific capacities are calculated based on the mass of active of M- $V_2O_5$  NR derived from TGA analysis (Table S3). (e) Comparison of galvanostatic charge-discharge profiles of the AZIBs at  $0.50 \text{ A g}^{-1}$  with the cathode made of  $V_2O_5$  NR (blue), (Mn+Zn)- $V_2O_5$  NR/rGO (red) and Zn- $V_2O_5$  NR/rGO (black), respectively.

(f) Comparison of CV curves of the AZIBs made of Zn-V <sub>2</sub> O <sub>5</sub> NR/rGO (black) and (Mn+Zn)-V <sub>2</sub> O <sub>5</sub> NR/rGO (red) cathodes at the scan rate of 0.50 mV s <sup>-1</sup> .....	83
Figure 5.1. . UV-Visible absorbance spectra of 3.00 mL of 3.0 m M solution of (a) Li <sub>2</sub> S <sub>8</sub> , (b) Li <sub>2</sub> S <sub>6</sub> and (c) Li <sub>2</sub> S <sub>4</sub> in 1:1 DOL/DME mixture (solvent) without adding any electrocatalyst (black) and in 12.0 hours after adding 15 mg of MoS <sub>2</sub> /rGO-600 (red), MoS <sub>2</sub> /rGO-250 (blue) and MoS <sub>3</sub> /rGO-intermediate (orange). .....	97
Figure 5.2. CV profiles in symmetric cell setup in (a) 0.2 M Li <sub>2</sub> S <sub>4</sub> , (b) 0.2 M Li <sub>2</sub> S <sub>6</sub> and (c) 0.2M Li <sub>2</sub> S <sub>8</sub> in the potential window of -1.0 V till +1.0 V at a scan rate of 50 mV/s with the various electrocatalytic materials such as bare Al (orange), commercial MoS <sub>2</sub> (black), MoS <sub>2</sub> /rGO-600 (green), MoS <sub>2</sub> /rGO-250 (red) and MoS <sub>3</sub> /rGO-intermediate (blue).....	99

### List of Appendix Figures

Figure A.1. The full scale and expanded region of Raman spectra of (a, b) MoS <sub>2</sub> /rGO-325, (c, d) MoS <sub>2</sub> /rGO-250 and (e, f) MoS <sub>3</sub> /rGO intermediate product.....	123
Figure A.2. Raman Spectra of graphene oxide (GO) precursor. ....	124
Figure A.3. TEM images of (a) bare rGO nanosheets and (b) the MoS <sub>3</sub> /rGO intermediate. (c) and (d): SEM images of these two samples, respectively. The bare rGO sample was prepared with microwave irradiation in absence of ATM precursors before subjected to thermal annealing at 600°C in 3% H <sub>2</sub> and 97% Ar. The MoS <sub>3</sub> /rGO intermediate was obtained after the microwave irradiation in presence of ATM precursors but was not subjected to the thermal annealing. ....	125
Figure A.4. Low- and higher-magnification FESEM images of (a, b) MoS <sub>2</sub> /rGO-600, (c, d) MoS <sub>2</sub> /rGO-325, (e, f) MoS <sub>2</sub> /rGO-325, and (g, h) MoS <sub>3</sub> /rGO-intermediate. ....	126
Figure A.5. TEM images of (a) MoS <sub>2</sub> /rGO-250, (b) MoS <sub>2</sub> /rGO-325, and (c) MoS <sub>2</sub> /rGO-600..	127
Figure A.6. SAED patterns of (a) MoS <sub>2</sub> /rGO-600, (b) MoS <sub>2</sub> /rGO-325, (e) MoS <sub>2</sub> /rGO-250, and (d) MoS <sub>3</sub> /rGO intermediate. The red-colored indices at the top indicate the isolated 2D electron diffraction spots with the six-fold symmetry from the rGO nanosheets, while the white indices at the bottom indicate the continuous rings of 2D powder electron diffraction from MoS <sub>2</sub> nanopatches with random rotational orientations in the rGO plane.....	128

Figure A.7. (a) Schematic illustration of the SAED with the electron beam perpendicular to the 2D crystal plane. (b) The relationship of the real space 2D hexagonal lattice  $a$  and  $b$  and the reciprocal diffraction lattice ( $a^*$  and  $b^*$ ). (c) The SAED pattern of MoS<sub>2</sub>/rGO-600. (d) The procedure to derive the MoS<sub>2</sub> lattice the MoS<sub>2</sub> lattice in reference to the sharp hexagonal SAED pattern of the 2D monocrystalline rGO nanosheets..... 129

Figure A.8. Thermogravimetric analyses of various hybrid materials and control samples (commercial MoS<sub>2</sub> powder and bare rGO synthesized at the same conditions as MoS<sub>2</sub>/rGO-600 but without presence of ATM precursors) ..... 131

Figure A.9. Rate Performance at varied current rates and representative galvanostatic charge/discharge curves of Li-ion half cells with the cathode made of (a, b) MoS<sub>2</sub>/rGO-600, (c, d) MoS<sub>2</sub>/rGO-325 (1.44 mg), (e, f) MoS<sub>2</sub>/rGO-250 (0.82 mg) and (g, h) MoS<sub>3</sub>/rGO intermediate material (1.76 mg). Panels (a), (c) and (e) have the same legend as panel (g). ..... 133

Figure A.10. Long term stability test of Li ion half cells with anode made of MoS<sub>2</sub>/rGO-600. 134

Figure A.11. Rate performance test of Li-ion battery half cells with the cathode made of (a) control rGO-600 (1.13 mg), (b) control rGO-325 (2.0 mg), (c) control rGO-250 (1.03 mg) and (d) control rGO-intermediate (1.25 mg). Panels (a), (b) and (c) follow the same legend as panel (d). ..... 137

Figure A.12. Galvanostatic charge-discharge curves and the rate performance of Zn-ion battery half-cells with the cathode made of (a, b) MoS<sub>2</sub>/rGO-600 (0.87 mg), (c, d) MoS<sub>2</sub>/rGO-325 (1.36 mg), (e, f) MoS<sub>2</sub>/rGO-250 (1.28 mg), and (g, h) MoS<sub>3</sub>/rGO-intermediate hybrid material (0.88 mg). Panels (a), (c) and (e) follow same legend as panel (g). ..... 138

Figure A.13. The cycle stability of Zn-ion battery half cells with the cathode made of (a) MoS<sub>2</sub>/rGO-250 (2.16 mg) and (b) MoS<sub>3</sub>/rGO-intermediate (0.88 mg). The charge/discharge was carried out at 0.25 – 1.30 V vs Zn<sup>2+</sup>/Zn. .... 139

Figure A.14. Rate performance test of Zn ion battery half cells with the cathode made of (a) control rGO-600 (1.38 mg) (b) control rGO-325 (2.0 mg) (c) control sample-250 (0.90 mg) (d) control rGO-intermediate (1.50 mg). Panels (a), (b) and (c) follow same legend as panel (d). ..... 140

Figure B.1. The optical images of the homogeneous aqueous suspensions (in DI water) of (a) V<sub>2</sub>O<sub>5</sub> NRs, (b) GO precursor and (c) V<sub>2</sub>O<sub>5</sub> NRs and GO mixture. (d) The optical image of a gel-

like precipitate after adding divalent cations (such as $Zn^{2+}$ or $Mn^{2+}$ ) into the mixed suspension of $V_2O_5$ NRs and GO during the coprecipitation process. (e) The optical image of the dried co-precipitated hybrids, i.e., M- $V_2O_5$ NR/GO. ....	143
Figure B.2. TEM images of (a) bulk $V_2O_5$ and (b) as-exfoliated $V_2O_5$ nanoribbons. ....	144
Figure B.3. The three-dimensional representation of the unit cell of orthorhombic $\alpha$ - $V_2O_5$ with $a = 11.516 \text{ \AA}$ , $b = 3.566 \text{ \AA}$ , $c = 4.373 \text{ \AA}$ and all angles between the lattice vectors of $90^\circ$ (based on the standard pattern of JCPDS:41-1426). The atomic structures were rendered with the open web-access tool provided by “The Materials Project” at: <a href="https://materialsproject.org">https://materialsproject.org</a> . ....	145
Figure B.4. (a) The raw image of the Selected Area Electron Diffraction (SAED) pattern of the $V_2O_5$ nanoribbon marked in Figure 2(b). (b) The enlarged area near (000) to illustrate that the SAED pattern matches the rectangular lattice of the (001) plane of orthorhombic $\alpha$ - $V_2O_5$ crystal, with the electron beam perpendicular to the (001) plane. ....	146
Figure B.5. The XPS spectra of V2p (512 – 528 eV) and O 1s (528 – 535 eV) of (a) $V_2O_5$ NRs and (b) bulk $V_2O_5$ powder. The C 1s XPS spectra of (c) Zn- $V_2O_5$ NR/rGO and (d) (Mn+Zn)- $V_2O_5$ NR/rGO. ....	148
Figure B.6. (a) Thermogravimetric Analysis of various hybrid materials and control samples. (b) TGA plots of control samples (calcinated Zinc Acetate – red; calcinated mixture of Manganese acetate and Zinc acetate – black). ....	150
Figure B.7. The rate-performance behavior of AZIB at different current densities with the cathode material of ( $V_2O_5$ NRs and (b) bulk $V_2O_5$ powder. Galvanostatic charge-discharge profiles of (c) $V_2O_5$ NRs and (d) bulk $V_2O_5$ powder at different current densities ( $0.5 \text{ A g}^{-1}$ , $1.0 \text{ A g}^{-1}$ , $2.0 \text{ A g}^{-1}$ , $4.0 \text{ A g}^{-1}$ ). All the above tests are performed in the potential window of 0.20-1.80 V. ....	152
Figure B.8. Rate-performance behavior of AZIBs in the potential window of 0.20-1.80 V at different current densities with (a) control rGO and (b) physically mixed $V_2O_5$ NR and rGO without the incorporation of divalent metal cations. ....	153
Figure B.9. (a) Schematic illustration of the $Zn^{2+}$ ion transport during the charge -discharge processes in AZIB with a Zn metal anode and a cathode made of $V_2O_5$ NR/rGO hybrids. Galvanostatic charge discharge profiles and CV curves in the potential window of 0.20 – 1.80 V; (b, d) with Zn- $V_2O_5$ NR/rGO cathode and (c, e) with (Mn+Zn)- $V_2O_5$ NR/rGO. ....	154

Figure C.1. Systematic analysis of lithium polysulfide adsorption capacities of MoS<sub>2</sub>/rGO-600(a, d, g); MoS<sub>2</sub>/rGO-250 (b, e, h); and MoS<sub>3</sub>/rGO-intermediate (c, f, i) electrocatalysts. Time-dependent UV-Visible absorbance measurements of the 3.0 mL of 3.0 mM Lithium polysulfide solutions in 1:1 DOL/DME solvent, (a-c) Li<sub>2</sub>S<sub>8</sub>, (d-f) Li<sub>2</sub>S<sub>6</sub>, (g-i) Li<sub>2</sub>S<sub>4</sub> before (red curve) and after adding 5 mg/mL electrocatalysts samples. Measurement was done for 12 hours at a constant interval of every one hour after stirring for 40 minutes and resting for 20 minutes..... 155

Figure C.2. Systematic analysis of lithium polysulfide adsorption capacities of MW-rGO-600(a, d, g); MW-rGO-250 (b, e, h); and MW-rGO-intermediate (c, f, i) electrocatalysts. Time-dependent UV-Visible absorbance measurements of the 3.0 mL of 3.0 mM Lithium polysulfide solutions in 1:1 DOL/DME solvent (a-c) Li<sub>2</sub>S<sub>8</sub>, (d-f) Li<sub>2</sub>S<sub>6</sub>, (g-i) Li<sub>2</sub>S<sub>4</sub> before (red curve) and after adding 5 mg/mL electrocatalysts samples. Measurement was done for 12 hours at a constant interval of every one hour after stirring for 40 minutes and resting for 20 minutes..... 156

Figure C.3. Analysis of time vs concentration of lithium polysulfide solutions after adding various MoS<sub>2</sub>/rGO hybrid electrocatalysts based on the absorbance measured in Figure C.1. (MoS<sub>2</sub>/rGO-600 – Red curve; MoS<sub>2</sub>/rGO-250 – Black curve; MoS<sub>3</sub>/rGO-intermediate – Blue curve). (a) Li<sub>2</sub>S<sub>4</sub>, (b) Li<sub>2</sub>S<sub>6</sub>, (c) Li<sub>2</sub>S<sub>8</sub>. ..... 156

## List of Tables

Table 5.1. Adsorption capacity of MoS <sub>2</sub> /rGO-600, MoS <sub>2</sub> /rGO-250 and MoS <sub>3</sub> /rGO-intermediate and the atomic ratio of Mo:S estimated from the XPS Analysis in Table A.2 .....	100
---	-----

### List of Tables in Appendix

Table A.1. Raman Analysis of GO precursor and MoS <sub>2</sub> /rGO.....	124
Table A.2. The parameters derived from deconvolution of Mo 3d and S 2p XPS spectra in section 3.3.4. ....	130
Table A.3. Elemental Analysis of MoS <sub>x</sub> /rGO.....	132
Table A.4. Estimation of contribution to the specific capacity by rGO and MoS <sub>x</sub> in LIB. ....	136
Table B.1. Measured zeta potential values of V <sub>2</sub> O <sub>5</sub> NRs and control GO precursors.....	143
Table B.2. XPS analysis of V <sub>2</sub> O <sub>5</sub> NRs and V <sub>2</sub> O <sub>5</sub> NR /rGO hybrids .....	149
Table B.3. Weight percentage of M-V <sub>2</sub> O <sub>5</sub> in divalent metal ion coprecipitated M-V <sub>2</sub> O <sub>5</sub> NR/rGO hybrids, control V <sub>2</sub> O <sub>5</sub> NR and control rGO samples calculated based on TGA plots in Figure B.6. ....	151
Table C.1. Adsorption capacities of MoS <sub>2</sub> electrocatalysts after the deduction of the adsorption capacities of control rGO from the adsorption capacities of MoS <sub>2</sub> /rGO based on the formula described below. The weight percentages were taken from the elemental analysis of MoS <sub>2</sub> /rGO shown in table A.3. ....	156

## **Acknowledgements**

Firstly, I would like to express my sincere and heartfelt gratitude to my advisor Prof. Dr. Jun Li for his support and guidance throughout my graduate school career. I would like to thank my supervisory committee members Dr. Christopher Culbertson, Dr. Christer B. Aakeroy, Dr. Suprem Das and Dr. Bin Liu for agreeing to be in my committee and appreciate their invaluable time. My sincere thanks to Michael Hinton, Dr. TingTing Liu for their help in teaching. I would also like to thank Ron Jackson, Tobe Eggers, Mary Dooley, Kimberly Ross for all their help in making my research go smooth during this entire term. I would like to thank Dr. Dan Boyle of Kansas State University and Dr. Balamurugan from the University of Nebraska - Lincoln for their help with material characterization. My heartfelt appreciation and thanks to Dr. Ya Chen, visiting professor from Central South University, China, for his expert opinions and help during his visit here.

My special thanks to my colleagues Dr. Emery Brown, Dr. Yang Song, Levon Leban II, Archana Sekar, Sabari Rajendran, and Zawad Hossain, for their support and encouragement. My heartfelt gratitude to my friends Kathryn Tanahill, Sofiya Sabreen, Rohan Amare, Avantika Ramekar, Pavithra Natarajan, Charu Jagadeesan for their support and love during my graduate career. I would like to express my indebtedness and love to Dr. Shruthi. T. Kumarraj, Ashwin Ramanujam, Srianuradha Kandavel, Dr. Vinu Varghese Panikkattu and Prakashsamy for being my friends, my confidants, philosophers, therapists, travel buddies, and my family away from home. Without them, I wouldn't have made it here.

Finally, I would like to thank my parents, Muthukumar and Usha, brother Murugadoss, aunt and uncle Kannan and Shanthi, grandparents Rajamani and Doss. I owe it all to them for their unbreakable trust and confidence in me. Many, many thanks to them for making me who I am today.

## **Dedication**

“To my mother Usha Raju, my father Muthukumar Doss, my brother Murugadoss and  
my grandmother Rajamani Doss.”

## Preface

The work in this thesis have led to manuscripts listed below:

1. Muthukumar, K.; Leban, L.; Sekar, A.; Elangovan, A.; Sarkar, N.; Li, J., Tuning the defects in MoS<sub>2</sub>/reduced graphene oxide 2D hybrid materials for optimizing battery performance. Sustainable Energy & Fuels 2021, 5 (16), 4002-4014. <https://doi.org/10.1039/D1SE00729G>
2. Muthukumar, K.; Chen Ya; Sekar, A.; Li, J., Coprecipitation Synthesis of V<sub>2</sub>O<sub>5</sub> Nanoribbons on Reduced Graphene Oxide Nanosheets through Divalent Transition Metal Cations for High-Capacity and Stable Aqueous Zinc Ion Batteries. (Manuscript in Communication)

# **Chapter 1 - Introduction**

## **1.1. Motivation**

The increasing global energy consumption and limited fossil fuel resources have driven the community towards utilization of renewable energy sources such as solar, wind, tidal power, etc. However, such energy sources are intermittent, regional, and seasonal. This has increased the requirement of large-scale electrical energy storage systems (EES) to ensure the continuous supply of energy worldwide. In addition to that, the increase in the use of electric vehicles and portable electronic devices, including mobile phones and laptops, has raised the demand for energy storage devices with improved energy storage and rapid-charging capability. However, the available electrode materials have practically reached their limit in terms of energy density which calls for the study into other electrode materials with higher energy density. The rising safety issues and high cost of the prevailing EES systems demand the exploration of alternative EES systems that are safe, environmentally benign, and affordable. The aqueous multivalent metal-ion batteries, especially Aqueous Zinc Ion Batteries (AZIB), are a promising candidate for large-scale EES systems. The research, development, and commercialization of such aqueous EES systems can be a better alternative to the existing large scale energy storage systems.

## **1.2. Electrical Energy Storage Systems**

EES systems play a vital role in the uniform distribution of energy globally. The electrical energy storage systems can be classified into four broad categories: mechanical, chemical, electrochemical, and electrical approaches, which show a wide range of performance characteristics originating from the different fundamental mechanisms<sup>5, 6</sup>. The electrical energy storage mechanism of any system is governed by the first law of thermodynamics that clearly states



is the product of the number of charges transported ( $z$ ), the cell voltage ( $E$ ), and the faraday's constant ( $F$ ) as given in equation (5)<sup>11</sup>,

$$\Delta G = zEF \dots\dots\dots (5)$$

### 1.3. Working Principle of Electrochemical Energy Storage

The electrochemical EES comprises two electrodes, a cathode, and an anode,<sup>12</sup> physically separated by the ionically conducting solid or liquid electrolyte medium<sup>13</sup>. In general, they store energy predominantly as chemical energy in the bonds on the electroactive species and subsequently convert the chemical energy into electrical energy supplied to the electrical device. Electrochemical capacitors and batteries collectively make up most of the electrochemical energy storage devices<sup>14</sup>. This dissertation work primarily focuses on battery storage systems. Batteries can be classified into two types: primary i.e., non-rechargeable and secondary batteries that are rechargeable. Secondary batteries are the preferred type when it comes to electrical storage purposes. The secondary batteries are rechargeable as the chemical reactions involved are essentially and utterly reversible in most cases<sup>15, 16</sup>. The active material in the cathode undergoes reduction, and anode undergoes oxidation during discharge or power generation, and the reverse happens during the storage or charging process. Most rechargeable batteries are assembled in a discharged state, and they are subsequently charged first after assembly. The electrode reactions can be written as follows<sup>17</sup>,

During discharge,



In the above equations, M and X represent the active species in cathode and anode respectively. During charge, the reverse of the abovementioned equations occurs in the respective electrodes.

#### 1.4. Commercialized EES Systems

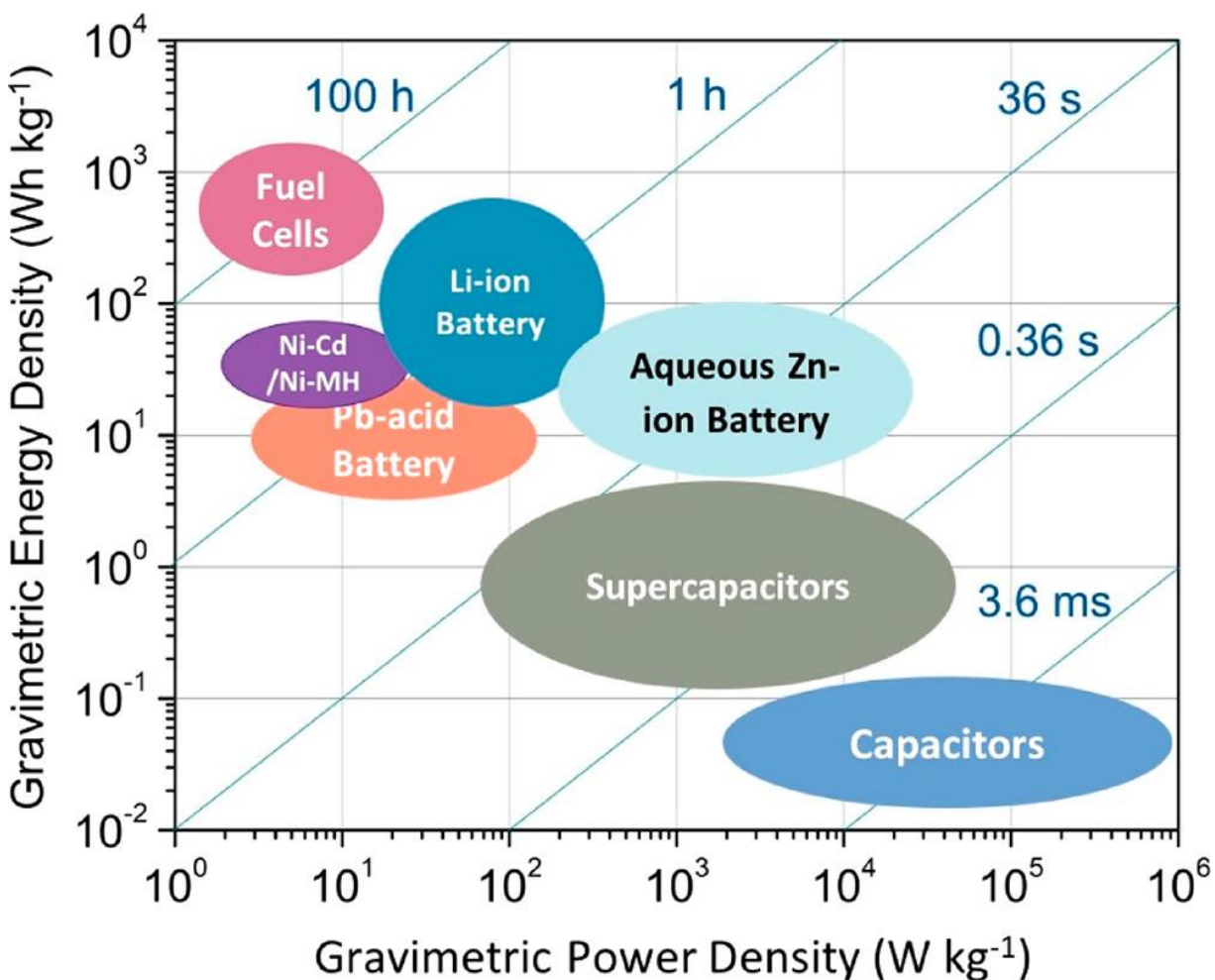


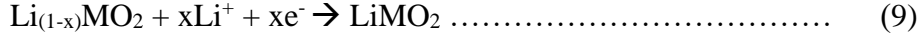
Figure 1.1. Ragone plot comparing the gravimetric energy density and gravimetric power density of various commercial electrical energy storage systems and aqueous zinc ion battery<sup>2</sup> (the AZIB data was collected from current research publication<sup>4</sup>). Adapted with permission from Jia, X.; Liu, C.; Neale, Z. G.; Yang, J.; Cao, G., Active Materials for Aqueous Zinc Ion Batteries: Synthesis, Crystal Structure, Morphology, and Electrochemistry. *Chemical Reviews* **2020**, *120* (15), 7795-7866. Copyright © 2020, American Chemical Society.

Several deciding factors in developing an ideal electrical energy storage device include low cost, high reliability, increased safety, environmental benignity, higher gravimetric energy density, and power density<sup>18-20</sup>. The scientific community has researched several EES systems based on the abovementioned factors. As discussed before, the EES systems branch into two broad families

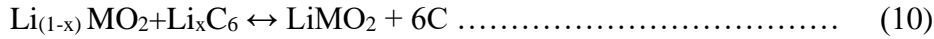
of electrochemical capacitors and batteries<sup>14</sup>. The charge storage in electrochemical capacitors is primarily based on the surface adsorption and desorption of charged carriers along with the electrode/electrolyte interface, which depends predominantly on the surface area of the electrode material. However, the charge storage mechanism in the batteries is based on the redox reactions occurring in the electrodes. A battery is one or more electrochemical cells connected in series or parallel or a combination of series and parallel based on the requirement. Batteries have a higher gravimetric energy density, high working voltages, and higher capacities than electrochemical capacitors. Still, they possess comparatively lower power density due to their mass transport limited diffusion kinetics. The Ragone plot is generally used in literature to compare the gravimetric energy density and power densities of various electrochemical energy storage systems. The Ragone plot in Figure 1.1 compares the commercial and new electrochemical energy storage devices, including electrochemical capacitors, lead-acid batteries, Ni-MH and Nickel-cadmium batteries, lithium-ion batteries, and fuel cells<sup>2</sup>. Among them, lithium-ion batteries are widespread and have dominated the markets for several decades owing to their higher energy density, long cycle life, lightweight, and can be made into various shapes and sizes to fit the device in need. Compared to lead-acid and Nickel-cadmium batteries, li-ion batteries do not suffer much from the memory effect. Lithium-ion batteries usually comprise transition metal oxide cathode<sup>21</sup>, preferably LiCoO<sub>2</sub><sup>22</sup>, and a graphite anode<sup>23, 24</sup>. The graphite anode undergoes oxidation during discharge, releasing li<sup>+</sup> ions as shown in equation (8).



The dissolved Li<sup>+</sup> ions migrate from the anode towards the cathode through the electrolyte medium. At the same time, the electrons reach the cathode via the external circuit, and reduction occurs at the cathode generating LiMO<sub>2</sub> as in equation (9).



The reverse of the reactions (8) and (9) occurs at anode and cathode during the charging process. During charge, the cathode undergoes oxidation releasing Li<sup>+</sup> ions into the electrolyte that migrate towards the anode, where they undergo reduction and get stored as Li<sup>+</sup> ions into the graphene layers. A conventional LIB's overall charge discharge reaction can be illustrated as equation (10)<sup>23</sup>.



However, the existing energy storage systems are barely suited for large-scale energy storage purposes. It is indispensable that we explore other alternative options for large-scale energy storage systems.

**1.4. Challenges with Commercialized Battery Energy Storage (BES) Systems**

Despite several decades of research and development, only a handful of battery energy storage systems have been successfully commercialized due to the challenges involved in large-scale electrical energy storage systems. Battery energy storage systems, especially the advanced Li-ion batteries, offer multipurpose applications, including uninterrupted power supply systems for houses and small-scale industrial complexes<sup>25</sup>, electric vehicles<sup>26, 27</sup>, portable electronic devices<sup>28</sup>, transportation facilities, etc., owing to their high-power density and energy density features. Despite the several advantages of lithium-ion batteries, it still suffers from poor rechargeability and safety concerns originating from the usage of flammable organic electrolytes such as LiPF<sub>6</sub><sup>29</sup>. There have been several incidents where the user overcharges the battery and causes abnormal heat dissipation, which can eventually lead to an explosion. This process is called thermal runaway, which cannot be eliminated with the usage of organic electrolyte, which renders such batteries practically unsafe to be employed in large-scale grid storage systems<sup>30</sup>. In addition to that, the toxic nature of the lithium/sodium metal and its associated compounds makes it difficult

for waste disposal, and the chemicals involved in the manufacture of lithium-ion battery cathodes contribute to the increasing carbon content and climate change. Even though recent reports suggest that the rapid exhaustion of lithium sources might not greatly affect the production of lithium-ion batteries, as it can be compensated by the recycling and reuse of used lithium<sup>31</sup>. The high cost associated with the recycling of used lithium and the assembly of li-ion batteries will collectively increase the cost of the lithium-ion batteries in the future. The recycling processes of the batteries also cause the emission of greenhouse gases. Hence, it becomes imperative that we explore alternative options for the application of large-scale electric energy storage devices with comparable energy density, higher safety, non-toxic, increased environmental benignity, and substantially lower cost than the existing commercialized electrical energy storage systems.

### **1.5. Aqueous Zinc Ion Batteries (AZIB)**

In the past decade, there has been an enormous increase in the research and development associated with aqueous multivalent ion batteries, especially aqueous zinc ion batteries. Aqueous zinc ion batteries possess several advantages, such as high volumetric capacity (5855 mAh/cm<sup>3</sup>) and comparable gravimetric ability (820 mAh/g), and low redox potential (-0.76 V vs SHE) of the zinc metal anode<sup>1, 32-34</sup>. The aqueous electrolyte medium provides high safety and significantly higher ionic conductivity of 1 S cm<sup>-1</sup>, which is a few orders of magnitude higher than the organic electrolytes ( $\sim 10^{-3} - 10^{-2}$  S cm<sup>-1</sup>)<sup>35</sup>, which substantially improves the rate performance, power density and reduces the ohmic resistance. The high reliability, increased safety, low cost, faster charge/discharge capability, and environmental friendliness of the aqueous zinc ion batteries make them a promising candidate for the existing large scale electrical energy storage systems. As illustrated in Figure 1.2, the AZIB comprises a zinc anode, a cathode physically separated by an aqueous electrolyte medium. In 2011, Feiyu Kang's group successfully exhibited the reversible

$Zn^{2+}$  insertion/extraction into the tunnel-shaped structures of  $\alpha$ - $MnO_2$  cathode material<sup>36</sup>. Since then, many reports have illustrated the application of various cathode structures for reversible  $Zn^{2+}$  storage. Despite the extensive research, the commercialization of aqueous zinc ion batteries is seriously hindered by the lack of appropriate cathode materials<sup>37,38</sup>.

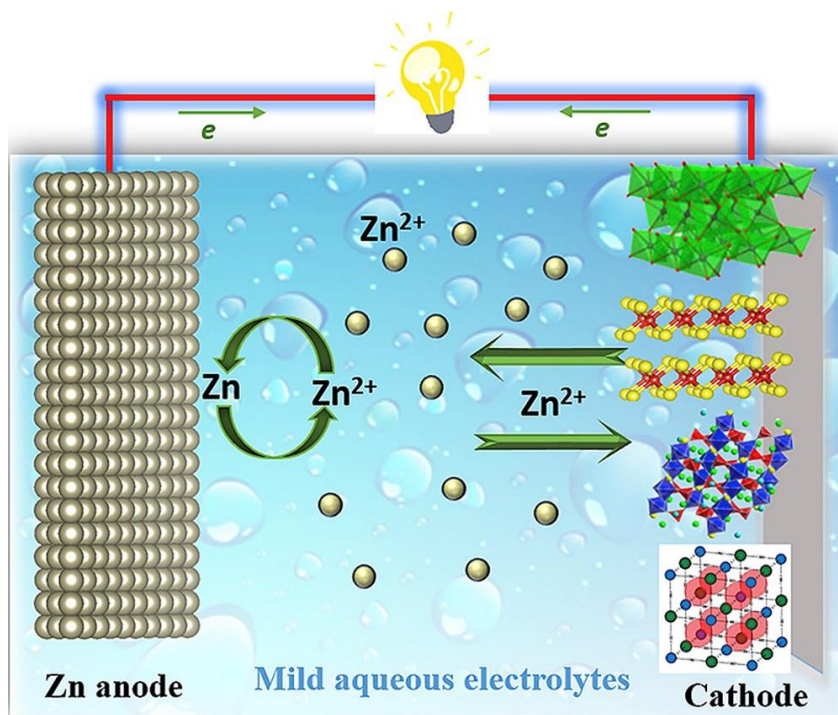


Figure 1.2. Representative schematic of aqueous zinc ion batteries showing the three integral components of AZIB- Zinc metal anode, aqueous electrolyte, and cathode<sup>3</sup>. Adapted with permission from Zeng, X.; Hao, J.; Wang, Z.; Mao, J.; Guo, Z., Recent progress and perspectives on aqueous Zn-based rechargeable batteries with mild aqueous electrolytes. *Energy Storage Materials* **2019**, *20*, 410-437. Copyright © 2019 Elsevier B.V.

Aqueous zinc ion batteries comprise three integral components: the zinc anode, cathode, and aqueous electrolyte. The zinc anode and cathode materials of the aqueous zinc ion batteries have several critical disadvantages despite the advantages mentioned above. Zinc anode suffers from a non-homogenous zinc deposition and dissolution process, leading to dendritic growth, which eventually causes loss of active material, capacity decay, and short-circuit<sup>32,39</sup>. Great efforts

have been devoted to solving the problems faced by the zinc anode, including surface modification of zinc anodes<sup>40</sup>, improvement in the structural design of the anodes<sup>41, 42</sup>, development of zinc-free anodes<sup>43</sup>, and optimization of the composition of electrolytes<sup>44, 45</sup>. Whereas there is still a long way to go in the case of cathode materials to fully utilize the potential of the zinc anode as the specific capacity of AZIB is limited by the capacity of the cathode. The ionic radii of  $\text{Zn}^{2+}$  ions (0.74 Å) are similar to that of the monovalent  $\text{Li}^+$  ions which make the cathode structures used for  $\text{Li}^+$  ion intercalation can be applied for  $\text{Zn}^{2+}$  storage. However, the mechanism of  $\text{Zn}^{2+}$  intercalation is not straightforward as that of  $\text{Li}^+$  ions. The ionic radii of the hydrated  $\text{Zn}^{2+}$  ions (5.5 Å) in the aqueous electrolyte medium are approximately 7.4 times larger than the anhydrate  $\text{Zn}^{2+}$  ions, making their reversible insertion/extraction more difficult. In addition to that the divalent charge of the  $\text{Zn}^{2+}$  ions increases their electrostatic interaction with the host structure. Hence the existing cathode structures need certain structural modifications to facilitate smoother and reversible  $\text{Zn}^{2+}$  intercalation/deintercalation process. In order to adopt an appropriate modification strategy, the mechanism of energy storage based on  $\text{Zn}^{2+}$  ions needs to be understood.

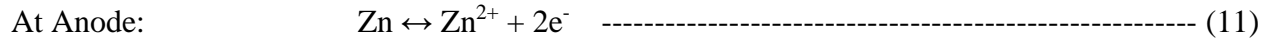
## **1.6. Energy Storage Mechanisms in AZIB**

Unlike other established battery energy storage systems such as lithium-ion batteries and sodium-ion batteries, the  $\text{Zn}^{2+}$  storage mechanism of AZIB is still complicated and unclear. This  $\text{Zn}^{2+}$  storage reportedly occurs via three different mechanisms that are: (1)  $\text{Zn}^{2+}$  insertion/extraction, (2) Co-insertion of  $\text{H}^+$  and  $\text{Zn}^{2+}$  and (3) chemical conversion reaction.

### **1.6.1. Reversible $\text{Zn}^{2+}$ Insertion and Extraction Mechanism**

The conventionally studied  $\text{Zn}^{2+}$  storage mechanism is the reversible intercalation and deintercalation of  $\text{Zn}^{2+}$  into the cathodic host materials analogous to the  $\text{Li}^+$  intercalation

mechanism. The zinc metal anode undergoes oxidation during the discharge and dissolves into the electrolyte medium as  $Zn^{2+}$  ions. The dissolved divalent  $Zn^{2+}$  ions intercalate into the cathode, where it receives electrons and undergoes oxidation. During charging, the reverse happens. The overall  $Zn^{2+}$  insertion/extraction mechanism can be defined as:



Most tunnel-shaped layered cathode structures such as Manganese oxides and vanadium-based oxides store the  $Zn^{2+}$  ions preferably via the intercalation/deintercalation process.

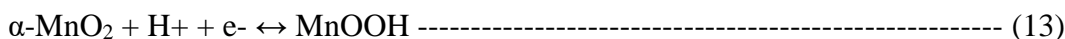
### 1.6.2. Co-insertion of $Zn^{2+}$ and $H^+$ ions:

Owing to the sluggish intercalation kinetics of  $Zn^{2+}$  in the cathode structure because of the larger ionic radii of hydrated  $Zn^{2+}$  and significant electrostatic repulsion, there is a simultaneous insertion of other ions with much higher diffusion kinetics compared to that of  $Zn^{2+}$ . This phenomenon was first investigated by Wang et al.<sup>46</sup>, where  $MnO_2$  underwent a simultaneous co-insertion of  $H^+$  and  $Zn^{2+}$  in the structure, which promotes the performance and specific capacity of the AZIB. The dual ion co-insertion mechanism was investigated using discharge galvanostatic intermittent titration technique, where two definitive voltage plateaus were observed. The overvoltage for the second plateau is estimated to be much larger (0.6 V) than the first region (0.08 V). This difference in the observed overvoltage was attributed to the insertion mechanism of two different ions. The higher overvoltage region was attributed to the insertion of much larger  $Zn^{2+}$  because of its slower diffusion kinetics and higher electrostatic interactions with the host. A similar mechanism is also observed in vanadium-based oxides by Chen et al.<sup>47</sup>

### 1.6.3. Chemical Conversion Reaction:

Unlike the conventional  $Zn^{2+}$  intercalation/deintercalation mechanism, Liu et al. introduced a new mechanism of  $Zn^{2+}$  storage in  $MnO_2$  based on the chemical conversion reaction between  $MnO_2$  and  $MnOOH$ .  $MnO_2$  reacts with the  $H^+$  ions in an aqueous electrolyte at a fully discharged state. To reach a neutral charge system, the  $OH^-$  ions react with  $ZnSO_4$  and  $H_2O$  in the electrolyte to form a  $ZnSO_4[Zn(OH)_2]_3 \cdot xH_2O$  phase. The reaction mechanism can be illustrated as below<sup>48</sup>:

At the Cathode:



At Anode:



### 1.7. Categories of Cathode Materials

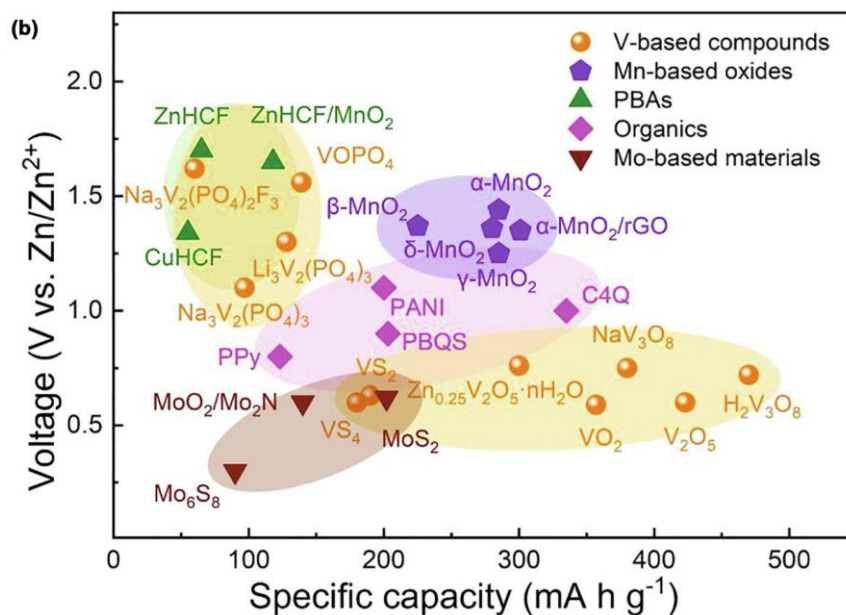


Figure 1.3. Comparison of specific capacities and average operating voltages of cathode materials for neutral aqueous ZIBs<sup>1</sup>. Adapted with permission from Liu, H.; Wang, J.-G.; You, Z.; Wei, C.; Kang, F.; Wei, B., Rechargeable aqueous zinc-ion batteries: Mechanism, design strategies and future perspectives. *Materials Today* **2021**, *42*, 73-98. Copyright © 2020 Elsevier Ltd.

During discharge, the  $\text{Zn}^{2+}$  ions are dissolved from the anode and migrate towards the cathode, where they get stored as charge carriers. The commercialization of the aqueous zinc ion batteries is largely limited by the lack of performance cycling stability of the cathode materials. Several cathode materials were studied for the aqueous zinc ion battery systems in the past years. They can be broadly grouped into three major categories such as inorganic materials<sup>49</sup> (transition metal oxides<sup>50-52</sup>, transition metal dichalcogenides<sup>53, 54</sup>, etc.), Organic materials (chloranil, phenanthrenequinone triangles, and covalent organic frameworks)<sup>55-57</sup>, and a third group comprised of a combination of inorganic and organic structures mainly including metal-organic frameworks<sup>58</sup>. Inorganic materials have caught much attention due to their versatile nature, higher specific capacity, and multiple valence states. Such inorganic materials can be divided into layered and non-layered materials. Layered materials predominantly include transition metal oxides such as  $\text{MnO}_2$ <sup>59</sup>,  $\text{V}_2\text{O}_5$ <sup>60</sup>,  $\text{MoO}_3$ <sup>52</sup>, etc., and transition metal dichalcogenides  $\text{MoS}_2$ <sup>61</sup>,  $\text{VS}_2$ <sup>62</sup>,  $\text{TiS}_2$ <sup>63</sup>, etc.; layered inorganic materials are generally made up of several monolayers bonded by weak van der Waals interaction. However, the non-layered materials include olivines and spinel-type structures such as ( $\text{ZnMn}_2\text{O}_4$ <sup>64</sup>,  $\text{Mn}_3\text{O}_4$ <sup>65</sup>,  $\text{Co}_3\text{O}_4$ <sup>66</sup>, etc.). Layered inorganic materials can effectively (de)intercalate  $\text{Zn}^{2+}$  ions with high cycling stability and coulombic efficiency, In contrast, the non-layered inorganic cathode structures have a comparatively higher specific capacity than the layered structures but lack cycling stability as the structures pulverize after a few intercalations/deintercalation processes. Hence layered structures offer better advantages in terms of specific capacity, cycling stability, and decreased capacity fading when considered for practical grid-scale storage applications. The specific capacities and operating voltages of various cathode materials are compared in Figure 1.3. In this thesis, Vanadium pentoxide ( $\text{V}_2\text{O}_5$ ) and Molybdenum

disulfide ( $\text{MoS}_2$ ) are considered representative members of the broader layered inorganic materials group.

### 1.7.1. Layered Manganese Based Oxides

There are different types of Manganese oxide structures reported with various crystallographic polymorphs such as  $\alpha$  (pyrolusite)<sup>59</sup>,  $\beta$  (ramsdellite)<sup>36</sup> with tunnel type structures, spinel-type structures ( $\lambda$ - $\text{MnO}_2$ )<sup>67</sup> and  $\delta$ -birnessite type  $\text{MnO}_2$  with layered structure<sup>68</sup>. All manganese dioxide materials have been applied as cathodes in aqueous zinc ion batteries. Manganese oxides are particularly attractive due to their increased safety, abundance, and multiple oxidation states. Among the different manganese oxides, the birnessite  $\delta$ - $\text{MnO}_2$  is the classic layered type made up of several layers of  $\text{MnO}_6$  octahedra weakly bound by the edges by van der Waals attraction with an optimal interlayer spacing of  $\sim 0.7$  nm. The layered type  $\delta$ - $\text{MnO}_2$  was applied as ZIB cathode material by Mo et al. in 1997<sup>69</sup>. However, this material experienced severe capacity fading after a few  $\text{Zn}^{2+}$  (de)intercalation cycles. This can be explained by the irreversible dissolution of  $\text{Mn}^{2+}$  into the electrolyte leading to the structural disintegration and loss of active material. Recently Alfaruqui et al. investigated the structural evolution of layered  $\text{MnO}_2$  cathode during the  $\text{Zn}^{2+}$  intercalation with the help of in situ characterization techniques. The layered  $\text{MnO}_2$  undergoes an irreversible phase transformation into spinel structure, causing the volumetric expansion and subsequent structural degradation and capacity fading. Overall, the Mn-based cathode structures face three major complications<sup>70</sup>, including: 1)  $\text{Mn}^{2+}$  dissolution, 2) Structural disintegration and irreversible phase transformation, and 3) Complicated  $\text{Zn}^{2+}$  storage mechanisms. Such complications can be overcome by incorporating structural modifications, protective surface coating, and the inclusion of  $\text{Mn}^{2+}$  additive to the electrolyte to prevent the  $\text{Mn}^{2+}$

dissolution, which have been extensively studied over the past few years to improve the electrochemical performance of the Mn-based cathode materials<sup>71</sup>.

### **1.7.2. Layered Vanadium Based Oxides**

Vanadium-based oxides are particularly interesting owing to their flexible crystal structures, open frameworks, and multiple valence states of the vanadium metal centers such as  $V^{3+}$ ,  $V^{4+}$ , and  $V^{5+}$  that allow increased redox-active sites, significantly enhancing the specific capacity and improves the cycling stability. The Vanadium oxide materials reported with tetrahedral  $VO_x$  structures with mixed  $V^{4+}/V^{5+}$  oxidation states such as  $V_3O_7$ <sup>72</sup> and  $V_4O_9$ <sup>73</sup> are not much explored for the AZIB applications. This can be attributed to irreversible structural change due to the reduction in the  $V^{5+}$  metal centers and the complex  $Zn^{2+}$  storage mechanism in such compounds. However, the tetrahedral structures can be converted into trigonal bipyramidal or square pyramidal structures by introducing one or more oxygen atoms to the structure. The four oxygen atoms in the bottom of the trigonal bipyramidal structure and square pyramidal structures are non-coplanar and coplanar respectively<sup>74</sup>. At the same time, the sixth oxygen atoms in the nearest unit cell can convert the square pyramidal structure into regular/distorted octahedral structure. Such continuous polyhedral structures can form into various layered and three-dimensional open structures that enable reversible intercalation/deintercalation of  $Zn^{2+}$  ions without much structural and phase change and thus avoiding structural disintegration resulting in much higher cycling stability<sup>75</sup>. However, the vanadium-based oxide structures suffer from a few other disadvantages such as low operating voltages (generally 0.2-1.6 V), higher toxicity, and slower  $Zn^{2+}$  diffusion kinetics. Several structural modification strategies such as interlayer expansion through the insertion of water molecules/other alkali metal ions/copolymer structures,

development of nanostructures, the introduction of conductive carbon additives, defect engineering, and morphology control will be discussed further in later sections.

### **1.7.3. Layered Transition Metal Dichalcogenides**

Transition metal dichalcogenides are an exciting class of inorganic layered materials with a general elemental formula of  $\text{MX}_2$ . M represents the transition metal atom from groups IV-VII B, and X represents the chalcogenides, usually S, Se, and Te. There are various transition metal dichalcogenide materials, including  $\text{MoS}_2$ <sup>61</sup>,  $\text{WS}_2$ <sup>76</sup>,  $\text{MoSe}_2$ <sup>77</sup>,  $\text{TiS}_2$ <sup>63</sup>,  $\text{WTe}_2$ <sup>78</sup>, etc., Among them,  $\text{MoS}_2$  is the main element that is reportedly abundant in nature and can be widely found in many geological formations such as granite pegmatite veins, granite cracks, Cu-Mo, and Mo-mineralization. The high abundance and high quality of the naturally occurring  $\text{MoS}_2$  crystals make them interesting for energy-related research purposes. The bulk structure of the transition metal dichalcogenides resembles the stacked-layer structure of graphite. In contrast, bulk TMDs exhibit a wide range of polymorphs and polytypes. The atoms X-M-X in the individual monolayer are usually bound by strong covalent bonds and the monolayers are assembled by weak van der Waals interactions making it feasible for the insertion and storage of charged species making them a promising material for energy storage applications. Based on the different stacking polytypes, each  $\text{MoS}_2$  exhibits a wide variety of polymorphs such as 1T, 2H, and 3R representing the trigonal, hexagonal, and rhombohedral crystal structures<sup>79</sup>. Unlike graphite, which exhibits a semimetal nature with a bandgap of 0 eV,  $\text{MoS}_2$  structures exhibit variable bandgap ranging from 0 eV – 2 eV showing both semi-metallic and semiconducting properties depending on the elemental composition, number of layers, and presence of heteroatoms and doping atom<sup>80</sup>. The band gap of the  $\text{MoS}_2$  structures can be effectively tuned to improve their respective electronic, optical, and electrochemical properties of the compounds. The layered  $\text{MoS}_2$  structure consists of a few

monolayers with an interlayer spacing of approximately 0.67 nm, and the Mo-Mo bond length varies between 3.15 Å<sup>80</sup>.

## 1.8. Overview of Challenges with AZIB

Despite the advantages of the cathode materials, they have some disadvantages that need to be addressed to commercialize the AZIB battery systems successfully. The disadvantage of their practical applications originates from the two major obstacles<sup>41</sup> namely 1) the larger size of the hydrated zinc with ionic radii of approximately 4.3 Å formed as a result of the coordination bond formed between the Zn<sup>2+</sup> ions and the surrounding six water molecules in the aqueous electrolytes. (2) the increased electrostatic attraction between the divalent zinc ions and the cathodic host structures causing the sluggish transport kinetics of Zn<sup>2+</sup> ions. These abovementioned problems can seriously affect the storage of Zn<sup>2+</sup> in the existing cathode structures rendering poor cycling stability and specific capacity. The sluggish transport kinetics of the hydrated divalent Zn<sup>2+</sup> ion can be improved by improving the structural design of the cathode materials. The enhanced ion and electron transport properties, sufficiently high electrical conductivity, shorter ion diffusion length and profuse transport channels in the cathodic structure helps in improving the electrochemical performance of the electrode.

The effective diffusion coefficient of any given electrode can be defined by the following equation:

$$D_{\text{eff}} = D_0 (\varepsilon/\tau) \text{----- (16)}$$

Where  $D_{\text{eff}}$  and  $D_0$  are the effective ion diffusion coefficient inside the electrode and the bulk electrolyte,  $\varepsilon$  and  $\tau$  are the porosity and channel tortuosity of the electrode structure. Based on this equation, the effective ion diffusion coefficient can be manipulated by carefully engineering the pore size and increasing the tortuosity of the ion diffusion channels within the electrode. In addition

to improving the ionic conductivity of the electrode, the electronic conductivity of the electrode material also needs to be improved simultaneously to achieve the desired battery performance.

## **1.9. Design Strategies and Structural Engineering in AZIB Cathodes**

As discussed in the previous section, the cathode structures need to be carefully engineered with higher ionic conductivity, well-connected and continuous electrical network, enhanced electron transport kinetics to improve the electrochemical performance of the AZIBs. Several strategies for the modification of cathodic architectures has been reported previously which can be broadly classified into: 1) Introduction of foreign molecules or alkali metal ions to expand the interlayer distance in the layered cathode materials, 2) Effectively reduce the electrostatic effect of divalent  $\text{Zn}^{2+}$  ions by screening the charge with incorporation of water molecules, 3) Introduction of structural defects to improve the electrical conductivity and improve the electron transfer between the redox sites and  $\text{Zn}^{2+}$  ions, and 4) Shorten the ion diffusion distance by effectively controlling the nanostructure morphology of the cathode structure. The advantages and limitations of these methods are further discussed in detail in this section.

### **1.9.1. Interlayer Intercalation Strategy**

Layered structures are comprised of several atomic monolayers bound by weak van der Waals interaction with a much stronger in-plane chemical bonds between the atoms. The larger interlayer distance between the adjacent monolayers provides wider two-dimensional diffusion channel and possesses higher ionic/charge transfer dynamics facilitation increased  $\text{Zn}^{2+}$  ion storage. However, such layered materials often show severe structural disintegration and end up pulverizing after few intercalation/deintercalation of  $\text{Zn}^{2+}$  ions<sup>75</sup>. Intercalation engineering is particularly beneficial as structural pillars to hold the layered structures together over several

(de)intercalation cycles and the comparatively larger alkali metal ions expands the interlayer spacing further reducing the energy barrier for the insertion/extraction of the divalent ion.

In 2016, Nazar et al.<sup>12</sup>, reported the Zinc vanadate with the formula  $Zn_{0.25}V_2O_5 \cdot nH_2O$  obtained by the interlayer ionic insertion of  $Zn^{2+}$  ions into the layered  $V_2O_5$  structures as a ultrastable aqueous zinc ion battery cathode material with a high specific capacity of 220 mAh/g at a 15C rate and excellent long-term stability with a capacity retention of about 80% after 1000 cycles. This can be attributed to the strong covalent bond formed between the  $Zn^{2+}$  ions to the two apical oxygen atoms within the  $V_2O_5$  layers along with four  $H_2O$  molecules forming  $ZnO_6$  octahedra which showed much longer cycling stability than the pristine  $V_2O_5$  structures. Similar to this, Mai et al.<sup>81</sup>, reported the introduction of  $Na^+$  ions in the interlayers of classic layered  $V_2O_5$  structure converts the crystal structure into an open tunnel framework. The strong chemical bond formed between  $Na^+$  ion and the single bonded oxygen atoms between the tunnels provides more stable binding between the layers than the intercalating  $Zn^{2+}$  ions rendering excellent long term cycling stability of 93% for over 1000 cycles as evidence to the structural integrity of sodium ions intercalated vanadium pentoxide nanowires. There are other similar materials subsequently reported in the research community including  $Ca_{0.25}V_2O_5 \cdot nH_2O$ <sup>82</sup>,  $K_{0.25}V_2O_5 \cdot nH_2O$ <sup>83</sup> and layer expanded  $MoS_2$ <sup>84</sup> etc., signifies the impact of the introduction of guest ions into the layered structure.  $H_2O$  is another species that are interesting as a guest molecule for the interlayer engineering procedure in the layered cathode structures<sup>85</sup>. In addition to mechanically supporting the host structure,  $H_2O$  also has the ability to shield the divalent charge of the  $Zn^{2+}$  ions and thereby reduce the electrostatic attraction between the charge carrier and cathode structure and also acts as lubricant to facilitate faster and smoother  $Zn^{2+}$  transport kinetics. In 2018, Yan et al.<sup>86</sup>, investigated the role of interlayer  $H_2O$  molecules in layered  $V_2O_5$  cathode structures in details and reported that

in addition to increasing the interlayer spacing, the introduction of approximately 0.2 mol of H<sub>2</sub>O shows effective charge shielding behavior and improves the interfacial electron transport and significantly enhanced Zn<sup>2+</sup> diffusion property. He also suggested that the water lubricated V<sub>2</sub>O<sub>5</sub> cathode coupled with zinc anode can be a promising alternative to the traditional LiCoO<sub>2</sub>/graphite lithium-ion battery systems providing power densities up to 10<sup>2</sup> – 10<sup>4</sup> W/Kg which is 30 times larger than the mentioned lithium-ion battery system.

### **1.9.2. Defect Engineering**

Defect engineering is considered an influential strategy to improve the electronic conductivity, ionic conductivity and affect the crystal structures in such a way to enhance the Zn<sup>2+</sup> storage properties of the AZIB cathode materials. Introduction of defects in the structure can be of different types such anionic defects including oxygen vacancy and sulfur deficiencies, cationic vacancies or a combination of both<sup>87</sup>. So far, oxygen deficient defects were widely studied as an effective strategy to increase the Zn<sup>2+</sup> storage capacity of the vanadium oxide-based cathode structures. Introduction of oxygen vacancies in the cathode structures can be achieved in highly reducing environments that are widely done using one of the two methods. The first method suggests the use of chemical reagents with strong reducing properties. For instance, oxygen deficient VO<sub>2</sub> material was successfully synthesized by reducing it with NaBH<sub>4</sub> producing VO<sub>1.88</sub><sup>88</sup>. The second method suggests the use of heat treatment in the highly reducing atmosphere such as 3% H<sub>2</sub> or 5% H<sub>2</sub> gas. In addition to the oxygen defects in oxide compounds, sulfur vacancies and cationic vacancies were also studied in the sulfur-based cathode materials which are generally obtained by annealing the MoS<sub>2</sub> compounds in various annealing temperatures in the H<sub>2</sub> atmosphere<sup>89</sup>.

The presence of oxygen defects or sulfur vacancies in the structure exhibits several advantages such as improved electronic transfer properties, enhanced  $\text{Zn}^{2+}$  adsorption and desorption and shows the presence of larger volume of active sites for  $\text{Zn}^{2+}$  interaction. The deficiency of electronegative oxygen ions in the vanadium oxides reportedly weakens the electrostatic attraction between the  $\text{Zn}^{2+}$  ions and the cathode structure and promotes the  $\text{Zn}^{2+}$  diffusion coefficient than their defect free counterparts. The oxygen vacancy also opens up more ion transport channels along with the usual pathways. Wang et al.<sup>90</sup>, reported that oxygen defects substantially reduce the energy barrier for  $\text{Zn}^{2+}$  ion diffusion in potassium vanadate by two times than the pristine potassium vanadate structure. Apart from that, the presence of sulfur vacancies in the  $\text{MoS}_2$  structures improved the electrochemical performance with a specific capacity of 135.5 mAh/g at 100 mA/g by increasing the active sulfur edge sites.

### **1.9.3. Composite Engineering**

Most of the cathode materials including transition metal oxides and transition metal dichalcogenides have inherently poor electrical conductivity and low mechanical strength causing the structural instability and cathode dissolution during the multiple  $\text{Zn}^{2+}$  intercalation processes. Such challenges can be overcome by the incorporation of conductive framework in the cathode that primarily helps in improving the electrical conductivity and acts as a suitable to buffer to withstand the volume expansion that occurs during the  $\text{Zn}^{2+}$  insertion/extraction. Carbon materials such as reduced graphene oxide<sup>91</sup>, carbon nanofibers<sup>92</sup>, carbon nanotubes<sup>93</sup>, amorphous carbon<sup>94</sup>, super-p are often used as conductive carbon additives in the AZIB cathode structure. There are two methods of incorporation of conductive carbon additives are widely reported in literatures so far. First technique is physically mixing the carbon additive to the active material along with a polymer binder and solvent to prepare a homogeneous slurry and uniformly coated on the current

collector substrate. Second is used to use the hydrothermal method to uniformly grow the electrochemically active structures on the conductive carbon skeleton using them as template for the growth. AZIB using functionalized holey graphene as cathode showed exceptional specific capacity of 234 mAh/g at 0.1 A/g and 43% and excellent long cycling stability with 98% capacity retention after 4000 cycles at a higher current density of 10 A/g<sup>95</sup>. Zhou et al., first demonstrated a binder free Zn-MnO<sub>2</sub>/rGO synthesized via vacuum filtration technique exhibited exceptional specific capacity of 332.2 mAh/g at 0.3 A/g and a capacity retention of 96% after 500 cycles at 6 A/g. Among the different methods, the physical mixing of active cathode materials and conductive carbon additives is generally simpler of all to incorporate the conductive additives. However, it often leads to insufficient contact between the active material and agglomeration which can further be improved using other techniques including vacuum filtration. Hydrothermal method is widely applied to synthesize hybrid cathode materials that ensures improved contact between the cathode active material and the conductive carbon template. This was first reported by Yang et al. in VS<sub>4</sub>/rGO nanocomposite showing improved specific capacity of 297 mAh/g at 0.2 A/g<sup>96</sup>. After that, the hydrothermal technique is vastly improved and developed and is now trusted as a more reliable and reproducible technique to incorporate conductive carbon additive in the cathode structure.

#### **1.9.4. Nanostructure Engineering and Morphology Control:**

Nano structuring of the bulk structures and by effectively controlling the dimensions and shape of the cathode materials can improve their electrochemical performance. The nanostructures improve the ion diffusion coefficient, accommodate the structural stress, and buffers the volume changes occurring during the intercalation/deintercalation of the hydrated Zn<sup>2+</sup> ions and thus alleviating the structural collapse resulting in improved reversibility and cycling stability. For

example, MnO<sub>2</sub> based cathode structures encounter severe capacity degradation due to the multiple phase transformation during the intercalation/deintercalation of Zn<sup>2+</sup> ions in the structure<sup>59</sup>. This has been alleviated using the polyaniline intercalated MnO<sub>2</sub> nanolayers which exhibited an exceptional stability for over 200 cycles with a high specific capacity of 280 mAh/g at 0.2 A/g suggesting more than 90 % utilization of the MnO<sub>2</sub> active materials<sup>97</sup>. Similarly, several nanostructured cathode structures show improved Zn<sup>2+</sup> storage capacity and high cycling stability due to the increased ion diffusion coefficient, high tolerance towards volume changes and increased active sites for Zn<sup>2+</sup> interaction.

### 1.10. Summary:

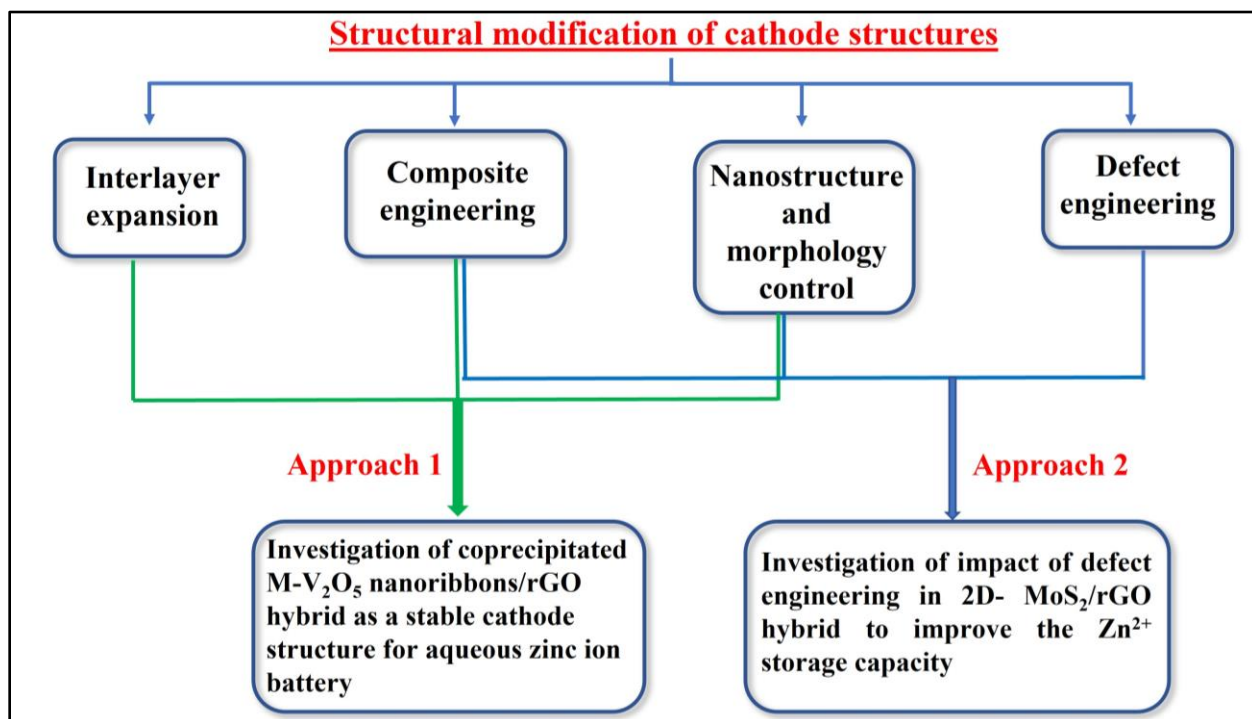


**Figure 1.4.** Schematic flowchart illustrating the design strategies adapted in the different approaches in this thesis dissertation.

In summary, the optimal design of cathode structures involves four different structural modification strategies as discussed above. Each modification has a few advantages and disadvantages which needs to carefully be controlled and manipulated to achieve higher Zn<sup>2+</sup>

storage capacity with higher stability towards multiple  $\text{Zn}^{2+}$  intercalation/deintercalation cycles. Several common cathode materials including manganese and vanadium-based oxides suffer from poor electrical conductivity and cycling stability. The poor electrical conductivity can be improved by the addition of conductive carbon templates such as rGO, CNFs etc., which can collectively improve the electrical conductivity of the hybrid. The carbon-based templates also possess higher mechanical strength compared to that of the active cathode structure which can help in upholding the structural integrity of the hybrid cathode structures over several cycles. However, most of these carbon materials do not actively participate in the  $\text{Zn}^{2+}$  storage, which reduces the gravimetric energy density and specific capacity if used in larger amounts. Hence, the gravimetric composition of the conductive carbon additive needs to be carefully controlled to improve the specific capacity as well as the cycling stability of the hybrid cathode structure. The development of nanostructures of the bulk cathode structures can effectively increase the interaction between the  $\text{Zn}^{2+}$  ions and the active material and reduces the length of the ion diffusion pathway which improves the ion transport kinetics of the  $\text{Zn}^{2+}$  ion in the active cathode structures. However, the nano structuring of the bulk cathode structure also has few disadvantages such as decrease in the particle size can cause severe agglomeration of the active material which defeats the purpose by reducing the active specific surface area for the ion interaction and leads to the dissolution of active materials into the electrolyte. The abovementioned factors reduce the overall utilization of the active cathode materials and consequentially lower the obtained specific capacity and cycling stability. In this thesis, we have reported two different approaches after systematically investigating the impacts of the different modification strategies in the performance of the layered cathode structures. Both the works involves the composition engineering and nano structuring strategies to avoid the interference of intrinsically poor electrical conductivity and mechanical strength in studying the

influence of other strategies in the  $\text{Zn}^{2+}$  storage behavior of the cathode structure. In chapter 3, the effect of concentration of the Mo-deficient defects in the few layered  $\text{MoS}_2$  nanopatches are studied after carefully tuning the defect density in the structure. Whereas in chapter 4, the impact of interlayer expansion in the layered  $\text{V}_2\text{O}_5$  nanoribbons after the introduction of single and dual cations have been compared to analyze the effect of different cations in the  $\text{Zn}^{2+}$  storage process of the layer expanded  $\text{V}_2\text{O}_5$  nanoribbons.

## Chapter 2 - Synthesis and Electrochemical Characterization of Cathode Materials for AZIB

### 2.1. Introduction to Microwave Assisted Synthesis Process

Since its introduction in 1986, microwave assisted synthesis procedure have been extensively researched and applied in various fields including the organic and inorganic synthesis, synthesis of advanced functional nanomaterials etc., Microwaves are a part of electromagnetic spectra with frequency and wavelength in the range of 300 MHz – 300 GHz and 1m-1mm respectively<sup>98</sup>. Microwave radiation is capable of penetrating deep inside the medium and gets converted into heat energy depending on the intrinsic properties of the reacting medium. Microwave heating mechanisms are of two types of namely dipolar polarization and ionic conduction<sup>99</sup>. Application of microwave irradiation to a given sample causes alignment of dipoles or ions with respect to the electric field. Upon the application of electromagnetic field, the dipoles are subjected to continuous alignment and realignment to the electric field. Based on the time taken by a sample ion/molecule to orient and disorient to the applied electric field, different amounts of heat are produced through either molecular friction or dielectric loss. If the dipole does not have enough time to realign or if it realigns very quickly, there will be no heating of the sample which is dependent on the frequency of microwave irradiation. Based on the experimental evidence in the past years, it is suggested that 2.45 GHz is the optimum frequency which induces electric field oscillation and thereby heating a wide range of molecules. The dielectric property of any given material is generally defined by two properties (i) its dielectric constant  $\epsilon'$ , ability of absorption of applied electromagnetic radiation, (ii) its dielectric loss  $\epsilon''$ , its ability to convert the absorbed electromagnetic radiation into heat. The ratio of dielectric loss to dielectric constant of a given

material at a particular frequency is called tangent loss,  $\tan \delta = \epsilon'' / \epsilon'$ . The tangent loss factor of the materials elucidates the ability of the material to convert the microwave radiation to heat at a given frequency and temperature. The materials with high  $\tan \delta$  values effectively absorb the microwave irradiation and rapidly heat the system. The controlled heating mechanism of the microwave assisted synthesis technique provides great control over the morphologies and crystal structures of the products. The crystal size and shape of the nanomaterials are significant factors contributing to their functional properties<sup>100</sup>. The broad range of tangent loss values of various organic solvents and the precursors offers a wide range of combinations to effectively control the morphology of the synthesized nanomaterials.

## **2.2. Microwave Synthesis Vs. Conventional Hydrothermal Synthesis**

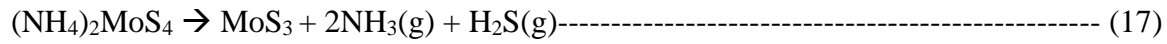
The inorganic synthesis has been conventionally carried out using conductive heating process via external source, for example using an oil bath. However, this has been long called as a slow and inefficient process as it primarily depends on the intrinsic thermal conductivity of the various reactants in the mixture which affects the penetration of heat energy and its homogenous distribution throughout the reaction system. This non-uniform distribution of temperature leads to unwanted side reaction and thus low yield of desired reaction products as a result. Whereas, in the case of microwave irradiation, uniform and efficient heat transfer by creating several internal microwave hotspots by directly coupling the dipolar molecules with applied microwave energy<sup>101</sup>. In contrary to the conventional hydrothermal technique, the microwave irradiation technique possesses certain unique properties<sup>102</sup> such as: 1) the superheating effect of solvents at atmospheric pressure, 2) the selective heating of different reacting species based on their microwave absorbing capability. Selective heating property of the microwave irradiation has been specifically exploited in the works in later chapters. The microwave absorbing ability of different

reactants can differ in several orders of magnitude which plays a vital role in the synthesis of hybrid and hierarchical nanostructures which find widespread application in most of the energy conversion and storage devices<sup>103</sup>. Selective heating helps in controlling the heating pattern within a heterogenous reaction system where a specific material can be selectively heated whereas the other materials can stay unaffected either as a template or due to its temperature intolerance which is practically impossible in a conventional hydrothermal synthesis method. Selective heating has also been reported to play a major role in the uninterrupted growth of micron sized patterns consisting of nanoparticles with uniform morphology and dimensions in contrary to the hydrothermal process where the inhomogeneities are often enhanced by the inbuilt temperature gradient which causes poor nucleation process and broad size distributions<sup>104</sup>. In addition to that, the microwave irradiation process is considered eco-friendly compared to the conventional hydrothermal process considering the volume of the solvent used, volume of the toxic byproducts generated during the hydrothermal process. Despite showing enormous improvement in the rate of the reaction, yield and the unique properties of the products due to selective heating, there is still a question regarding the energy efficiency of the process especially when it is scaled up since the conversion of electric energy to microwave energy is reported only in the range of 50 – 65 % which still needs substantial improvement<sup>100</sup>.

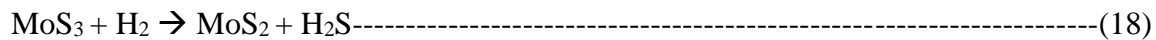
### **2.2.1. Synthesis of Two Dimensional MoS<sub>2</sub>/rGO hybrid<sup>105</sup>**

The specific heating by microwave irradiation is used to convert the ammonium tetrathiomolybdate (ATM) and GO precursors in tetrahydrofuran (THF) solution. At the reaction conditions of 170 °C and ~21 bar, a large portion of the adsorbed ATM molecules are converted into solid MoS<sub>3</sub> nanoparticles while the GO precursors are converted into reduced graphene oxide

(rGO) nanosheets, forming the intermediate MoS<sub>3</sub>/rGO hybrid material<sup>106</sup> via the following reaction:



The deep red-brown colored ATM/GO precursors are converted into the dark brown MoS<sub>3</sub>/rGO intermediate in this process. As will be discussed in later sections, the MoS<sub>3</sub> intermediate has an amorphous chain structure with a composition of Mo<sup>4+</sup>(S<sup>2-</sup>)(S<sub>2</sub><sup>2-</sup>). The Mo is reduced from Mo<sup>6+</sup> to Mo<sup>4+</sup> while some S<sup>2-</sup> is oxidized into S<sub>2</sub><sup>2-</sup>. In the 2<sup>nd</sup> step, the intermediate MoS<sub>3</sub>/rGO powder is further converted to black/grey MoS<sub>2</sub>/rGO hybrids by thermal reduction of S<sub>2</sub><sup>2-</sup> into S<sup>2-</sup> at 250 to 600 °C in a mixed gas of 3% H<sub>2</sub> and 97% Ar in a quartz tube furnace, following the reaction<sup>107</sup>:



The obtained MoS<sub>2</sub> varies from crystalline materials at high annealing temperature (up to 600 °C) to defective materials at lower annealing temperature (down to 250 °C). At the meantime, the quality of rGO is further improved by the thermal annealing. The properties of the material is further discussed in detail in chapter 3. It is noteworthy that the microwave-assisted technique is not only used to synthesize the high-quality 2D hybrid materials<sup>99</sup> but also help to control the defects in the MoS<sub>2</sub> structure in this structure. Comparing to the conventional hydrothermal process, the microwave-assisted synthesis reduces the reaction time by more than 70 times, i.e. from more than 12 hours to ~10 minutes<sup>99</sup>. The microwave energy directly activates the molecules that possess large dipole moments or ionic groups and thus heats the reaction system rapidly and uniformly<sup>108</sup>

### 2.2.2. Synthesis of V<sub>2</sub>O<sub>5</sub> Nanoribbons:

Over the past decade, the V<sub>2</sub>O<sub>5</sub> nanostructures have been investigated widely as efficient electrode materials for EESs such as lithium-ion batteries<sup>109</sup>, supercapacitors<sup>110</sup>, sodium ion batteries<sup>111</sup>, zinc ion batteries<sup>112</sup> etc. It has also been proven that the V<sub>2</sub>O<sub>5</sub> nanostructures such as nanorods<sup>113</sup>, nanowires<sup>114</sup>, nanospheres<sup>112</sup>, nanoribbons<sup>115, 116</sup> perform better with higher specific capacity and stability compared to its bulk counterparts. In the past, V<sub>2</sub>O<sub>5</sub> nanostructures were synthesized with solvothermal/hydrothermal methods<sup>115, 116</sup>, template-based methods<sup>117</sup>, and electrochemical deposition<sup>118</sup>. Among them, hydrothermal technique is considered easier and effective. The bulk V<sub>2</sub>O<sub>5</sub> is soaked in distilled water to intercalate the water molecules in between the V<sub>2</sub>O<sub>5</sub> layers. The microwave-assisted synthesis used in this work has been reported to be a faster and environmental-friendly technique compared to the conventional hydrothermal technique.<sup>119</sup> The microwave absorbing capacity of a material is defined by its dielectric loss, i.e., the  $\tan\delta$  value. The pre-intercalated V<sub>2</sub>O<sub>5</sub> structure contains water molecule (with  $\tan\delta = \sim 0.1$ ) is then dispersed in the microwave transparent THF solvent with a comparatively lower  $\tan\delta$  value (0.042). The specific heating of the microwave to the intercalated water molecules<sup>99</sup> leads to the breaking down and separation of the V<sub>2</sub>O<sub>5</sub> layers which are bonded by weak Van der Waals interaction and thus exfoliate the bulk V<sub>2</sub>O<sub>5</sub>  $\alpha$ -orthorhombic structure into V<sub>2</sub>O<sub>5</sub> NRs. The material and electrochemical properties of the V<sub>2</sub>O<sub>5</sub> nanoribbons are further discussed in detail in chapter 4.

### 2.3. Electrochemical Characterization

The general procedures used for the preparation of electrodes, coin cell assembly and electrochemical characterization techniques and their respective parameters are described in this

section. However, the specific procedure for each electrode material is presented in the chapters 3 and 4.

### 2.3.1. Preparation of Electrode

The active material is mixed with conductive carbon additive (super-p) and polymeric binder (Poly Vinylidene Fluoride (PVDF)) in appropriate proportions [80:10:10 (*w/w*) - for MoS<sub>2</sub>/rGO for V<sub>2</sub>O<sub>5</sub>/rGO cathode] and actively grinded for over 25 minutes using mortar and pestle. Approximate volume of N-methyl-2-pyrrolidone (NMP) was added to the mixture to form a homogenous slurry. The slurry is then uniformly coated on the titanium (16 mm) current collector substrate. The coated electrodes are then vacuum-dried at 80°C for about 12 – 14 hours to evaporate the organic NMP solvent in the electrode. The dried electrodes are then used for the coin cell assembly.

### 2.3.2. Coin Cell Assembly

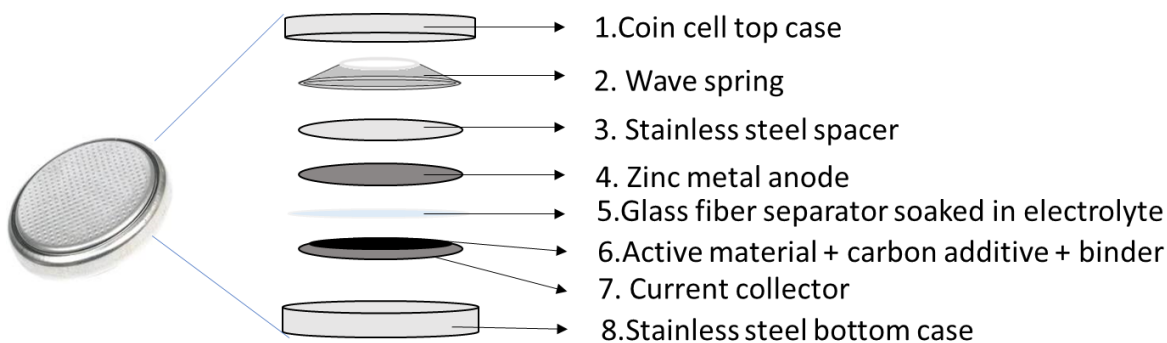


**Figure 2.1.** Schematic representation of AZIB Coin cell and the components.

All the coin cells are assembled using CR 2025 stainless steel casing. The components used to assemble the aqueous zinc ion battery coin cell are shown in the schematic figure. The coin cell consists of cathode where a homogenous slurry is coated on a titanium foil with 16 mm diameter and 0.1 mm thickness. The glass fiber separator is soaked with approximately 200  $\mu$ L of 2.0 M

ZnSO<sub>4</sub> aqueous electrolyte. The Zinc metal disc of 16.0 mm diameter and 0.1 mm thickness is used as anode. A stainless-steel spacer of 15.0 mm diameter and 0.5 mm thickness is used on the top of the anode to facilitate good contact between the electrode and the connecting lead. Over that, a wave spring of 15.0 mm diameter and 0.3 mm thickness is used to provide a spring effect to the coin cell.

### **2.3.3. Electrochemical Characterization**

The electrochemical properties of any AZIB cathode structure is studied using electrochemical characterization tests such as 1) Galvanostatic charge discharge tests, 2) Cyclic Voltammetry, 3) Long term cycling, 4) Electrochemical Impedance Spectroscopy. To perform these tests, instruments such as battery testers including Neware battery tester, MTI-8 channel battery tester, CHI Electrochemical Workstation, Princeton Applied Research PARSTAT 2273 Advanced Electrochemical System and Ivium-n-stat Multichannel Potentiostat.

#### **2.3.3.1. Galvanostatic Charge Discharge Process**

In a galvanostatic charge discharge process (GCD), a fixed current is applied to the working electrode to discharge and charge the electrode in a set potential window. Once the set potential limit is reached in a discharge process, the current is reversed, and the charge process occurs. The slope of the charge discharge curve is defined by the amount of charge stored per volt. A cycle is completed when a full charge and discharge process is over. The applied current is chosen based on the mass of the active material loading in the working electrode. Figure shows the representative charge discharge curve of an Aqueous Zinc Ion Battery. The specific capacity of an active material is calculated from the charge discharge profile of the cell. The charge stored in the active material is the product of the applied current (mA) and the time taken to complete one charge or discharge

cycle (hours). The specific capacity of the active material is calculated as the charge stored (Q) in the active material per gram mass of the active material (g) in the working electrode of the cell.

$$Q = i \text{ (mA)} * t \text{ (hours)} \text{ ----- (19)}$$

$$\text{Specific capacity} = Q / \text{mass of the active material (g)} \text{----- (20)}$$

The reversibility of the intercalation/deintercalation process is defined by the coulombic efficiency (CE). The coulombic efficiency of any working electrode is defined as the ratio of the amount of charge extracted during the discharge ( $\text{Zn}^{2+}$  deintercalation) process, i.e.,  $Q_{\text{dchg}}$ , to the amount of charge stored during the charging ( $\text{Zn}^{2+}$  intercalation) process, i.e.,  $Q_{\text{chg}}$ .

$$\text{CE} = Q_{\text{chg}}/Q_{\text{dchg}} \text{ -----(21)}$$

The cell is charged and discharged over several cycles at a specific current density and the capacity retention is measured after that to evaluate the stability of the intercalation and deintercalation of the charge carriers in the given cathode structure and structural integrity of the cathode to withstand multiple intercalation/deintercalation process.

### **2.3.3.2. Cyclic Voltammetry**

Cyclic voltammetry is one of the widely used electrochemical techniques to study the reduction and oxidation processes between the electrochemically active species in the working electrode and the charge carrier. The cyclic voltammetry is performed by sweeping the potential from a high voltage ( $E_1$ ) till low voltage ( $E_2$ ) in the negative direction at a particular scan rate, this is referred as cathodic scan. Upon reaching  $E_2$ , the direction is reversed and swept till  $E_1$  which is referred to as anodic scan. The peak obtained during the cathodic scan is referred to as cathodic peak and the peak current is called cathodic current and the anodic scan provides oxidation potential and anodic current. The cyclic voltammetry is also used to examine the reversibility of the desired electrochemical reaction. Electrochemical reversibility can be defined as the electron

transfer kinetics between the working electrode and the analyte or charge carrier. When a reaction involving soluble redox species in solution is electrochemically reversible, the peak separation between the cathodic and the anodic peak is reported to be  $\Delta E_p = 57 \text{ mV}^{120}$ . However not all the electrochemical reaction is reversible which can be analyzed based on the resulting peak separation. Particularly, the  $\text{Zn}^{2+}$  intercalation/deintercalation processes are much slower and limited by the slow diffusion process in the solid host materials. However, depending on the number of phase transitions, multiple pairs of insertion and extraction peaks can often be observed. The capacity can be calculated by integrating the CV curves, however, these curves are often used as a qualitative assessment rather than a quantitative measurement. It should be noted that the incorporation of low dimension nanostructures provides a much larger specific surface area. over that of traditional battery materials which results in more pseudocapacitive features.

## Chapter 3 - Tuning Defects in the MoS<sub>2</sub>/Reduced Graphene Oxide

### 2D Hybrid Materials for Optimizing Battery Performance

(This part of work was published in the journal of sustainable energy and fuels<sup>105</sup>)

#### 3.1. Introduction

Electrical energy storage (EES) has become an essential part of the modern world. The rising energy consumption and the global demand for clean energy are driving the development of EES systems that can be integrated with the existing energy systems. At present, an unmet demand is the large-scale EES systems<sup>121, 122</sup> to support the electrical grids and intermittent renewable energy techniques. Many EES systems such as Nickel-cadmium, Ni-MH, Lead acid batteries and Li-ion batteries (LIBs) have been extensively studied in the past years for this application. LIB is the leading technology due to its high specific capacity and decent lifetime. However, LIBs are limited by the high cost, low materials abundance, usage of flammable and toxic electrolytes, and environmental or safety issues. Multivalent metal-ion batteries such as Mg-ion batteries (MIBs) and Zn-ion batteries (ZIBs) have been identified as alternatives for the large-scale EES systems due to their divalent nature, higher volumetric capacity, high natural abundance and superior safety features<sup>122-125</sup>. The aqueous ZIBs are particularly attractive due to the environmental compatibility and low cost<sup>126</sup>. Many materials, including manganese oxides<sup>59, 126, 127</sup>, vanadium oxides<sup>116, 128</sup> and metal organic frameworks (such as Prussian blue analogues)<sup>129, 130</sup>, have been explored as the cathode materials for ZIBs. Most of these materials are based on intercalation of the multivalent ions in the host materials, which exhibits strong interactions with the host lattice and largely varied results. For example, the NASICON-structured Na<sub>3</sub>V<sub>2</sub>(PO<sub>4</sub>)<sub>3</sub> cathode showed a moderate capacity of 97 mAh g<sup>-1</sup> at 0.5 C and was able to retain 74% of the capacity after 100 cycles<sup>131</sup> and the MoO<sub>2</sub>/Mo<sub>2</sub>N heterostructured nanobelts showed a similar capacity of 113 mAh g<sup>-1</sup> at 1 A g<sup>-1</sup> for

1000 cycles<sup>132</sup>. In contrast, the layered  $\text{H}_2\text{V}_3\text{O}_8$  nanowire cathode exhibited a much higher capacity of 423.8 mAh  $\text{g}^{-1}$  at 0.1 A  $\text{g}^{-1}$  with 84.3% capacity retention after 1000 cycles<sup>133</sup>. Recently, it has been proposed that the proton intercalation may be the dominant reaction in these materials instead of intercalation by the divalent metal ions<sup>124, 125</sup>.

Transition metal dichalcogenides such as  $\text{MoS}_2$  have caught attention as a potential host for both monovalent and divalent ions due to their unique two-dimensional (2D) layered structure and the high theoretical capacity for Li-ion storage (up to 669 mAh  $\text{g}^{-1}$ )<sup>61, 134-136</sup>. The  $\text{MoS}_2$  structure consists of a layer of molybdenum atoms covalently bonded between two layers of sulfur atoms. The triatomic layers of  $\text{MoS}_2$  are linked by weak van der Waals forces<sup>137, 138</sup> similar to graphene, which can effectively accommodate the volume expansion to facilitate reversible intercalation/deintercalation of metal ions. The sulfur atoms in  $\text{MoS}_2$  have higher softness than oxygen atoms in metal oxides, which further improves the reversibility of intercalation/deintercalation of divalent metal ions<sup>124, 125</sup>. Despite the high theoretical capacity,  $\text{MoS}_2$  suffers from the low electrical conductivity and pulverization of the structure after a few cycles. The specific capacity for zinc-ion storage in high-quality  $\text{MoS}_2$ <sup>89</sup> was found to be only a few mAh  $\text{g}^{-1}$ <sup>89</sup>. These problems can be mitigated by modifying the structure through (1) increasing the interlayer spacing<sup>84, 128</sup>, (2) introducing active defects in the  $\text{MoS}_2$  structure to enhance  $\text{Zn}^{2+}$  ion adsorption<sup>89</sup>, and (3) forming a hybrid structure with carbonaceous materials to improve the electrical conductivity, mechanical strength and structural stability of  $\text{MoS}_2$  layers<sup>139, 140</sup>. Among which, defect engineering has been recently explored as an effective approach to enhance the specific capacity of  $\text{MoS}_2$  towards the storage of monovalent and divalent ions including  $\text{Li}^+$ ,  $\text{Na}^+$ ,  $\text{Zn}^{2+}$  ions<sup>89, 141, 142</sup>. The defect-rich  $\text{MoS}_2$  with sulfur vacancies was found to be effective in boosting the zinc-ion storage to 88.6 mAh  $\text{g}^{-1}$  at 1 A  $\text{g}^{-1}$  which was stable over 1,000 cycles when compared

to pristine MoS<sub>2</sub><sup>89</sup>. So far, the physical and chemical exfoliation techniques tend to form sulfur defects rather than molybdenum defects. Despite the high formation energy of 6.93 eV, Mo vacancies present many advantages including increased active sites, low diffusion energy, improved electrical conductivity and enhanced charge transfer ability. The Mo vacancies in the structure is reported to accelerate the charge transfer process and has strong binding affinity for the intercalating cations<sup>142</sup>. However, Mo vacancies have not been adequately explored for ion storage applications due to the poor stability. The rapid quenching in microwave-assisted synthesis was found to be effective in reducing the mobility of precursors and intermediate species, prevent the agglomeration and preserve the integrity of the defective MoS<sub>2</sub> structure<sup>143</sup>. It could be an efficient method towards the synthesis of hybrid nanomaterial structures with controlled defect engineering<sup>144</sup>. In addition, the rapid heating and cooling processes of microwave-assisted synthesis leads to fast phase transitions and produce nanostructures with small and uniform size distributions, which helps to enhance the ion transport.

In this study, we use a two-step reaction based on the specific microwave heating of the molecular Molybdenum (Mo) precursors and the dispersed graphene oxide (GO) flakes, which is followed by a thermal annealing in 3% H<sub>2</sub> and 97% Ar. Compared to the conventional hydrothermal process, the microwave-assisted synthesis significantly reduces reaction time<sup>99</sup> by directly activating the polar molecules and heating the reaction system uniformly<sup>108</sup>. The high dissipation factor (or tan  $\delta$  value) of the Mo precursor and GO is utilized to generate specific microwave heating to effectively convert GO into reduced graphene oxide (rGO) and induce the growth of MoS<sub>3</sub> intermediate material over the rGO template. By applying thermal annealing, the MoS<sub>3</sub> intermediate is converted into MoS<sub>2</sub> nanopatches anchored on the large monocrystalline rGO nanosheets. The 2D layered structure of MoS<sub>2</sub> and rGO enables them to remain stacked as a

stable hybrid material. The defect density in the MoS<sub>2</sub> nanopatches is tuned from the highly defective form with abundant S-rich (or Mo-deficient) defects at the annealing temperature of 250 °C to much less defective form at 600 °C. The unique structure and composition of these hybrid materials are systematically characterized and their energy storage properties as the LIB anodes and ZIB cathodes have been assessed. The results reveal that the defects in MoS<sub>2</sub>/rGO hybrids are insignificant for Li-ion storage based on the interlayer intercalation but have a dramatic effect on Zn-ion storage. The highly defective MoS<sub>2</sub>/rGO hybrid works the best for Zn-ion storage which is dominated by pseudocapacitive surface reactions. These results provide new insights in developing ZIB cathode materials.

## **3.2. Experimental**

### **3.2.1. Materials**

The precursors including Ammonium tetrathiomolybdate (ATM) and single-layer GO powder were purchased from Sigma Aldrich (St. Louis, MO) and ACS material LLC (Pasadena, CA), respectively. The CR2025 and CR2032 coin cell components were purchased from MTI corporation (Richmond, CA). The ZIB electrolyte was prepared with commercial zinc sulfate monohydrate from Sigma Aldrich (St. Louis, MO). The LIB electrolyte of Purolyte A4 series with 1.0 M LiPF<sub>6</sub> was purchased from Novolyte Battery Materials Co., Ltd. (Suzhou, Jiangsu, China).

### **3.2.2. Preparation of MoS<sub>2</sub>/rGO hybrid**

To synthesize MoS<sub>2</sub>/rGO, 15.0 mM ATM and 5.0 mg GO were dispersed in 6.0 ml tetrahydrofuran (THF) mixed with 1.0 ml distilled water. This mixture was ultrasonicated for about 20 minutes to obtain a homogenous suspension, which was then transferred to a 10 ml Pyrex glass microwave tube and put into an automated microwave system (Discover SP, CEM Corp., Matthews, NC) to irradiate with a microwave power of 300 W under the dynamic mode. It took

approximately 7 minutes for the temperature to ramp up to the setting of 170°C and then the system was held at this temperature for 10 min. During the reaction, the pressure went up to ~21 bar depending on the reaction conditions. After the reaction is over, the system was vented with compressed air and cooled down to the room temperature. The product was collected and centrifuged at 2000 rpm for about 15 min. The solid precipitate was collected and dried on a hotplate in the air at ~80 °C overnight. The dried material was further annealed in 3% H<sub>2</sub> and 97% Ar at 250°C, 325°C, and 600 °C, respectively. The corresponding samples were denoted as MoS<sub>2</sub>/rGO-250, MoS<sub>2</sub>/rGO-325 and MoS<sub>2</sub>/rGO-600, respectively. The control sample of bare rGO was synthesized following the same procedure as the MoS<sub>2</sub>/rGO samples except without adding any ATM precursor in the reaction mixture.

### **3.2.3. Material Characterization**

The Raman spectroscopy analysis was performed with a DXR<sup>TM</sup> Raman microscope (Thermo fisher Scientific, Madison, WI) with a 532 nm laser at the power of 10 mW, under a 10X objective lens with a slit width of 50 μm. The X-ray diffraction (XRD) study was done with a D8 Advance diffractometer (Bruker Corporation, Karlsruhe, Germany) with a Cu Kα radiation of wavelength 0.15418 nm and a slit width of 2 mm. The obtained XRD spectra of MoS<sub>2</sub>/rGO materials were further smoothed with origin pro software using a 5-point adjacent average filter. The surface composition and chemical environment of MoS<sub>2</sub>/rGO hybrids were analyzed using a PHI 5000 Versa XPS system (Chanhassen, MN) with a monochromatized Al Kα source (1486.7 eV). The transmission electron microscopy (TEM) images were obtained using Philips CM 100 with a tungsten source and a high tension of 100 kV. The field emission scanning electron microscopy (FESEM) images were obtained using a Topcon/ISI/ABT DS 130F FESEM microscope (Akashi Beam Technology Corporation, Tokyo, Japan). Thermogravimetric analysis

(TGA) was carried out with TGA Q50 system (TA instruments - Waters LLC, New Castle, DC) from the room temperature to 600 °C in the air. Elemental analysis results (%C, %H, %N, %S) presented in this work were acquired using a PE 2100 Series II combustion analyzer (Perkin Elmer Inc., Waltham, MA). The combustion tube packing was supplied with the instrument and consisted of the following components: copper oxide wires and electrolytic copper was used for CHNS reduction, and the oxygen reduction tube was packed with nickel plated carbon and quartz turning. The compounds were sampled using pressed tin capsules for CHNS Analysis and silver capsules for O analysis. 2,5-Bis(5-tert-butyl-benzoxazol-2-yl) thiophene was used as calibration standard for all the samples unless notified otherwise in the discussion. The combustion and reduction temperature were 975°C for CHNS analysis. All the standards and reagents were purchased from Perkin Elmer or Elemental America's Inc. The precision and accuracy of the results were estimated to be as low as +/- 0.3%. Vanadium pentoxide was used as combustion aid for sulfur analysis.

### **3.2.4. Electrochemical Characterization**

A slurry was prepared by mixing the active material (i.e. MoS<sub>x</sub>/rGO), carbon additive (Super-P, Alfa Aesar Co. Ltd., Massachusetts, USA) and a poly(vinylidene fluoride-co-hexafluoropropylene) (PVDF, Sigma Aldrich Co., St. Louis, MO) binder at the weight ratio of 8:1:1 with approximately 150 µL of N-methyl-2-pyrrolidone (NMP, Sigma Aldrich, St. Louis, MO) as the solvent. The homogenous slurry was then brush-coated onto a 0.10 mm thick titanium disk (MTI Corporation, Richmond, CA) with a diameter of 15 mm for ZIB half-cell tests. The coated electrodes were vacuum dried at 110°C overnight and used as the cathode in ZIBs. A Zn disk (Sigma Aldrich, St. Louis, Mo) of 0.25 mm thickness and 15 mm diameter was used as the anode. Commercially purchased glass fiber disk (El-Cell, Hamburg, Germany) of 18 mm diameter and 0.65 mm thickness was used as the separator. A 0.3 mm thick stainless-steel wave spring and

a 0.5 mm thick stainless spacer were placed behind the cathode to protect the electrode structure. The electrode and separator stacks were assembled into stainless steel coin cells (CR 2025, MTI Corporation, Richmond, CA) in the ambient atmosphere with 2.0 M ZnSO<sub>4</sub> aqueous solution as the electrolyte. Electrochemical characterization of the cells was carried out in the cell voltage window of 0.25 - 1.3 V in ZIB half-cell tests.

The MoS<sub>2</sub>/rGO material was also tested as the LIB anode in a half-cell in stainless steel coin cells (CR-2032, MTI Corporation, Richmond, CA). The MoS<sub>2</sub>/rGO slurry was prepared like ZIB cathode described above. The prepared MoS<sub>2</sub> slurry was brush-coated on a copper disk of 0.10 mm in thickness and 15 mm in diameter. The electrolyte used in LIB tests was 1.0 M LiPF<sub>6</sub> in a mixture of 1:1:1 (v/v/v) ethylene carbonate (EC), ethyl methyl carbonate (EMC) and dimethyl carbonate (DMC) with 2% vinylene carbonate additive. All LIB cells were assembled in an argon-filled LabStar 50 stainless steel glovebox (MBraun, Garching, Germany) in a controlled atmosphere of < 0.5 ppm O<sub>2</sub> and < 0.5 ppm H<sub>2</sub>O. The tests were carried out in the cell voltage window of 0.50 - 3.0 V. All battery tests were done with a BTS 4000 5V 50 mA Battery Tester (Neware, Shenzhen, China) and the CV tests were performed using CHI 440A (CH Instruments Inc., Austin, TX).

The galvanostatic charge/discharge curves were measured at constant cell current at preset values. However, the mass of the coated material varied between 1.0 and 2.0 mg on each electrode, which can be determined by measuring the weight of bare Ti or Cu disks and those after coating and drying the active materials. In order to compare electrode performance at similar current densities, the cell currents were converted into the current densities in some figures. The control rGOs were measured in the same way for both Li-ion and Zn-ion half cells by replacing the active materials with corresponding rGOs.

### 3.3. Results and Discussion

#### 3.3.1. Synthesis design

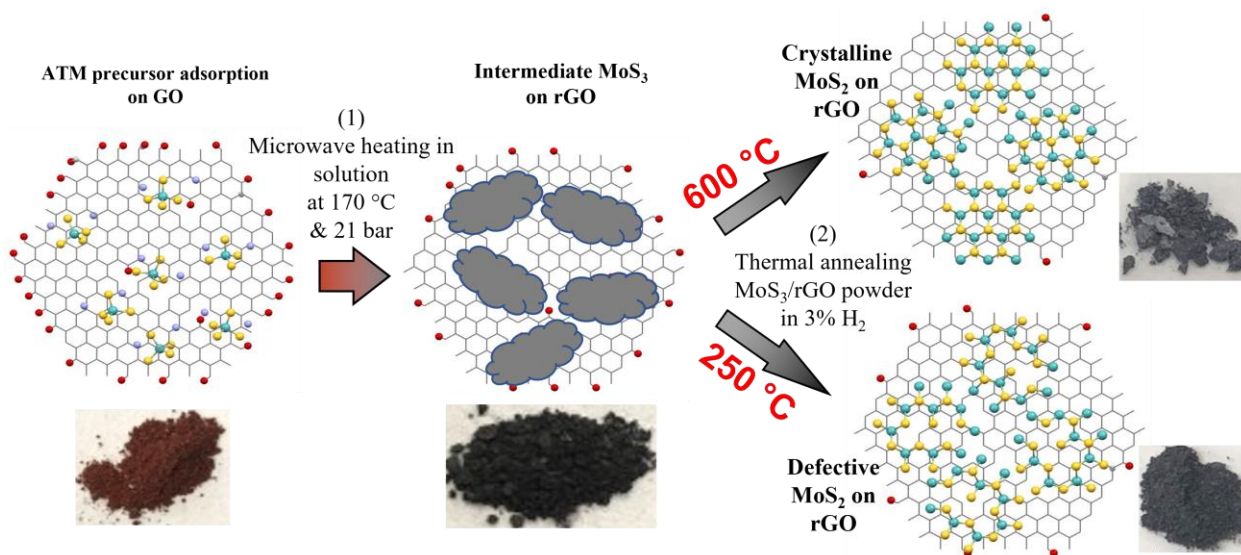
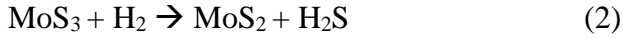


Figure 3.1. Schematic illustration of the two-step synthesis of MoS<sub>2</sub>/rGO hybrid materials by microwave-heating of ATM and GO precursors in THF followed by thermal annealing the intermediate MoS<sub>3</sub>/rGO powder at varied temperature in 3%H<sub>2</sub>/97%Ar in a tube furnace. Reproduced from Muthukumar, K.; Leban, L.; Sekar, A.; Elangovan, A.; Sarkar, N.; Li, J., Tuning the defects in MoS<sub>2</sub>/reduced graphene oxide 2D hybrid materials for optimizing battery performance. *Sustainable Energy & Fuels* **2021**, 5 (16), 4002-4014 with permission from the Royal Society of Chemistry

Microwave irradiation technique is reported to be a facile technique for the rapid synthesis of hybrid materials. A two-step method has been employed here to synthesize the MoS<sub>2</sub>/rGO hybrid materials with tunable defect densities. As shown in Figure 3.1, in the first step, the 10 min specific heating by microwave irradiation is used to convert the ammonium tetra thiomolybdate (ATM) and GO precursors in tetrahydrofuran (THF) solution. At the reaction conditions of 170 °C and ~21 bar, a large portion of the adsorbed ATM molecules are converted into solid MoS<sub>3</sub> nanoparticles while the GO precursors are converted into reduced graphene oxide (rGO) nanosheets, forming the intermediate MoS<sub>3</sub>/rGO hybrid material<sup>106</sup> via the following reaction:



The deep red-brown colored ATM/GO precursors are converted into the dark brown MoS<sub>3</sub>/rGO intermediate in this process. As will be discussed in later sections, the MoS<sub>3</sub> intermediate has an amorphous chain structure with a composition of Mo<sup>4+</sup>(S<sup>2-</sup>)<sub>3</sub>(S<sub>2</sub><sup>2-</sup>). The Mo is reduced from Mo<sup>6+</sup> to Mo<sup>4+</sup> while some S<sup>2-</sup> is oxidized into S<sub>2</sub><sup>2-</sup>. In the 2<sup>nd</sup> step, the intermediate MoS<sub>3</sub>/rGO powder is further converted to black/grey MoS<sub>2</sub>/rGO hybrids by thermal reduction of S<sub>2</sub><sup>2-</sup> into S<sup>2-</sup> at 250 to 600 °C in a mixed gas of 3% H<sub>2</sub> and 97% Ar in a quartz tube furnace, following the reaction<sup>107</sup>:



The obtained MoS<sub>2</sub> varies from crystalline materials at high annealing temperature (up to 600 °C) to defective materials at lower annealing temperature (down to 250 °C). At the meantime, the quality of rGO is further improved by the thermal annealing.

It is noteworthy that the microwave-assisted technique is not only used to synthesize the high-quality 2D hybrid materials<sup>99</sup> but also help to control the defects in the MoS<sub>2</sub> structure in this structure. Comparing to the conventional hydrothermal process, the microwave-assisted synthesis reduces the reaction time by more than 70 times, i.e. from more than 12 hours to ~10 minutes<sup>99</sup>. The microwave energy directly activates the molecules that possess large dipole moments or ionic groups and thus heats the reaction system rapidly and uniformly<sup>108</sup>. A material's ability to absorb the microwave radiation and convert the energy into heat is determined by its dissipation factor or the tanδ value. This allows to rapidly initiate the nucleation and growth of EES materials on carbon templates by specific heating to form hybrid structures with strong interfacial interactions<sup>102, 145</sup>. In this study, the tanδ values are 0.8 - 1 for GO and rGO<sup>146</sup>, 0.16 for MoS<sub>2</sub><sup>147</sup> and 0.042 for THF

solvent<sup>98</sup>, respectively. Thus, the conversion of ATM into MoS<sub>3</sub> mostly occurs on the hot GO/rGO surface, forming an amorphous MoS<sub>3</sub> layer on the rGO template. As shown in Figure 3.1 and supported by the characterization results below, the adsorbed MoS<sub>3</sub> intermediate is subsequently converted into randomly oriented small 2D MoS<sub>2</sub> nanopatches lying flatly on the planar rGO nanosheets.

### 3.3.2. Structure Characterization

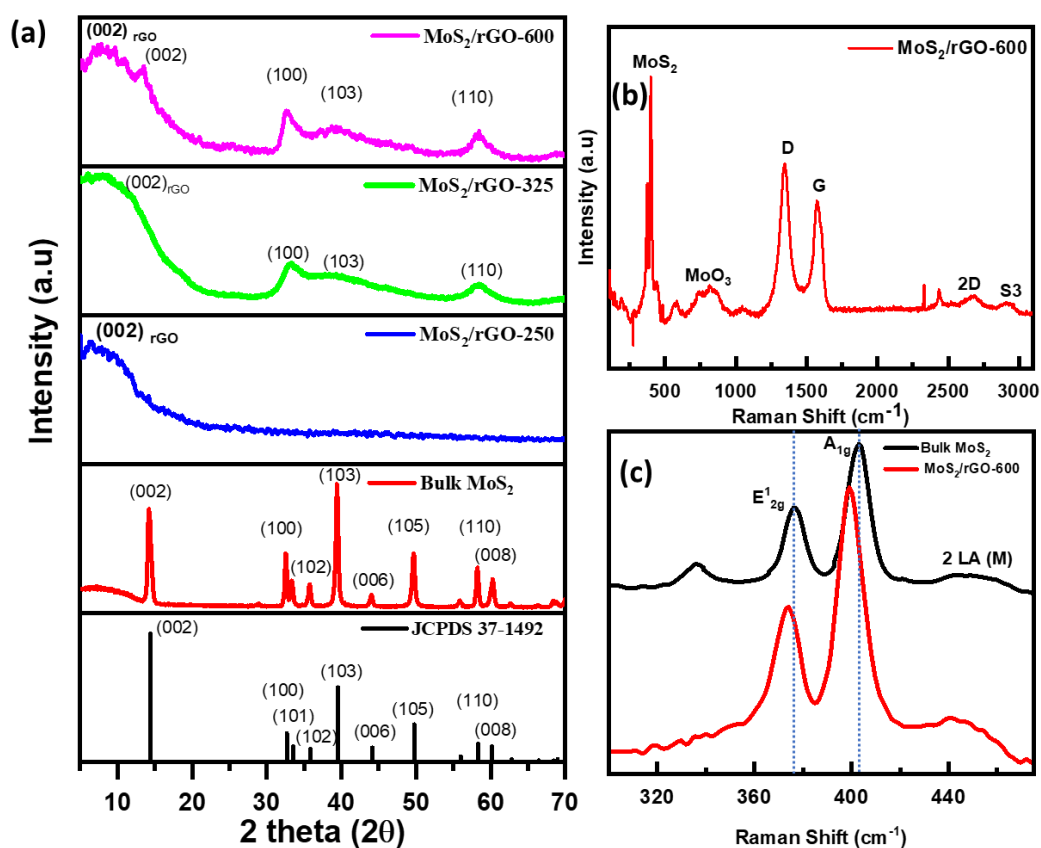


Figure 3.2. (a) Powder XRD spectra of MoS<sub>2</sub>/rGO prepared by annealing at 600 °C (MoS<sub>2</sub>/rGO-600), 325 °C (MoS<sub>2</sub>/rGO-325) and 250 °C (MoS<sub>2</sub>/rGO-250) in comparison to a bulk MoS<sub>2</sub> powder. (b) The full scale and (c) the expanded region of Raman spectra of MoS<sub>2</sub>/rGO-600 and the bulk MoS<sub>2</sub> powder. Reproduced from Muthukumar, K.; Leban, L.; Sekar, A.; Elangovan, A.; Sarkar, N.; Li, J., Tuning the defects in MoS<sub>2</sub>/reduced graphene oxide 2D hybrid materials for optimizing battery performance. *Sustainable Energy & Fuels* **2021**, 5 (16), 4002-4014 with permission from the Royal Society of Chemistry

Figure 3.2(a) shows the powder XRD spectra of the MoS<sub>2</sub>/rGO hybrids after annealing in 3% H<sub>2</sub> and 97% Ar at 600, 325 and 250 °C, respectively, denoted as MoS<sub>2</sub>/rGO-600, MoS<sub>2</sub>/rGO-325 and MoS<sub>2</sub>/rGO-250. The XRD spectrum of MoS<sub>2</sub>/rGO-600 consists of four broad peaks around 2θ angle of 13.4°, 32.6°, 39.5° and 58.3°, which can be attributed to the (002), (100), (103) and (110) diffraction of MoS<sub>2</sub> crystallites. These are consistent with the hexagonal 2H-MoS<sub>2</sub> structure as shown by the standard spectrum of JCPDS card No. 37-1492 and the spectrum of the commercial bulk MoS<sub>2</sub> powders. The (100) peak shows an asymmetric shape, likely due to overlap with the weaker (101) peak at 2θ = 33.5°. The 2θ angle of (002) peak is notably shifted from 14.38° in the standard to 13.44°, indicating a small increase of interlayer distance from 0.615 nm to 0.66 nm likely due to the presence of defects in the MoS<sub>2</sub> layers. The (002) peak of MoS<sub>2</sub>/rGO-600 is quite broad with a full width at the half-maximum (FWHM) of Δ2θ = ~5°. Following the Scherrer equation

$$\tau = \frac{K\lambda}{(\Delta 2\theta) \cos\theta} \quad (3)$$

where the shape factor is assumed to be K = 0.9 and the X-ray wavelength is λ = 0.154 nm, the mean size of the ordered (crystalline) domains normal to the MoS<sub>2</sub> layer is estimated as τ = ~1.6 nm. This value corresponds to an ordered stack of only 3 or 4 MoS<sub>2</sub> layers, which is expected to be smaller than the physical grain thickness. Associated with this, the higher order diffraction peaks, such as (006) and (008) peaks shown in bulk MoS<sub>2</sub> powder, are not observed in MoS<sub>2</sub>/rGO-600 hybrid. The FWHM of (100) peak is Δ2θ = ~1.84°, giving the ordered in-plane domain size of τ = ~4.5 nm, which is three times of the ordered stack thickness but is still very small. Thus, they are referred to as “nanopatches”. In addition, a broad peak at 2θ = 8.1° is attributed to (002) diffraction from rGO layers. The d-spacing is calculated to be ~0.55 nm, which is larger than 0.34

nm of the interlayer spacing in graphite. It is likely that the rGO layers are defective and wrinkled, preventing them from forming compact stacks.

As the annealing temperature decreases, the (002) peak of MoS<sub>2</sub> in the MoS<sub>2</sub>/rGO-325 sample shifts to a lower 2θ angle and presumably overlaps with the broad (002) peak of rGO, making it difficult to identify. The (100), (103) and (110) diffraction peaks become broader and weaker due to disordering caused by the defects in the MoS<sub>2</sub> layers. With further reduction in the annealing temperature to 250 °C, all the major peaks corresponding to 2H-MoS<sub>2</sub> have disappeared in the sample MoS<sub>2</sub>/rGO-250, suggesting the amorphous nature of the MoS<sub>2</sub> structure. Interestingly, the (002) diffraction from rGO in the MoS<sub>2</sub>/rGO-250 sample still preserves but shifts to lower angle at 2θ = 7.1°, corresponding to an expanded interlayer spacing of 0.62 nm which is consistent with higher defect density in rGO. The broad rGO diffraction peaks in all samples indicate that there is little re-stacking of rGO layers, likely due to blocking by the MoS<sub>2</sub> adlayers.

Figure 3.2(b) shows the full Raman spectra of MoS<sub>2</sub>/rGO-600 which consists of the signature peaks attributed to MoS<sub>2</sub> and rGO. The peaks at 1,341 cm<sup>-1</sup> and 1,582 cm<sup>-1</sup><sup>148, 149</sup> are attributed to the D and G bands originating from the vibrational modes of sp<sup>3</sup> carbon atoms in the defect sites and the in-plane vibration of sp<sup>2</sup>-bonded carbon atom, respectively<sup>150</sup>. The intensity ratio between D band and G band (I<sub>D</sub>/I<sub>G</sub>) is as large as 1.3, suggesting the high degree of defects in the sp<sup>2</sup> lattice after the removal of the oxygenated functional groups in the microwave process<sup>151, 152</sup>. There are also two low-intensity peaks around 2,675 cm<sup>-1</sup> and 2,913 cm<sup>-1</sup>, corresponding to the 2D and S3 bands of rGO. The intensity ratio between 2D and S3 peaks is approximately ~2.60 suggesting the presence of a high density of defect sites which is consistent with the XRD results

in Figure 3.2(a). In this study, proper amount of defects may facilitate stronger interaction between the rGO template and the MoS<sub>2</sub> adlayers which are necessary to form stable hybrid materials.

Figure 3.2(c) illustrates the three signature bands of MoS<sub>2</sub> at 374.12 cm<sup>-1</sup>, 399.19 cm<sup>-1</sup> and ~445 cm<sup>-1</sup> in MoS<sub>2</sub>/rGO-600, which are attributed to E<sup>1</sup><sub>2g</sub>, A<sub>1g</sub> and 2 LA(M) modes, respectively<sup>139, 153</sup>. The E<sup>1</sup><sub>2g</sub> band arises from the in-plane vibration of the two S atoms with respect to the Mo atom and the A<sub>1g</sub> band is due to the out-of-plane vibration of the S atoms<sup>80, 154</sup>. The broader 2 LA(M) band originates from the second order zone edge phonon. It is noteworthy that the E<sup>1</sup><sub>2g</sub> and A<sub>1g</sub> bands of MoS<sub>2</sub>/rGO-600 are red-shifted by ~1.9 and ~3.82 cm<sup>-1</sup> from 376.02 and 403.01 cm<sup>-1</sup>, respectively, of the reference bulk MoS<sub>2</sub> powder. This was reported as an evidence of the formation of MoS<sub>2</sub>/rGO hybrids in which the MoS<sub>2</sub> layer becomes more n-doped<sup>155</sup>. The intensity of A<sub>1g</sub> peak in Figure 3.2(c) is much higher than that of the E<sup>1</sup><sub>2g</sub> peak. In principle, the ratio of the integrated intensity of E<sup>1</sup><sub>2g</sub> band to A<sub>1g</sub> band may provide the information of number of MoS<sub>2</sub> layers in the stack<sup>156</sup>, but this is difficult for the powder sample since the intensity ratio strongly depends on the orientation of the MoS<sub>2</sub> crystals<sup>80, 157</sup>. However, the difference in the Raman shifts between the A<sub>1g</sub> and E<sup>1</sup><sub>2g</sub> bands can be accurately read as 25.07 cm<sup>-1</sup>, which suggests that the MoS<sub>2</sub> nanopatches deposited on the rGO template consist of about 5 to 6 layers in average. The Raman spectra of other samples, including MoS<sub>2</sub>/rGO-325, MoS<sub>2</sub>/rGO-250 and the unannealed MoS<sub>3</sub>/rGO intermediate in Figure A.1 of the Appendix A (SI) show very similar features as those of MoS<sub>2</sub>/rGO-600 in Figures 3.2(b) and (c). The ratio of MoS<sub>2</sub> peaks to the G and D bands of rGO clearly increases with the annealing temperature but the peak positions are unchanged. Also, a weaker peak can be seen at 816 cm<sup>-1</sup> in Figures 3.2(b) and S1, indicating the presence of a small amount of MoO<sub>3</sub> in all hybrid MoS<sub>2</sub>/rGO samples.

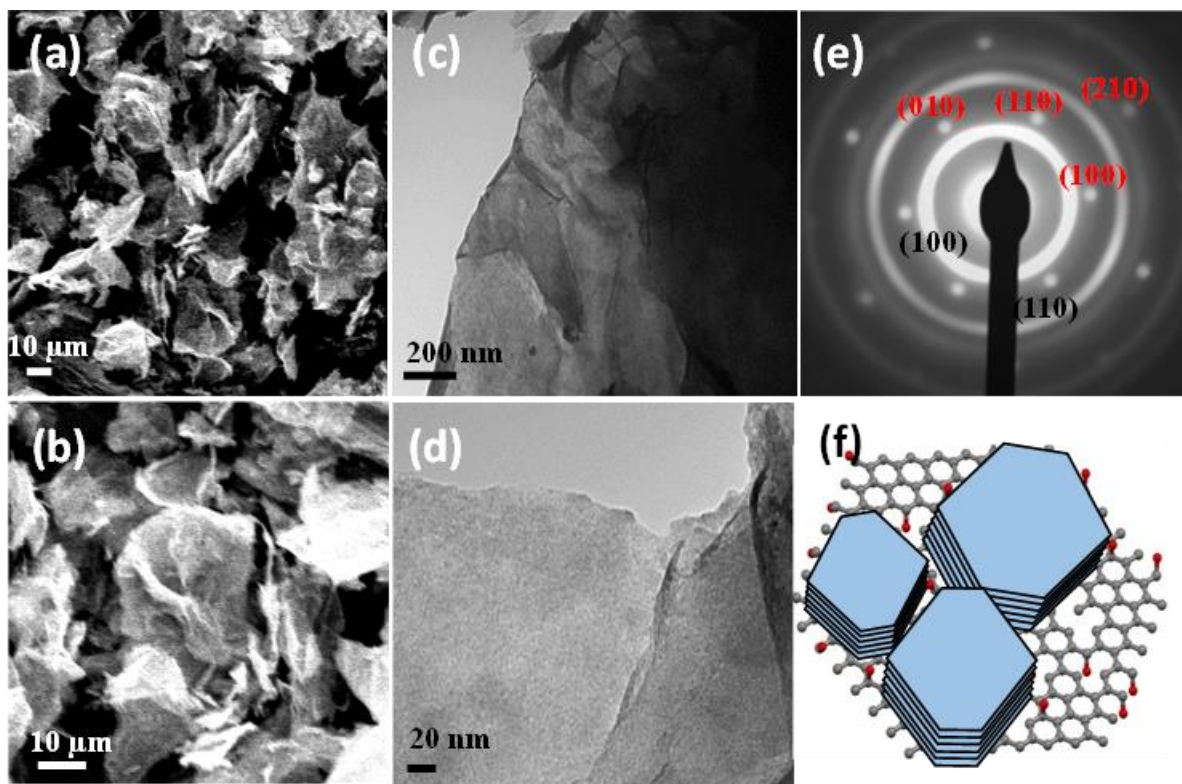


Figure 3.3. Characterization of the MoS<sub>2</sub>/rGO hybrid material annealed at 600 °C (i.e. MoS<sub>2</sub>/rGO-600) by FESEM at (a) a lower and (b) a higher magnification, by TEM at (c) a lower and (d) a higher magnification, and (e) by the selected area electron diffraction (SAED) from the frame in (d). The red-colored indices at the top portion in panel (e) indicate the isolated hexagonal 2D electron diffraction spots from the monocrystalline rGO nanosheets while the black indices at the bottom indicate the continuous rings of 2D powder electron diffraction from the MoS<sub>2</sub> adlayers. (f) Schematic illustration of the hybrid structure of MoS<sub>2</sub> nanopatches with random rotational orientations on the rGO nanosheet. Reproduced from Muthukumar, K.; Leban, L.; Sekar, A.; Elangovan, A.; Sarkar, N.; Li, J., Tuning the defects in MoS<sub>2</sub>/reduced graphene oxide 2D hybrid materials for optimizing battery performance. *Sustainable Energy & Fuels* **2021**, 5 (16), 4002-4014 with permission from the Royal Society of Chemistry.

The FESEM images in Figures 3.3(a) and 3.3(b) show the representative thin-flake morphology of the MoS<sub>2</sub>/rGO-600 hybrid material. Uniform MoS<sub>2</sub> layers have been deposited over the rGO nanosheets varying from ~ 5 to 30 μm in size. The TEM images in Figures 3.3(c) and 3.3(d) show the similar flake-like hybrid structure. Due to the small size of MoS<sub>2</sub> nanopatches,

it is difficult to clearly see them via TEM imaging. More TEM and FESEM images of the bare rGO nanosheets (synthesized with the same process as MoS<sub>2</sub>/rGO-600 except without adding ATM precursors) and the MoS<sub>3</sub>/rGO intermediate are shown in Figure A.2. The bare rGO shows the typical nanoflake structure with small wrinkles due to its softness. After depositing the MoS<sub>3</sub> intermediate material with the microwave synthesis, the adlayers sandwich the rGO nanosheets to form more rigid planar hybrid structures. The morphology of the MoS<sub>3</sub>/rGO intermediate is retained during thermal annealing at the temperature from 250 to 600 °C, as shown by more FESEM images in Figure A.3 and TEM images in Figure A.4.

The crystallinity of the MoS<sub>2</sub>/rGO hybrid has been further analyzed using Selected Area Electron Diffraction (SAED). The SAED image of MoS<sub>2</sub>/rGO-600 in Figure 3.3(e) is taken from the area shown in Figure 3.3(d). It clearly shows two distinct patterns. The dots in the hexagonal lattice are originated from 2D electron diffraction from the monocrystalline rGO nanosheet<sup>158</sup> and the continuous rings are attributed to the randomly oriented polycrystalline 2H-MoS<sub>2</sub> nanopatches on the rGO template. The SAED patterns of MoS<sub>2</sub>/rGO-600, MoS<sub>2</sub>/rGO-325 and MoS<sub>2</sub>/rGO-250 are compared with the un-annealed MoS<sub>3</sub>/rGO intermediate in Figure A.5. The sharpness and contrast decrease with the annealing temperature, which indicates the presence of more defects in the MoS<sub>2</sub>/rGO structure at the lower annealing temperature. It is notable that the un-annealed MoS<sub>3</sub>/rGO intermediate shows well-defined hexagonal diffraction spots but no continuous rings, indicating that the microwave irradiation is able to convert GO into monocrystalline rGO nanosheets while the adlayers are dominated by the amorphous MoS<sub>3</sub> intermediate and possibly some ATM precursors.

Figure A.6 illustrates how to derive the two-dimensional (2D) lattice of MoS<sub>2</sub> in the MoS<sub>2</sub>/rGO hybrid structure from the SAED pattern. At a proper orientation, the incident electron

beam is perpendicular to the rGO plane and thus a 2D hexagonal diffraction pattern can be obtained. The diffraction spots with a six-fold symmetry represent the reciprocal lattice of rGO, which are defined by the instrumental setup and the hexagonal real-space lattice with  $a = b = 2.46 \text{ \AA}$ . The first and second rings are indexed as (100) and (110) diffraction from the hexagonal lattice of MoS<sub>2</sub>. Using the rGO diffraction spots as the reference, the 2D lattice parameters for MoS<sub>2</sub> can be derived as  $a = b = 3.16 \text{ \AA}$ , which match well with the structure of bulk 2H-MoS<sub>2</sub> crystals. Interestingly, the SAED pattern also indicates that the MoS<sub>2</sub> layers are in parallel with the rGO plane but the size of MoS<sub>2</sub> crystals is much smaller than the rGO nanosheets. The small 2H-MoS<sub>2</sub> crystals form a 2D powder with random rotational orientations in the rGO plane, thus giving continuous rings in SAED. The XRD, Raman spectroscopy, SEM and TEM results consistently indicate the in-plane growth of few-layer polycrystalline MoS<sub>2</sub> nanopatches on the large monocrystalline rGO nanosheets, forming a unique MoS<sub>2</sub>/rGO hybrid.

### 3.3.4. Materials Composition Analyses:

XPS was used to analyze the chemical composition of the synthesized MoS<sub>2</sub>/rGO hybrids. Figure 3.4 shows the Mo 3d spectra in the binding energy (B.E.) range of 222-240 eV and S 2p spectra in the B.E. range of 159-169 eV of MoS<sub>2</sub>/rGO-600, MoS<sub>2</sub>/rGO-325, MoS<sub>2</sub>/rGO-250 and the MoS<sub>3</sub>/rGO intermediate material. The S 2p spectra of MoS<sub>2</sub>/rGO-600 consists of a pair of peaks at 162.09 eV (for 2p<sub>3/2</sub>) and 163.27 eV (for 2p<sub>1/2</sub>) with an intensity ratio of 2:1, attributed to S<sup>2-</sup> bridging sulfur of MoS<sub>2</sub> structure. At lower annealing temperatures of 325 °C, another small pair attributed to S<sub>2</sub><sup>2-</sup> sulfur (blue curves in Figure 3.4(d)) needs to be included in the deconvolution, which appear at higher B.E. of 163.41 eV and 164.58 eV. The relative ratio of the integrated peak

area of  $S_2^{2-}$  to  $S^{2-}$  increases from 0.16 in  $MoS_2/rGO-325$  to 1.15 as the annealing temperature drops to 250 °C, indicating the increase of atomic ratio in  $S_2^{2-}$  relative to  $S^{2-}$ .

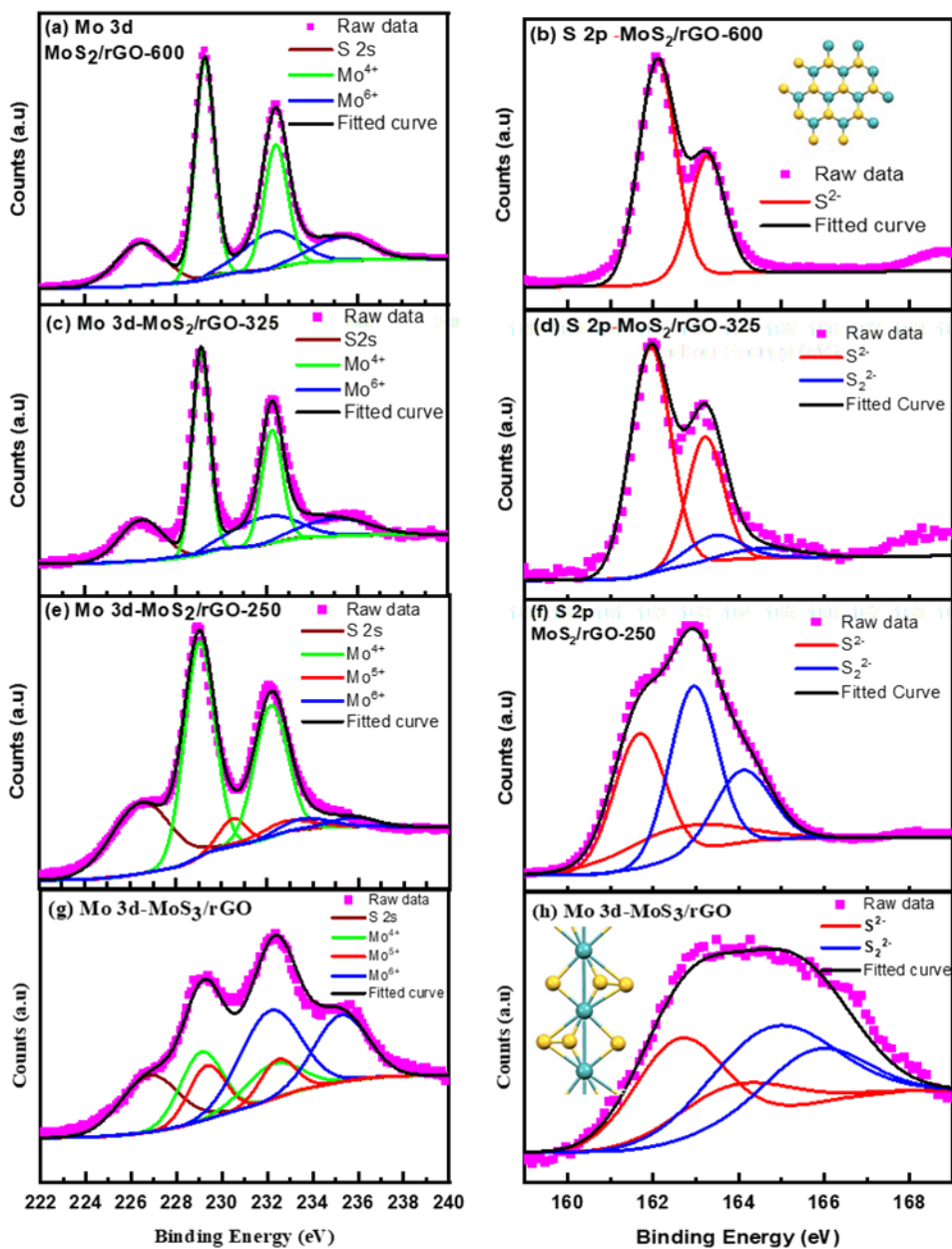


Figure 3.4. The Mo 3d and S 2p XPS spectra of (a,b)  $MoS_2/rGO-600$ , (c,d)  $MoS_2/rGO-325$ , (e,f)  $MoS_2/rGO-250$ , (g,h)  $MoS_3/rGO$ -intermediate product. The inset of panel (b) shows the schematic structure of the hexagonal  $MoS_2$  nanopatches. The inset of panel (h) shows the schematic structure of  $MoS_3$  chain. Reproduced from Muthukumar, K.; Leban, L.; Sekar, A.; Elangovan, A.; Sarkar, N.; Li, J., Tuning the defects in  $MoS_2$ /reduced graphene oxide 2D hybrid materials for optimizing battery performance. *Sustainable Energy & Fuels* **2021**, 5 (16), 4002-4014 with permission from the Royal Society of Chemistry

The MoS<sub>3</sub>/rGO intermediate gives an atomic ratio of S<sub>2</sub><sup>2-</sup> to S<sup>2-</sup> at 1.17, similar to the MoS<sub>2</sub>/rGO-250, but both S<sub>2</sub><sup>2-</sup> and S<sup>2-</sup> shift to higher BE. This is consistent with the fact that the intermediate product after microwave irradiation is dominated by amorphous MoS<sub>3</sub> which has a linear chain-like structure with a possible composition of Mo<sup>4+</sup>(S<sup>2-</sup>)(S<sub>2</sub><sup>2-</sup>) as refined by Hibble et al.<sup>159</sup> based on the original model proposed by Liang et al<sup>160-163</sup>. In this model, both S<sub>2</sub><sup>2-</sup> and S<sup>2-</sup> present as bridging atoms to link the adjacent two Mo<sup>4+</sup> atoms (as illustrated in the inset of Figure 3.4(h)).

However, the atomic ratio of S<sub>2</sub><sup>2-</sup> to S<sup>2-</sup> in both MoS<sub>3</sub>/rGO intermediate and MoS<sub>2</sub>/rGO-250 is lower than the ratio of 2 in pure MoS<sub>3</sub>, indicating the presence of extra S<sup>2-</sup> atoms due to partial formation of MoS<sub>2</sub> and some unreacted ATM precursors. It is known that, in inert gas at ~1 bar pressure, ATM thermally decomposes into MoS<sub>3</sub> between 260 to 300 °C and is then further converted into microcrystalline MoS<sub>2</sub><sup>164</sup>. The high pressure (~21 bar) during the microwave process in this study may facilitate the partial conversion of ATM precursor into MoS<sub>3</sub> at lower temperature (~170 °C), yielding a mixture of MoS<sub>3</sub>, MoS<sub>2</sub> and ATM residue. During thermal annealing in H<sub>2</sub> at 600 °C, the amorphous MoS<sub>3</sub> chains are converted into nearly perfect MoS<sub>2</sub> layers as shown in the inset of Figure 3.4 (b). At the lower annealing temperature at 250 °C, a high density of MoS<sub>3</sub> residue is retained and presents as S-rich (or Mo-deficient) defects. This is very different from the commonly studied S-deficient defects in the MoS<sub>2</sub> nanosheets prepared by the hydrothermal method<sup>89</sup>. Among the four samples, the atomic percentage of S in form of S<sub>2</sub><sup>2-</sup> increases from 0% in MoS<sub>2</sub>/rGO-600 to 13.5% in MoS<sub>2</sub>/rGO-325, 53.5% in MoS<sub>2</sub>/rGO-250 and 54.0% in un-annealed MoS<sub>3</sub>/rGO intermediate.

The Mo 3d spectra of MoS<sub>2</sub>/rGO-600 and MoS<sub>2</sub>/rGO-325 can be nicely fit with two pairs of 3d peaks with the area ratio between 3d<sub>5/2</sub> and 3d<sub>3/2</sub> maintained as 3:2 and the splitting energy

between them set as 3.13 eV. However, the Mo 3d spectrum of MoS<sub>2</sub>/rGO-250 need to include one more pair of peaks in the curve fitting. As shown in Table A.1, among these de-convoluted peaks, the B.E. of 3d<sub>5/2</sub> peaks at 229.28 eV, 229.12 eV and 229.03 eV in MoS<sub>2</sub>/rGO-600, MoS<sub>2</sub>/rGO-325 and MoS<sub>2</sub>/rGO-250 can be attributed to the Mo<sup>4+</sup> composition of MoS<sub>2</sub> in these samples. The smaller 3d<sub>5/2</sub> peaks at higher B.E. around 232.18 eV, 231.90 eV and 232.68 eV can be attributed to the Mo<sup>6+</sup> in either the ATM residue or MoO<sub>3</sub> in the samples (as revealed by the Raman spectrum in Figure 3.2(b)). In addition to the above-mentioned two pairs of peaks, there is a small additional pair of peaks with 3d<sub>5/2</sub> at around 230.52 eV, which can be attributed to Mo<sup>5+</sup> in MoS<sub>2</sub>/rGO-250. It is worth noting that the Mo<sup>4+</sup> 3d<sub>5/2</sub> peak slightly shifts to lower binding energy with the decreasing temperature. This correlates with the increasing S<sub>2</sub><sup>2-</sup> percentage as the annealing temperature is reduced. The elemental ratio of Mo:S is about 1:1.9, 1:2.3 and 1:2.9 in MoS<sub>2</sub>/rGO-600, MoS<sub>2</sub>/rGO-325 and MoS<sub>2</sub>/rGO-250, respectively. As a result, either a large number of molybdenum vacancies or increased sulfur contents at the edge of MoS<sub>2</sub> nanopatches present in the low-temperature annealed samples, both of which is beneficial to Zn<sup>2+</sup> ion storage. For the un-annealed MoS<sub>3</sub>/rGO intermediate sample, both the S 2p spectrum (Figure 3.4(h)) and the Mo 3d spectrum (Figure 3.4(g)) are more complicated due to the presence of a mixture of MoS<sub>3</sub>, ATM residue and MoS<sub>2</sub>. The S 2s peak is also observed at the B.E. of ~226.4 - 226.9 eV in panel (a), (c), (e) and (g) of Figure 3.4, which increases as the annealing temperature is decreased, consistent with the increased ratio of S 2p and Mo 3d peaks.

The composition of the hybrid materials is further analyzed with thermogravimetric analysis (TGA) from room temperature to 600 °C in the air atmosphere. Figure A.7 shows the TGA curves of MoS<sub>2</sub>/rGO-600, MoS<sub>2</sub>/rGO-325, MoS<sub>2</sub>/rGO-250, MoS<sub>3</sub>/rGO intermediate and two control samples (commercial MoS<sub>2</sub> flakes and bare rGO). The MoS<sub>2</sub> standard (blue curve) remains

stable till 370 °C but shows a weight loss of 10.1% between 370 °C and 550°C due to the conversion of MoS<sub>2</sub> to MoO<sub>3</sub>. The bare rGO (green curve) illustrates a rapid weight loss starting from 420 °C till 563 °C by 93.36% due to oxidation of rGO into CO<sub>2</sub>, with about 6.64% of graphitic carbon remaining up to 600 °C. The MoS<sub>2</sub>/rGO-600 (purple curve) demonstrates a weight loss of 27.34% from 370 °C till 600 °C, attributed to the concurrent effects of rGO decomposition and the conversion of MoS<sub>2</sub> to MoO<sub>3</sub>. The weight percentage of MoS<sub>2</sub> in the MoS<sub>2</sub>/rGO-600 is calculated to be 79.29% and the rest 20.71% is rGO (see the description in the Appendix A following Figure A.7). This estimation is in good agreement with the XRD, Raman and XPS analyses. The TGA curves of the other samples including MoS<sub>2</sub>/rGO-325, MoS<sub>2</sub>/rGO-250 and MoS<sub>3</sub>/rGO intermediate show a consistent trend, but the weight loss starts from the room temperature and continues up to ~560 °C. The overlap of multiple reactions of the unstable intermediate species makes it difficult to derive the accurate composition based on the stoichiometric calculations.

A combustion CHNS elemental analysis was employed to determine the more accurate weight percentage (wt%) of the elements including C, O, N, H and S, as listed in Table A.2. The approximate wt% of MoS<sub>x</sub> is calculated to be 78.40%, 71.99%, 74.86% and 65.81% for MoS<sub>2</sub>/rGO-600, MoS<sub>2</sub>/rGO-325, MoS<sub>2</sub>/rGO-250 and MoS<sub>3</sub>/rGO-intermediate, respectively. The corresponding wt% of carbon in these hybrid materials are 19.98%, 22.46%, 18.62% and 20.31%. It is significant to note that the wt% of oxygen is determined to be 11.07% in MoS<sub>3</sub>/rGO-intermediate and 1.17% in MoS<sub>2</sub>/rGO-600. This decrease in oxygen wt% at the higher annealing temperature can be attributed to the further reduction of rGO. It is noteworthy that it is not possible to separate the contributions of MoS<sub>3</sub>, MoS<sub>2</sub> and MoO<sub>3</sub> by these elemental analyses. Thus, to make a consistent comparison, we use the total mass of Mo compounds in the MoS<sub>x</sub>/rGO hybrid material, denoted as MoS<sub>x</sub>, in calculating the specific capacity in the following section for battery tests.

### 3.3.5. Electrochemical Evaluation of Energy Storage:

The MoS<sub>2</sub>/rGO hybrid materials are first tested as the anode in half-cells versus a Li counter electrode in the voltage range of 0.50 to 3.0 V. The low voltage limit is set at 0.50 V to avoid irreversible reduction of MoS<sub>x</sub> into Mo metal. Figure 3.5(a) shows the representative results from two rate-performance sequences of the MoS<sub>2</sub>/rGO-600 electrode at the current density of 145, 217, 434 and 867 mA g<sup>-1</sup> which corresponds to the approximate experimental C-rates of C/5.5, C/2.2, 1C and 2C, respectively. Figure 3.5(a) illustrates an impressive initial specific discharge capacity of 580 mAh g<sub>MoS<sub>x</sub></sub><sup>-1</sup> at 145 mA g<sup>-1</sup>, which then falls rapidly to 519 mAh g<sub>MoS<sub>x</sub></sub><sup>-1</sup> (corresponding to ~3.1 Li<sup>+</sup> ion insertion per MoS<sub>2</sub>) in the 10<sup>th</sup> cycle due to irreversible changes in the structure caused by the intercalation of more than one Li<sup>+</sup> ion per MoS<sub>2</sub>. In the meantime, the coulombic efficiency (CE) defined as the ratio of the discharge capacity to the preceding charge capacity (see Equation (2) in SI) quickly increases from 86.6% in the first cycle to 98.3% in the 5<sup>th</sup> cycle and maintains over 99.6% after the 10<sup>th</sup> cycle, indicating the good reversibility of the electrode. The electrode stability is improved after extended cycling or at higher current rates. The MoS<sub>2</sub> nanopatches grown on the rGO template using the microwave irradiation are more uniform and homogeneous than the previously reported hydrothermal methods<sup>165</sup>. This leads to slightly higher specific capacity and better stability than the MoS<sub>2</sub> nanosheets deposited on electrospun carbon nanofibers by Wang et al<sup>166</sup>. Other samples including MoS<sub>2</sub>/rGO-325, MoS<sub>2</sub>/rGO-250 and MoS<sub>3</sub>/rGO intermediate show the similar behavior (Figure S8) but with slightly smaller specific capacity at the lower annealing temperature. However, the materials annealed at lower temperature become stabilized slightly faster in the initial cycles. The overall effect of the annealing temperature on Li-ion storage is rather small.

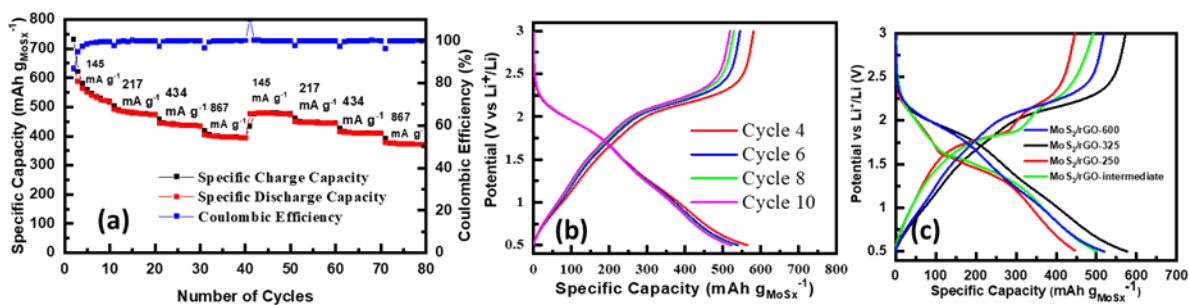


Figure 3.5. (a) The rate-performance tests of the LIB half-cell with the  $\text{MoS}_2/\text{rGO-600}$  cathode vs. a Li disk anode at 100, 150, 300, 600 mA cell current in the cell voltage window of 0.50 – 3.0 V. (b) The galvanostatic charge/discharge curves in the initial 10 cycles at  $145 \text{ mA g}^{-1}$  ( $\sim C/4$  rate) in (a). (c) The galvanostatic charge/discharge curves of LIB half-cells made of  $\text{MoS}_2/\text{rGO-600}$  at  $145 \text{ mA g}^{-1}$  (blue),  $\text{MoS}_2/\text{rGO-325}$  at  $97 \text{ mA g}^{-1}$  (black),  $\text{MoS}_2/\text{rGO-250}$  at  $160 \text{ mA g}^{-1}$  (red) and  $\text{MoS}_2/\text{rGO}$  intermediate material at  $87 \text{ mA g}^{-1}$  (green) in the 10<sup>th</sup> cycle at 100 mA cell current rate. Be noted that all measurements in panels (b) and (c) were done at  $100 \mu\text{A}$  cell current but are translated into different current densities due to variation of mass loading on each electrode. Reproduced from Muthukumar, K.; Leban, L.; Sekar, A.; Elangovan, A.; Sarkar, N.; Li, J., Tuning the defects in  $\text{MoS}_2/\text{reduced}$  graphene oxide 2D hybrid materials for optimizing battery performance. *Sustainable Energy & Fuels* **2021**, 5 (16), 4002-4014 with permission from the Royal Society of Chemistry

Lithiation in  $\text{MoS}_2$  occurs via two processes including intercalation and conversion reaction. Initial lithiation process in the potential window of 1.0-3.0 V involves the intercalation of  $\text{Li}^+$  ions into the interlayer spacing of  $\text{MoS}_2$  resulting in the formation of intermediate  $\text{Li}_x\text{MoS}_2$  ( $0 < x \leq 1$ ) rendering a theoretical capacity of  $167 \text{ mAh g}^{-1}$  ( $n=1$ ) for one  $\text{Li}^+$  insertion<sup>167</sup>. The conversion reaction of  $\text{Li}_x\text{MoS}_2$  into metallic Mo and  $\text{Li}_2\text{S}$  takes place around at lower potential between 0.57 V and 0.34 V<sup>168</sup>, which gives further increased capacity up to  $664 \text{ mAh g}^{-1}$  (Corresponding to  $\sim 4 \text{ Li}^+$  ion insertion), but also causes the structural degradation and shuttle effect. In this study, we have applied a potential window of 0.5 – 3.0 V to limit the irreversible conversion of  $\text{Li}_x\text{MoS}_2$  into metallic molybdenum and  $\text{Li}_2\text{S}$ . Thus the specific capacity is comparable to studies in the similar potential window<sup>165, 169</sup>. On the other hand, the larger interlayer spacing and the presence of defects (Mo-vacancies) in the  $\text{MoS}_2$  structure facilitates intercalation

of more  $\text{Li}^+$  ions and thereby increases the specific capacity of the  $\text{Li}_x\text{MoS}_2$  phase up to  $x = \sim 3.0$ . The galvanostatic charge/discharge curves of  $\text{MoS}_2/\text{rGO}-600$  in the first 10 cycles in Figure 3.5(b) only show a few weak kinks during  $\text{Li}^+$  insertion, but a clear voltage plateau is observed around 2.10 V in the extraction curves, indicating that it indeed involves  $\text{Li}^+$  ion intercalation/deintercalation between the  $\text{MoS}_2$  layers. The long-term stability of  $\text{MoS}_2/\text{rGO}-600$  is shown in Figure A.9 with a higher initial specific capacity of  $393.5 \text{ mAh g}_{\text{MoS}_x}^{-1}$  and the capacity retention of  $\sim 89.12\%$  after 50 cycles.

Figure 3.5(c) further shows that the  $\text{MoS}_2/\text{rGO}-600$  and  $\text{MoS}_2/\text{rGO}-325$  electrodes behave similarly. The  $\text{MoS}_2/\text{rGO}-250$  and  $\text{MoS}_3/\text{rGO}$  intermediate electrodes, however, show slightly lower specific capacity of  $\sim 446 - 492 \text{ mAh g}_{\text{MoS}_x}^{-1}$  in the 10<sup>th</sup> cycle at  $100 \mu\text{A}$ . The difference in the obtained specific capacity is mainly attributed to the varied mass loadings of  $\text{MoS}_3/\text{rGO}$  materials in each electrode (which translate into different current densities of  $\sim 76$  to  $173 \text{ mA g}^{-1}$ ) rather than the intrinsic materials properties. All the four electrodes show substantially higher specific capacities than  $167 \text{ mAh g}_{\text{MoS}_x}^{-1}$  for one  $\text{Li}^+$  insertion. The rGO (with the approximate wt% of 21.15% to 31.38%) also exhibits low Li ion storage capacities ( $\sim 53 - 110 \text{ mAh g}_{\text{rGO}}^{-1}$ ) as shown in the tests with control rGO samples in Figure A.10. This contribution, however, only accounts for less than 8% of the specific capacity in Figure 3.5 and Figure A.8, as described Table A.3 of the Appendix A. The calibrated specific capacity attributed to  $\text{MoS}_x$  varies from 446 to 573  $\text{mAh g}_{\text{MoS}_x}^{-1}$ , which still well exceeds the theoretical value of one  $\text{Li}^+$  ion intercalation per  $\text{MoS}_2$ . This can be attributed to the (i) enhanced electrical conductivity by rGO in the structure and (ii) increased number of active sites with large number of Mo vacancies even in the  $600^\circ\text{C}$  annealed  $\text{MoS}_2$  nanopatches.

The MoS<sub>2</sub>/rGO hybrid materials are further assessed as the cathode in aqueous Zn-ion half-cells in the voltage range of 0.25 to 1.30 V versus a Zn anode. Aqueous zinc ion batteries (ZIBs) have been intensively studied as a suitable alternative to Lithium ion batteries (LIBs) for large-scale energy storage systems owing to the high volumetric capacity (5,854 mAh cm<sup>-3</sup>) and increased safety. MoS<sub>2</sub> has been studied as a potential host for the divalent Zn<sup>2+</sup> cations due to its unique 2D layered structure analogous to graphene and the increased interlayer distance of ~0.62 nm. The weak van der Waals forces between the layers make the intercalation of larger Na<sup>+</sup> ions (1.02 Å in radius)<sup>153, 166, 170</sup> and multivalent Zn<sup>2+</sup> ions (0.74 Å in radius)<sup>128</sup> more feasible due to the ability to accommodate the volume expansion during the intercalation process.

In contrast to Li<sup>+</sup> ion storage, the defects in the MoS<sub>x</sub>/rGO hybrid materials show a much stronger effect on the Zn<sup>2+</sup>-ion storage performance. The more defective sample MoS<sub>2</sub>/rGO-250 behaves much better than other samples. Figure 3.6(a) illustrates the rate performance of the defective MoS<sub>2</sub>/rGO-250 cathode. In the initial cycle, a high specific charge capacity of 336 mAh g<sub>MoS<sub>x</sub></sub><sup>-1</sup> is obtained at 104 mA g<sup>-1</sup> current rate (~C/1.8), but the CE is only 88%. The specific charge capacity rapidly drops to 196 mAh g<sub>MoS<sub>x</sub></sub><sup>-1</sup> in the 3<sup>rd</sup> cycle while the CE quickly rises to ~100% and maintains at this value in later cycles. The capacity becomes more stable after 10 cycles but drops to 130 mAh g<sub>MoS<sub>x</sub></sub><sup>-1</sup>. The stability is further improved as the current density is increased to 208 mA g<sup>-1</sup> (~2C) followed by 313 mA g<sup>-1</sup> (~4C) and 418 mA g<sup>-1</sup> (~7.5C). The CE maintains at 100%. The electrode becomes much more stable in the 2<sup>nd</sup> rate sequence starting at the 41<sup>st</sup> cycle at 104 mA g<sup>-1</sup>. The CV curves of the MoS<sub>2</sub>/rGO-250 cathode in Figure 3.6(b) show the continuous supercapacitor-like feature without any clear redox peaks. The corresponding charge/discharge curves in the 2<sup>nd</sup> cycles from different samples in Figure 3.6(c) are smooth without any voltage plateaus. Clearly, the Zn-ion storage is mostly based on surface reactions at the edges or the defect

sites of the MoS<sub>2</sub> nanopatches. As a result, the annealing temperature (and resulted defect density) has a much more dramatic effect on the Zn-ion storage capacity and stability. Comparing to MoS<sub>2</sub>/rGO-250, the specific charge capacity of the MoS<sub>2</sub>/rGO-325 cathode is only ~56 mAh g<sup>-1</sup> in the 2<sup>nd</sup> cycle and that of MoS<sub>2</sub>/rGO-600 is almost negligible (~5.8 mAh g<sup>-1</sup>), as shown in Figure 3.6(c).

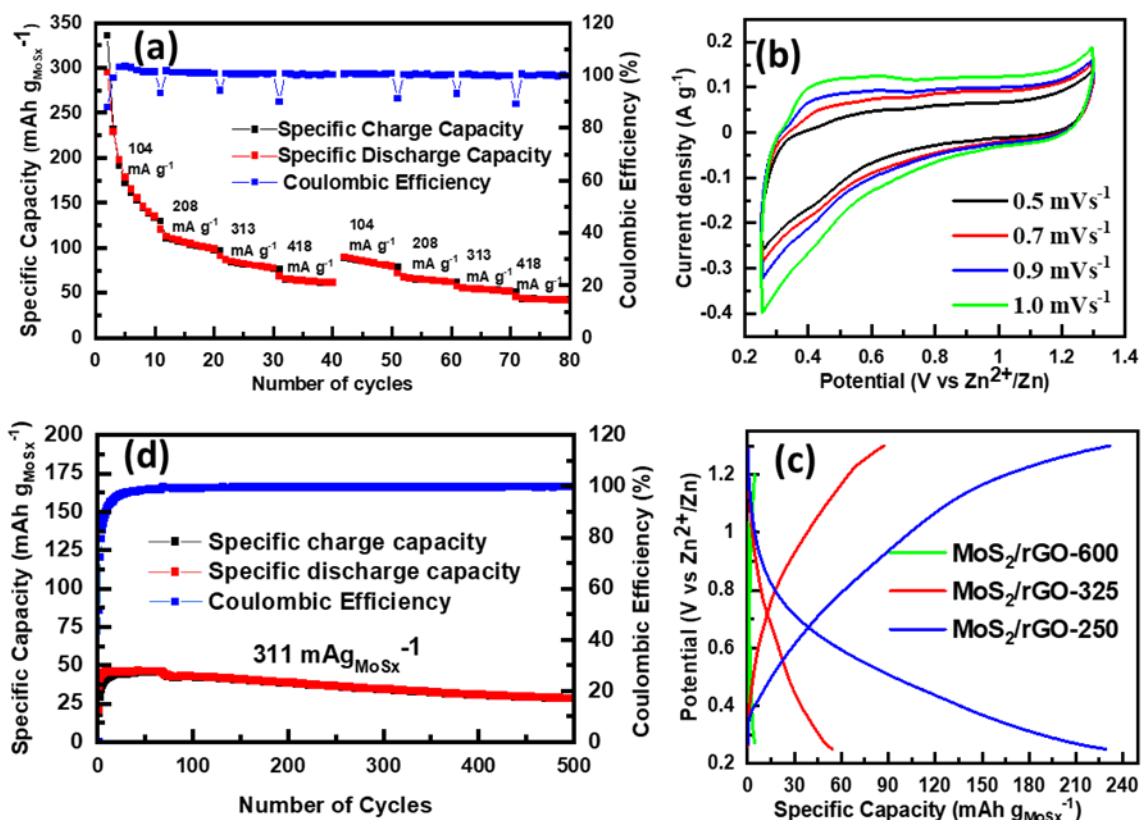


Figure 3.6. (a) Rate performance of MoS<sub>2</sub>/rGO-250 in a Zn-ion battery half-cell at 100, 200, 300 and 400 mA cell currents, which are converted to corresponding current densities for ease of comparison among different cells. (b) CV curves of MoS<sub>2</sub>/rGO-250 at various scan rates in the cell voltage window of 0.25 – 1.30 V (vs. Zn<sup>2+</sup>/Zn). (c) Galvanostatic charge-discharge curves in the 2<sup>nd</sup> cycle of Zn-ion battery half-cells at 78 mA g<sup>-1</sup> with MoS<sub>2</sub>/rGO-600, MoS<sub>2</sub>/rGO-325 and MoS<sub>2</sub>/rGO-250 cathode, respectively. (d) Long-term stability of a Zn-ion half-cell with the MoS<sub>2</sub>/rGO-250 cathode at the charge/discharge current density of 311 mA g<sup>-1</sup>. Reproduced from Muthukumar, K.; Leban, L.; Sekar, A.; Elangovan, A.; Sarkar, N.; Li, J., Tuning the defects in MoS<sub>2</sub>/reduced graphene oxide 2D hybrid materials for optimizing battery performance. *Sustainable Energy & Fuels* **2021**, 5 (16), 4002-4014 with permission from the Royal Society of Chemistry

As shown in Figure A.11, MoS<sub>2</sub>/rGO-600 and MoS<sub>2</sub>/rGO-325 not only show lower capacities, but also lower CEs than MoS<sub>2</sub>/rGO-250. In contrast, the un-annealed MoS<sub>3</sub>/rGO intermediate sample shows the similar behavior as MoS<sub>2</sub>/rGO-250 and remains stable over 100 cycles (Figures A.12 (b)) at 200  $\mu$ A current rate ( $\sim 345 \text{ mA g}^{-1}$ ). But MoS<sub>2</sub>/rGO-250 shows higher capacity than the MoS<sub>3</sub>/rGO intermediate, i.e.  $\sim 336$  to  $130 \text{ mAh g}_{\text{MoS}_x}^{-1}$  in the first 10 cycles at  $104 \text{ mA g}^{-1}$  in Fig. 3.6(a) vs.  $\sim 152$  to  $58 \text{ mAh g}_{\text{MoS}_x}^{-1}$  at  $75 \text{ mA g}^{-1}$  in Figure A.11(g). This confirms that the major Zn-ion storage host is the defective MoS<sub>2</sub> rather than MoS<sub>3</sub> intermediate (or ATM residue). The stability of MoS<sub>2</sub>/rGO-250 cathode is further demonstrated in long cycling results in Figure 3.6(d). The capacity at the  $311 \text{ mA g}^{-1}$  current rate ( $\sim 7.5\text{C}$ ) only drops by  $\sim 38\%$  from the highest value of  $\sim 45 \text{ mAh g}_{\text{MoS}_x}^{-1}$  at the initial cycles to  $\sim 29 \text{ mAh g}_{\text{MoS}_x}^{-1}$  at the 500<sup>th</sup> cycle. In contrast to Li-ion storage, the contribution of rGO to Zn<sup>2+</sup> ion storage is only  $\sim 1.5$  to  $4 \text{ mAh g}_{\text{rGO}}^{-1}$  (as shown in Figure A.13), which is negligible.

It is interesting that the defect density in the MoS<sub>2</sub>/rGO samples has little effects on the Li-ion storage while the highly defective MoS<sub>2</sub>/rGO-250 sample prepared by annealing at  $250 \text{ }^\circ\text{C}$  performs the best for Zn-ion storage with a very high initial capacity of  $\sim 300 \text{ mAh g}_{\text{MoS}_x}^{-1}$  at the low current density but fades quickly. The Zn-ion storage seems to be mainly based on pseudocapacitive surface reactions at the edge or defect sites of the MoS<sub>2</sub> nanopatches. Overall, the stability and CE are lower at low current rates, particularly for Zn-ion storage. But they can be dramatically improved at higher current rates. The high CE and reversible Zn<sup>2+</sup> ion storage can be obtained in the defective MoS<sub>2</sub>/rGO-250 sample, which may be attributed to the increased defect density and terminal S<sub>2</sub><sup>2-</sup> edges, as revealed by the XPS analysis. The produced small MoS<sub>2</sub> nanopatches are favorable for Zn<sup>2+</sup> adsorption and fast surface reactions. The ability to increase Zn<sup>2+</sup> ion storage by introducing more defects in MoS<sub>2</sub> is consistent with the study by Xu et al.<sup>89</sup>

Our stabilized specific capacity with the MoS<sub>2</sub>/rGO-250 sample (~128 mAh g<sub>MoS<sub>x</sub></sub><sup>-1</sup> at ~104 mA g<sup>-1</sup> after 10 cycles) is comparable to that by Xu et al. (~110 mAh g<sup>-1</sup> at ~200 mA g<sup>-1</sup>)<sup>89</sup>. However, the nature of the defects is very different. The S-rich defects in MoS<sub>2</sub>/rGO-250 in this study (with a S:Mo ratio of ~2.9:1) likely present larger electrostatic interactions with the divalent Zn<sup>2+</sup> cations than that in the S-deficient MoS<sub>2</sub> (with a S:Mo ratio of 1.5:1) by Xu et al.<sup>89</sup>. This may cause irreversible structural changes during insertion of large amount of Zn<sup>2+</sup> ions in MoS<sub>2</sub>/rGO-250. At high current rates, there is less intercalation into the MoS<sub>2</sub> layers and thus the performance is dominated by fast surface reactions at the edges and defect sites, making it much more stable. It is interesting that all MoS<sub>2</sub>/rGO hybrid materials are much more stable in intercalation/deintercalation of smaller Li<sup>+</sup> ions. Further study to find a way to maintain the high Zn-ion storage capacity of the defective MoS<sub>2</sub>/rGO-250 hybrid as shown in the initial cycles would be important in ZIB development.

### 3.4. Conclusion

In summary, a set of MoS<sub>2</sub>/rGO hybrid materials were prepared by applying the microwave specific heating on graphene oxide and molecular Mo precursors followed by the thermal annealing in 3% H<sub>2</sub> and 97% Ar at different temperature. The microwave process was able to convert graphene oxide to ordered rGO nanosheets, which were sandwiched with uniform thin layers of intermediate materials dominated by amorphous MoS<sub>3</sub>. The thermal annealing process converted the amorphous MoS<sub>3</sub> layers into 2D MoS<sub>2</sub> nanopatches, whose defect density can be tuned by controlling the annealing temperature at 250, 325 and 600 °C. The MoS<sub>2</sub>/rGO sample annealed at 600 °C was found to consist of 2D nanopatches of MoS<sub>2</sub> crystals randomly oriented on monocrystalline reduced graphene surface while the samples annealed at 250 and 325 °C showed a S to Mo ratio larger than 2:1, indicating the presence of high-density S-rich or Mo-

deficient defects which are different from the S-deficient defects by hydrothermal synthesis in literature. All three MoS<sub>2</sub>/rGO samples and the MoS<sub>3</sub>/rGO intermediate showed high Li-ion intercalation capacities in initial cycles (over ~519 mAh g<sub>MoS<sub>x</sub></sub><sup>-1</sup>, ~3.1 Li<sup>+</sup> ions per MoS<sub>2</sub>). The effect of the defects in MoS<sub>2</sub> was found insignificant for Li-ion storage. In contrast, the Zn-ion storage properties strongly depended on the defects in the sample. The highly defective MoS<sub>2</sub>/rGO sample prepared by annealing at 250 °C provided the highest initial Zn-ion storage capacity (~300 mAh g<sub>MoS<sub>x</sub></sub><sup>-1</sup>) and nearly 100% coulombic efficiency, which was dominated by pseudocapacitive behavior based on surface reactions at the edges or defects in the MoS<sub>2</sub> nanopatches. Even though significant fading in specific capacity occurred at the initial cycles at low current densities, stable charge/discharge can be obtained at higher charge/discharge current densities or after extended cycles. This study validates that defect engineering is critical in the divalent Zn-ion storage.

# **Chapter 4 - Coprecipitation Synthesis of V<sub>2</sub>O<sub>5</sub> Nanoribbons on Reduced Graphene Oxide Nanosheets through Divalent Transition Metal Cations for High-Capacity and Stable Aqueous Zinc Ion Batteries**

## **4.1. Introduction**

The increasing energy consumption and limited fossil fuel resources have driven the broader utilization of renewable energy sources. But the intermittent nature of the renewable energy sources requires sustainable electrical energy storage systems (EES) to support the continuous energy supply. Currently, lithium-ion batteries (LIBs) are the primary commercial EES system owing to its high energy density and long-cycling stability<sup>171</sup>. However, the limited lithium resources and safety concerns make LIBs inadequate for grid-scale energy storage<sup>172</sup>. There is a strong need to develop suitable alternatives for LIBs. Divalent metal ion batteries such as Zn-ion batteries and Mg-ion batteries are considered as promising candidates due to their high theoretical specific capacity and environmentally benign nature<sup>173, 174</sup>. Among them, aqueous zinc ion batteries (AZIB) have attracted a lot of attention because of Zn metal's higher abundance and high specific volumetric capacity (5,844 mAh cm<sup>-3</sup>)<sup>175</sup>. In addition, Zn metal anodes have higher redox potential (-0.76 V versus standard hydrogen electrode (SHE)) than other metal anodes, which makes them stable in aqueous solutions and thus usable in the safer and more conductive aqueous electrolytes<sup>113, 126, 175</sup>. Despite the advantages, AZIBs face some challenges, including the large radius of the hydrated Zn<sup>2+</sup> ions (5.5 Å)<sup>176</sup> though the Shannon's ionic radius of Zn<sup>2+</sup> is comparable to that of Li<sup>+</sup> ions (0.74 Å versus 0.76 Å)<sup>126</sup>. The high electrostatic interaction due to Zn<sup>2+</sup> ions' divalent cationic nature also causes large structural disruption to the host materials, leading to low coulombic efficiency and low electrode stability<sup>51</sup>. One of the top priorities in AZIB research is to realize its theoretical capacity with suitable cathode materials that can facilitate reversible

intercalation/deintercalation of  $\text{Zn}^{2+}$  ions. In the past, transition metal oxides and sulfides (such as  $\text{V}_2\text{O}_5$ ,  $\text{MnO}_2$ ,  $\text{MoS}_2$ ,  $\text{VS}_2$  etc.)<sup>51, 59, 62</sup>, Prussian blue analogues<sup>132</sup> and other inorganic materials<sup>177, 178</sup> have been studied as cathode materials for reversible  $\text{Zn}^{2+}$  ion storage.

Among the transition metal oxides, the orthorhombic  $\alpha\text{-V}_2\text{O}_5$  is particularly attractive due to its low cost, high theoretical specific gravimetric capacity (294 mAh  $\text{g}^{-1}$  for 1  $\text{Zn}^{2+}$  per  $\text{V}_2\text{O}_5$ ), layered structure and tunable oxidation states (as  $\text{V}^{5+}$ ,  $\text{V}^{4+}$  and  $\text{V}^{3+}$ )<sup>177, 178</sup>. But pure-phase bulk  $\text{V}_2\text{O}_5$  suffers from low  $\text{Zn}^{2+}$  ion diffusion coefficient, poor electronic conductivity, and structural instability<sup>179</sup>. Nanostructures have been explored to make use of their increased specific surface area (SSA), larger electrode-electrolyte interface, and shortened  $\text{Zn}^{2+}$  ion diffusion distance. However, the nanostructures have even lower electronic conductivity and still suffer from structural disintegration. One strategy to improve this is to incorporate conductive carbon materials as the stable structural supports and electronic pathways<sup>180</sup>. For example, Wang et al.<sup>94</sup> reported a unique amorphous  $\text{V}_2\text{O}_5$ /graphene heterostructure, synthesized via solvothermal process followed by freeze-drying, as a highly efficient AZIB cathode with an exceptionally high capacity of 489 mAh  $\text{g}^{-1}$  at 0.1 A  $\text{g}^{-1}$ , a good high-rate capability, and over 83% capacity retention after 3500 cycles. Wang et al.<sup>181</sup> also reported the layer-by-layer controlled assembly of amorphous  $\text{V}_2\text{O}_5$ /graphene heterostructures using a novel 2D-template ion absorption strategy. Such  $\text{V}_2\text{O}_5$ /graphene heterostructures exhibit a high specific capacity of 447 mAh  $\text{g}^{-1}$  at 0.3 A  $\text{g}^{-1}$  and a good cycling stability up to 20,000 cycles at a very high current density of 30 A  $\text{g}^{-1}$ . Min et al. reported a novel bottom-up approach based on the electrostatic layer-by-layer self-assembly to bind the positively charged modified graphene with negatively charged single-layer  $\text{V}_2\text{O}_5$  nanoribbons via a facile hydrothermal method and studied it as an efficient cathode material for

LIBs<sup>182</sup>. In general, most of the V<sub>2</sub>O<sub>5</sub>/graphene heterostructures were synthesized using the solvothermal synthesis procedures which are relatively time-consuming and energy-intensive<sup>181</sup>.

Another approach to improving the performance of V<sub>2</sub>O<sub>5</sub> as the AZIB cathode is to expand the interlayer spacing in V<sub>2</sub>O<sub>5</sub> by inserting water or metal cations. Nazar et al.<sup>12</sup> reported a fast microwave-assisted synthesis of a zinc vanadate composite structure with the elemental formula of Zn<sub>0.25</sub>V<sub>2</sub>O<sub>5</sub>·nH<sub>2</sub>O. The introduction of Zn<sup>2+</sup> cations into the interlayers as structural pillars to expand V<sub>2</sub>O<sub>5</sub> layers and hold them together was found to effectively improve the structural stability and facilitate the repeated Zn<sup>2+</sup> intercalation/deintercalation processes in AZIB, yielding a relatively high specific capacity of 220 mAh g<sup>-1</sup> at a current rate of 15C with an exceptional capacity retention of over 80% after 1000 cycles. These were significantly better than the pure-phase V<sub>2</sub>O<sub>5</sub><sup>12</sup>. Pre-intercalation of Na<sup>+</sup> cations in the V<sub>2</sub>O<sub>5</sub> structure, in form of Na<sub>0.33</sub>V<sub>2</sub>O<sub>5</sub>, was also found to stabilize the layered structure and provided a high specific capacity of 360.7 mAh g<sup>-1</sup> in AZIBs with good stability<sup>183</sup>. Other metal cation inserted V<sub>2</sub>O<sub>5</sub> materials, such as Ca<sub>0.25</sub>V<sub>2</sub>O<sub>5</sub>·nH<sub>2</sub>O<sup>82</sup>, K<sub>0.25</sub>V<sub>2</sub>O<sub>5</sub><sup>83</sup> and Mg<sub>x</sub>V<sub>2</sub>O<sub>5</sub>·nH<sub>2</sub>O<sup>184</sup>, were reported to show enhanced performance and long-term cycling stability in AZIBs. However, such layer-expanded materials in general suffered from poor electronic conductivity which prevented them from achieving the theoretical potential at high charge-discharge rates, which can be improved by incorporating conductive carbon-based templates<sup>60</sup>, as discussed above.

Inspired by the aforementioned studies, we have previously developed a liquid phase exfoliation (LPE) technique to synthesize V<sub>2</sub>O<sub>5</sub> nanoribbons (NRs) using a microwave-assisted process<sup>119</sup>, which is ~12 times faster than the conventional hydrothermal methods. Subsequently, the V<sub>2</sub>O<sub>5</sub> NRs were assembled with graphene oxide (GO) nanosheets by neutralizing the negative charges on the surface of both materials using Na<sup>+</sup> cations in a Na<sub>2</sub>SO<sub>4</sub> solution, forming an

intimate  $V_2O_5$  NR/GO hybrid, which was then converted into a more conductive  $V_2O_5$  NR/rGO hybrid material by thermal annealing in  $N_2$  atmosphere. Thus-prepared  $V_2O_5$  NR/rGO hybrid material showed a high performance as electrochemical supercapacitors<sup>119</sup>.

Here we extend this method using divalent transition metal ions  $M^{2+}$  (such as  $Zn^{2+}$  or  $Mn^{2+}$ ) to bind the 2D GO nanosheets (as the structural support) with the long 1D  $V_2O_5$  NRs (as the active host materials) for  $Zn^{2+}$  ion storage in AZIBs. Our in-depth materials characterization studies indicate that the microwave-exfoliated  $V_2O_5$  NRs are single-crystalline orthorhombic  $\alpha$ - $V_2O_5$  materials with well-defined crystal orientations and present a high negative charge density on the surface. The divalent metal ions effectively neutralize the negative charges on the surfaces of  $V_2O_5$  NRs and GO nanosheets and bridge them during a coprecipitation process to form strongly bound  $V_2O_5$  NR/GO assemblies. After converting GO into more conductive rGO by thermal annealing, the formed M- $V_2O_5$  NR/rGO hybrids can utilize the highly conductive rGO nanosheets as the effective electron pathway and the improved ion transport in 1D  $V_2O_5$  NRs to achieve reversible  $Zn^{2+}$  intercalation/deintercalation. In the initial coprecipitation process, the divalent transition metal ions  $M^{2+}$  mainly bind to the surface of negatively charged  $V_2O_5$  NRs and GO nanosheets with little intercalation into  $\alpha$ - $V_2O_5$  crystals. It was found that they were able to insert between  $V_2O_5$  layers during the thermal annealing process and disrupt the crystal structure, making it a disordered  $V_2O_5$  material, which has the similar positive effect on  $Zn^{2+}$  ion storage as the aforementioned cation-expanded  $V_2O_5$  materials.

With only  $Zn^{2+}$  ions present during coprecipitation, the produced Zn- $V_2O_5$  NR/rGO hybrid has been determined to have an estimated elemental metal oxide formula as  $Zn_{0.42}V_2O_{7.54}$ , which presents a high reversible specific capacity of  $\sim 386$  mAh  $g^{-1}$  at 0.50 A  $g^{-1}$  current density ( $\sim 1.3C$  rate) with nearly 100% coulombic efficiency but drops to  $\sim 216$  mAh  $g^{-1}$  at 4.0 A  $g^{-1}$ . The capacity

fading is rather large, losing ~75% of the specific capacity after 500 cycles at fixed 4.0 A g<sup>-1</sup> current density, among which ~29% occurs at the first 10 cycles. The stability is significantly improved by mixing some Mn<sup>2+</sup> ions with the Zn<sup>2+</sup> ions during the coprecipitation process, which leads to a binary divalent metal ion mediated hybrid (Mn+Zn)-V<sub>2</sub>O<sub>5</sub> NR/rGO. The elemental composition is determined to be Zn<sub>0.12</sub>Mn<sub>0.14</sub>V<sub>2</sub>O<sub>7.16</sub>. This approach sacrifices a small portion of the specific capacity for Zn<sup>2+</sup> ion storage, with a lower specific capacity of ~289 mAh g<sup>-1</sup> at 0.5 A g<sup>-1</sup>. But the rate-performance is substantially improved, showing only a small decrease in the specific capacity to ~222 mAh g<sup>-1</sup> at 4.0 A g<sup>-1</sup>. The long cycling test at 4.0 A g<sup>-1</sup> shows a much-improved stability with the specific capacity dropping only by ~20% at the 500th cycle from the highest point (after the quick rise at the first 20 cycles). This is benefited from the stronger binding of Mn<sup>2+</sup> ions with the V<sub>2</sub>O<sub>5</sub> host, which makes them as more stable pillars to expand the V<sub>2</sub>O<sub>5</sub> layers as reported in literature<sup>85, 185</sup>. This strategy can be further optimized to achieve both high specific capacity and good long-cycling stability.

## 4.2. Experimental Methods

### 4.2.1. Chemicals and Materials:

The following chemicals were used in this work: Vanadium Pentoxide (V<sub>2</sub>O<sub>5</sub>, 99.6%) and Manganese acetate tetrahydrate (Mn (CH<sub>3</sub>COO)<sub>2</sub>·4H<sub>2</sub>O) (ACROS Organics, Pittsburg, PA, USA), Zinc acetate (Zn (CH<sub>3</sub>COO)<sub>2</sub>, 99.9%, Sigma Aldrich, St. Louis, MO, USA), single layer GO powder (ACS material LLC, Pasadena, CA), and Tetrahydrofuran (THF, 99.9%, Fisher Scientific, Hampton, NH, USA). The CR2025 and CR2032 coin cell components were purchased from MTI corporation (Richmond, CA, USA). The AZIB electrolyte was prepared with commercial zinc sulfate monohydrate from Sigma Aldrich (St. Louis, MO, USA). The commercial V<sub>2</sub>O<sub>5</sub> powder

(bulk  $V_2O_5$ ) was used both as the starting materials and the reference sample in material and electrochemical characterizations.

#### **4.2.2. Material Characterization:**

The Raman spectroscopy analysis was performed with a DXR<sup>TM</sup> Raman microscope (Thermo Fisher Scientific, Madison, WI) with a 532 nm laser at the power of 10 mW, under a 10X objective lens with a slit width of 50  $\mu$ m. The powder X-ray diffraction (XRD) study was done with a D8 Advance diffractometer (Bruker Corporation, Karlsruhe, Germany) with a Cu  $K\alpha$  radiation of wavelength 0.15418 nm and slit width of the detector was set as 2 mm. The surface composition and chemical environment of  $V_2O_5$ /rGO hybrids were analyzed using a PHI 5000 Versa XPS system (Chanhasen, MN) with a monochromatized Al  $K\alpha$  source (1486.7 eV). The transmission electron microscopy (TEM) images were obtained using Philips CM 100 with a tungsten source and a high tension of 100 kV. The field emission scanning electron microscopy (FESEM) images were obtained using a Topcon/ISI/ABT DS 130F FESEM microscope (Akashi Beam Technology Corporation, Tokyo, Japan). Thermogravimetric analysis (TGA) was carried out with TGA Q50 system (TA instruments - Waters LLC, New Castle, DE) from the room temperature to 550 °C in the air. The zeta potential measurements were carried out using ZetaPALS Zeta Potential analyzer (Brookhaven Instruments Corporation, NY, USA).

#### **4.2.3. Electrochemical Characterization:**

A slurry was prepared by mixing the active material (i.e.,  $V_2O_5$  NR/rGO, Zn- $V_2O_5$  NR/rGO and (Mn+Zn)- $V_2O_5$  NR/rGO), carbon additive (Super-P, Alfa Aesar Co. Ltd., Haverhill, Massachusetts, USA) and a poly (vinylidene fluoride) (PVDF, Sigma Aldrich Co., St. Louis, MO) binder at the weight ratio of 8:1:1 with approximately 150  $\mu$ L of N-methyl-2-pyrrolidone (NMP, Sigma Aldrich, St. Louis, MO) as the solvent. The homogenous slurry was then brush-coated onto

a 0.10 mm thick titanium disk (MTI Corporation, Richmond, CA) with a diameter of 15 mm for AZIB half-cell tests. The coated electrodes were vacuum dried at 110°C overnight and used as the cathode in AZIBs. A Zn disk (Sigma Aldrich, St. Louis, Mo) of 0.25 mm thickness and 15 mm diameter was used as the anode. Commercially purchased glass fiber disk (El-Cell, Hamburg, Germany) of 18 mm diameter and 0.65 mm thickness was used as the separator. A 0.3 mm thick stainless-steel wave spring and a 0.5 mm thick stainless-steel disk were placed behind the cathode to support the electrode structure. The electrode and separator stacks were assembled into stainless steel coin cells (CR 2025, MTI Corporation, Richmond, CA, USA) in the ambient atmosphere with 2.0 M ZnSO<sub>4</sub> aqueous solution as the electrolyte. Electrochemical characterization of the cells was carried out in the cell voltage window of 0.25 - 1.80 V in AZIB tests with a Neware battery testing system (Shenzhen, China).

#### **4.2.4. Synthesis of V<sub>2</sub>O<sub>5</sub> Nanoribbons:**

V<sub>2</sub>O<sub>5</sub> NRs were synthesized using the microwave-assisted exfoliation technique reported in our previous work<sup>119</sup>. About 0.37 g ( $\pm$  0.05 g) of commercial V<sub>2</sub>O<sub>5</sub> (bulk V<sub>2</sub>O<sub>5</sub>) powder was soaked in approximately 7.0 ml deionized (DI) water for about 4 hours to facilitate the intercalation of water molecules between the V<sub>2</sub>O<sub>5</sub> layers. The soaked V<sub>2</sub>O<sub>5</sub> powder was then filtered and transferred to a 10 ml Pyrex glass microwave vial and dispersed in 7.0 ml Tetrahydrofuran (THF) solvent. A uniform microwave field with a constant power of 300 W was applied to the reactant mixture. Temperature was ramped in ~9 minutes to attain a set temperature of 150°C and maintained at the constant temperature for an hour. After microwave reaction, the obtained product was allowed to cool down and washed (~ 2 times) with DI water and centrifuged to remove the THF solvent. The washed product is a mixture of exfoliated V<sub>2</sub>O<sub>5</sub> NRs and bulk V<sub>2</sub>O<sub>5</sub> powder. Approximately 7 mL of DI water was added to the washed mixture which was subject to

ultrasonication for 30 minutes and left undisturbed for about 4 hours. The exfoliated  $V_2O_5$  NRs (Figure S1(a)) was then collected as the liquid supernatant to be separated from the bulk unexfoliated  $V_2O_5$  precipitate through centrifugation. Thus-obtained exfoliated  $V_2O_5$  NR suspension was further used for the coprecipitation to form  $V_2O_5$  NR/GO hybrids.

#### **4.2.5. Preparation of $V_2O_5$ NR/rGO hybrids by coprecipitation:**

The  $V_2O_5$  NR/rGO hybrid materials were prepared by divalent cation mediated coprecipitation. Both the exfoliated  $V_2O_5$  NR (Figure S1(a)) and the commercial single-layer GO (Figure S1(b)) were negatively charged in DI water and formed stable homogeneous suspensions due to the electrostatic repulsion. Approximately 3.3 mg of GO nanoflakes was added to ~10 mL of homogenous suspension containing ~13.0 mg of  $V_2O_5$  NRs and the mixture was ultrasonicated for about 20 minutes to form a stable, yellow-colored homogeneous binary suspension with 20% of GO and 80% of  $V_2O_5$  (Figure S1(c)). Then about 1.30 ml of freshly prepared aqueous solution of 0.10 M Zinc Acetate or 0.10 M (Mn+Zn) acetate (containing 0.0357M Manganese acetate and 0.0643M Zinc acetate) was added dropwise to the mixed  $V_2O_5$  NR and GO suspension to form a gel-like precipitate (with grey-yellow color) at the bottom part, clearly separated from the clear water in the top part (Figure S1(d)). The gel-like precipitates are denoted as the Zn- $V_2O_5$  NR/GO or (Mn+Zn)- $V_2O_5$  NR/GO gel, respectively, which were collected and washed with DI water and then dried overnight on a hotplate at 70°C to remove any excess water from the mixture to get a black coprecipitated solid powder (Figure S1(e)). After investigating various amounts of divalent metal salts, it was found that 0.10 M concentration provided sufficient divalent metal ions ( $M^{2+}$ ) to bind  $V_2O_5$  NRs and GO nanosheets together, while the extra ions were washed off. The dried Zn- $V_2O_5$  NR/GO and (Mn+Zn)- $V_2O_5$  NR/GO precipitates were then annealed at 300°C in  $N_2$  atmosphere for 2 hours (at an initial ramping rate of 10°C/min) to reduce the GO structure into

rGO, forming the hybrid materials referred to as Zn-V<sub>2</sub>O<sub>5</sub> NR/rGO and (Mn+Zn)-V<sub>2</sub>O<sub>5</sub> NR/rGO, respectively, or generally as M-V<sub>2</sub>O<sub>5</sub> NR/rGO.

### 4.3. Results and discussion:

#### 4.3.1. Synthesis Design:

The synthesis of M-V<sub>2</sub>O<sub>5</sub> NR/rGO hybrids is illustrated in Figure 1. Over the past decade, the V<sub>2</sub>O<sub>5</sub> nanostructures have been investigated widely as efficient electrode materials for EESs such as lithium-ion batteries<sup>109</sup>, supercapacitors<sup>110</sup>, sodium ion batteries<sup>111</sup>, zinc ion batteries<sup>112</sup> etc. It has also been proven that the V<sub>2</sub>O<sub>5</sub> nanostructures such as nanorods<sup>113</sup>, nanowires<sup>114</sup>, nanospheres<sup>112</sup>, nanoribbons<sup>115, 116</sup> perform better with higher specific capacity and stability compared to its bulk counterparts. In the past, V<sub>2</sub>O<sub>5</sub> nanostructures were synthesized with solvothermal/hydrothermal methods<sup>115, 116</sup>, template-based methods<sup>117</sup>, and electrochemical deposition<sup>118</sup>. Among them, hydrothermal technique is considered easier and effective. In this work, we report a novel coprecipitation method to synthesize the hybrid material of microwave exfoliated V<sub>2</sub>O<sub>5</sub> NRs and GO structures. The bulk V<sub>2</sub>O<sub>5</sub> is soaked in distilled water to intercalate the water molecules in between the V<sub>2</sub>O<sub>5</sub> layers. The microwave-assisted synthesis used in this work has been reported to be a faster and environmental-friendly technique compared to the conventional hydrothermal technique.<sup>119</sup> The microwave absorbing capacity of a material is defined by its dielectric loss, i.e., the  $\tan\delta$  value. The pre-intercalated V<sub>2</sub>O<sub>5</sub> structure contains water molecule (with  $\tan\delta = \sim 0.1$ ) is then dispersed in the microwave transparent THF solvent with a comparatively lower  $\tan\delta$  value (0.042). The specific heating of the microwave to the intercalated water molecules<sup>99</sup> leads to the breaking down and separation of the V<sub>2</sub>O<sub>5</sub> layers which are bonded by weak Van der Waals interaction and thus exfoliate the bulk V<sub>2</sub>O<sub>5</sub>  $\alpha$ -orthorhombic structure into V<sub>2</sub>O<sub>5</sub> NRs.

The surface of the as-exfoliated  $V_2O_5$  NRs and GO precursors are negatively charged with zeta potentials of -32.16 mV and -31.55 mV, respectively (Table B.1). Each material forms a homogenous suspension in the DI water as shown in Figures B.1(a) and B.1(b) and remains as a stable homogeneous suspension after mixing due to their repulsive electrostatic interaction as shown in Figure B.1(c). This prevents them from assembling into intimate hybrid materials. However, they easily coprecipitate into a gel-like material (Figure B.1 (d)) after addition of divalent metal cations (such as  $Zn^{2+}$  and  $Mn^{2+}$ ), which neutralize the negative charges and assemble  $V_2O_5$  NRs and GO nanosheets together as schematically illustrated in Figure 4.1. This forms a hybrid material with  $V_2O_5$  NRs uniformly anchored on GO nanosheets. The divalent metal cations act as connecting bridges not only hold  $V_2O_5$  NRs and GO nanosheets together, but also provide continuous electron and ion conduction pathways in the porous structure. The coprecipitated  $V_2O_5$  NR/GO was further annealed in the inert  $N_2$  atmosphere at  $300^\circ C$  to convert the GO into less defective rGO with higher electrical conductivity.

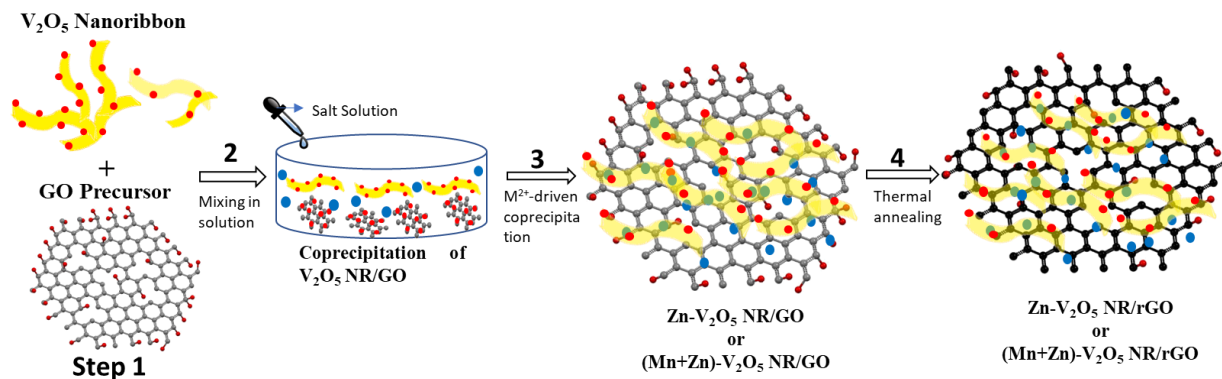


**Figure 4.1.** Schematic illustration of synthesis by coprecipitated  $V_2O_5$  NR/rGO hybrid. 1:  $V_2O_5$  NRs and Graphene Oxide (GO) precursors are dispersed in water to form stable suspensions by ultrasonication; 2: The mixed  $V_2O_5$  and GO precursors remain as a homogeneous suspension due to electrostatic repulsion; 3: Zinc acetate or Manganese acetate solutions are added dropwise to coprecipitate the negatively charged  $V_2O_5$  NRs and GO nanosheets into a gel-like precipitate which is collected and dried by heating for approximately 6 hours at  $70^\circ C$  on a hotplate; and 4: The dried  $V_2O_5$  NR/GO is further annealed in a tube furnace at  $300^\circ C$  for 2 hours in  $N_2$  atmosphere to convert GO to rGO and form the hybrid material of  $V_2O_5$  NR/rGO.

### 4.3.2. Morphological Characterization:

TEM was performed first to investigate the morphology and crystal structure of  $V_2O_5$  NRs,  $Zn-V_2O_5$  NR/rGO and  $(Mn+Zn)-V_2O_5$  NR/rGO. Figures 4.2(a) and 4.2(b) show the representative TEM images of bare rGO and  $V_2O_5$  NRs before the coprecipitation process, respectively. The morphology of the bare rGO resembles the typical nanoflake-like structure with many wrinkles on the surface due to its softness. The TEM image of the microwave-exfoliated  $V_2O_5$  NRs in Figure 4.2 (b) shows the random stack of long ribbon structures with the width of 10 to 30 nm and the length over hundreds of nanometers. The morphology of the microwave-exfoliated  $V_2O_5$  NRs is clearly different from that of the bulk  $V_2O_5$  crystalline powder as compared in Figures B.2(a) and B.2(b). They illustrate that bulk  $V_2O_5$  particles have disintegrated and subsequently grown along a specific lattice direction to produce ultralong nanoribbons during the microwave process.

Interestingly, the selected area electron diffraction (SAED) pattern in Figure 4.2(c), measured from the red-circled area in Figure 4.2(b), shows extended sharp diffraction spots forming a well-defined rectangular lattice matching the 2D in-plane diffraction of (001) plane of the orthorhombic  $\alpha$ - $V_2O_5$  crystals. For clarity, only the SAED pattern in a darker area off from the high background region around (000) spot was shown in Figure 4.2(c). The SAED pattern clearly illustrates the single crystalline nature of the exfoliated  $V_2O_5$  NRs. It reveals that the NRs preserve the main orthorhombic  $\alpha$ - $V_2O_5$  structure of the starting bulk crystal<sup>186, 187</sup>. As shown in Figure S3, the orthorhombic  $\alpha$ - $V_2O_5$  structure has three orthogonal lattices:  $a = 11.516 \text{ \AA}$ ,  $b = 3.566 \text{ \AA}$  and  $c = 4.373 \text{ \AA}$  (based on JCPDS: 41-1426). The selected  $V_2O_5$  NR in Figures 4.2(b) and 4.2(c) predominantly lies flat on the TEM grid with the crystal plane (001) perpendicular to the electron beam. Thus, all SAED spots can be indexed as (hk0) of the bulk orthorhombic  $\alpha$ - $V_2O_5$  crystal. The full raw SAED pattern in Figure B.4(a) and the enlarged area near (000) in Figure B.4(b)

reveal the same information. Further analysis of the orientation of the rectangular SAED pattern is discussed in the text following Figure B.4 in the Supporting Information, which indicates that the (010) direction (lattice  $b$ ) of this  $V_2O_5$  NR is perpendicular to the long ribbon axis while the (100) direction (lattice  $a$ ) is along the long ribbon axis, as illustrated in Figure 4.2(d). Furthermore, the SAED pattern shows systematic variations among the (hk0) spots, with some spots, such as (200), (020), (110), (220), etc., appearing bright while others, such as (100), (010), (120), (210), etc., being dark. These are consistent with the variation of the form factor of the large orthorhombic  $\alpha$ - $V_2O_5$  unit cell as shown in the JCPDS: 41-1426 file, which further validates that the exfoliated  $V_2O_5$  NRs preserve the orthorhombic  $\alpha$ - $V_2O_5$  crystal structure<sup>186, 187</sup>.

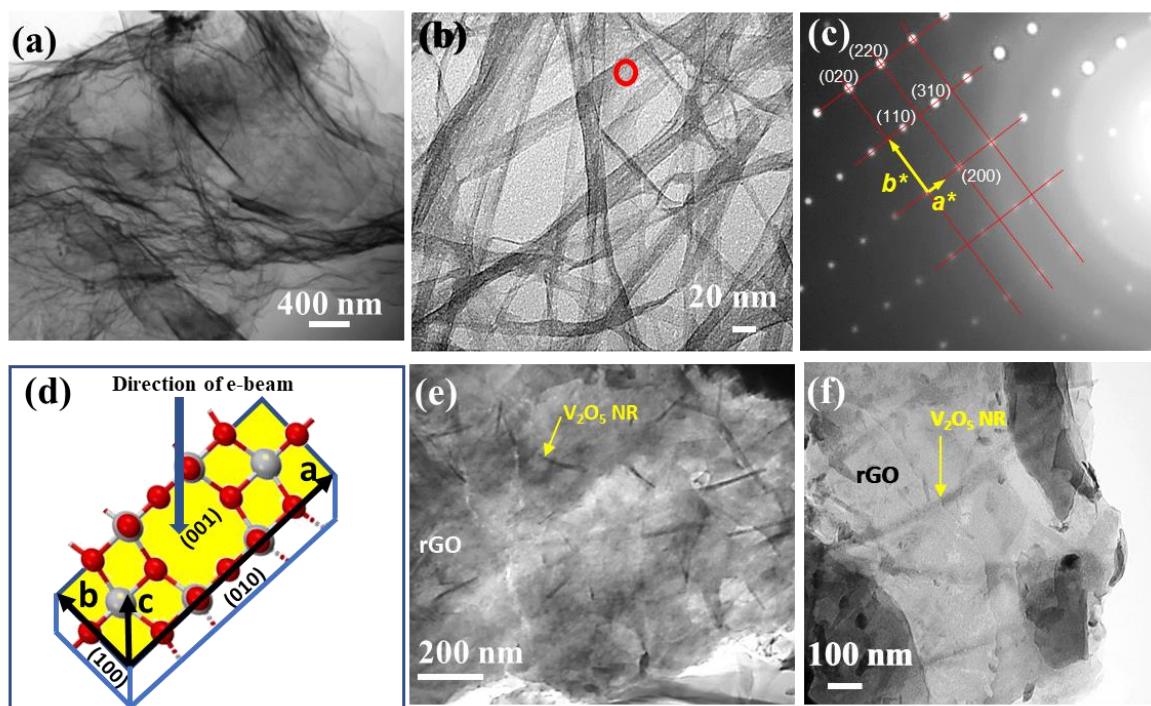


**Figure 4.2.** TEM images of (a) bare rGO and (b) as-exfoliated  $V_2O_5$  NRs. (c) The selected area electron diffraction (SAED) pattern of the  $V_2O_5$  NR red-circled in panel (b) and the (hk0) index according to orthorhombic  $\alpha$ - $V_2O_5$  crystal structure (based on standard pattern of JCPDS:41-1426) with the (001) plane perpendicular to the electron beam. (d) Illustration of the crystal orientation of the  $V_2O_5$  NRs. TEM images of the coprecipitated hybrid materials of  $V_2O_5$  NRs on rGO nanosheets in form of (e) Zn- $V_2O_5$  NR/rGO and (f) (Mn+Zn)- $V_2O_5$  NR/rGO.

Figures 4.2(e) and 4.2(f) show the representative TEM images of Zn-V<sub>2</sub>O<sub>5</sub> NR/rGO and (Mn+Zn)-V<sub>2</sub>O<sub>5</sub> NR/rGO hybrids respectively. The TEM images show two distinct morphological features attributed to V<sub>2</sub>O<sub>5</sub> NRs (indicated by the yellow arrows) sandwiched between rGO nanosheets to form a hybrid structure. This further proves the successful assembly of V<sub>2</sub>O<sub>5</sub> NRs on rGO nanosheets through bridging by divalent metal cations.

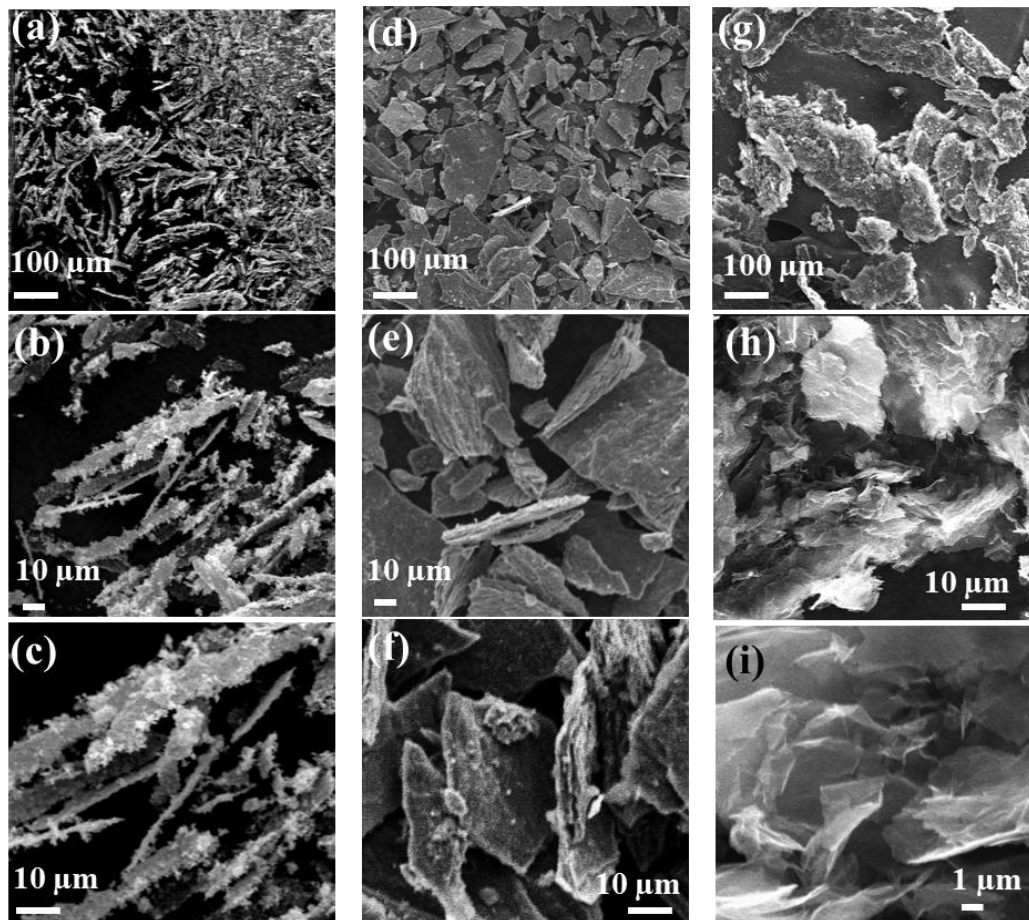


**Figure 4.3.** FESEM images at low to higher magnifications of (a-c) V<sub>2</sub>O<sub>5</sub> NR, (d-f) Zn-V<sub>2</sub>O<sub>5</sub> NR/rGO, and (g-i) (Mn+Zn)-V<sub>2</sub>O<sub>5</sub> NR/rGO.

The morphology of the dried V<sub>2</sub>O<sub>5</sub> NR and the coprecipitated V<sub>2</sub>O<sub>5</sub> NR/rGO hybrids are further characterized with FESEM. As shown in Figures 4.3(a-c), the dried V<sub>2</sub>O<sub>5</sub> NRs aggregate into rigid ribbon-like structures with the length ranging from several to tens of microns and the

width of approximately 1-10 microns. which are much larger than the dispersed NRs observed under TEM in Figure 4.2(b). Figures 4.3(d-f) shows the FESEM images of Zn-V<sub>2</sub>O<sub>5</sub> NR/rGO which present flat plate-like structures with the thickness ranging from 1-5 μm and lateral size over 50 μm. The large plate size and thickness indicate that they likely consist of a random stacking of many V<sub>2</sub>O<sub>5</sub> NRs and rGO nanosheets during the self-assembly process, which is consistent with the TEM images. The Zn-V<sub>2</sub>O<sub>5</sub> NR/rGO hybrid plates appear to be more rigid than the thinner single GO nanosheets shown in Figure 4.2(a). In contrast, the FESEM images of (Mn+Zn)-V<sub>2</sub>O<sub>5</sub> NR/rGO in Figure 4.3(g-i) show much thinner (< 1 μm) and wrinkled plates compared to Zn-V<sub>2</sub>O<sub>5</sub> NR/rGO. The surface is rougher, indicating a more disordered structure than Zn-V<sub>2</sub>O<sub>5</sub> NR/rGO. The incorporation of mixed Mn<sup>2+</sup> and Zn<sup>2+</sup> cations seem to disrupt the tight packing of the V<sub>2</sub>O<sub>5</sub> NR/rGO, which could facilitate faster ion intercalation in batteries.

#### **4.3.3. Structural Characterization:**

The microstructure of microwave-exfoliated V<sub>2</sub>O<sub>5</sub> NR, Zn-V<sub>2</sub>O<sub>5</sub> NR/rGO and (Mn+Zn)-V<sub>2</sub>O<sub>5</sub> NR/rGO is further studied using Raman spectroscopy and XRD analyses. Figure 4.4(a) presents the Raman spectra of bulk V<sub>2</sub>O<sub>5</sub> (black), V<sub>2</sub>O<sub>5</sub> NR (red), Zn-V<sub>2</sub>O<sub>5</sub> NR/rGO (blue) and (Mn+Zn)-V<sub>2</sub>O<sub>5</sub> NR/rGO (green). The Raman spectrum of V<sub>2</sub>O<sub>5</sub> NR matches well with that of the commercial V<sub>2</sub>O<sub>5</sub> powder suggesting that the microwave-assisted exfoliation process does not disrupt the local crystal structure of α-V<sub>2</sub>O<sub>5</sub><sup>117, 188, 189</sup>. The Raman spectra of all samples show distinct peaks at 140.9 cm<sup>-1</sup>, 281.6 cm<sup>-1</sup>, 403.1 cm<sup>-1</sup>, 529.4 cm<sup>-1</sup>, 695.3 cm<sup>-1</sup> and 991.3 cm<sup>-1</sup> which are attributed to the -O-V-O-V- stretching, V-O<sub>1</sub> bending, V-O<sub>3</sub> bending, V-O<sub>2</sub> stretching, V-O<sub>3</sub> stretching and V-O<sub>1</sub> stretching of the V<sub>2</sub>O<sub>5</sub> layers in the α-V<sub>2</sub>O<sub>5</sub> structure<sup>119, 188, 189</sup>. In addition to the peaks attributed to V<sub>2</sub>O<sub>5</sub>, the Raman spectra of Zn-V<sub>2</sub>O<sub>5</sub> NR/rGO and (Mn+Zn)-V<sub>2</sub>O<sub>5</sub> NR/rGO show an additional broad peak around 870 cm<sup>-1</sup> (marked with the arrows) that can be attributed to

the presence of multiple oxidation states of vanadium due to the intercalation or surface binding of  $\text{Zn}^{2+}$  and  $\text{Mn}^{2+}$  cations<sup>190</sup>. The Raman spectra of the  $\text{Zn-V}_2\text{O}_5$  NR/rGO and  $(\text{Mn+Zn})\text{-V}_2\text{O}_5$  NR/rGO also show two major peaks at around  $1350\text{ cm}^{-1}$  and  $1598.1\text{ cm}^{-1}$  attributing to the D and G bands of the rGO nanosheets, originating from the vibrational modes of  $\text{sp}^3$  carbon at the defect sites and the in-plane vibration of  $\text{sp}^2$ -bonded carbon atoms. The  $I_D/I_G$  ratio of  $\text{Zn-V}_2\text{O}_5$  NR/rGO and  $(\text{Mn+Zn})\text{-V}_2\text{O}_5$  NR/rGO is estimated to be 0.83 and 0.92, respectively, suggesting the success conversion of GO to rGO which still consists of a high degree of defects in the  $\text{sp}^2$  lattice upon removal of the oxygenated functional groups by thermal annealing<sup>151</sup>.

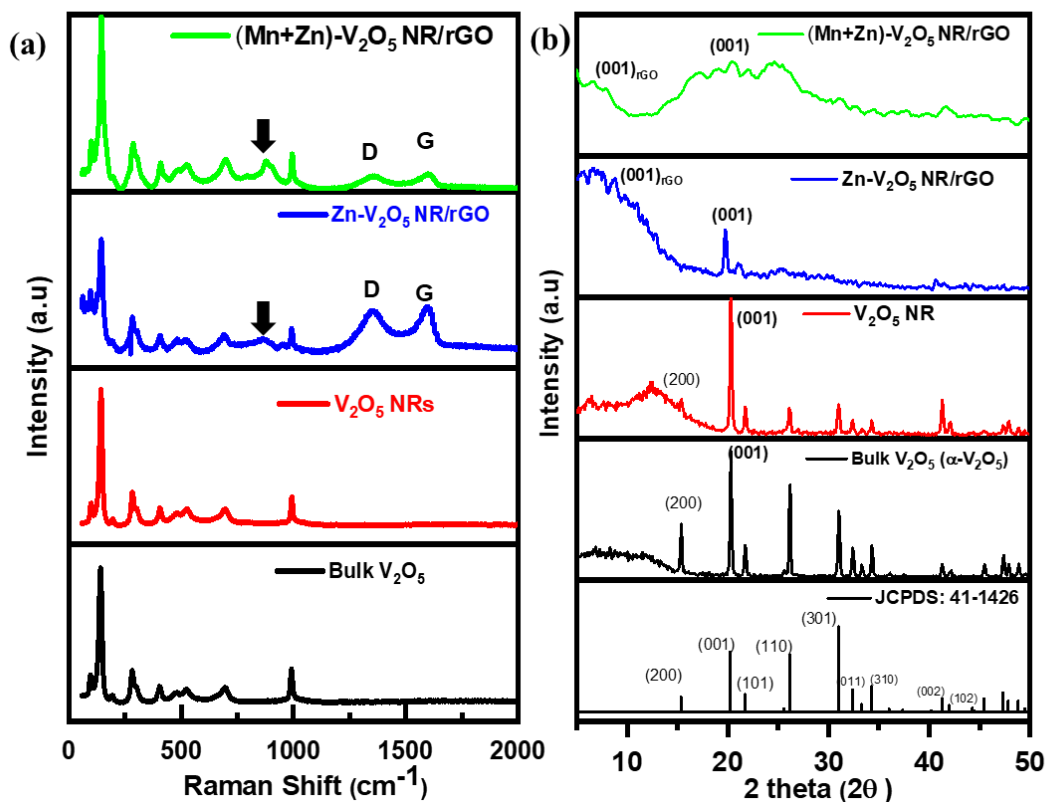


**Figure 4.4.** (a) Raman spectra and (b) powder XRD spectra of  $\text{Zn-V}_2\text{O}_5$  NR/rGO (blue),  $(\text{Mn+Zn})\text{-V}_2\text{O}_5$  NR/rGO (green)) in comparison to the control samples of  $\text{V}_2\text{O}_5$  NR (red) and bulk  $\text{V}_2\text{O}_5$  powder (black). The bottom part of panel (b) is the standard pattern of orthorhombic  $\alpha\text{-V}_2\text{O}_5$  crystal (JCPDS:41-1426).

The XRD spectra of bulk  $V_2O_5$  (black),  $V_2O_5$  NR (red), Zn- $V_2O_5$  NR/rGO (blue) and (Mn+Zn)- $V_2O_5$  NR/rGO (green) are compared with the standard reference pattern of orthorhombic  $\alpha$ - $V_2O_5$  structure (black) (JCPDS: 41-1426) at the bottom in Figure 4.4(b). The XRD spectra of bulk  $V_2O_5$  powder and  $V_2O_5$  NR show very similar well-defined sharp peaks exactly matching the standard reference pattern of  $\alpha$ - $V_2O_5$  (JCPDS: 41-1426), suggesting that  $V_2O_5$  NRs preserve the bulk orthorhombic crystal structure as revealed by SAED in the earlier discussion. This again validates that the microwave-assisted exfoliation process did not disrupt the internal crystal structure in the  $V_2O_5$  NRs<sup>191</sup>. The (001) diffraction peak of  $V_2O_5$  NRs is comparatively more intense than the other peaks, such as (110) and (301), suggesting the higher order of stacking of  $V_2O_5$  layers in the (001) direction<sup>192</sup>. The d-spacing of the commercial bulk  $V_2O_5$  and exfoliated  $V_2O_5$  NRs are calculated to be 0.437 nm based on (001) peak at the  $2\theta$  value of  $20.26^\circ$ . An additional peak of  $V_2O_5$  NR is observed at  $2\theta = 12.5^\circ$  (corresponding to  $d = 0.706$  nm), which may be due to some disordered  $V_2O_5$  bilayer residue<sup>193</sup>. The peak is quite broad with a full width at the half-maximum (FWHM) of  $\Delta 2\theta = \sim 2.5^\circ$ . Following the Scherrer equation,

$$\tau = \frac{K\lambda}{(\Delta 2\theta) \cos\theta} \quad (1)$$

where the shape factor is assumed to be  $K = 0.9$  and the X-ray wavelength is  $\lambda = 0.154$  nm, the mean crystal thickness of the  $V_2O_5$  bilayered stacking can be estimated as  $\tau = \sim 3.2$  nm (only about 5-6 layers). The XRD spectrum of Zn- $V_2O_5$  NR/rGO shows only two weak diffraction peaks at the  $2\theta$  value of  $19.80^\circ$  and  $21.05^\circ$ , attributed to the (001) and (101) diffraction of  $V_2O_5$ . The absence of other diffraction peaks can be due to the disordering caused by intercalation of some guest  $Zn^{2+}$  ions in the  $V_2O_5$  structure. This is further supported by the shift of (001) peak from  $20.26^\circ$  in the exfoliated  $V_2O_5$  NRs to a lower value of  $19.80^\circ$  in Zn- $V_2O_5$  NR/rGO, suggesting a slightly larger d-spacing of 0.447 nm due to intercalation of  $Zn^{2+}$  ions. However, the XRD spectrum of (Mn+Zn)-

V<sub>2</sub>O<sub>5</sub> NR/rGO only shows uncharacteristic broad peaks which might contain a peak around 20° corresponding to V<sub>2</sub>O<sub>5</sub>. These broad peaks reflect much higher disordering in V<sub>2</sub>O<sub>5</sub> NRs owing to the intercalation of mixed Mn<sup>2+</sup> and Zn<sup>2+</sup> ions, which is consistent with the FESEM images in Figures 4.3(g-i). In addition to the peaks corresponding to V<sub>2</sub>O<sub>5</sub> NRs in the composite, the XRD spectra of Zn-V<sub>2</sub>O<sub>5</sub> NR/rGO and (Mn+Zn)-V<sub>2</sub>O<sub>5</sub> NR/rGO also show a broad shoulder below 9°, attributed to the (001) diffraction from the disordered rGO stacking in the hybrids<sup>194</sup>.

#### 4.3.4. XPS Analysis:

The chemical composition of bulk V<sub>2</sub>O<sub>5</sub>, V<sub>2</sub>O<sub>5</sub> NR, Zn-V<sub>2</sub>O<sub>5</sub> NR/rGO and (Mn+Zn)-V<sub>2</sub>O<sub>5</sub> NR/rGO were investigated using X-ray photoelectron spectroscopy (XPS) analysis. The XPS analysis discusses the composition, oxidation states and binding environment of different elements involved in the composites with high-resolution spectra in different binding energy (BE) ranges, including V2p (512 eV - 528 eV), O1s (528 eV - 535 eV), C1s (280 eV – 294 eV), Zn2p (1010 eV – 1050 eV) and Mn2p (638 eV – 662 eV). The high-resolution spectra are analyzed by careful deconvolution of potential components. The area ratio of 2p<sub>3/2</sub> and 2p<sub>1/2</sub> peaks in each species is fixed at 2:1.

Figures B.5(a) and B.5(b) compares the high resolution V2p and O1s spectra of V<sub>2</sub>O<sub>5</sub> NRs and bulk V<sub>2</sub>O<sub>5</sub> powder. The V2p spectra of V<sub>2</sub>O<sub>5</sub> NRs consists of two distinct pairs of 2p<sub>3/2</sub> and 2p<sub>1/2</sub> peaks around (515.55 eV and 522.75 eV) and (517.04 eV and 524.50 eV), attributed to the presence of V<sup>4+</sup> and V<sup>5+</sup> metal centers, respectively, in the NRs. Similar features present in bulk V<sub>2</sub>O<sub>5</sub>, Zn-V<sub>2</sub>O<sub>5</sub> NR/rGO and (Mn+Zn)-V<sub>2</sub>O<sub>5</sub> NR/rGO. The binding energy values of all the peaks in all four samples are listed in Table S2. The O1s spectra of bulk V<sub>2</sub>O<sub>5</sub> shows a distinct peak at 530.71 eV attributed to V-O species in addition to that of physisorbed oxygen at 529 eV. However, the O1s spectra of V<sub>2</sub>O<sub>5</sub> NRs possess an extra peak at 532.75 eV in addition to that of physisorbed

oxygen and V-O peak in the bulk  $V_2O_5$ , which can be attributed to the cleavage of -V-O-V- bond between the layers due to microwave exfoliation.

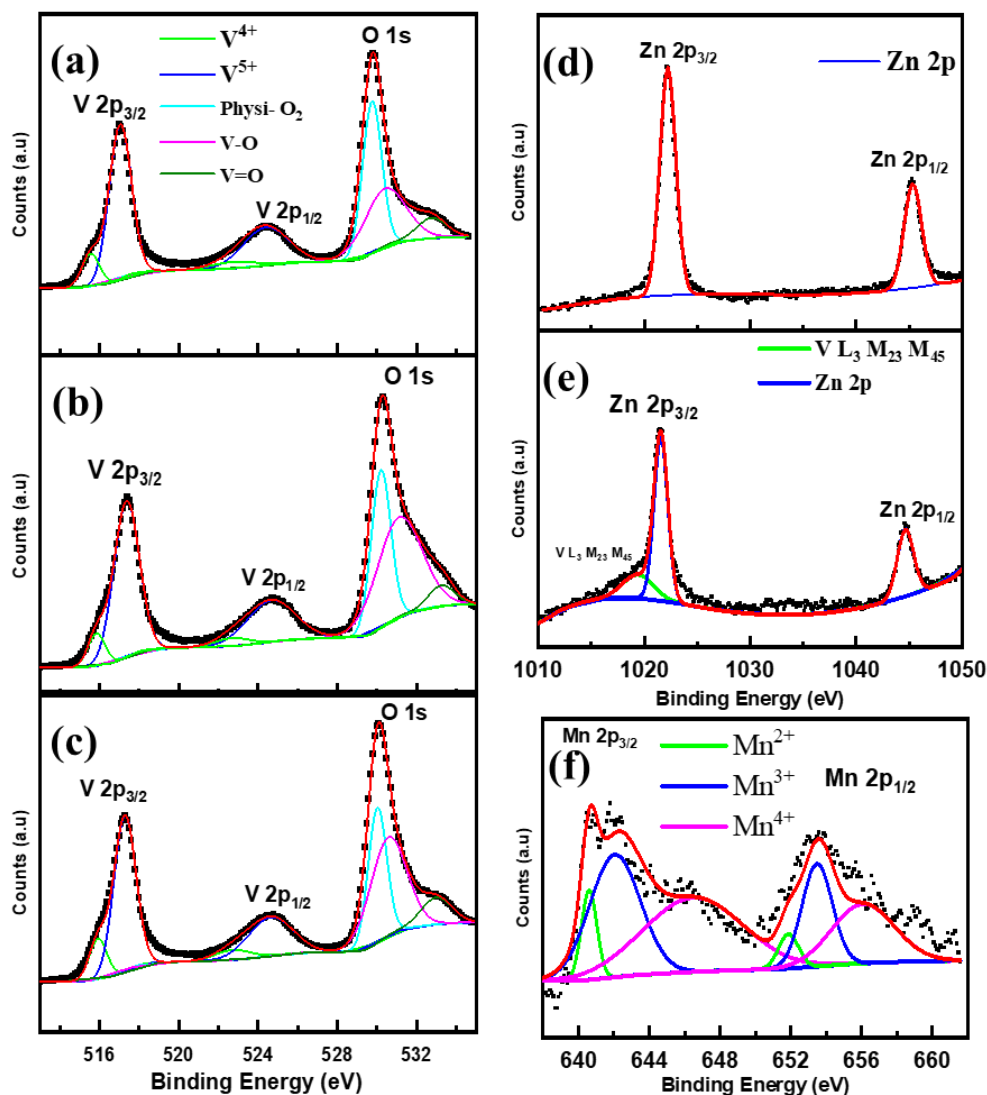


**Figure 4.5.** The high-resolution XPS spectra of V 2p (510-528 eV) and O1s (528-534 eV) from (a)  $V_2O_5$  NR, (b) Zn- $V_2O_5$  NR/rGO and (c) (Mn+Zn)- $V_2O_5$  NR/rGO. The Zn2p spectra of (d) Zn- $V_2O_5$  NR/rGO and (e) (Mn+Zn)- $V_2O_5$  NR/rGO. (f) The Mn2p spectra of (Mn+Zn)- $V_2O_5$  NR/rGO.

The features similar to V2p and O1s XPS spectra of  $V_2O_5$  NR also present in Zn- $V_2O_5$ /rGO and (Mn+Zn)- $V_2O_5$  NR/rGO, as shown in Figures 4.5(b) and 4.5(c). The vanadium atoms in all

these samples present in both  $V^{5+}$  or  $V^{4+}$  states but are dominated by  $V^{5+}$  (>82%). The at% of  $V^{4+}$  in  $V_2O_5$  NR and M- $V_2O_5$  NR/rGO hybrids is about 12-17%, slightly higher than that in the bulk  $V_2O_5$  powder. Comparing to  $V_2O_5$  NR, there is a slight shift in the  $V^{4+}$   $2p_{3/2}$  peak to a higher binding energy by 0.29 eV and 0.37 eV in Zn- $V_2O_5$  NR/rGO and (Mn+Zn)- $V_2O_5$  NR/rGO, respectively, indicating a stronger interaction predominantly between the intercalated  $Zn^{2+}$  and  $Mn^{2+}$  ions with the  $V^{4+}$  metal centers in the coprecipitated M- $V_2O_5$  NR/rGO hybrids. However, there is no shift in the  $V^{5+}$   $2p_{3/2}$  peak, suggesting that the pre-intercalated  $Zn^{2+}$  and  $Mn^{2+}$  ions do not bind on the  $V^{5+}$  centers, leaving a major part of  $V_2O_5$  host available for reversible  $Zn^{2+}$  ion storage.

The high-resolution Zn2p spectra of the Zn- $V_2O_5$  NR/rGO and (Mn+Zn)- $V_2O_5$  NR/rGO are shown in Figures 4.5(d) and 4.5(e), respectively. The Zn2p spectrum of Zn- $V_2O_5$  NR/rGO shows a pair of peaks at 1022.21 eV and 1045.32 eV, attributed to the  $2p_{3/2}$  and  $2p_{1/2}$  peaks respectively. Likewise, the Zn2p spectrum of (Mn+Zn)- $V_2O_5$  NR/rGO also shows a pair of  $2p_{3/2}$  and  $2p_{1/2}$  peaks at 1021.49 eV and 1044.73 eV, respectively. It is notable that the  $2p_{3/2}$  peak of (Mn+Zn)- $V_2O_5$  NR/rGO slightly shifts towards lower BE, suggesting a possible electron transfer from  $V^{4+}$  metal center to  $Zn^{2+}$ , which is consistent with the positive shift in the  $V^{4+}$   $2p_{3/2}$  peak. The Mn2p spectrum of (Mn+Zn)- $V_2O_5$  NR/rGO in Figure 5(f) shows three pairs of  $2p_{3/2}$  and  $2p_{1/2}$  peaks at (640.57 eV and 651.81 eV), (642.07 eV and 653.51 eV) and (646.70eV and 656.20eV), suggesting the presence of Mn ions in three oxidation states as  $Mn^{2+}$  (9.21%),  $Mn^{3+}$  (41.50%) and  $Mn^{4+}$  (49.29%), respectively. A large portion of  $Mn^{2+}$  is apparently oxidized to higher valence states during the thermal annealing process, which is expected to bind stronger with the  $V_2O_5$  host and rGO. Figures B.5(c) and B.5(d) show the C1s spectra of Zn- $V_2O_5$  NR/rGO and (Mn+Zn)- $V_2O_5$  NR/rGO, respectively, which consist of three distinct peaks. The peaks at 284 eV and 285 eV are attributed to C=C and C-O primarily in the rGO while the peak at 286.81 eV in Zn- $V_2O_5$  NR/rGO

or 287.26 eV in (Mn+Zn)-V<sub>2</sub>O<sub>5</sub> NR/rGO is attributed to the carbon atoms in rGO that are bound with the metal ions.<sup>195</sup> It is worth noting that the C-metal ion peak in (Mn+Zn)-V<sub>2</sub>O<sub>5</sub> NRs/rGO is shifted to a higher BE of 287.26 eV from 286.81 eV in Zn-V<sub>2</sub>O<sub>5</sub>/rGO, which suggests a stronger interaction between the transition metal ions and rGO after addition of Mn<sup>2+</sup>.

Table B.2 summarizes the estimated atomic percentages based on the XPS spectra. The atomic ratio of V<sup>4+</sup>/V<sup>5+</sup> is 0.10, 0.17, 0.14 and 0.21 for bulk V<sub>2</sub>O<sub>5</sub>, V<sub>2</sub>O<sub>5</sub> NRs, Zn-V<sub>2</sub>O<sub>5</sub> NR/rGO and (Mn+Zn)-V<sub>2</sub>O<sub>5</sub> NR/rGO respectively. V<sup>5+</sup> is the dominating oxidation state in all these samples while the 12% – 17% V at the V<sup>4+</sup> oxidation state has an important effect in the specific capacity and long-term stability of the electrode<sup>50</sup>. Based on the XPS spectra, the atomic ratio of V to O is estimated to be 1:2.7, 1:3.13, 1:3.77, 1:3.58 in bulk V<sub>2</sub>O<sub>5</sub>, V<sub>2</sub>O<sub>5</sub> NR, Zn-V<sub>2</sub>O<sub>5</sub> NR/rGO and (Mn+Zn)-V<sub>2</sub>O<sub>5</sub> NR/rGO, respectively. The V:O ratio in all these samples is lower than the stoichiometric ratio of 1:2.5 for pure in the V<sub>2</sub>O<sub>5</sub>. The extra O atoms can be attributed to absorption of water from the environmental moisture. The nanostructure of V<sub>2</sub>O<sub>5</sub> NRs presents a higher O content than the bulk V<sub>2</sub>O<sub>5</sub> due to easier water absorption and small intercalation of water molecules during the microwave exfoliation. The Zn-V<sub>2</sub>O<sub>5</sub> NR/rGO and (Mn+Zn)-V<sub>2</sub>O<sub>5</sub> NR/rGO hybrids present further increased O atoms which can be attributed to the formation of metal oxides during the coprecipitation/annealing processes and some oxygen-containing groups in rGO. The elemental formula of the Zn-V<sub>2</sub>O<sub>5</sub> NR/rGO and (Mn+Zn)-V<sub>2</sub>O<sub>5</sub> NR/rGO can be estimated as Zn<sub>0.42</sub>V<sub>2</sub>O<sub>7.54</sub> and Zn<sub>0.12</sub>Mn<sub>0.14</sub>V<sub>2</sub>O<sub>7.16</sub>, respectively, based on the atomic ratios listed in Table B.2.

#### **4.3.5. Thermogravimetric Analysis:**

The TGA was carried out in the temperature range from room temperature to 550 °C in air at a heating rate of 10 °C/min to derive the weight percentages of V<sub>2</sub>O<sub>5</sub> NRs and rGO in the composites. Figure B.6(a) presents the comparison of different TGA curves of V<sub>2</sub>O<sub>5</sub> NR, bare

rGO, Zn-V<sub>2</sub>O<sub>5</sub> NR/rGO and (Mn+Zn)-V<sub>2</sub>O<sub>5</sub> NR/rGO. The TGA curve of V<sub>2</sub>O<sub>5</sub> NR (green) shows almost a flat line with a negligible weight loss of only 1.7% at 550 °C which is mostly due to the loss of physisorbed and intercalated water. However, the TGA curve of bare rGO (black) shows a rather stable curve till 300°C with a weight loss of 4.1% which is probably due to the loss of physisorbed water and then shows a rapid weight loss from 400 °C to 490 °C by 89.84% due to oxidation of rGO into CO<sub>2</sub>. Only 10.16% of graphitic carbon was left at 550 °C. The TGA curve of (Mn+Zn)-V<sub>2</sub>O<sub>5</sub> NR/rGO shows stable behavior with no significant loss till 350°C and then gradually loses weight from 350°C to 550°C by 11.66%, predominantly due to decomposition of rGO in the composite. Whereas, the TGA curve of Zn-V<sub>2</sub>O<sub>5</sub> NR/rGO shows a significant weight loss of about 19.46% that occurs in three distinct steps: (i) a considerable amount of weight loss of about 7.45% starting from 60 °C till 120 °C due to the loss of physisorbed water; (ii) a gradual weight loss of about 2.72 % from 120 °C to 325 °C due to the loss of structural water in the composite, and (iii) finally a weight loss of about 9.29% from 325°C to 550°C attributed to the oxidation of rGO. The weight loss due to decomposition of zinc and manganese oxides can be neglected as no observable loss in weight up to 550 °C is shown in Figure B.6(b). The wt% of V<sub>2</sub>O<sub>5</sub> NR and rGO in the composites derived using this method are listed in Table B.3 in the Supporting Information.

#### **4.3.6. Electrochemical Characterization:**

The Zn<sup>2+</sup> ion storage properties of Zn-V<sub>2</sub>O<sub>5</sub> NR/rGO and (Mn+Zn)-V<sub>2</sub>O<sub>5</sub> NR/rGO cathodes are systematically investigated using galvanostatic charge-discharge tests for rate performance and long-term cycling evaluation, and cyclic voltammetry tests for understanding the mechanism. The rate performance of Zn-V<sub>2</sub>O<sub>5</sub> NR/rGO in the AZIB is shown in Figures 4.6(a), with the current density sequentially set at 0.50 Ag<sup>-1</sup>, 1.0 Ag<sup>-1</sup>, 2.0 Ag<sup>-1</sup>, 4.0 Ag<sup>-1</sup> and 6.0 Ag<sup>-1</sup> (calculated with the

total mass of Zn-V<sub>2</sub>O<sub>5</sub> NR/rGO) in the potential window 0.20 V – 1.80 V. Ten charge-discharge cycles are applied at each current density value. The starting current density (0.50 A g<sup>-1</sup>) is about 1.7C rate based on the theoretical capacity of 294 mAh g<sup>-1</sup> (corresponding to one Zn<sup>2+</sup> ion per V<sub>2</sub>O<sub>5</sub>). The (Mn+Zn)-V<sub>2</sub>O<sub>5</sub> NR/rGO is characterized in the same way except that the current density of 6 A g<sup>-1</sup> is not applied. In the following discussions for the hybrid materials, the specific capacity is calculated using the mass of the active Zn<sup>2+</sup> storage materials, i.e., Zn-V<sub>2</sub>O<sub>5</sub> NR or (Mn+Zn)-V<sub>2</sub>O<sub>5</sub> NR, derived from the TGA analysis shown in Table B.3.

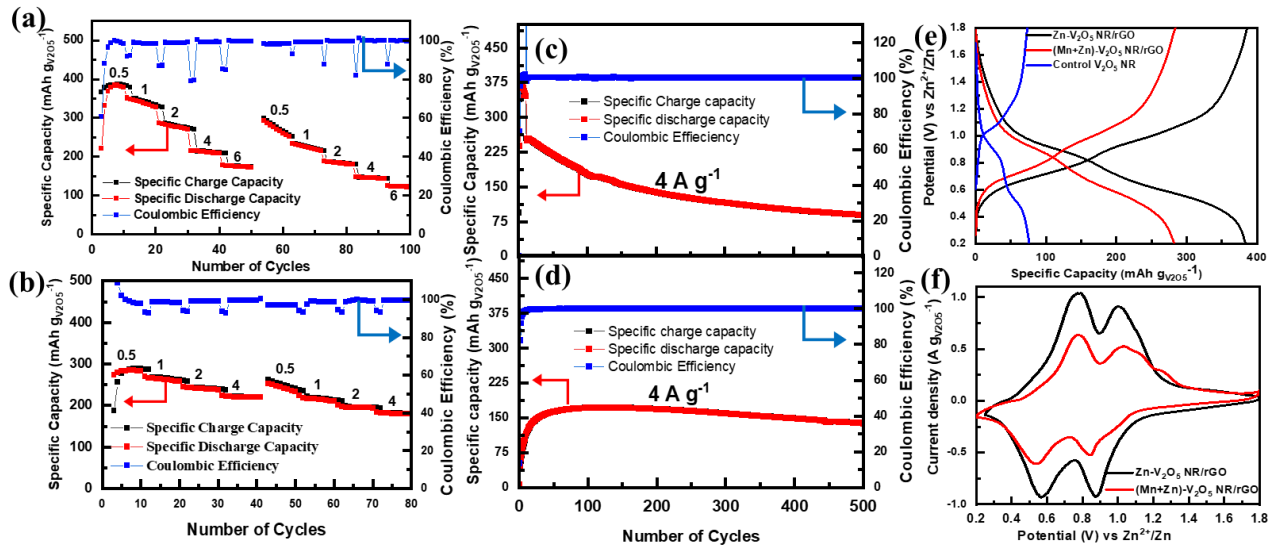


**Figure 4.6.** Galvanostatic charge-discharge characterization of the aqueous ZIBs in the potential window of 0.20 – 1.80 V. (a) The rate-performance plots measured sequentially at different current densities (i.e., 0.5 A g<sup>-1</sup>, 1.0 A g<sup>-1</sup>, 2.0 A g<sup>-1</sup>, 4.0 A g<sup>-1</sup> and 6.0 A g<sup>-1</sup>) for (a) Zn-V<sub>2</sub>O<sub>5</sub> NR/rGO cathode and (b) (Mn+Zn)-V<sub>2</sub>O<sub>5</sub> NR/rGO cathode. Long-cycle tests of the aqueous ZIBs at the fixed current density of 4.0 A g<sup>-1</sup> with (c) Zn-V<sub>2</sub>O<sub>5</sub> NR/rGO cathode and (d) (Mn+Zn)-V<sub>2</sub>O<sub>5</sub> NR/rGO cathode. The current densities are calculated based on the total mass of M-V<sub>2</sub>O<sub>5</sub> NR/rGO materials while the specific capacities are calculated based on the mass of active of M-V<sub>2</sub>O<sub>5</sub> NR derived from TGA analysis (Table S3). (e) Comparison of galvanostatic charge-discharge profiles of the AZIBs at 0.50 A g<sup>-1</sup> with the cathode made of V<sub>2</sub>O<sub>5</sub> NR (blue), (Mn+Zn)-V<sub>2</sub>O<sub>5</sub> NR/rGO (red) and Zn-V<sub>2</sub>O<sub>5</sub> NR/rGO (black), respectively. (f) Comparison of CV curves of the AZIBs made of Zn-V<sub>2</sub>O<sub>5</sub> NR/rGO (black) and (Mn+Zn)-V<sub>2</sub>O<sub>5</sub> NR/rGO (red) cathodes at the scan rate of 0.50 mV s<sup>-1</sup>.

The rate performance of Zn-V<sub>2</sub>O<sub>5</sub>/rGO in Figure 4.6(a) shows that it quickly rises to a very high specific capacity of 386 mAh g<sup>-1</sup> after stabilized in the first 4 cycles at the lowest current density (0.50 A g<sup>-1</sup>), which is equivalent to the storage of ~1.32 Zn<sup>2+</sup> per V<sub>2</sub>O<sub>5</sub>. However, as the current density increases to 1.0 A g<sup>-1</sup>, 2.0 A g<sup>-1</sup>, 4.0 A g<sup>-1</sup> and 6.0 A g<sup>-1</sup>, the specific capacity decreases to 351 mAh g<sup>-1</sup>, 287 mAh g<sup>-1</sup>, 216 mAh g<sup>-1</sup> and 178 mAh g<sup>-1</sup>, respectively, corresponding to about 9.1%, 25.6%, 44.0% and 53.9% drop compared to the initial stabilized specific capacity at 0.50 A g<sup>-1</sup>. A considerably lower capacity retention of 75.9 % (with a specific capacity of 293 mAh g<sup>-1</sup>) is observed when the measurement is switched back to the initial current density of 0.5 A g<sup>-1</sup> after completing the first rate-performance sequence of 50 cycles. The columbic efficiency is 99% to 100% in all cycles except the initial 4 cycles for activation/stabilization, indicating the highly reversible nature of the Zn<sup>2+</sup> ion storage. The rate performance of (Mn+Zn)-V<sub>2</sub>O<sub>5</sub> NR/rGO cathode in Figure 4.6(b) shows a slightly lower initial specific capacity of 289 mAh g<sup>-1</sup> at 0.5 A g<sup>-1</sup>. The specific capacity subsequently decreases to 268 mAh g<sup>-1</sup>, 243 mAh g<sup>-1</sup> and 224 mAh g<sup>-1</sup> as the current density is increased to 1.0 A g<sup>-1</sup>, 2.0 A g<sup>-1</sup> and 4.0 A g<sup>-1</sup>, respectively. The magnitude of the decrease at higher rates is significantly lower than that of Zn-V<sub>2</sub>O<sub>5</sub>/rGO. For example, at 4.0 A g<sup>-1</sup>, the specific capacity drops by 44.0% from that at 0.5 A g<sup>-1</sup> with Zn-V<sub>2</sub>O<sub>5</sub>/rGO while it only drops by 22.5% with (Mn+Zn)-V<sub>2</sub>O<sub>5</sub> NR/rGO. A higher capacity retention of over 84% is obtained when switched back to the low current density of 0.50 A g<sup>-1</sup>.

The long-term cycling performance of Zn-V<sub>2</sub>O<sub>5</sub> NR/rGO and (Mn+Zn)-V<sub>2</sub>O<sub>5</sub> NR/rGO with the current density fixed at 4.0 A/g are shown in Figures 4.6(c) and 4.6(d), respectively. The Zn-V<sub>2</sub>O<sub>5</sub> NR/rGO AZIB exhibits a high initial specific capacity of 254 mAh g<sup>-1</sup> after stabilized in the 4<sup>th</sup> cycle, consistent with the previously discussed rate-performance tests. But it suffers from a fast capacity fading with the specific capacity dropping to 89 mAh g<sup>-1</sup> (35 % of the initial value) after

500 cycles. This test indicates a poor cycling stability of the electrode material. In contrast, the long-term cycling test of (Mn+Zn)-V<sub>2</sub>O<sub>5</sub> NR/rGO AZIB at 4.0 A g<sup>-1</sup> shows a much higher capacity retention, with 81% in the 500th cycle comparing the highest point. The initial specific capacity is below 75 mAh g<sup>-1</sup> but steadily increases to 163 mAh g<sup>-1</sup> at the 50<sup>th</sup> cycle and retains fairly stable after that. It is worth noting that both of Zn-V<sub>2</sub>O<sub>5</sub> NR/rGO and (Mn+Zn)-V<sub>2</sub>O<sub>5</sub> NR/rGO cathodes show good reversibility with a coulombic efficiency of 99% to 100% during the long cycles. The high initial specific capacity of Zn-V<sub>2</sub>O<sub>5</sub> NR/rGO exceeding the theoretical limit can be primarily attributed to the reversible extraction/insertion of the pre-inserted bridging Zn<sup>2+</sup> ions (during coprecipitation). But the repeated extraction/insertion of the bridging Zn<sup>2+</sup> ions cause disruption to the structure of the hybrid material, leading to rapid capacity fading. On the other hand, (Mn+Zn)-V<sub>2</sub>O<sub>5</sub> NR/rGO consists of an increased V<sup>4+</sup>/V<sup>5+</sup> ratio, which improves the redox kinetics of Zn<sup>2+</sup> ions<sup>196</sup>. In addition, the Mn<sup>n+</sup> ions (with n = 2, 3 and 4) present stronger binding to V<sub>2</sub>O<sub>5</sub><sup>197</sup> and rGO compared to Zn<sup>2+</sup> ions, which makes the hybrid structure more stable and facilitates faster electronic and ionic conduction transport, leading to better rate-performance and higher capacity retention<sup>198</sup>. It is expected that the Mn<sup>n+</sup> ions remain in the hybrid material during charge-discharge cycles, which block some of the active sites and cause certain degree of deduction in the specific capacity at the low current density (0.5 A g<sup>-1</sup>). The stronger binding of Mn<sup>2+</sup> ions serving as stable pillars for Zn<sup>2+</sup> ion storage in expanded V<sub>2</sub>O<sub>5</sub> layers have been reported in literature<sup>85, 185</sup>.

For comparison, the rate performance, and charge-discharge curves of V<sub>2</sub>O<sub>5</sub> NRs and bulk V<sub>2</sub>O<sub>5</sub> are shown in Figure B.7. It is clear that the specific capacity of Zn<sup>2+</sup> storage in the bulk V<sub>2</sub>O<sub>5</sub> is negligible (< 15 mAh g<sup>-1</sup>). The V<sub>2</sub>O<sub>5</sub> NRs offer much higher specific capacity than the bulk V<sub>2</sub>O<sub>5</sub> at the similar current densities, to about 80 mAh g<sup>-1</sup> at 0.5 A g<sup>-1</sup>, but it is substantially smaller than M-V<sub>2</sub>O<sub>5</sub> NR/rGO hybrids. Interestingly, the specific capacity only slightly drops as the current

density is raised, which can be attributed to the increase in the active sites for  $\text{Zn}^{2+}$  storage in the NRs compared to bulk  $\text{V}_2\text{O}_5$  particles. Similarly, the rate-performance tests of physically mixed  $\text{V}_2\text{O}_5$  NR and rGO, prepared with the same procedure except without incorporation of the divalent metal cations, are compared with the bare rGO in Figure B.8. The bare rGO in Figure B.8(a) shows a negligible specific capacity below  $12 \text{ mAh g}^{-1}$  which is less than 5% of the specific capacity of Zn- $\text{V}_2\text{O}_5$  NR/rGO. It clearly explains that the  $\text{Zn}^{2+}$  ion storage in the hybrid materials is dominated by the  $\text{V}_2\text{O}_5$  NRs. The physically mixed  $\text{V}_2\text{O}_5$  NR and rGO shows an initial specific capacity of  $78 \text{ mAh g}^{-1}$  at  $0.5 \text{ A g}^{-1}$ , which is comparable to that of the bare  $\text{V}_2\text{O}_5$  NRs (with super-P additive) but decreases faster as the current density is raised. Clearly, simply mixing  $\text{V}_2\text{O}_5$  NR and rGO is not efficient to improve the  $\text{Zn}^{2+}$  ion storage properties. The divalent metal cation mediated coprecipitation is critical in creating an intimate hybrid material to yield much higher specific capacity in Zn- $\text{V}_2\text{O}_5$  NRs/rGO (by 4.9 times) and (Mn+Zn)- $\text{V}_2\text{O}_5$  NRs/rGO (by 3.7 times).

The galvanostatic charge-discharge profiles of the Zn- $\text{V}_2\text{O}_5$  NR/rGO and (Mn+Zn)- $\text{V}_2\text{O}_5$  NR/rGO are compared to that of pristine  $\text{V}_2\text{O}_5$  NRs in Figure 4.6(e). The charge-discharge curves look similar with two sloped plateaus in  $1.0 - 0.8 \text{ V}$  and  $0.6 - 0.5 \text{ V}$  during discharging, indicating that there is not much difference in the electrochemical kinetics among these materials. The cyclic voltammetry (CV) curves of Zn- $\text{V}_2\text{O}_5$  NR/rGO and (Mn+Zn)- $\text{V}_2\text{O}_5$  NR/rGO in Figure 4.6(f) show two distinct pairs of peaks centered around  $0.95 \text{ V}$  and  $0.65 \text{ V}$ , respectively, which are attributed to the two-step redox reactions in batteries, correlated well with the voltage plateaus in the charge-discharge curves. The CV of Zn- $\text{V}_2\text{O}_5$  NR/rGO shows higher peak currents due to the larger  $\text{Zn}^{2+}$  storage capacity. The separations in the peak potentials of all redox waves are larger than  $250 \text{ mV}$ , indicating a high energy barrier of  $\text{Zn}^{2+}$  ion insertion/extraction which can be improved. The more extensive charge-discharge curves and CVs of Zn- $\text{V}_2\text{O}_5$  NR/rGO and (Mn+Zn)- $\text{V}_2\text{O}_5$

NR/rGO are presented in Figure B.9. As the scan rate is increased from  $0.50 \text{ mV s}^{-1}$  to  $2 \text{ mV s}^{-1}$ , the peak separation increases to more than 350 mV, further indicating that the reaction kinetics is limited by the high energy barriers of the  $\text{Zn}^{2+}$  ion insertion/extraction. Using the host materials with a more open internal structure and smaller interaction with  $\text{Zn}^{2+}$  ions may be explored in the future to improve this.

#### 4.4. Conclusion

In summary, we report the synthesis of divalent metal ion mediated M- $\text{V}_2\text{O}_5$  NR/rGO hybrid materials as high-performance cathodes for AZIBs. The divalent metal ions  $\text{M}^{2+}$  (including  $\text{Zn}^{2+}$  and  $\text{Mn}^{2+}$ ) effectively neutralize the negative charges on the surface of microwave-exfoliated  $\text{V}_2\text{O}_5$  NRs and GO nanosheets to form a strongly bound  $\text{V}_2\text{O}_5$  NR/GO assembly by coprecipitation. A thermal annealing process in the nitrogen atmosphere converts the GO to rGO nanosheets which serve as the stable nanostructured template and highly conductive electron pathway. At the meantime, the single-crystalline  $\text{V}_2\text{O}_5$  NRs are converted into disordered  $\text{V}_2\text{O}_5$  materials possibly due to divalent metal cation insertion. Thus-formed M- $\text{V}_2\text{O}_5$  NR/rGO hybrid materials have shown improved electron transport and enhanced diffusion of  $\text{Zn}^{2+}$  ions during the charge-discharge processes in AZIBs. The Zn- $\text{V}_2\text{O}_5$  NR/rGO hybrid, with the elemental formula of the active host material as  $\text{Zn}_{0.42}\text{V}_2\text{O}_{7.54}$ , presents a very high reversible specific capacity of  $\sim 386 \text{ mAh g}^{-1}$  at  $0.50 \text{ A g}^{-1}$  but a poor stability. By mixing some  $\text{Mn}^{2+}$  with the  $\text{Zn}^{2+}$  ions during the coprecipitation process, a binary divalent metal cation mediated hybrid (Mn+Zn)- $\text{V}_2\text{O}_5$  NR/rGO is obtained, in which the active host material has an atomic formula of  $\text{Zn}_{0.12}\text{Mn}_{0.14}\text{V}_2\text{O}_{7.16}$ . The long-cycling stability and rate performance are substantially improved while a relatively high specific capacity of  $\sim 289 \text{ mAh g}^{-1}$  at  $0.5 \text{ A g}^{-1}$  is retained. The stronger binding of  $\text{Mn}^{n+}$  ions ( $n = 2, 3$  and  $4$ ) with the  $\text{V}_2\text{O}_5$  host makes them as more stable pillars to support the expanded  $\text{V}_2\text{O}_5$  layers and enables

the stronger attachment of the  $V_2O_5$  host to rGO templates. This strategy is effective to balance the need for high specific capacity and good long-cycling stability.

# **Chapter 5 - Promoting Electrocatalytic Conversion of Lithium Polysulfides to Suppress Polysulfide Shuttle Effect in Li-S Batteries**

## **(Current Work)**

### **5.1. Introduction:**

The increasing environmental pollution has pushed the community to focus more on the renewable energy sources. The regional, seasonal, and intermittent nature of the renewable energy sources has driven the need to explore more electrical energy storage systems (EES). The advent of electric vehicles demands much larger energy density of at least 550 Wh/kg<sup>199</sup>. However, the existing battery packs including lithium-ion batteries (LIB) has practically reached their theoretical limit in terms of energy density (200-250 Wh/Kg) which is far short from the requirements of the electric vehicles. This has led to the exploration of alternative EES systems. The lithium sulfur batteries (LSB) have attracted considerable attention because of the higher theoretical specific capacity (1675 mAh/g) and energy density (2600 Wh/kg) of the sulfur cathode that gives space for improvement in energy density and specific capacity especially for the portable electronic devices, electric vehicles, and grid scale energy storage system<sup>200</sup>. The low cost of sulfur compared to the cathode materials of the conventional LIBs (cobalt, nickel, and manganese) makes the LSBs cost effective. Despite several advantages, the sulfur cathode also possesses certain disadvantages such as (i) the insulating nature of sulfur with a very low intrinsic electrical conductivity of just  $5 \times 10^{-30}$  S/cm which renders some unreacted sulfur in the cathode even though the kinetics of the reduction of sulfur is comparatively faster. This insulating nature of the sulfur demands the addition of plenty of conductive matrix materials which consequently reduces the practical energy density (Wh/g) of the battery<sup>201</sup>, (ii) the intermediate products formed during the reduction of

sulfur (S<sub>8</sub>) to Li<sub>2</sub>S are comparatively easier to dissolve in the organic electrolytes. The dissolved polysulfides migrates through the separator and reacts with the lithium anode. This phenomenon is referred as “polysulfide shuttle effect”<sup>202</sup>. The shuttle effect results in the low coulombic efficiency, low cyclability and low sulfur utilization which reduces the specific capacity(mAh/g) of the battery. (iii) the repeated and reversible reduction elemental sulfur with a higher density (2.03 g cm<sup>-3</sup>) to a comparatively less dense Li<sub>2</sub>S (1.66 g cm<sup>-3</sup>) results in an increased volumetric expansion of about ~80% which leads to the degradation of the cathode matrix, loss of contact between the current collector and the cathode material<sup>203</sup>. These complications need to be addressed to encourage commercialization. This report discusses the effective strategies to suppress the polysulfide shuttle effect which was developed by the research community over the past decade elaborately with a few examples illustrating the advantages and disadvantages of the strategies.

## 5.2. Polysulfide Shuttle Effect:



The elemental sulfur, the cathode precursor, exist as an eight membered cyclo-S<sub>8</sub>. During the discharge or lithium insertion process, the elemental sulfur undergoes multi-step reduction reaction that converts the S<sub>8</sub> into Li<sub>2</sub>S. During this reduction reaction, the lithiation happens via multiple steps<sup>204</sup> resulting in the formation of several intermediate products such as Li<sub>2</sub>S<sub>8</sub>, Li<sub>2</sub>S<sub>6</sub>, Li<sub>2</sub>S<sub>4</sub>, Li<sub>2</sub>S<sub>3</sub> and Li<sub>2</sub>S<sub>2</sub> as shown in the equations (1)-(5)<sup>200</sup>. Among which there are three soluble long chain lithium polysulfides (LIPSS), Li<sub>2</sub>S<sub>8</sub>, Li<sub>2</sub>S<sub>6</sub> and Li<sub>2</sub>S<sub>4</sub>, that have been reported so far

based on experimental evidence<sup>205</sup>. These long chain polysulfides have relatively high solubility in the organic electrolytes used. Henceforth, these long chain polysulfides continuously dissolve into the electrolyte and promotes a concentration gradient between the cathode side and anode side. Due to this concentration gradient, the dissolved LIPSs diffuse through the polymer separator and migrate towards the anode compartment as illustrated in figure 1(b). The dissolved polysulfides reacts with lithium anode to form a part of the electrically insulating SEI layer which are passive to the further electrochemical reaction in terms of lithium anode<sup>200</sup>. This shuttle is also a problem in the case of non-lithium anode materials as well where the electrons and lithium ions migrate to the surface of the anode which reacts with the long chain polysulfide ( $\text{Li}_2\text{S}_8$  and  $\text{Li}_2\text{S}_6$ ) and undergoes an electrochemical reduction to get converted into shorter chain polysulfides ( $\text{Li}_2\text{S}_4$ ) which either diffuses back to the cathode or deposits on the surface and increases the charge transfer resistance of the anode<sup>206</sup>. The polysulfide shuttling also affects the utilization of sulfur and ends up reducing the sulfur utilization as it prohibits the complete reduction of  $\text{S}_8$  into  $\text{Li}_2\text{S}$  and leads to non-homogenous distribution of sulfur which increases the impedance and polarization. The decrease in sulfur utilization also results in reduction of specific gravimetric capacity and energy density outputs of the LSB. Since sulfur cathode is the most critical component of the LSB, the polysulfide shuttle effect needs to be addressed to encourage the commercial application of lithium sulfur batteries<sup>207</sup>. In the past decade, there has been a lot of strategies developed to mitigate the polysulfide shuttle effect. In 2012, Manthiram et al.<sup>208</sup>, reported a strategy of incorporating a free standing multi walled carbon nanotube interlayer between the cathode and separator which can effectively confine the lithium polysulfides within the cathode compartment and enhance the cycling stability of the LSB. Since that, there has been multiple approaches reported that can effectively confine the LIPSs in the cathode side which includes

porous carbon scaffolds<sup>209</sup>, polymer-based materials<sup>210, 211</sup>, metallic or inorganic matrices<sup>202</sup> and metal organic frameworks<sup>212</sup> that can encapsulate elemental sulfur as well as trap the polysulfides has opened up multiple directions to this research.

### **5.3. Strategies to Suppress the Polysulfide Shuttle Effect:**

Since sulfur cathode is the most critical component of the lithium sulfur battery. Alleviating the polysulfide shuttle effect becomes more important to achieve high specific gravimetric capacity, long term cycling stability and higher coulombic efficiency. In the past few years, there are two major strategies reported that can reduce the polysulfide shuttling. They are as follows:

- (1) Physical/chemical confinement of lithium polysulfides through strong anchoring of polysulfides within the cathode structure.
- (2) Promoting the adsorption and electrocatalytic conversion of long chain polysulfides into short chain polysulfide species.

The confinement of dissolved lithium polysulfide species within the cathode compartment can be achieved either by the incorporation of physical barrier in the form of interlayer placed between the cathode and separator as illustrated by Manthiram et al.<sup>208</sup>, in 2012. Following that, many similar materials especially porous, conductive carbon scaffolds have been studied as interlayers and host matrices for elemental sulfur precursors. Carbon materials, in addition to having high electrical conductivity, can also be tuned to possess multiple pores with various sizes ranging from micropores till mesopores that can effectively trap the polysulfides and confine the elemental sulfur within the host. It was soon realized that physical or chemical anchoring of lithium polysulfides within the cathode will not work effectively over long-term insertion/extraction process as the LIPS dissolution process is more thermodynamically favorable and only by improving the rate of conversion of long chain polysulfides and reducing the overpotential of the

active material associated with the redox kinetics of the polysulfide conversion can effectively alleviate the polysulfide shuttling over long term. Transition metal sulfides were identified to have higher catalytic activity and can improve the redox kinetics and rate. In 2020, Hu et al.<sup>201</sup>, reported that uniform deposition of Cobalt disulfide ( $\text{CoS}_2$ ) nanoparticles on reduced graphene oxide (rGO) nanosheets (rGO/ $\text{CoS}_2$ /S) (shown in figure 6(a)) exhibit much higher specific capacity of 1296 mAh/g compared to the commercial  $\text{CoS}_2$  mixed with sulfur ( $\text{CoS}_2$ /S) and bare rGO mixed with sulfur (rGO/S). The rGO/ $\text{CoS}_2$ /S also exhibit reduced polarization with ~200 mV compared to  $\text{CoS}_2$ /S and rGO/S as shown in figure 6(c). This improved performance of rGO/ $\text{CoS}_2$ /S can be attributed to the enhanced catalytic activity of the  $\text{CoS}_2$  nanoparticles, higher buffer capacity and electrical conductivity of the flexible rGO nanosheets and stronger interaction of lithium polysulfide species towards the sulfur edge sites of  $\text{CoS}_2$ . Similarly in 2020, Manthiram et al.<sup>209</sup>, suggested that the unique structure and the intrinsic metallic conductivity of the 1T'- $\text{ReS}_2$  grown on carbon nanotubes demonstrates improved electrocatalytic activity towards the polysulfide conversion leading to higher specific capacity of 1360 mAh/g at 0.1 C (1C=1675 mAh/g) and exceptional capacity retention at higher current density of 1C with capacity degradation of only 0.028% after 1000 cycles. To effectively promote electrocatalysis and convert the long chain lithium polysulfides to short chain insoluble end products, the ideal catalyst material needs to possess two significant properties namely 1) effective adsorb and anchor the long chain LiPS species on the surface and 2) higher electron transfer properties to effectively reduce the long chain polysulfides into shorter chain species.

Molybdenum disulfide structure is three atomic layers where the molybdenum atoms are sandwiched between two layers of sulfur atoms.  $\text{MoS}_2$  has been found to have exceptional catalytic properties and has found wide application in industrially important reactions such as hydrogen

evolution reaction (HER), Oxygen evolution reactions (OER) and Oxygen reduction reactions (ORR). In addition to that, MoS<sub>2</sub> reportedly possess higher electronic conductivity, faster Li-ion transport ability, higher affinity towards the intermediate LiPSs species. However, the low electrical conductivity of the molybdenum disulfide is still an issue, and usually composite engineering and combination with a conductive carbon substrate can improve the electrical conductivity of the molybdenum sulfides. Till date, there are no reports suggesting a catalyst substrate that can effectively adsorb all the lithium polysulfide intermediate species. The Lithium polysulfide species interacts only with certain atoms in a long range, highly ordered crystalline material. Whereas the amorphous nanostructures facilitate more efficient adsorption of LiPSs species and effective catalytic conversion of the intermediates into insoluble end products owing to their increased amount of defects on the surface, dangling bonds and improved charge transfer properties compared to their crystalline counterparts<sup>213</sup>. In this study, the LiPS adsorption capacity and their subsequent catalytic conversion of three different Molybdenum sulfide based electrocatalysts with various defect density and crystal structures have been systematically investigated using UV-Visible Absorption measurements and Cyclic Voltammetry techniques.

## **5.4. Experimental Methods:**

### **5.4.1. Synthesis of MoS<sub>2</sub>/rGO Electrocatalysts:**

To synthesize MoS<sub>2</sub>/rGO, 15.0 mM ATM and 5.0 mg GO were dispersed in 6.0 ml tetrahydrofuran (THF) mixed with 1.0 ml distilled water. This mixture was ultrasonicated for about 20 minutes to obtain a homogenous suspension, which was then transferred to a 10 ml Pyrex glass microwave tube and put into an automated microwave system (Discover SP, CEM Corp., Matthews, NC) to irradiate with a microwave power of 300 W under the dynamic mode. It took approximately 7 minutes for the temperature to ramp up to the setting of 170°C and then the system

was held at this temperature for 10 min. During the reaction, the pressure went up to ~21 bar depending on the reaction conditions. After the reaction is over, the system was vented with compressed air and cooled down to the room temperature. The product was collected and centrifuged at 2000 rpm for about 15 min. The solid precipitate was collected and dried on a hotplate in the air at ~80 °C overnight. This material is referred as MoS<sub>3</sub>/rGO-intermediate. The dried material was further annealed in 3% H<sub>2</sub> and 97% Ar at 250°C, and 600 °C, respectively. The corresponding samples were denoted as MoS<sub>2</sub>/rGO-250 and MoS<sub>2</sub>/rGO-600, respectively. The control sample of bare rGO was synthesized following the same procedure as the MoS<sub>2</sub>/rGO samples except without adding any ATM precursor in the reaction mixture.

#### **5.4.2. Preparation of Lithium Polysulfide Solutions:**

The Li<sub>2</sub>S<sub>6</sub> solution was prepared by mixing S and Li<sub>2</sub>S in a molar ratio of 5:1 in a mixture of 1,2-dimethoxyethane (DME) and 1,3-dioxolane (DOL) (1:1, v/v) under Argon atmosphere for about 24 hours. Li<sub>2</sub>S<sub>4</sub> and Li<sub>2</sub>S<sub>8</sub> solutions are also prepared in a similar way where the Li<sub>2</sub>S and S precursors are mixed in the molar ratio of 1:3 and 1:7 respectively.

#### **5.4.3. Lithium Polysulfide Adsorption Tests:**

To investigate the adsorption of lithium polysulfides on the surface of the electrocatalysts, approximately 5 mg/mL of all the MoS<sub>2</sub>/rGO samples (MoS<sub>2</sub>/rGO-600, MoS<sub>2</sub>/rGO-325, MoS<sub>2</sub>/rGO-250 and MoS<sub>3</sub>/rGO-intermediate) were added to 3 mL of 3mM lithium polysulfide solutions (Li<sub>2</sub>S<sub>4</sub>, Li<sub>2</sub>S<sub>6</sub> and Li<sub>2</sub>S<sub>8</sub>) inside the argon filled glovebox. The mixture was left to sit for 12 hours, and the supernatant was collected. Ultraviolet-visible (UV-Vis) absorbance measurement was carried out using the supernatant solution to determine the concentration of polysulfide species adsorbed on the catalyst surface. All the UV-Vis spectra were collected in the visible range (300 nm – 800 nm).

### 5.4.3. Symmetric Cell Measurements:

A slurry was prepared by mixing the active material (i.e., Commercial MoS<sub>2</sub>, MoS<sub>2</sub>/rGO-600, MoS<sub>2</sub>/rGO-250, MoS<sub>3</sub>/rGO-intermediate), carbon additive (Super-P, Alfa Aesar Co. Ltd., Haverhill, Massachusetts, USA) and a poly (vinylidene fluoride) (PVDF, Sigma Aldrich Co., St. Louis, MO) binder at the weight ratio of 8:1:1 with approximately 250 μL of N-methyl-2-pyrrolidone (NMP, Sigma Aldrich, St. Louis, MO) as the solvent. The homogenous slurry was uniformly coated on a carbon coated aluminum foil. The coated foil was air-dried at 70°C for about 24 hours. The dried electrodes were then punched into 15 mm discs. The symmetric cells were assembled with identical electrodes as working and counter electrode with 60 μL of electrolyte containing 0.20 M Lithium polysulfide mixed with 1M LiTFSI solution. The cyclic voltammetry was performed in the potential window of -1.0 V till +1.0 V in multiple scan rates of 1 mV/s, 5 mV/s and 50 mV/s.

## 5.5. Results and Discussion:

The concentration of defects in MoS<sub>2</sub>/rGO-600, MoS<sub>2</sub>/rGO-250 and MoS<sub>3</sub>/rGO-intermediate has been successfully studied using X-ray Photoelectron Spectroscopy (XPS) analysis and X-ray Diffraction (XRD) studies (see section 3.3 in chapter 3). As revealed by the material characterization results, the MoS<sub>2</sub>/rGO-600 obtained by annealing at 600°C renders a perfectly crystalline MoS<sub>2</sub> nanopatches uniformly deposited on the reduced graphene oxide (rGO) template. The atomic ratio of Mo:S in MoS<sub>2</sub>/rGO-600 is estimated to be 1:1.9 similar to that of MoS<sub>2</sub> suggesting no observable defects in the structure. But with the decrease in the annealing temperature to 250°C, the obtained MoS<sub>2</sub> structure is amorphous and highly disordered in nature with a larger volume of defects in the structure. The atomic ratio of Mo:S in MoS<sub>2</sub>/rGO-250 is calculated to be 1:2.9 with a higher amount of Mo-vacancies in the structure resulting in larger

exposed edge sites and dangling bonds that effectively improves the LiPSs adsorption and several unsaturated S atoms with improved charge transfer properties resulting in enhanced electrocatalytic activity. The MoS<sub>3</sub>/rGO-intermediate obtained by the microwave synthesis process possess a quasi one-dimensional structure unlike the hexagonal sheet like structure in defect-free MoS<sub>2</sub>/rGO-600 and defect-induced MoS<sub>2</sub>/rGO-250 with higher concentration of S<sub>x</sub><sup>2-</sup> atoms with reportedly increased interaction with the polar polysulfide species.

### 5.5.1. Physical Anchoring of LiPSs on the Surface of MoS<sub>2</sub>/rGO:

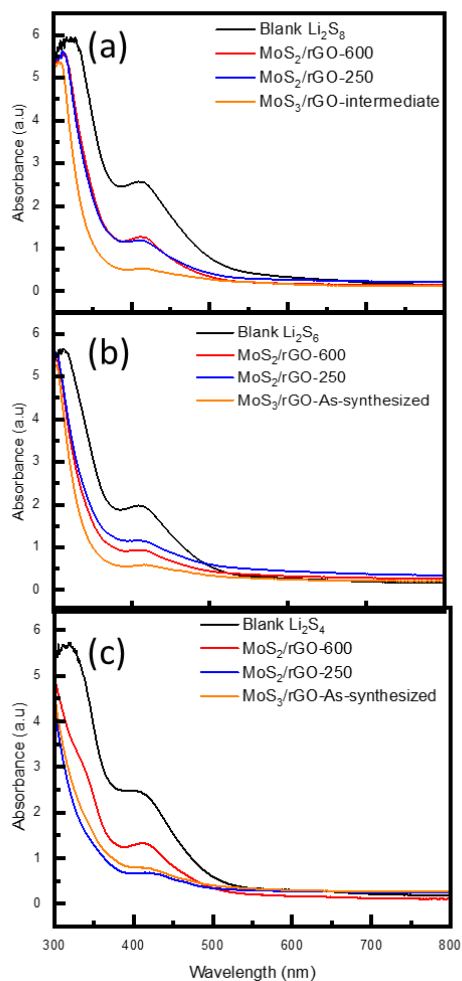


**Figure 5.1.** UV-Visible absorbance spectra of 3.00 mL of 3.0 m M solution of (a) Li<sub>2</sub>S<sub>8</sub>, (b) Li<sub>2</sub>S<sub>6</sub> and (c) Li<sub>2</sub>S<sub>4</sub> in 1:1 DOL/DME mixture (solvent) without adding any electrocatalyst (black) and in 12.0 hours after adding 15 mg of MoS<sub>2</sub>/rGO-600 (red), MoS<sub>2</sub>/rGO-250 (blue) and MoS<sub>3</sub>/rGO-intermediate (orange).

To study the chemical adsorption of lithium polysulfide species on the surface of the electrocatalysts, a series of systematic adsorption tests were carried out after adding approximately 15.0 mg of electrocatalysts in 3 mL of 3mM Lithium polysulfide solutions. Figure 5.1. (a), (b) and (c) shows the UV-Visible absorption spectra of  $\text{Li}_2\text{S}_4$ ,  $\text{Li}_2\text{S}_6$  and  $\text{Li}_2\text{S}_8$  solutions before and after the addition of electrocatalysts. UV-vis spectroscopy was used to measure the concentration of lithium polysulfide species in the supernatants after the adsorption of polysulfide species. The UV-Visible spectra of all the blank lithium polysulfide solutions (black curve) show a broad peak around 420 nm. After extrapolating the data, the absorbance at 411 nm was used to determine the concentration of LiPSs in the solution. The UV-Vis spectra of the supernatants collected after the chemical adsorption by the  $\text{MoS}_2/\text{rGO}$  catalysts are plotted in the same scale and their respective adsorption capacities were calculated. The UV-Vis spectra of supernatants from  $\text{MoS}_2/\text{rGO-600}$  (red),  $\text{MoS}_2/\text{rGO-250}$  (blue) and  $\text{MoS}_3/\text{rGO-intermediate}$  (Orange) show the representative absorption spectra of the respective catalysts. The estimated adsorption capacities of the  $\text{MoS}_2$  after the deduction of the contribution from rGO in the sample is given in table 5.1. The defect free  $\text{MoS}_2/\text{rGO-600}$  and  $\text{MoS}_3/\text{rGO-intermediate}$  shows higher adsorption towards  $\text{Li}_2\text{S}_8$  with the adsorption capacity of 0.28 mmol/g<sub>MoS<sub>x</sub></sub> and 0.39 mmol/g<sub>MoS<sub>x</sub></sub> respectively compared to that of  $\text{MoS}_2/\text{rGO-250}$  (0.20 mmol/g<sub>MoS<sub>x</sub></sub>). Whereas the adsorption capacity of  $\text{MoS}_2/\text{rGO-250}$  towards short chain  $\text{Li}_2\text{S}_4$  than other two electrocatalysts. The higher adsorption of  $\text{Li}_2\text{S}_6$  and  $\text{Li}_2\text{S}_8$  can be attributed to increased interaction of lithium polysulfides with the sulfur atoms in the basal planes and the bridging sulfur atoms in  $\text{MoS}_2/\text{rGO-600}$  and  $\text{MoS}_3/\text{rGO-intermediate}$  structures respectively. Whereas the dangling bonds and the unsaturated S atoms in  $\text{MoS}_2/\text{rGO-250}$  shows increased interaction towards  $\text{Li}_2\text{S}_4$  with the adsorption capacity of 0.38 mmol/g<sub>MoS<sub>x</sub></sub> compared to  $\text{MoS}_2/\text{rGO-600}$  and  $\text{MoS}_3/\text{rGO-intermediate}$ . The time-dependent lithium polysulfide

adsorption on the surface of the electrocatalyst materials have been systematically investigated by taking the absorbance measurements every one hour for a period of 12 hours after adding the electrocatalyst in the LiPS solution. The time dependent studies of the MoS<sub>2</sub>/rGO and the control rGO is shown in Figure C.1 and Figure C.2 in appendix C. Figure C.3 shows the decreasing trend of the peak absorbance at a wavelength of 411 nm illustrating the rather slower adsorption kinetics of lithium polysulfide species on the electrocatalyst surface. The table C.1 shows the specific adsorption capacities of MoS<sub>2</sub>/rGO (Ads.<sub>total</sub>), control rGO (Ads.<sub>rGO</sub>) and the adsorption capacity of MoS<sub>2</sub> (Ads.<sub>MoS<sub>2</sub></sub>) in the sample after the deduction of the contribution of rGO based on the formula described below table C.1.

### 5.5.2. Electrochemical Characterization:

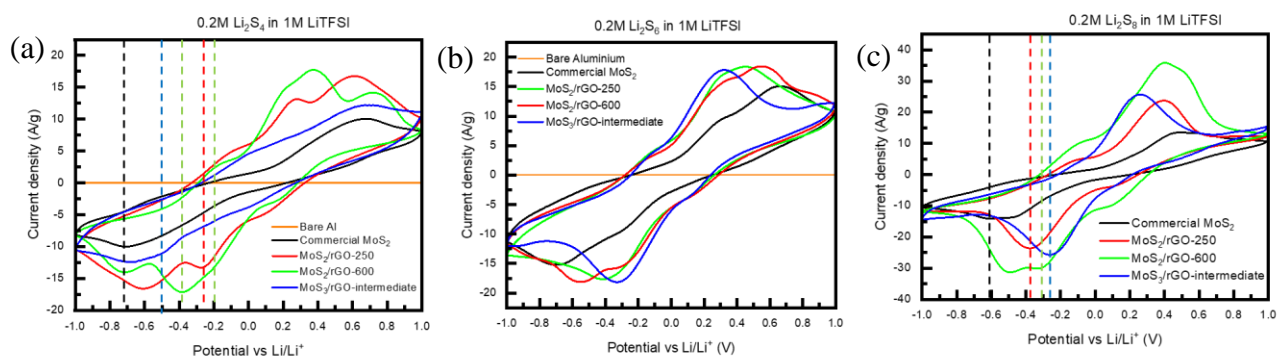


**Figure 5.2.** CV profiles in symmetric cell setup in (a) 0.2 M Li<sub>2</sub>S<sub>4</sub>, (b) 0.2 M Li<sub>2</sub>S<sub>6</sub> and (c) 0.2M Li<sub>2</sub>S<sub>8</sub> in the potential window of -1.0 V till +1.0 V at a scan rate of 50 mV/s with the various electrocatalytic materials such as bare Al (orange), commercial MoS<sub>2</sub> (black), MoS<sub>2</sub>/rGO-600 (green), MoS<sub>2</sub>/rGO-250 (red) and MoS<sub>3</sub>/rGO-intermediate (blue).

The electrocatalytic activity of the MoS<sub>2</sub>/rGO samples were estimated using the cyclic voltammetry measurements with identical working and counter electrodes. The CV profiles of MoS<sub>2</sub>/rGO symmetric cells are shown in figure 5.3. Figure 5.3. (a), (b) and (c) shows the CV profile of MoS<sub>2</sub>/rGO-600 (green), MoS<sub>2</sub>/rGO-250 (red), MoS<sub>3</sub>/rGO-intermediate (blue) and commercial MoS<sub>2</sub> (black) symmetric cells with Li<sub>2</sub>S<sub>4</sub>, Li<sub>2</sub>S<sub>6</sub> and Li<sub>2</sub>S<sub>8</sub> polysulfide species in 50

mV/s respectively. The commercial MoS<sub>2</sub> shows a broad CV profile with a typical pseudocapacitive behavior owing to the surface charge transfer between the MoS<sub>2</sub> and the lithium polysulfides. However, the CV curves of MoS<sub>2</sub>/rGO-600 and MoS<sub>2</sub>/rGO-250 in Li<sub>2</sub>S<sub>4</sub> shows two pairs of well-defined reduction and oxidation peaks. MoS<sub>2</sub>/rGO-600 shows the first reduction peak R<sub>1</sub> at -0.38 V and another peak -0.73 V attributing to the reduction of long chain polysulfides to short chain polysulfides and further reduction of shorter chain polysulfides to insoluble Li<sub>2</sub>S<sub>2</sub> respectively. The peak separation between reduction and oxidation peaks is approximately 740 mV. However, the reduction peaks shift to higher potential of -0.34 V and -0.49 V respectively suggesting higher charge transfer kinetics towards the reduction of shorter chain polysulfides. In contrast to that, there is only one peak observed in Li<sub>2</sub>S<sub>6</sub> instead of two suggesting comparatively slower diffusion kinetics of Li<sub>2</sub>S<sub>6</sub>

**Table 5.1.** Adsorption capacity of MoS<sub>2</sub>/rGO-600, MoS<sub>2</sub>/rGO-250 and MoS<sub>3</sub>/rGO-intermediate and the atomic ratio of Mo:S estimated from the XPS Analysis in Table A.2

Sample	Mo:S	Adsorption Capacity (mmoles /g <sub>MoS<sub>x</sub></sub> ) (Li <sub>2</sub> S <sub>4</sub> )	Adsorption Capacity (mmoles /g <sub>MoS<sub>x</sub></sub> ) (Li <sub>2</sub> S <sub>6</sub> )	Adsorption Capacity (mmoles /g <sub>MoS<sub>x</sub></sub> ) (Li <sub>2</sub> S <sub>8</sub> )
MoS <sub>2</sub> /rGO-600	1:1.9	0.22	0.27	0.28
MoS <sub>2</sub> /rGO-250	1:2.9	0.38	0.19	0.20
MoS <sub>3</sub> /rGO As synth	1:2.4	0.16	0.21	0.39

on MoS<sub>2</sub>/rGO-600. The peak separation in Li<sub>2</sub>S<sub>6</sub> and Li<sub>2</sub>S<sub>8</sub> is approximately 850 mV and 740 mV respectively. MoS<sub>2</sub>/rGO-250 also shows a two well defined oxidation and reduction peaks similar to MoS<sub>2</sub>/rGO-600. The reduction peaks R<sub>1</sub>/R<sub>2</sub> are observed at -0.27V/-0.61V and -0.30V/-0.55V with Li<sub>2</sub>S<sub>4</sub> and Li<sub>2</sub>S<sub>6</sub> respectively. The peak separation of MoS<sub>2</sub>/rGO-250 in Li<sub>2</sub>S<sub>4</sub> and Li<sub>2</sub>S<sub>6</sub>

between the reduction and oxidation peaks are calculated to be 520 mV and 610 mV respectively which is approximately 220 mV lower than MoS<sub>2</sub>/rGO-600 suggesting enhanced catalytic activity of the defect induced MoS<sub>2</sub>/rGO-250 towards the conversion of shorter chain lithium polysulfides. Whereas the reduction peak for Li<sub>2</sub>S<sub>8</sub> appears at a slightly higher potential than MoS<sub>2</sub>/rGO-600 owing to the increased interaction of Li<sub>2</sub>S<sub>8</sub> with MoS<sub>2</sub>/rGO-600 which is consistent with the adsorption capacities calculated in the UV-Vis analysis. In contrast to MoS<sub>2</sub>/rGO-600 and MoS<sub>2</sub>/rGO-250, MoS<sub>3</sub>/rGO-intermediate shows only one reduction peak instead of two in all the Lithium polysulfides suggesting slower diffusion kinetics in MoS<sub>3</sub>/rGO-intermediate. The peak separation is calculated to be 1.32 V, 610 mV and 510 mV in Li<sub>2</sub>S<sub>4</sub>, Li<sub>2</sub>S<sub>6</sub> and Li<sub>2</sub>S<sub>8</sub> respectively attributed to comparatively higher charge transfer between Li<sub>2</sub>S<sub>8</sub> and MoS<sub>3</sub> chain like structure<sup>214</sup>. Although the symmetric cell measurements are more direct to study the enhancement in redox kinetics of the polysulfides, the asymmetric cell measurements would be more precise to investigate the enhancement in reaction kinetics.

## 5.6. Conclusion

In summary, the UV-Visible absorption studies suggests that the MoS<sub>2</sub>/rGO-600 and MoS<sub>3</sub>/rGO-intermediate shows higher adsorption of long chain lithium polysulfide intermediate species (i.e., Li<sub>2</sub>S<sub>6</sub> and Li<sub>2</sub>S<sub>8</sub>). Whereas MoS<sub>2</sub>/rGO-250 with Mo-vacancies in the structure and more exposed sulfur edge sites shows higher adsorption of Li<sub>2</sub>S<sub>4</sub> in contrast to that of MoS<sub>2</sub>/rGO-600 and MoS<sub>3</sub>/rGO-intermediate. The CV profiles measured in the symmetric cell setup are also consistent with the UV-Vis absorption studies. Based on the symmetric cell CV measurements, MoS<sub>2</sub>/rGO-250 shows enhanced catalytic activity towards Li<sub>2</sub>S<sub>4</sub> and Li<sub>2</sub>S<sub>6</sub>. Whereas MoS<sub>3</sub>/rGO-intermediate and MoS<sub>2</sub>/rGO-600 shows comparatively higher catalytic conversion of long chain

LiPSs (i.e.,  $\text{Li}_2\text{S}_8$ ). However, these studies are qualitative and needs more quantitative investigation to firmly support the abovementioned results.

## Chapter 6 - Summary

The primary focus of this work is to investigate the impact of various strategies for structural modification of the cathode structures, including interlayer expansion, defect engineering, hybrid formation and nano structuring and morphology control, to facilitate the intercalation and deintercalation of  $\text{Zn}^{2+}$  ions and achieve higher specific capacity and long-term cycling stability without much capacity fading and structural disintegration.

In Chapter 3, a set of  $\text{MoS}_2/\text{rGO}$  hybrid materials were prepared by applying the microwave specific heating on graphene oxide and molecular Mo precursors followed by the thermal annealing in 3%  $\text{H}_2$  and 97% Ar at different temperature. The microwave specific heating process was able to convert graphene oxide to ordered rGO nanosheets, which were sandwiched with uniform thin layers of intermediate materials dominated by amorphous  $\text{MoS}_3$ . The thermal annealing process converted the amorphous  $\text{MoS}_3$  layers into 2D  $\text{MoS}_2$  nanopatches, whose defect density is tuned by controlling the annealing temperature at 250, 325 and 600 °C. The  $\text{MoS}_2/\text{rGO}$  sample annealed at 600 °C was found to consist of 2D nanopatches of  $\text{MoS}_2$  crystals randomly oriented on monocrystalline reduced graphene surface while the samples annealed at 250 and 325 °C showed a S to Mo ratio larger than 2:1, indicating the presence of high-density S-rich or Mo-deficient defects which are different from the S-deficient defects by hydrothermal synthesis in literature. The electrochemical  $\text{Zn}^{2+}$  storage properties of the different  $\text{MoS}_2/\text{rGO}$  materials were systematically investigated. It appears that the Zn-ion storage properties strongly depended on the defects in the sample. The highly defective  $\text{MoS}_2/\text{rGO}$  sample prepared by annealing at 250 °C offers the highest initial Zn-ion storage capacity ( $\sim 300 \text{ mAh g}_{\text{MoS}_x}^{-1}$ ) and nearly 100% coulombic efficiency, which was dominated by pseudocapacitive behavior owing to the surface reactions at the edges or defects in the  $\text{MoS}_2$  nanopatches whereas the defect-free  $\text{MoS}_2/\text{rGO}$ -600 gives only

negligible specific capacity of  $6 \text{ mAh g}_{\text{MoS}_2}^{-1}$  with a significantly lower coulombic efficiency. Even though  $\text{MoS}_2/\text{rGO}-250$  significant fading in specific capacity occurred at the initial cycles at low current densities, stable charge/discharge can be obtained at higher charge/discharge current densities or after extended cycles. This study validates that nano structuring and defect engineering is critical in the divalent Zn-ion storage.

In chapter 4, we report the synthesis of divalent metal ion mediated  $\text{M}-\text{V}_2\text{O}_5$  NR/rGO hybrid materials as high-performance cathodes for AZIBs. The  $\text{V}_2\text{O}_5$  nanoribbons were obtained by the microwave assisted exfoliation process. The  $\text{V}_2\text{O}_5$  nanoribbons were successfully deposited on GO nanosheets using the divalent metal ions  $\text{M}^{2+}$  (including  $\text{Zn}^{2+}$  and  $\text{Mn}^{2+}$ ) to neutralize the negative charges on the surface of microwave exfoliated  $\text{V}_2\text{O}_5$  NRs and GO nanosheets to form a strongly bound  $\text{V}_2\text{O}_5$  NR/GO assembly by coprecipitation. A thermal annealing process in the nitrogen atmosphere converts the GO to rGO nanosheets which serve as the stable nanostructured template and highly conductive electron pathway. At the meantime, the single-crystalline  $\text{V}_2\text{O}_5$  NRs are converted into disordered  $\text{V}_2\text{O}_5$  materials possibly due to divalent metal cation insertion. Thus-formed  $\text{M}-\text{V}_2\text{O}_5$  NR/rGO hybrid materials have shown improved electron transport and enhanced diffusion of  $\text{Zn}^{2+}$  ions during the charge-discharge processes in AZIBs. The  $\text{Zn}-\text{V}_2\text{O}_5$  NR/rGO hybrid, with the elemental formula of the active host material as  $\text{Zn}_{0.42}\text{V}_2\text{O}_{7.54}$ , presents a very high reversible specific capacity of  $\sim 386 \text{ mAh g}^{-1}$  at  $0.50 \text{ A g}^{-1}$  but a poor stability. By mixing some  $\text{Mn}^{2+}$  with the  $\text{Zn}^{2+}$  ions during the coprecipitation process, a binary divalent metal cation mediated hybrid  $(\text{Mn}+\text{Zn})-\text{V}_2\text{O}_5$  NR/rGO is obtained, in which the active host material has an atomic formula of  $\text{Zn}_{0.12}\text{Mn}_{0.14}\text{V}_2\text{O}_{7.16}$ . The long-cycling stability and rate performance are substantially improved while a relatively high specific capacity of  $\sim 289 \text{ mAh g}^{-1}$  at  $0.5 \text{ A g}^{-1}$  is retained. The stronger binding of  $\text{Mn}^{n+}$  ions ( $n = 2, 3$  and  $4$ ) with the  $\text{V}_2\text{O}_5$  host makes them as

more stable pillars to support the expanded  $V_2O_5$  layers and enables the stronger attachment of the  $V_2O_5$  host to rGO templates. This strategy is effective to balance the need for high specific capacity and good long-cycling stability.

In chapter 5, the two-dimensional  $MoS_2$ /rGO nanostructures prepared using the microwave specific heating is studied as electrocatalyst to promote the conversion of lithium polysulfides to mitigate the polysulfide shuttle effect in Li-S batteries. The LiPS adsorption capacity and their subsequent catalytic conversion of three different Molybdenum sulfide based electrocatalysts with various defect density and crystal structures have been systematically investigated using UV-Visible Absorption measurements and Cyclic Voltammetry techniques. The  $MoS_2$ /rGO-600 shows higher adsorption capacity towards  $Li_2S_6$  and  $Li_2S_8$  while the defect induced  $MoS_2$ /rGO-250 shows higher adsorption towards  $Li_2S_4$ . The CV profiles obtained using the symmetric cell setup also shows similar trend.

## Chapter 7 - Future Projects

### **Investigation of 2D MoS<sub>2</sub>/rGO hybrids as Electrocatalytic Additive in Sulfur cathode:**

The series of two dimensional MoS<sub>2</sub>/rGO hybrid structures synthesized via microwave specific heating show various concentration of Mo-vacancies in the structures as discussed in chapter 3. The increase in the Mo-vacancies leads to increase in the amount of exposed sulfur edges which are previously reported in literatures to be catalytically active than the defect free structures. This set of hybrid materials, incorporated into the sulfur cathodes in Li-S batteries, can effectively adsorb the lithium polysulfide intermediate species and improve the kinetics of conversion of long chain lithium polysulfides into insoluble Li<sub>2</sub>S<sub>2</sub>/Li<sub>2</sub>S end products, thus alleviating the polysulfide shuttle effect and improving the performance of the sulfur cathode. The physical confinement of the lithium polysulfide intermediates on the MoS<sub>2</sub>/rGO hybrid structures have been successfully demonstrated with the help of the UV-Vis spectroscopy results discussed in section 5.5.1. The cyclic voltammetry curves of the MoS<sub>2</sub>/rGO symmetric cell setups show exceptional catalytic activity towards the efficient conversion of long chain lithium polysulfides to shorter chain polysulfide species which can readily mitigate the loss of active sulfur in the cathode structure and reduce the polysulfide shuttle process in the Li-S batteries. However, this preliminary result needs to be validated by incorporating a small amount of electrocatalytic materials in the sulfur cathodes and investigating the promotion of electrocatalytic conversion of intermediate lithium polysulfide species.

### **Heteroatom doping of transition metal ions in the Mo-deficient MoS<sub>2</sub> structures:**

The Mo-deficient defects introduced in the few layered MoS<sub>2</sub> structures provide an open framework for the substitutional doping of foreign transition metal cations such vanadium in the structure. The substitutional doping of vanadium in the structure stabilizes the otherwise

metastable 1T-MoS<sub>2</sub>. Four different MoS<sub>2</sub> samples with varying concentration of vanadium precursor will be synthesized via microwave assisted hydrothermal method to obtain 1T/2H-V<sub>x</sub>Mo<sub>(1-x)</sub>S<sub>(2+x)</sub> by incorporating varying concentrations (x) of impurity atoms. The co-doping of vanadium heteroatoms in the Mo-deficient structure can effectively to transform the semiconducting 2H-MoS<sub>2</sub> structure with a huge bandgap of ~1.3 eV into metallic and more conducting 1T-structure with a reduced bandgap of ~0.7 eV. The doping of proper amount of V<sup>4+</sup> into defective few layered 2H MoS<sub>2</sub> to incorporate rapid and homogenous phase restructuring and form 1T/2H MoS<sub>2</sub> heterostructures. The electrochemical divalent ion storage properties of such heterostructures show improved performance compared to the pristine 1T and 2H-MoS<sub>2</sub> structures.

#### **Investigation of M-V<sub>2</sub>O<sub>5</sub> NR/rGO as Cathode Structure for Rechargeable Mg Ion Batteries:**

The vanadium oxide cathode materials show great potential towards rechargeable Mg ion batteries due to their tunable multiple oxidation states of the vanadium metal centers. The binary divalent metal cation mediated hybrid (Mn+Zn)-V<sub>2</sub>O<sub>5</sub> NR/rGO is obtained, in which the active host material has an atomic formula of Zn<sub>0.12</sub>Mn<sub>0.14</sub>V<sub>2</sub>O<sub>7.16</sub> discussed in chapter 4 shows exceptional long-cycling stability and rate performance are substantially improved while a relatively high specific capacity of ~289 mAh g<sup>-1</sup> at 0.5 A g<sup>-1</sup> is retained. The stronger binding of Mn<sup>n+</sup> ions (n = 2, 3 and 4) with the V<sub>2</sub>O<sub>5</sub> host makes them as more stable pillars to support the expanded V<sub>2</sub>O<sub>5</sub> layers and enables the stronger attachment of the V<sub>2</sub>O<sub>5</sub> host to rGO templates. The Zinc ions in the structure can be replaced with the divalent Mg<sup>2+</sup> ions which can effectively reduce the energy barrier for the Mg<sup>2+</sup> intercalation in the layered V<sub>2</sub>O<sub>5</sub> structures. The preintercalated Mg<sup>2+</sup> ions in the structure can provide the active sites for Mg<sup>2+</sup> storage in the structure. In addition to that, the stronger binding of Mn<sup>2+</sup> ions in the structure can facilitate reversible Mg<sup>2+</sup> intercalation/deintercalation over multiple cycles.



## References

1. Liu, H.; Wang, J.-G.; You, Z.; Wei, C.; Kang, F.; Wei, B., Rechargeable aqueous zinc-ion batteries: Mechanism, design strategies and future perspectives. *Materials Today* **2021**, *42*, 73-98.
2. Jia, X.; Liu, C.; Neale, Z. G.; Yang, J.; Cao, G., Active Materials for Aqueous Zinc Ion Batteries: Synthesis, Crystal Structure, Morphology, and Electrochemistry. *Chemical Reviews* **2020**, *120* (15), 7795-7866.
3. Zeng, X.; Hao, J.; Wang, Z.; Mao, J.; Guo, Z., Recent progress and perspectives on aqueous Zn-based rechargeable batteries with mild aqueous electrolytes. *Energy Storage Materials* **2019**, *20*, 410-437.
4. Zhou, M.; Chen, Y.; Fang, G.; Liang, S., Electrolyte/electrode interfacial electrochemical behaviors and optimization strategies in aqueous zinc-ion batteries. *Energy Storage Materials* **2022**, *45*, 618-646.
5. Hossain, E.; Faruque, H. M. R.; Sunny, M. S. H.; Mohammad, N.; Nawar, N., A Comprehensive Review on Energy Storage Systems: Types, Comparison, Current Scenario, Applications, Barriers, and Potential Solutions, Policies, and Future Prospects. *Energies* **2020**, *13* (14), 3651.
6. Arabkoohsar, A., Chapter One - Classification of energy storage systems. In *Mechanical Energy Storage Technologies*, Arabkoohsar, A., Ed. Academic Press: 2021; pp 1-12.
7. Gür, T. M., Review of electrical energy storage technologies, materials and systems: challenges and prospects for large-scale grid storage. *Energy & Environmental Science* **2018**, *11* (10), 2696-2767.
8. Arabkoohsar, A.; Namib, H., Chapter Four - Pumped hydropower storage. In *Mechanical Energy Storage Technologies*, Arabkoohsar, A., Ed. Academic Press: 2021; pp 73-100.
9. Arabkoohsar, A.; Sadi, M., Chapter Five - Flywheel energy storage. In *Mechanical Energy Storage Technologies*, Arabkoohsar, A., Ed. Academic Press: 2021; pp 101-124.
10. Revankar, S. T., Chapter Six - Chemical Energy Storage. In *Storage and Hybridization of Nuclear Energy*, Bindra, H.; Revankar, S., Eds. Academic Press: 2019; pp 177-227.
11. Sagadevan, S.; Marlinda, A. R.; Chowdhury, Z. Z.; Wahab, Y. B. A.; Hamizi, N. A.; Shahid, M. M.; Mohammad, F.; Podder, J.; Johan, M. R., Chapter two - Fundamental electrochemical energy storage systems. In *Advances in Supercapacitor and Supercapattery*, Arshid, N.; Khalid, M.; Grace, A. N., Eds. Elsevier: 2021; pp 27-43.
12. Kundu, D.; Adams, B. D.; Duffort, V.; Vajargah, S. H.; Nazar, L. F., A high-capacity and long-life aqueous rechargeable zinc battery using a metal oxide intercalation cathode. *Nature Energy* **2016**, *1* (10), 16119.
13. Mathis, T. S.; Kurra, N.; Wang, X.; Pinto, D.; Simon, P.; Gogotsi, Y., Energy Storage Data Reporting in Perspective—Guidelines for Interpreting the Performance of Electrochemical Energy Storage Systems. *Advanced Energy Materials* **2019**, *9* (39), 1902007.
14. Simon, P.; Gogotsi, Y., Perspectives for electrochemical capacitors and related devices. *Nature Materials* **2020**, *19* (11), 1151-1163.
15. Peng, B.; Chen, J., Functional materials with high-efficiency energy storage and conversion for batteries and fuel cells. *Coordination Chemistry Reviews* **2009**, *253* (23), 2805-2813.
16. Xu, J.; Thomas, H. R.; Francis, R. W.; Lum, K. R.; Wang, J.; Liang, B., A review of processes and technologies for the recycling of lithium-ion secondary batteries. *Journal of Power Sources* **2008**, *177* (2), 512-527.

17. Liu, C.; Cao, G., FUNDAMENTALS OF RECHARGEABLE BATTERIES AND ELECTROCHEMICAL POTENTIALS OF ELECTRODE MATERIALS. In *Nanomaterials for Energy Conversion and Storage*, pp 397-451.
18. Chen, H.; Cong, T. N.; Yang, W.; Tan, C.; Li, Y.; Ding, Y., Progress in electrical energy storage system: A critical review. *Progress in Natural Science* **2009**, *19* (3), 291-312.
19. Al Shaqsi, A. Z.; Sopian, K.; Al-Hinai, A., Review of energy storage services, applications, limitations, and benefits. *Energy Reports* **2020**, *6*, 288-306.
20. Behabtu, H. A.; Messagie, M.; Coosemans, T.; Berecibar, M.; Anlay Fante, K.; Kebede, A. A.; Mierlo, J. V., A Review of Energy Storage Technologies' Application Potentials in Renewable Energy Sources Grid Integration. *Sustainability* **2020**, *12* (24), 10511.
21. He, P.; Yu, H.; Li, D.; Zhou, H., Layered lithium transition metal oxide cathodes towards high energy lithium-ion batteries. *Journal of Materials Chemistry* **2012**, *22* (9), 3680-3695.
22. Ozawa, K., Lithium-ion rechargeable batteries with LiCoO<sub>2</sub> and carbon electrodes: the LiCoO<sub>2</sub>/C system. *Solid State Ionics* **1994**, *69* (3), 212-221.
23. Deng, D., Li-ion batteries: basics, progress, and challenges. *Energy Science & Engineering* **2015**, *3* (5), 385-418.
24. Manthiram, A., A reflection on lithium-ion battery cathode chemistry. *Nature Communications* **2020**, *11* (1), 1550.
25. Chen, T.; Jin, Y.; Lv, H.; Yang, A.; Liu, M.; Chen, B.; Xie, Y.; Chen, Q., Applications of Lithium-Ion Batteries in Grid-Scale Energy Storage Systems. *Transactions of Tianjin University* **2020**, *26* (3), 208-217.
26. Chen, X.; Shen, W.; Vo, T. T.; Cao, Z.; Kapoor, A. In *An overview of lithium-ion batteries for electric vehicles*, 2012 10th International Power & Energy Conference (IPEC), 12-14 Dec. 2012; 2012; pp 230-235.
27. Kennedy, B.; Patterson, D.; Camilleri, S., Use of lithium-ion batteries in electric vehicles. *Journal of Power Sources* **2000**, *90* (2), 156-162.
28. Liang, Y.; Zhao, C.-Z.; Yuan, H.; Chen, Y.; Zhang, W.; Huang, J.-Q.; Yu, D.; Liu, Y.; Titirici, M.-M.; Chueh, Y.-L.; Yu, H.; Zhang, Q., A review of rechargeable batteries for portable electronic devices. *InfoMat* **2019**, *1* (1), 6-32.
29. Hou, J.; Lu, L.; Wang, L.; Ohma, A.; Ren, D.; Feng, X.; Li, Y.; Li, Y.; Ootani, I.; Han, X.; Ren, W.; He, X.; Nitta, Y.; Ouyang, M., Thermal runaway of Lithium-ion batteries employing LiN(SO<sub>2</sub>F)<sub>2</sub>-based concentrated electrolytes. *Nature Communications* **2020**, *11* (1), 5100.
30. Ostanek, J. K.; Li, W.; Mukherjee, P. P.; Crompton, K. R.; Hacker, C., Simulating onset and evolution of thermal runaway in Li-ion cells using a coupled thermal and venting model. *Applied Energy* **2020**, *268*, 114972.
31. Janot, R.; Guérard, D., Ball-milling in liquid media: Applications to the preparation of anodic materials for lithium-ion batteries. *Progress in Materials Science* **2005**, *50* (1), 1-92.
32. Wang, J.; Yang, Y.; Zhang, Y.; Li, Y.; Sun, R.; Wang, Z.; Wang, H., Strategies towards the challenges of zinc metal anode in rechargeable aqueous zinc ion batteries. *Energy Storage Materials* **2021**, *35*, 19-46.
33. Tang, B.; Shan, L.; Liang, S.; Zhou, J., Issues and opportunities facing aqueous zinc-ion batteries. *Energy & Environmental Science* **2019**, *12* (11), 3288-3304.
34. Jian, Q.; Wan, Y.; Lin, Y.; Ni, M.; Wu, M.; Zhao, T., A Highly Reversible Zinc Anode for Rechargeable Aqueous Batteries. *ACS Applied Materials & Interfaces* **2021**, *13* (44), 52659-52669.

35. Fang, G.; Zhou, J.; Pan, A.; Liang, S., Recent Advances in Aqueous Zinc-Ion Batteries. *ACS Energy Letters* **2018**, *3* (10), 2480-2501.
36. Liu, W.; Zhang, X.; Huang, Y.; Jiang, B.; Chang, Z.; Xu, C.; Kang, F.,  $\beta$ -MnO<sub>2</sub> with proton conversion mechanism in rechargeable zinc ion battery. *Journal of Energy Chemistry* **2021**, *56*, 365-373.
37. Zhang, Y.; Chen, A.; Sun, J., Promise and challenge of vanadium-based cathodes for aqueous zinc-ion batteries. *Journal of Energy Chemistry* **2021**, *54*, 655-667.
38. Huang, C.; Wu, C.; Zhang, Z.; Xie, Y.; Li, Y.; Yang, C.; Wang, H., Crystalline and amorphous MnO<sub>2</sub> cathodes with open framework enable high-performance aqueous zinc-ion batteries. *Frontiers of Materials Science* **2021**, *15* (2), 202-215.
39. Li, C.; Xie, X.; Liang, S.; Zhou, J., Issues and Future Perspective on Zinc Metal Anode for Rechargeable Aqueous Zinc-ion Batteries. *ENERGY & ENVIRONMENTAL MATERIALS* **2020**, *3* (2), 146-159.
40. Tao, F.; Liu, Y.; Ren, X.; Wang, J.; Zhou, Y.; Miao, Y.; Ren, F.; Wei, S.; Ma, J., Different surface modification methods and coating materials of zinc metal anode. *Journal of Energy Chemistry* **2022**, *66*, 397-412.
41. Du, W.; Ang, E. H.; Yang, Y.; Zhang, Y.; Ye, M.; Li, C. C., Challenges in the material and structural design of zinc anode towards high-performance aqueous zinc-ion batteries. *Energy & Environmental Science* **2020**, *13* (10), 3330-3360.
42. Yi, Z.; Chen, G.; Hou, F.; Wang, L.; Liang, J., Strategies for the Stabilization of Zn Metal Anodes for Zn-Ion Batteries. *Advanced Energy Materials* **2021**, *11* (1), 2003065.
43. Tian, Y.; An, Y.; Wei, C.; Xi, B.; Xiong, S.; Feng, J.; Qian, Y., Recent Advances and Perspectives of Zn-Metal Free “Rocking-Chair”-Type Zn-Ion Batteries. *Advanced Energy Materials* **2021**, *11* (5), 2002529.
44. Gan, Y.; Wang, C.; Li, J.; Zheng, J.; Wu, Z.; Lv, L.; Liang, P.; Wan, H.; Zhang, J.; Wang, H., Stability Optimization Strategies of Cathode Materials for Aqueous Zinc Ion Batteries: A Mini Review. *Frontiers in Chemistry* **2022**, *9*.
45. Huang, S.; Zhu, J.; Tian, J.; Niu, Z., Recent Progress in the Electrolytes of Aqueous Zinc-Ion Batteries. *Chemistry – A European Journal* **2019**, *25* (64), 14480-14494.
46. Sun, W.; Wang, F.; Hou, S.; Yang, C.; Fan, X.; Ma, Z.; Gao, T.; Han, F.; Hu, R.; Zhu, M.; Wang, C., Zn/MnO<sub>2</sub> Battery Chemistry With H<sup>+</sup> and Zn<sup>2+</sup> Coinsertion. *Journal of the American Chemical Society* **2017**, *139* (29), 9775-9778.
47. Wan, F.; Zhang, L.; Dai, X.; Wang, X.; Niu, Z.; Chen, J., Aqueous rechargeable zinc/sodium vanadate batteries with enhanced performance from simultaneous insertion of dual carriers. *Nature Communications* **2018**, *9* (1), 1656.
48. Pan, H.; Shao, Y.; Yan, P.; Cheng, Y.; Han, K. S.; Nie, Z.; Wang, C.; Yang, J.; Li, X.; Bhattacharya, P.; Mueller, K. T.; Liu, J., Reversible aqueous zinc/manganese oxide energy storage from conversion reactions. *Nature Energy* **2016**, *1* (5), 16039.
49. Du, Y.; Wang, X.; Man, J.; Sun, J., A novel organic-inorganic hybrid V<sub>2</sub>O<sub>5</sub>@polyaniline as high-performance cathode for aqueous zinc-ion batteries. *Materials Letters* **2020**, *272*, 127813.
50. He, P.; Yan, M.; Liao, X.; Luo, Y.; Mai, L.; Nan, C.-W., Reversible V<sup>3+</sup>/V<sup>5+</sup> double redox in lithium vanadium oxide cathode for zinc storage. *Energy Storage Materials* **2020**, *29*, 113-120.

51. Zhou, J.; Shan, L.; Wu, Z.; Guo, X.; Fang, G.; Liang, S., Investigation of V<sub>2</sub>O<sub>5</sub> as a low-cost rechargeable aqueous zinc ion battery cathode. *Chemical Communications* **2018**, *54* (35), 4457-4460.
52. Liu, W.; Hao, J.; Xu, C.; Mou, J.; Dong, L.; Jiang, F.; Kang, Z.; Wu, J.; Jiang, B.; Kang, F., Investigation of zinc ion storage of transition metal oxides, sulfides, and borides in zinc ion battery systems. *Chemical Communications* **2017**, *53* (51), 6872-6874.
53. Hoang Huy, V. P.; Ahn, Y. N.; Hur, J., Recent Advances in Transition Metal Dichalcogenide Cathode Materials for Aqueous Rechargeable Multivalent Metal-Ion Batteries. *Nanomaterials (Basel)* **2021**, *11* (6).
54. Lee, W. S. V.; Xiong, T.; Wang, X.; Xue, J., Unraveling MoS<sub>2</sub> and Transition Metal Dichalcogenides as Functional Zinc-Ion Battery Cathode: A Perspective. *Small Methods* **2021**, *5* (1), 2000815.
55. Kundu, D.; Oberholzer, P.; Glaros, C.; Bouzid, A.; Tervoort, E.; Pasquarello, A.; Niederberger, M., Organic Cathode for Aqueous Zn-Ion Batteries: Taming a Unique Phase Evolution toward Stable Electrochemical Cycling. *Chemistry of Materials* **2018**, *30* (11), 3874-3881.
56. Cui, J.; Guo, Z.; Yi, J.; Liu, X.; Wu, K.; Liang, P.; Li, Q.; Liu, Y.; Wang, Y.; Xia, Y.; Zhang, J., Organic Cathode Materials for Rechargeable Zinc Batteries: Mechanisms, Challenges, and Perspectives. *ChemSusChem* **2020**, *13* (9), 2160-2185.
57. Zhang, S.; Long, S.; Li, H.; Xu, Q., A high-capacity organic cathode based on active N atoms for aqueous zinc-ion batteries. *Chemical Engineering Journal* **2020**, *400*, 125898.
58. Ma, X.; Cao, X.; Yao, M.; Shan, L.; Shi, X.; Fang, G.; Pan, A.; Lu, B.; Zhou, J.; Liang, S., Organic-Inorganic Hybrid Cathode with Dual Energy-Storage Mechanism for Ultrahigh-Rate and Ultralong-Life Aqueous Zinc-Ion Batteries. *Advanced Materials* **2022**, *34* (6), 2105452.
59. Alfaruqi, M. H.; Islam, S.; Gim, J.; Song, J.; Kim, S.; Pham, D. T.; Jo, J.; Xiu, Z.; Mathew, V.; Kim, J., A high surface area tunnel-type  $\alpha$ -MnO<sub>2</sub> nanorod cathode by a simple solvent-free synthesis for rechargeable aqueous zinc-ion batteries. *Chemical Physics Letters* **2016**, *650*, 64-68.
60. De Juan-Corpuz, L. M.; Corpuz, R. D.; Somwangthanaroj, A.; Nguyen, M. T.; Yonezawa, T.; Ma, J.; Kheawhom, S., Binder-Free Centimeter-Long V<sub>2</sub>O<sub>5</sub> Nanofibers on Carbon Cloth as Cathode Material for Zinc-Ion Batteries. *Energies* **2020**, *13* (1), 31.
61. Li, H.; Yang, Q.; Mo, F.; Liang, G.; Liu, Z.; Tang, Z.; Ma, L.; Liu, J.; Shi, Z.; Zhi, C., MoS<sub>2</sub> nanosheets with expanded interlayer spacing for rechargeable aqueous Zn-ion batteries. *Energy Storage Materials* **2019**, *19*, 94-101.
62. Chen, T.; Zhu, X.; Chen, X.; Zhang, Q.; Li, Y.; Peng, W.; Zhang, F.; Fan, X., VS<sub>2</sub> nanosheets vertically grown on graphene as high-performance cathodes for aqueous zinc-ion batteries. *Journal of Power Sources* **2020**, *477*, 228652.
63. Wang, L.; Jiang, M.; Liu, F.; Huang, Q.; Liu, L.; Fu, L.; Wu, Y., Layered TiS<sub>2</sub> as a Promising Host Material for Aqueous Rechargeable Zn Ion Battery. *Energy & Fuels* **2020**, *34* (9), 11590-11596.
64. Islam, S.; Alfaruqi, M. H.; Putro, D. Y.; Park, S.; Kim, S.; Lee, S.; Ahmed, M. S.; Mathew, V.; Sun, Y.-K.; Hwang, J.-Y.; Kim, J., In Situ Oriented Mn Deficient ZnMn<sub>2</sub>O<sub>4</sub>@C Nanoarchitecture for Durable Rechargeable Aqueous Zinc-Ion Batteries. *Advanced Science* **2021**, *8* (4), 2002636.

65. Chen, H.; Zhou, W.; Zhu, D.; Liu, Z.; Feng, Z.; Li, J.; Chen, Y., Porous cube-like  $\text{Mn}_3\text{O}_4@\text{C}$  as an advanced cathode for low-cost neutral zinc-ion battery. *Journal of Alloys and Compounds* **2020**, *813*, 151812.
66. Lu, Y.; Wang, J.; Zeng, S.; Zhou, L.; Xu, W.; Zheng, D.; Liu, J.; Zeng, Y.; Lu, X., An ultrathin defect-rich  $\text{Co}_3\text{O}_4$  nanosheet cathode for high-energy and durable aqueous zinc ion batteries. *Journal of Materials Chemistry A* **2019**, *7* (38), 21678-21683.
67. Tang, Z.; Chen, W.; Lyu, Z.; Chen, Q., Size-Dependent Reaction Mechanism of  $\text{MnO}_2$  Particles as Cathodes in Aqueous Zinc-Ion Batteries. *Energy Material Advances* **2022**, *2022*, 9765710.
68. Khamsanga, S.; Pornprasertsuk, R.; Yonezawa, T.; Mohamad, A. A.; Kheawhom, S.,  $\delta$ - $\text{MnO}_2$  nanoflower/graphite cathode for rechargeable aqueous zinc ion batteries. *Scientific Reports* **2019**, *9* (1), 8441.
69. Mo, Y.; Hu, Y.; Bae, I. T.; Miller, B.; Antonio, M. R.; Scherson, D. A., In Situ X-Ray Absorption Fine Structure Studies of a Manganese Dioxide Electrode in a Rechargeable  $\text{MnO}_2/\text{Zn}$  Alkaline Battery Environment. *Journal of The Electrochemical Society* **1997**, *144* (5), 1598-1603.
70. Zhao, Y.; Zhu, Y.; Zhang, X., Challenges and perspectives for manganese-based oxides for advanced aqueous zinc-ion batteries. *InfoMat* **2020**, *2* (2), 237-260.
71. Jiao, Y.; Kang, L.; Berry-Gair, J.; McColl, K.; Li, J.; Dong, H.; Jiang, H.; Wang, R.; Corà, F.; Brett, D. J. L.; He, G.; Parkin, I. P., Enabling stable  $\text{MnO}_2$  matrix for aqueous zinc-ion battery cathodes. *Journal of Materials Chemistry A* **2020**, *8* (42), 22075-22082.
72. Chen, D.; Lu, M.; Wang, B.; Cheng, H.; Yang, H.; Cai, D.; Han, W.; Fan, H. J., High-mass loading  $\text{V}_3\text{O}_7 \cdot \text{H}_2\text{O}$  nanoarray for Zn-ion battery: New synthesis and two-stage ion intercalation chemistry. *Nano Energy* **2021**, *83*, 105835.
73. Wang, Q.; Sun, T.; Zheng, S.; Li, L.; Ma, T.; Liang, J., A new tunnel-type  $\text{V}_4\text{O}_9$  cathode for high power density aqueous zinc ion batteries. *Inorganic Chemistry Frontiers* **2021**, *8* (20), 4497-4506.
74. Liu, S.; Kang, L.; Kim, J. M.; Chun, Y. T.; Zhang, J.; Jun, S. C., Recent Advances in Vanadium-Based Aqueous Rechargeable Zinc-Ion Batteries. *Advanced Energy Materials* **2020**, *10* (25), 2000477.
75. Liu, W.; Dong, L.; Jiang, B.; Huang, Y.; Wang, X.; Xu, C.; Kang, Z.; Mou, J.; Kang, F., Layered vanadium oxides with proton and zinc ion insertion for zinc ion batteries. *Electrochimica Acta* **2019**, *320*, 134565.
76. Tang, B.; Tian, N.; Jiang, J.; Li, Y.; Yang, J.; Zhu, Q., Investigation of zinc storage capacity of  $\text{WS}_2$  nanosheets for rechargeable aqueous Zn-ion batteries. *Journal of Alloys and Compounds* **2022**, *894*, 162391.
77. Zeng, L.; Fang, Y.; Xu, L.; Zheng, C.; Yang, M.-Q.; He, J.; Xue, H.; Qian, Q.; Wei, M.; Chen, Q., Rational design of few-layer  $\text{MoSe}_2$  confined within  $\text{ZnSe}-\text{C}$  hollow porous spheres for high-performance lithium-ion and sodium-ion batteries. *Nanoscale* **2019**, *11* (14), 6766-6775.
78. Xia, H.; Xu, Q.; Zhang, J., Recent Progress on Two-Dimensional Nanoflake Ensembles for Energy Storage Applications. *Nanomicro Lett* **2018**, *10* (4), 66-66.
79. Zhao, W.; Pan, J.; Fang, Y.; Che, X.; Wang, D.; Bu, K.; Huang, F., Metastable  $\text{MoS}_2$ : Crystal Structure, Electronic Band Structure, Synthetic Approach and Intriguing Physical Properties. *Chemistry – A European Journal* **2018**, *24* (60), 15942-15954.

80. Lee, C.; Yan, H.; Brus, L. E.; Heinz, T. F.; Hone, J.; Ryu, S., Anomalous Lattice Vibrations of Single- and Few-Layer MoS<sub>2</sub>. *ACS Nano* **2010**, *4* (5), 2695-2700.
81. Javed, M. S.; Lei, H.; Wang, Z.; Liu, B.-t.; Cai, X.; Mai, W., 2D V<sub>2</sub>O<sub>5</sub> nanosheets as a binder-free high-energy cathode for ultrafast aqueous and flexible Zn-ion batteries. *Nano Energy* **2020**, *70*, 104573.
82. Xia, C.; Guo, J.; Li, P.; Zhang, X.; Alshareef, H. N., Highly Stable Aqueous Zinc-Ion Storage Using a Layered Calcium Vanadium Oxide Bronze Cathode. *Angewandte Chemie International Edition* **2018**, *57* (15), 3943-3948.
83. Islam, S.; Alfaruqi, M. H.; Putro, D. Y.; Soundharrajan, V.; Sambandam, B.; Jo, J.; Park, S.; Lee, S.; Mathew, V.; Kim, J., K<sup>+</sup> intercalated V<sub>2</sub>O<sub>5</sub> nanorods with exposed facets as advanced cathodes for high energy and high rate zinc-ion batteries. *Journal of Materials Chemistry A* **2019**, *7* (35), 20335-20347.
84. Hu, Z.; Wang, L.; Zhang, K.; Wang, J.; Cheng, F.; Tao, Z.; Chen, J., MoS<sub>2</sub> nanoflowers with expanded interlayers as high-performance anodes for sodium-ion batteries. *Angewandte Chemie International Edition* **2014**, *53* (47), 12794-12798.
85. Liu, C.; Neale, Z.; Zheng, J.; Jia, X.; Huang, J.; Yan, M.; Tian, M.; Wang, M.; Yang, J.; Cao, G., Expanded hydrated vanadate for high-performance aqueous zinc-ion batteries. *Energy & Environmental Science* **2019**, *12* (7), 2273-2285.
86. Yan, M.; He, P.; Chen, Y.; Wang, S.; Wei, Q.; Zhao, K.; Xu, X.; An, Q.; Shuang, Y.; Shao, Y.; Mueller, K. T.; Mai, L.; Liu, J.; Yang, J., Water-Lubricated Intercalation in V<sub>2</sub>O<sub>5</sub>·nH<sub>2</sub>O for High-Capacity and High-Rate Aqueous Rechargeable Zinc Batteries. *Advanced Materials* **2018**, *30* (1), 1703725.
87. Nakamura, T.; Ohta, K.; Hou, X.; Kimura, Y.; Tsuruta, K.; Tamenori, Y.; Aso, R.; Yoshida, H.; Amezawa, K., Oxygen defect engineering for the Li-rich cathode material Li<sub>1.2</sub>Ni<sub>0.13</sub>Co<sub>0.13</sub>Mn<sub>0.54</sub>O<sub>2-δ</sub>. *Journal of Materials Chemistry A* **2021**, *9* (6), 3657-3667.
88. Zhu, K.; Wei, S.; Shou, H.; Shen, F.; Chen, S.; Zhang, P.; Wang, C.; Cao, Y.; Guo, X.; Luo, M.; Zhang, H.; Ye, B.; Wu, X.; He, L.; Song, L., Defect engineering on V<sub>2</sub>O<sub>3</sub> cathode for long-cycling aqueous zinc metal batteries. *Nature Communications* **2021**, *12* (1), 6878.
89. Xu, W.; Sun, C.; Zhao, K.; Cheng, X.; Rawal, S.; Xu, Y.; Wang, Y., Defect engineering activating (Boosting) zinc storage capacity of MoS<sub>2</sub>. *Energy Storage Materials* **2019**, *16*, 527-534.
90. Liang, H.; Cao, Z.; Ming, F.; Zhang, W.; Anjum, D. H.; Cui, Y.; Cavallo, L.; Alshareef, H. N., Aqueous Zinc-Ion Storage in MoS<sub>2</sub> by Tuning the Intercalation Energy. *Nano Letters* **2019**, *19* (5), 3199-3206.
91. Cao, H.; Zheng, Z.; Norby, P.; Xiao, X.; Mossin, S., Electrochemically Induced Phase Transition in V<sub>3</sub>O<sub>7</sub>·H<sub>2</sub>O Nanobelts/Reduced Graphene Oxide Composites for Aqueous Zinc-Ion Batteries. *Small* **2021**, *17* (24), 2100558.
92. Liu, X.; Wang, Z.; Niu, Y.; Liu, C.; Chen, H.; Ren, X.; Liu, Z.; Lau, W.-M.; Zhou, D., Electrospun V<sub>2</sub>O<sub>3</sub>@Carbon Nanofibers as a Flexible and Binder-Free Cathode for Highly Stable Aqueous Zn-Ion Full Batteries. *ACS Applied Energy Materials* **2022**.
93. Liu, Y.; Chi, X.; Han, Q.; Du, Y.; Huang, J.; Liu, Y.; Yang, J., α-MnO<sub>2</sub> nanofibers/carbon nanotubes hierarchically assembled microspheres: Approaching practical applications of high-performance aqueous Zn-ion batteries. *Journal of Power Sources* **2019**, *443*, 227244.
94. Wang, X.; Li, Y.; Wang, S.; Zhou, F.; Das, P.; Sun, C.; Zheng, S.; Wu, Z.-S., 2D Amorphous V<sub>2</sub>O<sub>5</sub>/Graphene Heterostructures for High-Safety Aqueous Zn-Ion Batteries

- with Unprecedented Capacity and Ultrahigh Rate Capability. *Advanced Energy Materials* **2020**, *10* (22), 2000081.
95. Liu, P.; Chen, X.; Ouyang, B.; Fan, X.; Liu, W.; Li, P.; Peng, J.; Yan, J.; Liu, K., Novel Energy Storage Center for High-Performance Rechargeable Aqueous Hybrid Zinc Energy Storage. *Energy & Fuels* **2021**, *35* (6), 5352-5359.
  96. Qin, H.; Yang, Z.; Chen, L.; Chen, X.; Wang, L., A high-rate aqueous rechargeable zinc ion battery based on the VS<sub>4</sub>@rGO nanocomposite. *Journal of Materials Chemistry A* **2018**, *6* (46), 23757-23765.
  97. Huang, J.; Wang, Z.; Hou, M.; Dong, X.; Liu, Y.; Wang, Y.; Xia, Y., Polyaniline-intercalated manganese dioxide nanolayers as a high-performance cathode material for an aqueous zinc-ion battery. *Nature Communications* **2018**, *9* (1), 2906.
  98. Kappe, C. O., Controlled Microwave Heating in Modern Organic Synthesis. *Angewandte Chemie International Edition* **2004**, *43* (46), 6250-6284.
  99. Hayes, B. L., Recent advances in microwave-assisted synthesis. *Aldrichim. Acta* **2004**, *37* (2), 66-76.
  100. Bilecka, I.; Niederberger, M., Microwave chemistry for inorganic nanomaterials synthesis. *Nanoscale* **2010**, *2* (8), 1358-1374.
  101. Rao, K. J.; Vaidyanathan, B.; Ganguli, M.; Ramakrishnan, P. A., Synthesis of Inorganic Solids Using Microwaves. *Chemistry of Materials* **1999**, *11* (4), 882-895.
  102. Zhu, Y.-J.; Chen, F., Microwave-Assisted Preparation of Inorganic Nanostructures in Liquid Phase. *Chemical Reviews* **2014**, *114* (12), 6462-6555.
  103. Dallinger, D.; Kappe, C. O., Microwave-Assisted Synthesis in Water as Solvent. *Chemical Reviews* **2007**, *107* (6), 2563-2591.
  104. Gawande, M. B.; Shelke, S. N.; Zboril, R.; Varma, R. S., Microwave-Assisted Chemistry: Synthetic Applications for Rapid Assembly of Nanomaterials and Organics. *Accounts of Chemical Research* **2014**, *47* (4), 1338-1348.
  105. Muthukumar, K.; Leban, L.; Sekar, A.; Elangovan, A.; Sarkar, N.; Li, J., Tuning the defects in MoS<sub>2</sub>/reduced graphene oxide 2D hybrid materials for optimizing battery performance. *Sustainable Energy & Fuels* **2021**, *5* (16), 4002-4014.
  106. Prasad, T. P.; Diemann, E.; Müller, A., Thermal decomposition of (NH<sub>4</sub>)<sub>2</sub>MoO<sub>2</sub>S<sub>2</sub>, (NH<sub>4</sub>)<sub>2</sub>MoS<sub>4</sub>, (NH<sub>4</sub>)<sub>2</sub>WO<sub>2</sub>S<sub>2</sub> and (NH<sub>4</sub>)<sub>2</sub>WS<sub>4</sub>. *Journal of Inorganic and Nuclear Chemistry* **1973**, *35* (6), 1895-1904.
  107. Brito, J. L.; Ilija, M.; Hernández, P., Thermal and reductive decomposition of ammonium thiomolybdates. *Thermochimica Acta* **1995**, *256* (2), 325-338.
  108. Bandyopadhyay, D.; Banik, B. K., Chapter 19 - Microwave-Induced Synthesis of Heterocycles of Medicinal Interests. In *Green Synthetic Approaches for Biologically Relevant Heterocycles*, Brahmachari, G., Ed. Elsevier: Boston, 2015; pp 517-557.
  109. Ng, S. H.; Chew, S. Y.; Wang, J.; Wexler, D.; Tournayre, Y.; Konstantinov, K.; Liu, H. K., Synthesis and electrochemical properties of V<sub>2</sub>O<sub>5</sub> nanostructures prepared via a precipitation process for lithium-ion battery cathodes. *Journal of Power Sources* **2007**, *174* (2), 1032-1035.
  110. Lee, H.; Kumbhar, V. S.; Lee, J.; Choi, Y.; Lee, K., Highly reversible crystal transformation of anodized porous V<sub>2</sub>O<sub>5</sub> nanostructures for wide potential window high-performance supercapacitors. *Electrochimica Acta* **2020**, *334*, 135618.

111. Tepavcevic, S.; Xiong, H.; Stamenkovic, V. R.; Zuo, X.; Balasubramanian, M.; Prakupenka, V. B.; Johnson, C. S.; Rajh, T., Nanostructured Bilayered Vanadium Oxide Electrodes for Rechargeable Sodium-Ion Batteries. *ACS Nano* **2012**, *6* (1), 530-538.
112. Liu, F.; Chen, Z.; Fang, G.; Wang, Z.; Cai, Y.; Tang, B.; Zhou, J.; Liang, S., V<sub>2</sub>O<sub>5</sub> Nanospheres with Mixed Vanadium Valences as High Electrochemically Active Aqueous Zinc-Ion Battery Cathode. *Nanomicro Lett* **2019**, *11* (1), 25.
113. Liang, X.; Yan, L.; Li, W.; Bai, Y.; Zhu, C.; Qiang, Y.; Xiong, B.; Xiang, B.; Zou, X., Flexible high-energy and stable rechargeable vanadium-zinc battery based on oxygen defect modulated V<sub>2</sub>O<sub>5</sub> cathode. *Nano Energy* **2021**, *87*, 106164.
114. Qin, X.; Wang, X.; Sun, J.; Lu, Q.; Omar, A.; Mikhailova, D., Polypyrrole Wrapped V<sub>2</sub>O<sub>5</sub> Nanowires Composite for Advanced Aqueous Zinc-Ion Batteries. *Frontiers in Energy Research* **2020**, *8* (199).
115. Chen, D.; Yi, R.; Chen, S.; Xu, T.; Gordin, M. L.; Lv, D.; Wang, D., Solvothermal synthesis of V<sub>2</sub>O<sub>5</sub>/graphene nanocomposites for high performance lithium ion batteries. *Materials Science and Engineering: B* **2014**, *185*, 7-12.
116. Li, Y.; Huang, Z.; Kalambate, P. K.; Zhong, Y.; Huang, Z.; Xie, M.; Shen, Y.; Huang, Y., V<sub>2</sub>O<sub>5</sub> nanopaper as a cathode material with high capacity and long cycle life for rechargeable aqueous zinc-ion battery. *Nano Energy* **2019**, *60*, 752-759.
117. Thiagarajan, S.; Thaiyan, M.; Ganesan, R., Physical vapor deposited highly oriented V<sub>2</sub>O<sub>5</sub> thin films for electrocatalytic oxidation of hydrazine. *RSC Advances* **2016**, *6* (86), 82581-82590.
118. Rehnlund, D.; Valvo, M.; Edström, K.; Nyholm, L., Electrodeposition of Vanadium Oxide/Manganese Oxide Hybrid Thin Films on Nanostructured Aluminum Substrates. *Journal of The Electrochemical Society* **2014**, *161* (10), D515-D521.
119. Chen, Y.; Muthukumar, K.; Leban, L.; Li, J., Microwave-assisted high-yield exfoliation of vanadium pentoxide nanoribbons for supercapacitor applications. *Electrochimica Acta* **2020**, *330*, 135200.
120. Elgrishi, N.; Rountree, K. J.; McCarthy, B. D.; Rountree, E. S.; Eisenhart, T. T.; Dempsey, J. L., A Practical Beginner's Guide to Cyclic Voltammetry. *Journal of Chemical Education* **2018**, *95* (2), 197-206.
121. Díaz-González, F.; Sumper, A.; Gomis-Bellmunt, O.; Villafáfila-Robles, R., A review of energy storage technologies for wind power applications. *Renewable and Sustainable Energy Reviews* **2012**, *16*, 2154-2171.
122. Yoo, H. D.; Markevich, E.; Salitra, G.; Sharon, D.; Aurbach, D., On the challenge of developing advanced technologies for electrochemical energy storage and conversion. *Materials Today* **2014**, *17* (3), 110-121.
123. Canepa, P.; Sai Gautam, G.; Hannah, D. C.; Malik, R.; Liu, M.; Gallagher, K. G.; Persson, K. A.; Ceder, G., Odyssey of Multivalent Cathode Materials: Open Questions and Future Challenges. *Chemical Reviews* **2017**, *117* (5), 4287-4341.
124. Whittingham, M. S.; Siu, C.; Ding, J., Can Multielectron Intercalation Reactions Be the Basis of Next Generation Batteries? *Accounts of Chemical Research* **2018**, *51* (2), 258-264.
125. Liang, Y.; Dong, H.; Aurbach, D.; Yao, Y., Current status and future directions of multivalent metal-ion batteries. *Nature Energy* **2020**.
126. Konarov, A.; Voronina, N.; Jo, J. H.; Bakenov, Z.; Sun, Y.-K.; Myung, S.-T., Present and Future Perspective on Electrode Materials for Rechargeable Zinc-Ion Batteries. *ACS Energy Letters* **2018**, *3* (10), 2620-2640.

127. Nam, K. W.; Kim, H.; Choi, J. H.; Choi, J. W., Crystal water for high performance layered manganese oxide cathodes in aqueous rechargeable zinc batteries. *Energy & Environmental Science* **2019**, *12* (6), 1999-2009.
128. Qin, H.; Chen, L.; Wang, L.; Chen, X.; Yang, Z., V<sub>2</sub>O<sub>5</sub> hollow spheres as high rate and long life cathode for aqueous rechargeable zinc ion batteries. *Electrochimica Acta* **2019**, *306*, 307-316.
129. Wang, B.; Han, Y.; Wang, X.; Bahlawane, N.; Pan, H.; Yan, M.; Jiang, Y., Prussian blue analogs for rechargeable batteries. *Isience* **2018**, *3*, 110-133.
130. Li, W. J.; Han, C.; Cheng, G.; Chou, S. L.; Liu, H. K.; Dou, S. X., Chemical properties, structural properties, and energy storage applications of prussian blue analogues. *Small* **2019**, *15* (32), 1900470.
131. Li, G.; Yang, Z.; Jiang, Y.; Jin, C.; Huang, W.; Ding, X.; Huang, Y., Towards polyvalent ion batteries: A zinc-ion battery based on NASICON structured Na<sub>3</sub>V<sub>2</sub>(PO<sub>4</sub>)<sub>3</sub>. *Nano Energy* **2016**, *25*, 211-217.
132. Xu, W.; Zhao, K.; Wang, Y., Electrochemical activated MoO<sub>2</sub>/Mo<sub>2</sub>N heterostructured nanobelts as superior zinc rechargeable battery cathode. *Energy Storage Materials* **2018**, *15*, 374-379.
133. He, P.; Quan, Y.; Xu, X.; Yan, M.; Yang, W.; An, Q.; He, L.; Mai, L., High-Performance Aqueous Zinc-Ion Battery Based on Layered H<sub>2</sub>V<sub>3</sub>O<sub>8</sub> Nanowire Cathode. *Small* **2017**, *13* (47), 1702551.
134. Liu, J.; Xu, P.; Liang, J.; Liu, H.; Peng, W.; Li, Y.; Zhang, F.; Fan, X., Boosting aqueous zinc-ion storage in MoS<sub>2</sub> via controllable phase. *Chemical Engineering Journal* **2020**, *389*, 124405.
135. An, V.; Bozheyev, F.; Richecoeur, F.; Irtegov, Y., Synthesis and characterization of nanolamellar tungsten and molybdenum disulfides. *Materials Letters* **2011**, *65* (15), 2381-2383.
136. Bozheyev, F.; Zhexembekova, A.; Zhumagali, S.; Molkenova, A.; Bakenov, Z., MoS<sub>2</sub> nanopowder as anode material for lithium-ion batteries produced by self-propagating high-temperature synthesis. *Materials Today: Proceedings* **2017**, *4* (3, Part A), 4567-4571.
137. Chang, K.; Chen, W., In situ synthesis of MoS<sub>2</sub>/graphene nanosheet composites with extraordinarily high electrochemical performance for lithium ion batteries. *Chemical Communications* **2011**, *47* (14), 4252-4254.
138. Matte, H. S. S. R.; Maitra, U.; Kumar, P.; Govinda Rao, B.; Pramoda, K.; Rao, C. N. R., Synthesis, Characterization, and Properties of Few-layer Metal Dichalcogenides and their Nanocomposites with Noble Metal Particles, Polyaniline, and Reduced Graphene Oxide. *Zeitschrift für anorganische und allgemeine Chemie* **2012**, *638* (15), 2617-2624.
139. You, Y.; Ye, Y.; Wei, M.; Sun, W.; Tang, Q.; Zhang, J.; Chen, X.; Li, H.; Xu, J., Three-dimensional MoS<sub>2</sub>/rGO foams as efficient sulfur hosts for high-performance lithium-sulfur batteries. *Chemical Engineering Journal* **2019**, *355*, 671-678.
140. Zhou, J.; Xiao, H.; Zhou, B.; Huang, F.; Zhou, S.; Xiao, W.; Wang, D., Hierarchical MoS<sub>2</sub>-rGO nanosheets with high MoS<sub>2</sub> loading with enhanced electro-catalytic performance. *Applied Surface Science* **2015**, *358*, 152-158.
141. Barik, G.; Pal, S., Defect Induced Performance Enhancement of Monolayer MoS<sub>2</sub> for Li- and Na-Ion Batteries. *The Journal of Physical Chemistry C* **2019**, *123* (36), 21852-21865.

142. Li, Y.; Zhang, R.; Zhou, W.; Wu, X.; Zhang, H.; Zhang, J., Hierarchical MoS<sub>2</sub> Hollow Architectures with Abundant Mo Vacancies for Efficient Sodium Storage. *ACS Nano* **2019**, *13* (5), 5533-5540.
143. Xu, S.; Zhong, G.; Chen, C.; Zhou, M.; Kline, D. J.; Jacob, R. J.; Xie, H.; He, S.; Huang, Z.; Dai, J.; Brozena, A. H.; Shahbazian-Yassar, R.; Zachariah, M. R.; Anlage, S. M.; Hu, L., Uniform, Scalable, High-Temperature Microwave Shock for Nanoparticle Synthesis through Defect Engineering. *Matter* **2019**, *1* (3), 759-769.
144. Song, Y.; Rong, H.; Li, Y.; Liu, W.; Zhang, X., Engineering defect concentrations of multiwalled carbon nanotubes by microwave irradiation for tunable electromagnetic absorption properties. *Journal of Materials Science* **2020**, *55* (28), 13871-13880.
145. Kitchen, H. J.; Vallance, S. R.; Kennedy, J. L.; Tapia-Ruiz, N.; Carassiti, L.; Harrison, A.; Whittaker, A. G.; Drysdale, T. D.; Kingman, S. W.; Gregory, D. H., Modern microwave methods in solid-state inorganic materials chemistry: from fundamentals to manufacturing. *Chem Rev* **2014**, *114* (2), 1170-206.
146. Wen, B.; Wang, X. X.; Cao, W. Q.; Shi, H. L.; Lu, M. M.; Wang, G.; Jin, H. B.; Wang, W. Z.; Yuan, J.; Cao, M. S., Reduced graphene oxides: the thinnest and most lightweight materials with highly efficient microwave attenuation performances of the carbon world. *Nanoscale* **2014**, *6* (11), 5754-5761.
147. Zhang, X.; Hayward, D.; Mingos, D. M., Dielectric Properties of MoS<sub>2</sub> and Pt Catalysts: Effects of Temperature and Microwave Frequency. *Catalysis Letters* **2002**, *84*.
148. Sole, C.; Drewett, N. E.; Hardwick, L. J., In situ Raman study of lithium-ion intercalation into microcrystalline graphite. *Faraday Discussions* **2014**, *172* (0), 223-237.
149. Bokobza, L.; Bruneel, J.-L.; Couzi, M., Raman spectroscopy as a tool for the analysis of carbon-based materials (highly oriented pyrolytic graphite, multilayer graphene and multiwall carbon nanotubes) and of some of their elastomeric composites. *Vibrational Spectroscopy* **2014**, *74*, 57-63.
150. Wang, H.; Robinson, J. T.; Li, X.; Dai, H., Solvothermal Reduction of Chemically Exfoliated Graphene Sheets. *Journal Of The American Chemical Society* **2009**, *131* (29), 9910-9911.
151. Cui, P.; Lee, J.; Hwang, E.; Lee, H., One-pot reduction of graphene oxide at subzero temperatures. *Chemical Communications* **2011**, *47* (45), 12370-12372.
152. Kumar, H.; Woltornist, S.; Adamson, D., Fractionation and Characterization of Graphene Oxide by Oxidation Extent Through Emulsion Stabilization. *Carbon* **2016**, *98*, 491-495.
153. Brown, E.; Yan, P.; Tekik, H.; Elangovan, A.; Wang, J.; Lin, D.; Li, J., 3D printing of hybrid MoS<sub>2</sub>-graphene aerogels as highly porous electrode materials for sodium ion battery anodes. *Materials & Design* **2019**, *170*, 107689.
154. Bertrand, P. A., Surface-phonon dispersion of MoS<sub>2</sub>. *Physical Review B* **1991**, *44* (11), 5745-5749.
155. Qin, W.; Chen, T.; Pan, L.; Niu, L.; Hu, B.; Li, D.; Li, J.; Sun, Z., MoS<sub>2</sub>-reduced graphene oxide composites via microwave assisted synthesis for sodium ion battery anode with improved capacity and cycling performance. *Electrochimica Acta* **2015**, *153*, 55-61.
156. Liang, L.; Meunier, V., First-principles Raman spectra of MoS<sub>2</sub>, WS<sub>2</sub> and their heterostructures. *Nanoscale* **2014**, *6* (10), 5394-5401.
157. Kong, D.; Wang, H.; Cha, J. J.; Pasta, M.; Koski, K. J.; Yao, J.; Cui, Y., Synthesis of MoS<sub>2</sub> and MoSe<sub>2</sub> Films with Vertically Aligned Layers. *Nano Letters* **2013**, *13* (3), 1341-1347.

158. Santha kumar, S.; Cherian, R.; Cheruvathor Poulouse, A.; Maekawa, T.; Sakthikumar, D.; Mohanan, P., Synthesis and characterization of pegylated reduced graphene oxide: Determination of toxicity using bone marrow mesenchymal stem cells. *Journal of Applied Chemical Science International* **2015**, *5*, 1-11.
159. Hibble, S. J.; Wood, G. B., Modeling the Structure of Amorphous MoS<sub>3</sub>: A Neutron Diffraction and Reverse Monte Carlo Study. *Journal of the American Chemical Society* **2004**, *126* (3), 959-965.
160. Liang, K. S.; Cramer, S. P.; Johnston, D. C.; Chang, C. H.; Jacobson, A. J.; deNeufville, J. P.; Chianelli, R. R., Amorphous MoS<sub>3</sub> and WS<sub>3</sub>. *Journal of Non-Crystalline Solids* **1980**, *42* (1), 345-356.
161. Liang, K. S.; deNeufville, J. P.; Jacobson, A. J.; Chianelli, R. R.; Betts, F., Structure of amorphous transition metal sulfides. *Journal of Non-Crystalline Solids* **1980**, *35-36*, 1249-1254.
162. Cramer, S. P.; Liang, K. S.; Jacobson, A. J.; Chang, C. H.; Chianelli, R. R., EXAFS studies of amorphous molybdenum and tungsten trisulfides and triselenides. *Inorganic Chemistry* **1984**, *23* (9), 1215-1221.
163. Chien, F. Z.; Moss, S. C.; Liang, K. S.; Chianelli, R. R., Local and intermediate-range structure of amorphous MoS<sub>3</sub>: Model calculation study. *Physical Review B* **1984**, *29* (8), 4606-4615.
164. Weber, T.; Muijsers, J. C.; Niemantsverdriet, J. W., Structure of Amorphous MoS<sub>3</sub>. *The Journal of Physical Chemistry* **1995**, *99* (22), 9194-9200.
165. Choi, M.; Hwang, J.; Setiadi, H.; Chang, W.; Kim, J., One-pot synthesis of molybdenum disulfide–reduced graphene oxide (MoS<sub>2</sub>-RGO) composites and their high electrochemical performance as an anode in lithium ion batteries. *The Journal of Supercritical Fluids* **2017**, *127*, 81-89.
166. Wang, J.; Luo, C.; Gao, T.; Langrock, A.; Mignerey, A. C.; Wang, C., An Advanced MoS<sub>2</sub>/Carbon Anode for High-Performance Sodium-Ion Batteries. *Small* **2015**, *11* (4), 473-481.
167. Budumuru, A. K.; Rakesh, B.; Sudakar, C., Enhanced high rate capability of Li intercalation in planar and edge defect-rich MoS<sub>2</sub> nanosheets. *Nanoscale* **2019**, *11* (18), 8882-8897.
168. Zhu, Z.; Tang, Y.; Leow, W. R.; Xia, H.; Lv, Z.; Wei, J.; Ge, X.; Cao, S.; Zhang, Y.; Zhang, W.; Zhang, H.; Xi, S.; Du, Y.; Chen, X., Approaching the Lithiation Limit of MoS<sub>2</sub> While Maintaining Its Layered Crystalline Structure to Improve Lithium Storage. *Angewandte Chemie International Edition* **2019**, *58* (11), 3521-3526.
169. Wu, Z.; Li, B.; Xue, Y.; Li, J.; Zhang, Y.; Gao, F., Fabrication of defect-rich MoS<sub>2</sub> ultrathin nanosheets for application in lithium-ion batteries and supercapacitors. *Journal of Materials Chemistry A* **2015**, *3* (38), 19445-19454.
170. Bang, G. S.; Nam, K. W.; Kim, J. Y.; Shin, J.; Choi, J. W.; Choi, S.-Y., Effective liquid-phase exfoliation and sodium ion battery application of MoS<sub>2</sub> nanosheets. *ACS applied materials & interfaces* **2014**, *6* (10), 7084-7089.
171. Li, M.; Lu, J.; Chen, Z.; Amine, K., 30 Years of Lithium-Ion Batteries. *Advanced Materials* **2018**, *30* (33), 1800561.
172. Jiang, F.; Peng, P., Elucidating the Performance Limitations of Lithium-ion Batteries due to Species and Charge Transport through Five Characteristic Parameters. *Scientific Reports* **2016**, *6* (1), 32639.

173. Zhang, Y.; Li, H.; Huang, S.; Fan, S.; Sun, L.; Tian, B.; Chen, F.; Wang, Y.; Shi, Y.; Yang, H. Y., Rechargeable Aqueous Zinc-Ion Batteries in MgSO<sub>4</sub>/ZnSO<sub>4</sub> Hybrid Electrolytes. *Nanomicro Lett* **2020**, *12* (1), 60.
174. Bae, J.; Park, H.; Guo, X.; Zhang, X.; Warner, J. H.; Yu, G., High-performance magnesium metal batteries via switching the passivation film into a solid electrolyte interphase. *Energy & Environmental Science* **2021**, *14* (8), 4391-4399.
175. Ming, J.; Guo, J.; Xia, C.; Wang, W.; Alshareef, H. N., Zinc-ion batteries: Materials, mechanisms, and applications. *Materials Science and Engineering: R: Reports* **2019**, *135*, 58-84.
176. Bock, C. W.; Katz, A. K.; Glusker, J. P., Hydration of Zinc Ions: A Comparison with Magnesium and Beryllium Ions. *Journal of the American Chemical Society* **1995**, *117* (13), 3754-3765.
177. Cheah, Y. L.; Aravindan, V.; Madhavi, S., Improved Elevated Temperature Performance of Al-Intercalated V<sub>2</sub>O<sub>5</sub> Electrospun Nanofibers for Lithium-Ion Batteries. *ACS Applied Materials & Interfaces* **2012**, *4* (6), 3270-3277.
178. Su, D. W.; Dou, S. X.; Wang, G. X., Hierarchical orthorhombic V<sub>2</sub>O<sub>5</sub> hollow nanospheres as high performance cathode materials for sodium-ion batteries. *Journal of Materials Chemistry A* **2014**, *2* (29), 11185-11194.
179. Liu, M.; Su, B.; Tang, Y.; Jiang, X.; Yu, A., Recent Advances in Nanostructured Vanadium Oxides and Composites for Energy Conversion. *Advanced Energy Materials* **2017**, *7* (23), 1700885.
180. Schoiswohl, J.; Surnev, S.; Netzer, F. P.; Kresse, G., Vanadium oxide nanostructures: from zero- to three-dimensional. *Journal of Physics: Condensed Matter* **2006**, *18* (4), R1-R14.
181. Wang, Y.; Meng, X.; Sun, J.; Liu, Y.; Hou, L., Recent Progress in “Water-in-Salt” Electrolytes Toward Non-lithium Based Rechargeable Batteries. *Frontiers in Chemistry* **2020**, *8*.
182. Zeng, J.; Huang, J.; Liu, J.; Xie, T.; Peng, C.; Lu, Y.; Lu, P.; Zhang, R.; Min, J., Self-assembly of single layer V<sub>2</sub>O<sub>5</sub> nanoribbon/graphene heterostructures as ultrahigh-performance cathode materials for lithium-ion batteries. *Carbon* **2019**, *154*, 24-32.
183. He, P.; Zhang, G.; Liao, X.; Yan, M.; Xu, X.; An, Q.; Liu, J.; Mai, L., Sodium Ion Stabilized Vanadium Oxide Nanowire Cathode for High-Performance Zinc-Ion Batteries. *Advanced Energy Materials* **2018**, *8* (10), 1702463.
184. Levi, E.; Gofer, Y.; Aurbach, D., On the Way to Rechargeable Mg Batteries: The Challenge of New Cathode Materials. *Chemistry of Materials* **2010**, *22* (3), 860-868.
185. Geng, H.; Cheng, M.; Wang, B.; Yang, Y.; Zhang, Y.; Li, C. C., Electronic Structure Regulation of Layered Vanadium Oxide via Interlayer Doping Strategy toward Superior High-Rate and Low-Temperature Zinc-Ion Batteries. *Advanced Functional Materials* **2020**, *30* (6), 1907684.
186. Zhu, Y.-H.; Zhang, Q.; Yang, X.; Zhao, E.-Y.; Sun, T.; Zhang, X.-B.; Wang, S.; Yu, X.-Q.; Yan, J.-M.; Jiang, Q., Reconstructed Orthorhombic V<sub>2</sub>O<sub>5</sub> Polyhedra for Fast Ion Diffusion in K-Ion Batteries. *Chem* **2019**, *5* (1), 168-179.
187. Bera, B.; Sekhar Das, P.; Bhattacharya, M.; Ghosh, S.; Mukhopadhyay, A. K.; Dey, A., Nanoscale contact resistance of V<sub>2</sub>O<sub>5</sub> xerogel films developed by nanostructured powder. *Journal of Physics D: Applied Physics* **2016**, *49* (8), 085303.
188. Ye, G.; Gong, Y.; Keyshar, K.; Husain, E. A. M.; Brunetto, G.; Yang, S.; Vajtai, R.; Ajayan, P. M., 3D Reduced Graphene Oxide Coated V<sub>2</sub>O<sub>5</sub> Nanoribbon Scaffolds for High-

- Capacity Supercapacitor Electrodes. *Particle & Particle Systems Characterization* **2015**, *32* (8), 817-821.
189. Castriota, M.; Cazzanelli, E.; Fasanella, A.; Teeters, D., Electrical conductivity and Raman characterization of V<sub>2</sub>O<sub>5</sub> grown by sol-gel technique inside nanoscale pores. *Thin Solid Films* **2014**, *553*, 127-131.
  190. Weimer, M. S.; Kim, I. S.; Guo, P.; Schaller, R. D.; Martinson, A. B. F.; Hock, A. S., Oxidation State Discrimination in the Atomic Layer Deposition of Vanadium Oxides. *Chemistry of Materials* **2017**, *29* (15), 6238-6244.
  191. Avansi Jr, W.; Ribeiro, C.; Leite, E. R.; Mastelaro, V. R., Vanadium Pentoxide Nanostructures: An Effective Control of Morphology and Crystal Structure in Hydrothermal Conditions. *Crystal Growth & Design* **2009**, *9* (8), 3626-3631.
  192. Zhu, J.; Shen, H.; Shi, X.; Yang, F.; Hu, X.; Zhou, W.; Yang, H.; Gu, M., Revealing the Chemical and Structural Evolution of V<sub>2</sub>O<sub>5</sub> Nanoribbons in Lithium-Ion Batteries Using in Situ Transmission Electron Microscopy. *Analytical Chemistry* **2019**, *91* (17), 11055-11062.
  193. Moretti, A.; Passerini, S., Bilayered Nanostructured V<sub>2</sub>O<sub>5</sub>·nH<sub>2</sub>O for Metal Batteries. *Advanced Energy Materials* **2016**, *6* (23), 1600868.
  194. Stobinski, L.; Lesiak, B.; Malolepszy, A.; Mazurkiewicz, M.; Mierzwa, B.; Zemek, J.; Jiricek, P.; Bieloshapka, I., Graphene oxide and reduced graphene oxide studied by the XRD, TEM and electron spectroscopy methods. *Journal of Electron Spectroscopy and Related Phenomena* **2014**, *195*, 145-154.
  195. Choi, S.; Kim, C.; Suh, J. M.; Jang, H. W., Reduced graphene oxide-based materials for electrochemical energy conversion reactions. *Carbon Energy* **2019**, *1* (1), 85-108.
  196. Zhao, X.; Yan, Y.; Mao, L.; Fu, M.; Zhao, H.; Sun, L.; Xiao, Y.; Dong, G., A relationship between the V<sup>4+</sup>/V<sup>5+</sup> ratio and the surface dispersion, surface acidity, and redox performance of V<sub>2</sub>O<sub>5</sub>-WO<sub>3</sub>/TiO<sub>2</sub> SCR catalysts. *RSC Advances* **2018**, *8* (54), 31081-31093.
  197. Deng, X.; Xu, Y.; An, Q.; Xiong, F.; Tan, S.; Wu, L.; Mai, L., Manganese ion pre-intercalated hydrated vanadium oxide as a high-performance cathode for magnesium ion batteries. *Journal of Materials Chemistry A* **2019**, *7* (17), 10644-10650.
  198. Yang, Y.; Tang, Y.; Liang, S.; Wu, Z.; Fang, G.; Cao, X.; Wang, C.; Lin, T.; Pan, A.; Zhou, J., Transition metal ion-preintercalated V<sub>2</sub>O<sub>5</sub> as high-performance aqueous zinc-ion battery cathode with broad temperature adaptability. *Nano Energy* **2019**, *61*, 617-625.
  199. Benveniste, G.; Rallo, H.; Canals Casals, L.; Merino, A.; Amante, B., Comparison of the state of Lithium-Sulphur and lithium-ion batteries applied to electromobility. *Journal of Environmental Management* **2018**, *226*, 1-12.
  200. Manthiram, A.; Chung, S.-H.; Zu, C., Lithium-Sulfur Batteries: Progress and Prospects. *Advanced Materials* **2015**, *27* (12), 1980-2006.
  201. Hu, Q.; Wang, B.; Lu, J.; Zhang, C.; Yang, C.; Chang, S.; Dong, H.; Wu, C.; Hong, Y.; Zhang, L., Promoting Electrocatalytic Conversion of Polysulfide using Cobalt Disulfide Nanocrystals for Lithium Sulfur Batteries. *The Journal of Physical Chemistry C* **2020**, *124* (39), 21319-21328.
  202. Dong, C.; Gao, W.; Jin, B.; Jiang, Q., Advances in Cathode Materials for High-Performance Lithium-Sulfur Batteries. *iScience* **2018**, *6*, 151-198.
  203. Song, J.; Yu, Z.; Gordin, M. L.; Wang, D., Advanced Sulfur Cathode Enabled by Highly Crumpled Nitrogen-Doped Graphene Sheets for High-Energy-Density Lithium-Sulfur Batteries. *Nano Letters* **2016**, *16* (2), 864-870.

204. Tang, X.; Xu, Z.; Sun, Z.; Zhou, J.; Wu, X.; Lin, H.; Rong, J.; Zhuo, S.; Li, F., Factors of Kinetics Processes in Lithium–Sulfur Reactions. *Energy Technology* **2019**, *7* (12), 1900574.
205. Manthiram, A.; Fu, Y.; Chung, S.-H.; Zu, C.; Su, Y.-S., Rechargeable Lithium–Sulfur Batteries. *Chemical Reviews* **2014**, *114* (23), 11751-11787.
206. Liu, J.; Lu, D.; Zheng, J.; Yan, P.; Wang, B.; Sun, X.; Shao, Y.; Wang, C.; Xiao, J.; Zhang, J.-G.; Liu, J., Minimizing Polysulfide Shuttle Effect in Lithium-Ion Sulfur Batteries by Anode Surface Passivation. *ACS Applied Materials & Interfaces* **2018**, *10* (26), 21965-21972.
207. Pang, Q.; Liang, X.; Kwok, C. Y.; Nazar, L. F., Advances in lithium–sulfur batteries based on multifunctional cathodes and electrolytes. *Nature Energy* **2016**, *1* (9), 16132.
208. Su, Y.-S.; Manthiram, A., A new approach to improve cycle performance of rechargeable lithium–sulfur batteries by inserting a free-standing MWCNT interlayer. *Chemical Communications* **2012**, *48* (70), 8817-8819.
209. He, J.; Bhargava, A.; Yaghoobnejad Asl, H.; Chen, Y.; Manthiram, A., 1T'-ReS<sub>2</sub> Nanosheets In Situ Grown on Carbon Nanotubes as a Highly Efficient Polysulfide Electrocatalyst for Stable Li–S Batteries. *Advanced Energy Materials* **2020**, *10* (23), 2001017.
210. Hencz, L.; Chen, H.; Ling, H. Y.; Wang, Y.; Lai, C.; Zhao, H.; Zhang, S., Housing Sulfur in Polymer Composite Frameworks for Li–S Batteries. *Nanomicro Lett* **2019**, *11* (1), 17.
211. Wang, J.; Yue, K.; Zhu, X.; Wang, K. L.; Duan, L., C–S@PANI composite with a polymer spherical network structure for high performance lithium–sulfur batteries. *Physical Chemistry Chemical Physics* **2016**, *18* (1), 261-266.
212. Liu, X.; Wang, S.; Wang, A.; Wang, Z.; Chen, J.; Zeng, Q.; Chen, P.; Liu, W.; Li, Z.; Zhang, L., A new cathode material synthesized by a thiol-modified metal–organic framework (MOF) covalently connecting sulfur for superior long-cycling stability in lithium–sulfur batteries. *Journal of Materials Chemistry A* **2019**, *7* (42), 24515-24523.
213. Jeon, T.; Lee, Y. C.; Hwang, J.-Y.; Choi, B. C.; Lee, S.; Jung, S. C., Strong lithium-polysulfide anchoring effect of amorphous carbon for lithium–sulfur batteries. *Current Applied Physics* **2021**, *22*, 94-103.
214. Huang, X.; Wang, Z.; Knibbe, R.; Luo, B.; Ahad, S. A.; Sun, D.; Wang, L., Cyclic Voltammetry in Lithium–Sulfur Batteries—Challenges and Opportunities. *Energy Technology* **2019**, *7* (8), 1801001.

## Appendix A - Supplementary Information for Chapter 3

Reproduced from [Muthukumar, K.; Leban, L.; Sekar, A.; Elangovan, A.; Sarkar, N.; Li, J., Tuning the defects in MoS<sub>2</sub>/reduced graphene oxide 2D hybrid materials for optimizing battery performance. *Sustainable Energy & Fuels* **2021**, 5 (16), 4002-4014] with permission from the Royal Society of Chemistry

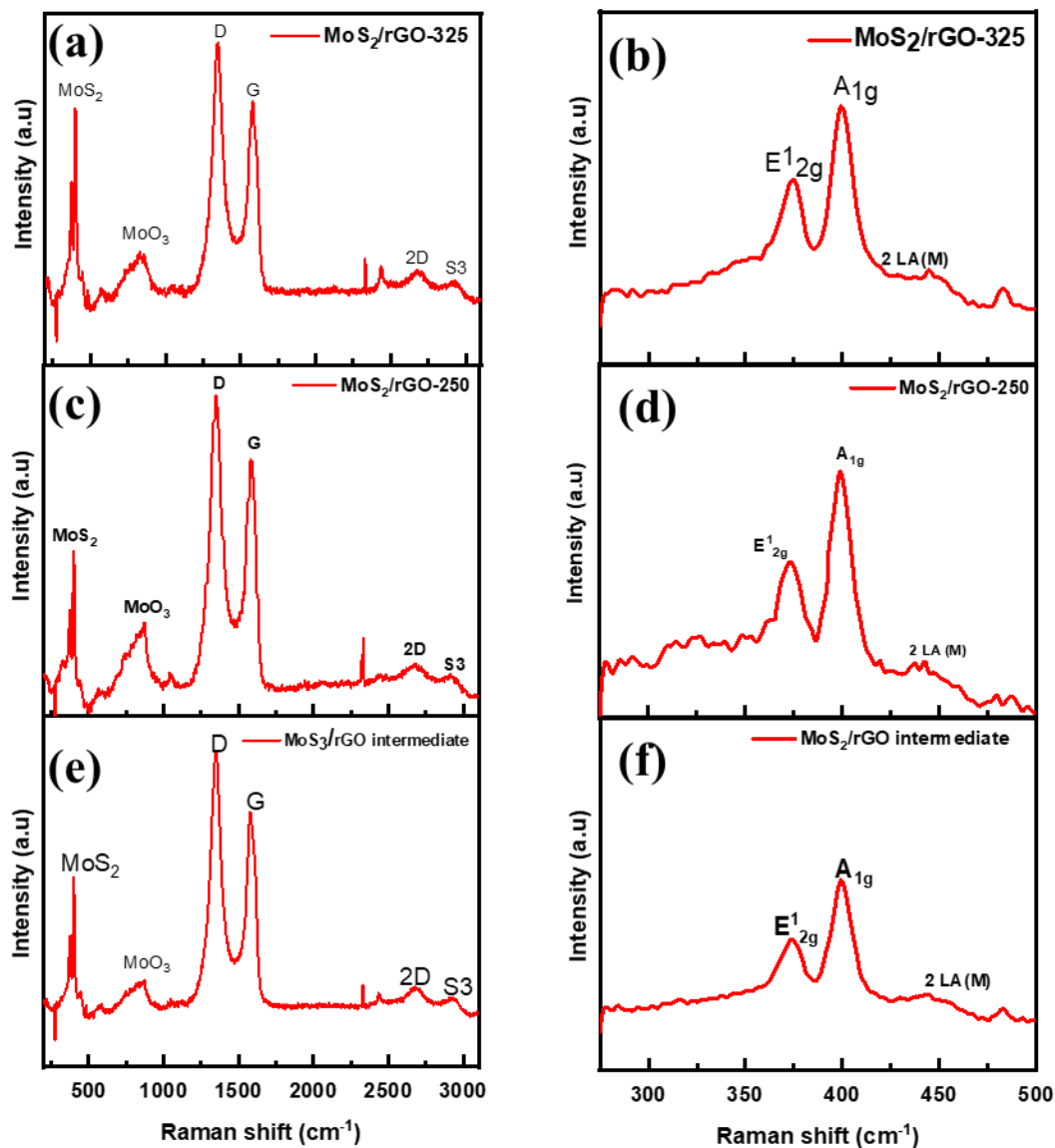


**Figure A.1.** The full scale and expanded region of Raman spectra of (a, b) MoS<sub>2</sub>/rGO-325, (c, d) MoS<sub>2</sub>/rGO-250 and (e, f) MoS<sub>3</sub>/rGO intermediate product.

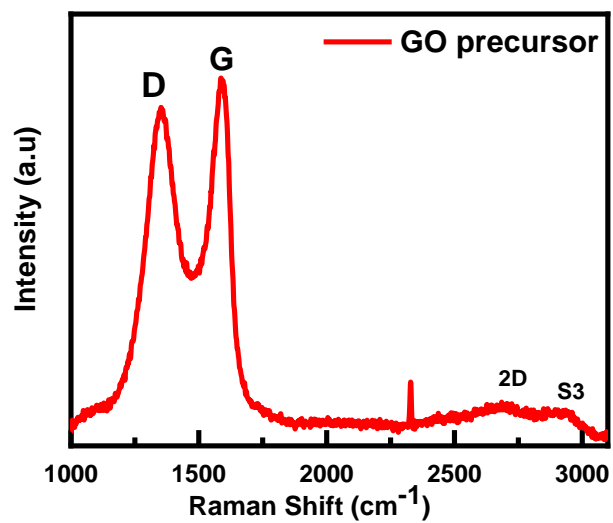


**Figure A.2.** Raman Spectra of graphene oxide (GO) precursor.

**Table A.1.** Raman Analysis of GO precursor and MoS<sub>2</sub>/rGO

Sample	$I_D/I_G$	$I_{S3}/I_{2D}$
GO Precursor	0.9	1.7
MoS <sub>3</sub> /rGO-intermediate	1.3	0.3
MoS <sub>2</sub> /rGO-250	1.3	0.3
MoS <sub>2</sub> /rGO-325	1.3	0.4
MoS <sub>2</sub> /rGO-600	1.3	0.4

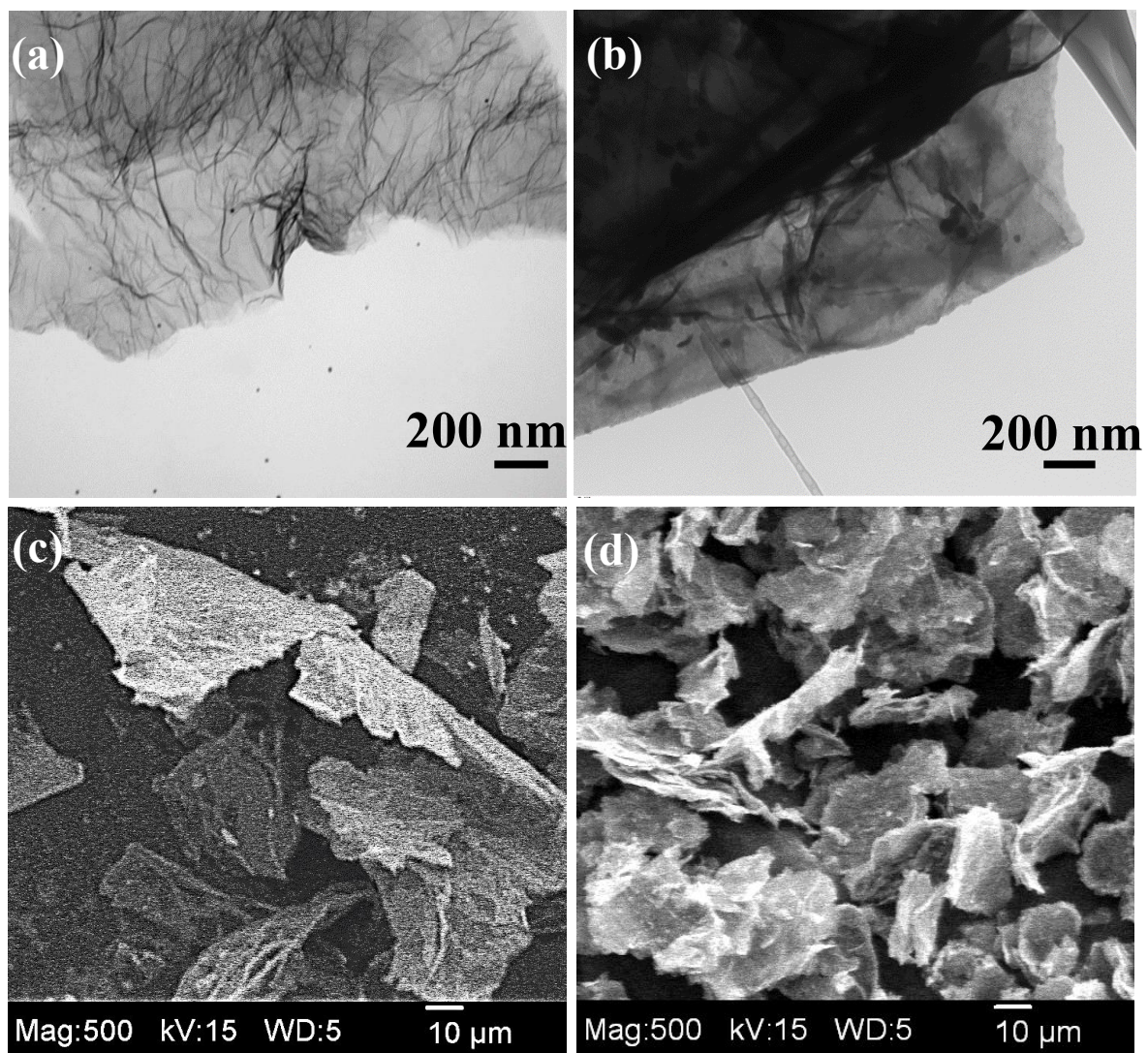


**Figure A.3.** TEM images of (a) bare rGO nanosheets and (b) the MoS<sub>3</sub>/rGO intermediate. (c) and (d): SEM images of these two samples, respectively. The bare rGO sample was prepared with microwave irradiation in absence of ATM precursors before subjected to thermal annealing at 600°C in 3% H<sub>2</sub> and 97% Ar. The MoS<sub>3</sub>/rGO intermediate was obtained after the microwave irradiation in presence of ATM precursors but was not subjected to the thermal annealing.

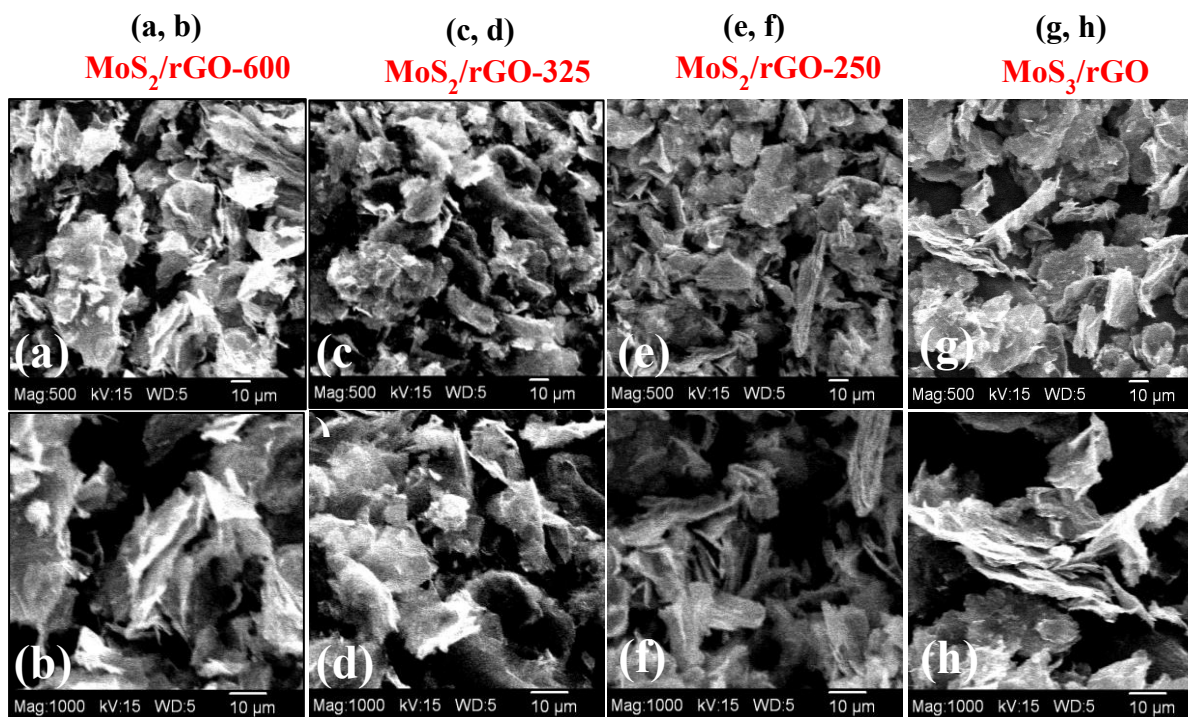


**Figure A.4.** Low- and higher-magnification FESEM images of (a, b) MoS<sub>2</sub>/rGO-600, (c, d) MoS<sub>2</sub>/rGO-325, (e, f) MoS<sub>2</sub>/rGO-250, and (g, h) MoS<sub>3</sub>/rGO-intermediate.

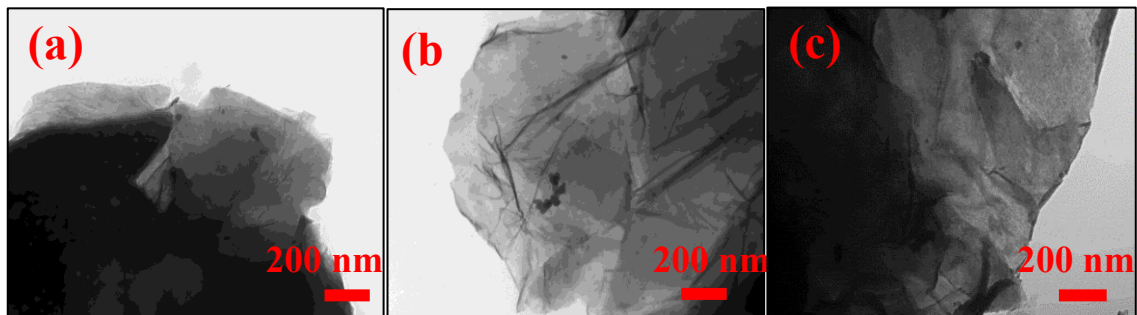


**Figure A.5.** TEM images of (a) MoS<sub>2</sub>/rGO-250, (b) MoS<sub>2</sub>/rGO-325, and (c) MoS<sub>2</sub>/rGO-600.

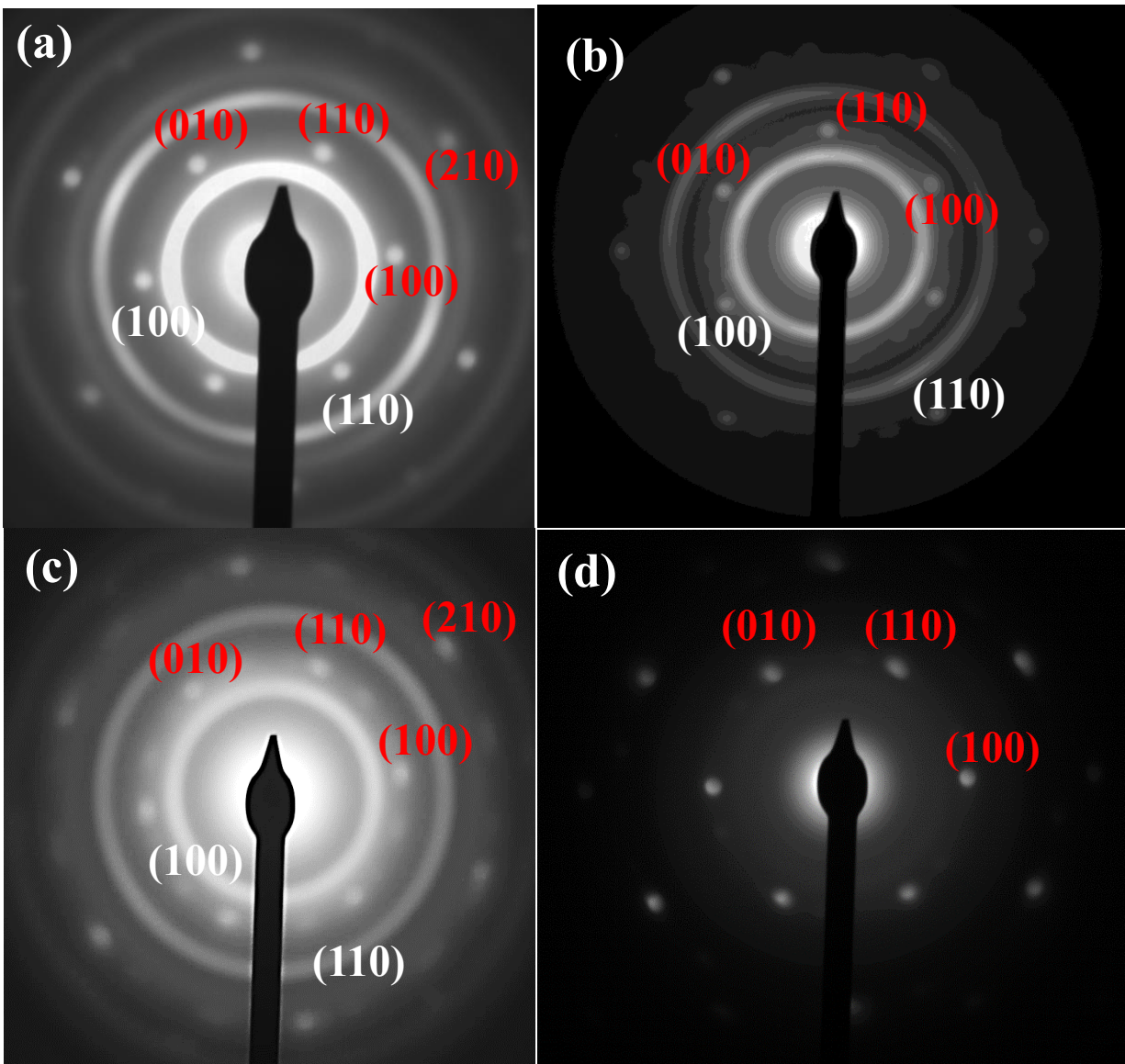
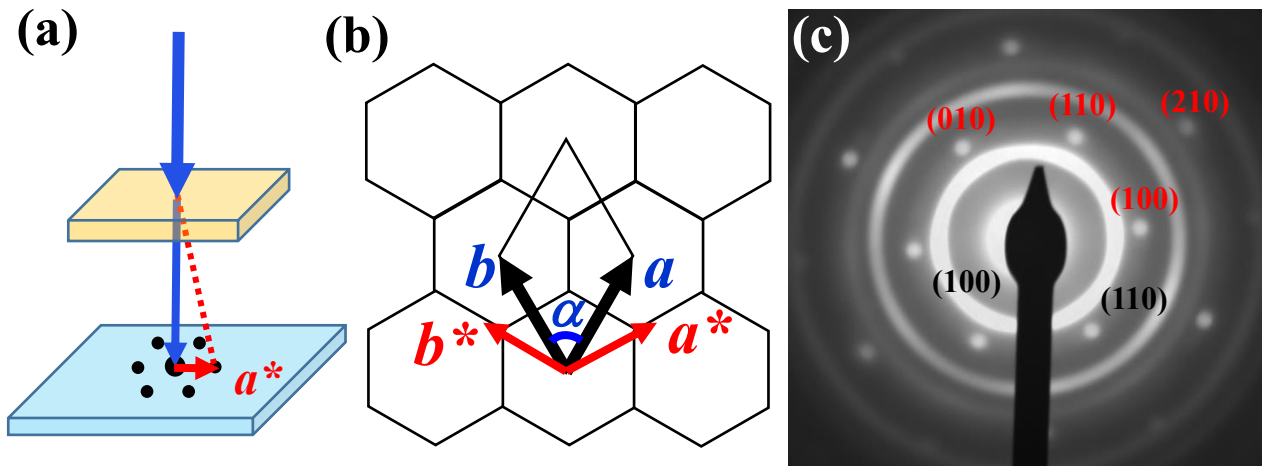


**Figure A.6.** SAED patterns of (a) MoS<sub>2</sub>/rGO-600, (b) MoS<sub>2</sub>/rGO-325, (e) MoS<sub>2</sub>/rGO-250, and (d) MoS<sub>3</sub>/rGO intermediate. The red-colored indices at the top indicate the isolated 2D electron diffraction spots with the six-fold symmetry from the rGO nanosheets, while the white indices at the bottom indicate the continuous rings of 2D powder electron diffraction from MoS<sub>2</sub> nanopatches with random rotational orientations in the rGO plane.



- (d)**
- **For 2D crystals with a hexagonal lattice:**  
 $a = b, \alpha = 60^\circ$   
 $a$  - real space lattice;  $a^*$  - reciprocal space lattice  
 $a \cdot a^* = 2\pi$  i.e.  $a \times a^* \times \cos 30^\circ = 2\pi$   
 $a^* = 2\pi / (a \times \cos 30^\circ)$  or  $a = 2\pi / (a^* \times \cos 30^\circ)$
  - **For isolated SAED spots from rGO:**  
rGO:  $a = 2.46 \text{ \AA} \Rightarrow a^* = 2.948 \text{ \AA}^{-1}$
  - **Use  $a^*$  of rGO to calibrate the  $a^*$  of the continuous rings from  $\text{MoS}_2$ :**  
(100) ring of  $\text{MoS}_2$ ;  $a^* = 2.29 \text{ \AA}^{-1} \Rightarrow a = 3.17 \text{ \AA}$

**Figure A.7.** (a) Schematic illustration of the SAED with the electron beam perpendicular to the 2D crystal plane. (b) The relationship of the real space 2D hexagonal lattice  $a$  and  $b$  and the reciprocal diffraction lattice ( $a^*$  and  $b^*$ ). (c) The SAED pattern of  $\text{MoS}_2/\text{rGO-600}$ . (d) The procedure to derive the  $\text{MoS}_2$  lattice in reference to the sharp hexagonal SAED pattern of the 2D monocrystalline rGO nanosheets.

**Table A.2.** The parameters derived from deconvolution of Mo 3d and S 2p XPS spectra in section 3.3.4.

		MoS <sub>3</sub> /rGO intermediate		MoS <sub>2</sub> /rGO-250		MoS <sub>2</sub> /rGO-325		MoS <sub>2</sub> /rGO-600	
		B.E. (eV)	Atomic % in the same element	B.E. (eV)	Atomic % in the same element	B.E. (eV)	Atomic % in the same element	B.E. (eV)	Atomic % in the same element
Mo <sup>4+</sup>	3d <sub>5/2</sub>	229.08	28.58	229.03	83.08	229.12	66.41	229.28	68.24
	3d <sub>3/2</sub>	232.21		232.16		232.25		232.41	
Mo <sup>5+</sup>	3d <sub>5/2</sub>	229.32	19.39	230.52	9.44	Mo <sup>5+</sup> is not present in this sample		Mo <sup>5+</sup> is not present in this sample	
	3d <sub>3/2</sub>	232.45		233.65					
Mo <sup>6+</sup>	3d <sub>5/2</sub>	232.11	52.03	232.68	7.48	231.90	33.58	232.18	31.75
	3d <sub>3/2</sub>	235.24		235.81		235.03		235.31	
S <sup>2-</sup>	2p <sub>3/2</sub>	162.59	45.99	161.68	46.46	161.93	86.50	162.09	100
	2p <sub>1/2</sub>	163.78		162.47		163.21		163.27	
S <sub>2</sub> <sup>2-</sup>	2p <sub>3/2</sub>	164.76	54.01	162.94	53.54	163.41	13.50		
	2p <sub>1/2</sub>	165.79		164.10		164.58			
Mo : S		1:2.4		1:2.9		1:2.3		1:1.9	

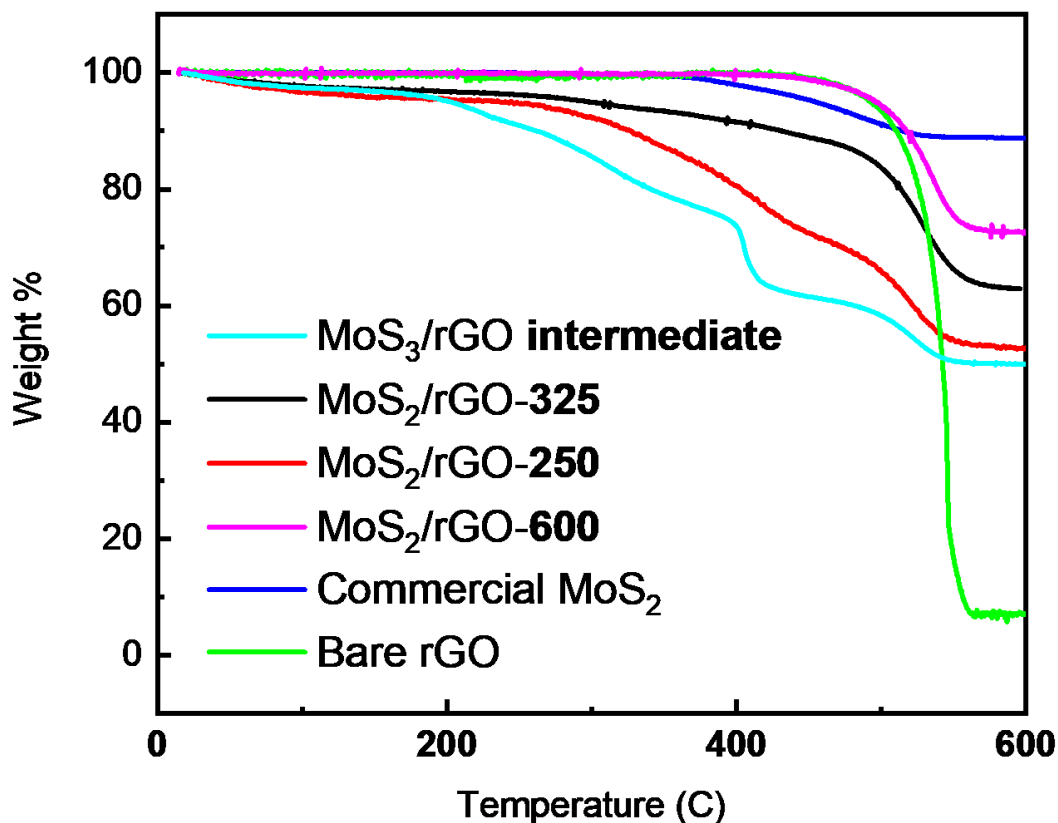


**Figure A.8.** Thermogravimetric analyses of various hybrid materials and control samples (commercial MoS<sub>2</sub> powder and bare rGO synthesized at the same conditions as MoS<sub>2</sub>/rGO-600 but without presence of ATM precursors)

**Determination of weight % of MoS<sub>2</sub> in MoS<sub>2</sub>/rGO-600:**

1. Bulk MoS<sub>2</sub> shows gradual weight loss of 10.1% from 370 °C to 600°C due to the conversion of MoS<sub>2</sub> to MoO<sub>3</sub>.
2. Control rGO shows a steep weight loss of 93.36% at 420 °C due to the conversion of rGO to graphitic carbon.
3. Based on the above-mentioned weight loss of control samples
4. Weight loss from 370 °C till 600 °C = Weight loss of MoS<sub>2</sub>+Weight loss of rGO  

$$= (\text{Weight\% of MoS}_2) * 10.1\% + (1 - \text{Weight\% of MoS}_2) * 93.36\%$$
5. Weight% of rGO = 1-Weight% of MoS<sub>2</sub>
6.  $(99.91\% - 72.57\%) = (\text{Weight \% of MoS}_2) * 10.1\% + (1 - \text{Weight \% of MoS}_2) * 93.36\%$

**Table A.3.** Elemental Analysis of MoS<sub>x</sub>/rGO

Samples	wt% of N	wt% of C	wt% of H	wt% of O	wt% of S	wt% of Mo <sup>a</sup>	wt% of MoS <sub>x</sub> <sup>b</sup>	wt% of rGO <sup>c</sup>	at% of Mo <sup>d</sup>	at% of S <sup>d</sup>	Mo:S <sup>e</sup>
MoS <sub>2</sub> /rGO-600	0.30	19.98	0.15	1.17	33.52	44.88	78.40	21.15	13.51	30.69	1:2.3
MoS <sub>2</sub> /rGO-325	0.62	22.46	0.31	4.62	31.17	40.82	71.99	27.08	9.58	21.60	1:2.3
MoS <sub>2</sub> /rGO-250	1.07	18.62	0.31	5.14	38.56	36.30	74.86	23.76	9.90	31.25	1:3.2
MoS <sub>3</sub> /rGO-intermediate	1.82	20.31	0.99	11.07	35.38	30.43	65.81	31.38	6.50	22.36	1:3.4

**Note:**

**Elements:** N - Nitrogen; C - Carbon; H - Hydrogen; O - Oxygen; S - Sulfur; Mo - Molybdenum.

<sup>a</sup> Weight percentage of Mo = 100 % - (wt% of C + wt% of N + wt% of H + wt% of O + wt% of S)

<sup>b</sup> Weight percentage of MoS<sub>x</sub> = wt% of Mo + wt% of S

<sup>c</sup> Weight percentage of rGO = wt% of C + wt% of O

<sup>d</sup> at% of x =  $\frac{\text{wt\% of x/AW of X}}{\sum_i^n (\text{wt\% of i/AW of i})}$ , AW = atomic weight

<sup>e</sup> Atomic ratio of Mo:S =  $\frac{\text{at\% of Mo}}{\text{at\% of S}}$

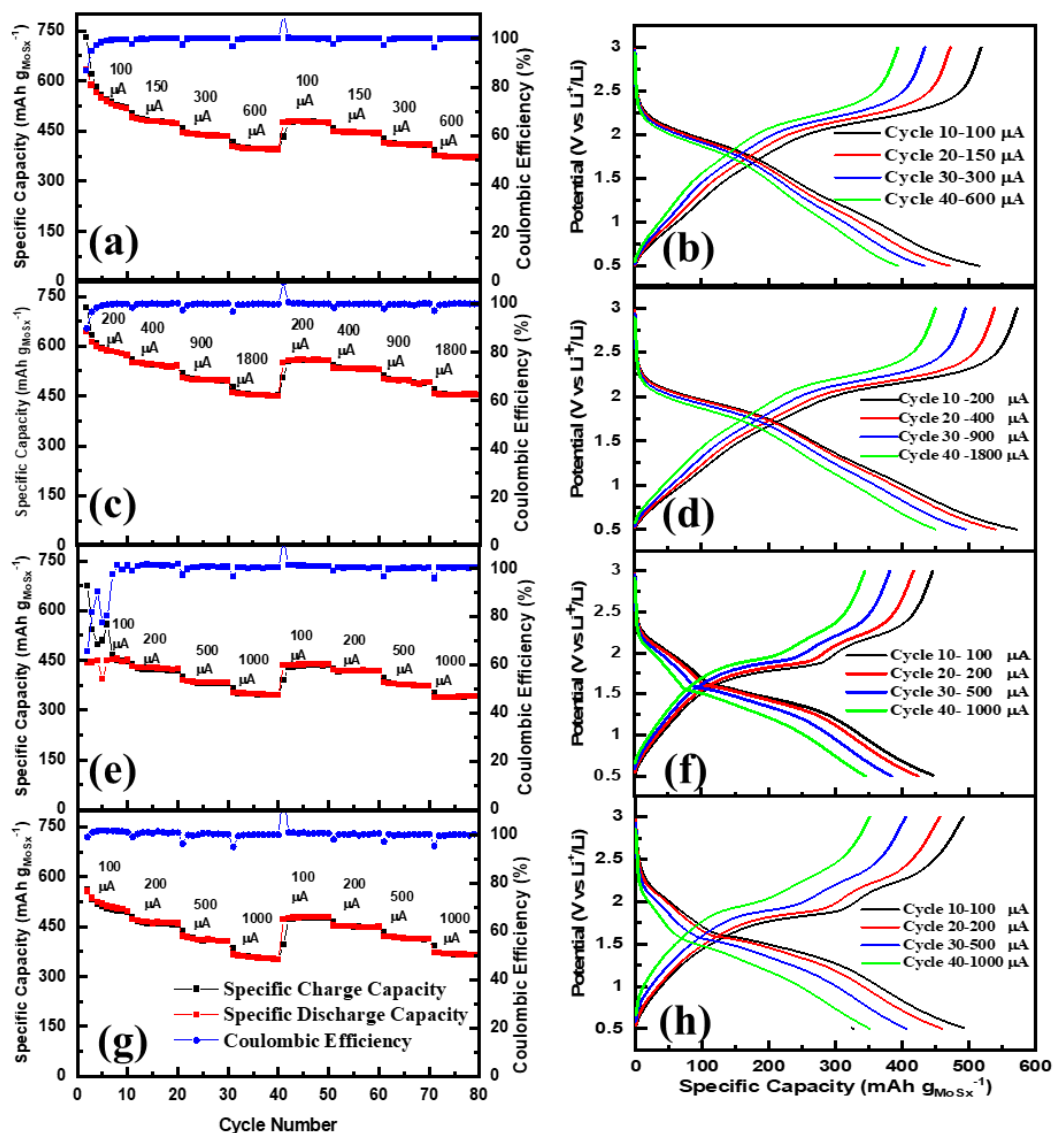


**Figure A.9.** Rate Performance at varied current rates and representative galvanostatic charge/discharge curves of Li-ion half cells with the cathode made of (a, b) MoS<sub>2</sub>/rGO-600, (c, d) MoS<sub>2</sub>/rGO-325 (1.44 mg), (e, f) MoS<sub>2</sub>/rGO-250 (0.82 mg) and (g, h) MoS<sub>3</sub>/rGO intermediate material (1.76 mg). Panels (a), (c) and (e) have the same legend as panel (g).

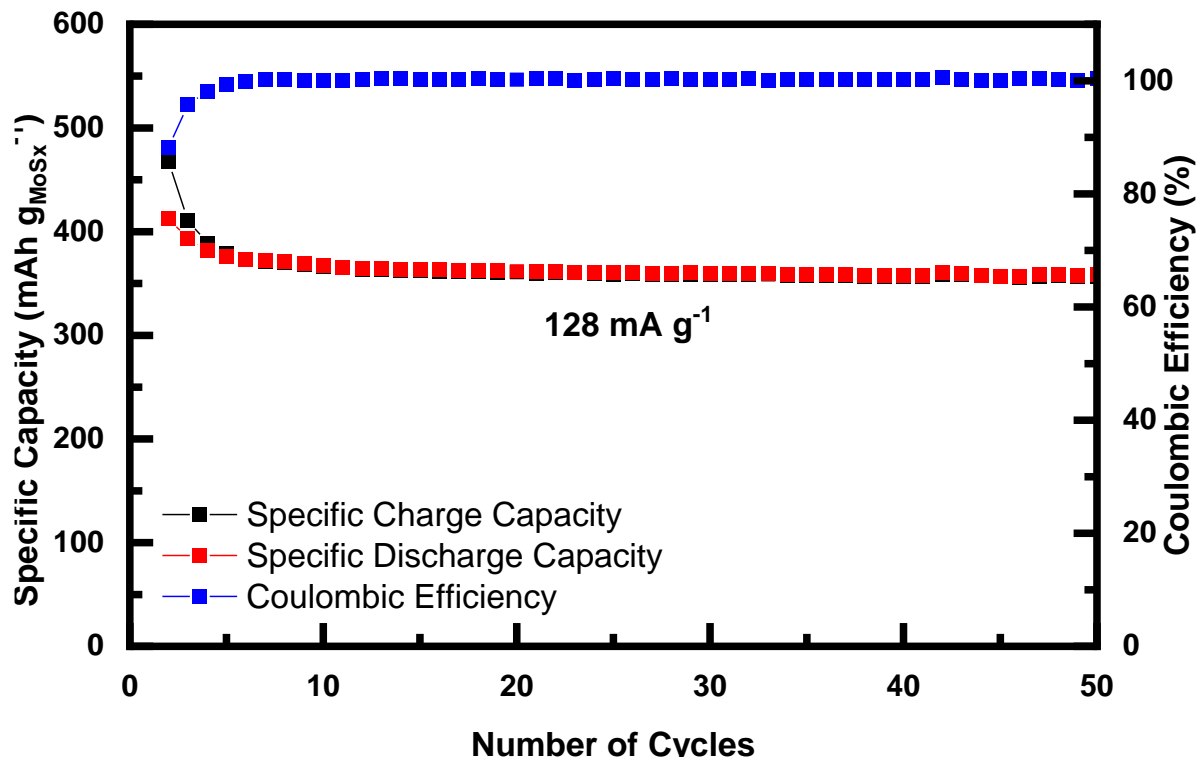


Figure A.10. Long term stability test of Li ion half cells with anode made of MoS<sub>2</sub>/rGO-600.

**Calculation of the Coulombic efficiency of battery tests:**

$$\text{Coulombic Efficiency of MoS}_x \text{ in LIB} = \frac{\text{Specific Discharge Capacity}}{\text{Specific Charge Capacity}} * 100 \rightarrow (1)$$

**Calculation of the specific capacity of MoS<sub>x</sub>/rGO samples in battery tests:**

$$\text{Specific capacity of MoS}_x = \frac{\text{measured capacity}}{\text{Total Mass of hybrid x (wt\% of MoS}_x)} \rightarrow (2)$$

**Discussion on rGO contribution to the Li-ion storage capacity:**

The small contribution from rGO can be deducted from the specific capacity. As shown in Table S3, the stabilized specific capacity at 100  $\mu$ A charge/discharge current is about 73, 86, 111 and 53 mAh g<sub>rGO</sub><sup>-1</sup> for the corresponding control samples rGO-600, rGO-325, rGO-250 and rGO-intermediate. After deducting these contributions based on the wt% of rGO by equations below Table S3, the specific capacity attributed to MoS<sub>x</sub> is adjusted to 499, 540, 411 and 467 mAh g<sub>MoS<sub>x</sub></sub><sup>-1</sup> for MoS<sub>2</sub>/rGO-600, MoS<sub>2</sub>/rGO-325, MoS<sub>2</sub>/rGO-250 and MoS<sub>3</sub>/rGO-intermediate, respectively. The contribution by rGO is only 3.9%, 5.7%, 8.0% and 5.1% in MoS<sub>2</sub>/rGO-600, MoS<sub>2</sub>/rGO-325, MoS<sub>2</sub>/rGO-250 and MoS<sub>3</sub>/rGO-intermediate, respectively. These small corrections are insignificant to the conclusions in the main manuscript.

**Table A.4.** Estimation of contribution to the specific capacity by rGO and MoS<sub>x</sub> in LIB.

Sample	Specific Capacity of MoS <sub>x</sub> (mAh/g <sub>MoS<sub>x</sub></sub> ) <sup>a</sup>	Specific Capacity of rGO (mAh/g <sub>rGO</sub> ) <sup>b</sup>	(wt% of rGO / wt% of MoS <sub>x</sub> ) <sup>c</sup>	Corrected Specific Capacity <sup>d</sup> (mAh/g <sub>MoS<sub>x</sub></sub> )	Relative Contribution of rGO <sup>e</sup>
MoS <sub>2</sub> /rGO-600	519	73	0.27	499	3.9
MoS <sub>2</sub> /rGO-325	573	86	0.38	540	5.7
MoS <sub>2</sub> /rGO-250	446	111	0.32	411	8.0
MoS <sub>3</sub> /rGO-intermediate	492	53	0.48	467	5.1

**Note:**

<sup>a</sup> Based on the 10<sup>th</sup> cycle at 100 mA in Figure S8.

<sup>b</sup> Based on the 10<sup>th</sup> cycle at 100 mA in Figure S10.

<sup>c</sup> Based on the values from Table S2.

<sup>d</sup> Corrected specific capacity = (Specific capacity of MoS<sub>x</sub>) - [(Specific capacity of rGO) \* ( $\frac{\text{wt\% of rGO}}{\text{wt\% of MoS}_x}$ )]

<sup>e</sup> Relative contribution of rGO =  $\frac{\text{Specific Capacity of MoS}_x - \text{Corrected Specific capacity}}{\text{Specific Capacity of MoS}_x} * 100$

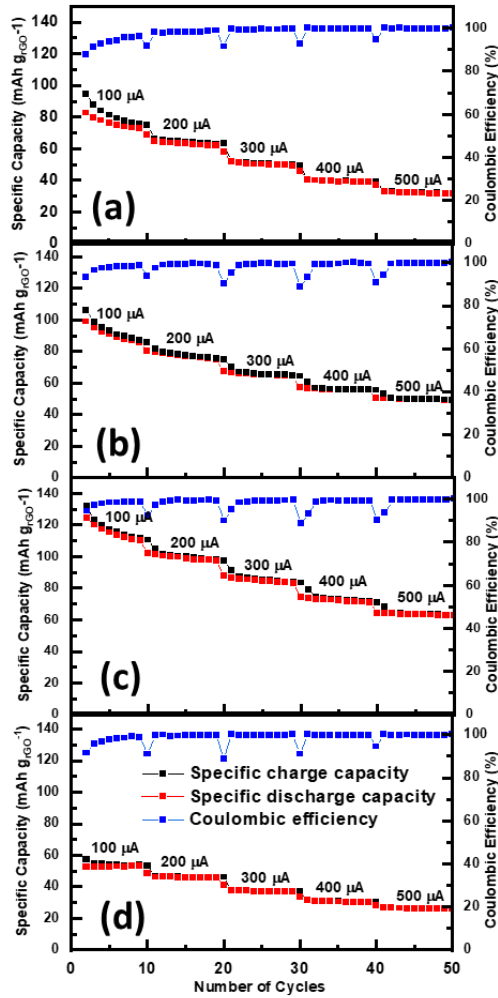


**Figure A.11.** Rate performance test of Li-ion battery half cells with the cathode made of (a) control rGO-600 (1.13 mg), (b) control rGO-325 (2.0 mg), (c) control rGO-250 (1.03 mg) and (d) control rGO-intermediate (1.25 mg). Panels (a), (b) and (c) follow the same legend as panel (d).

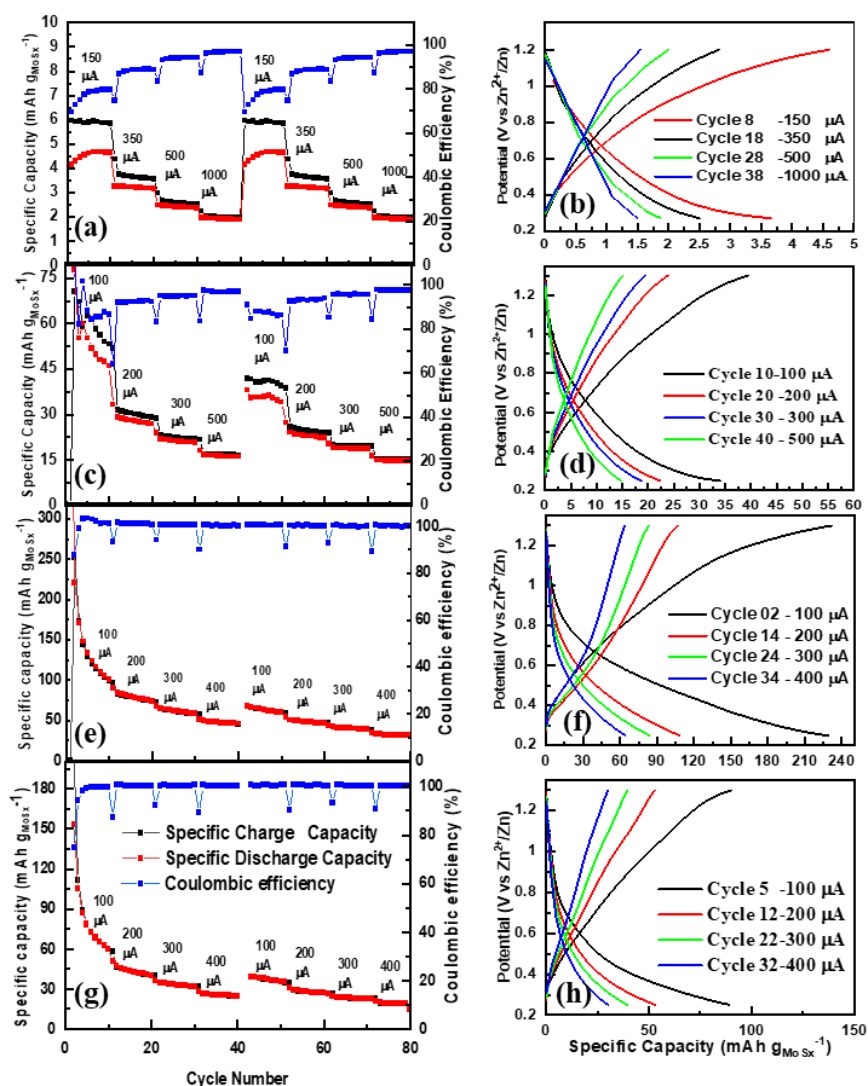


**Figure A.12.** Galvanostatic charge-discharge curves and the rate performance of Zn-ion battery half-cells with the cathode made of (a, b) MoS<sub>2</sub>/rGO-600 (0.87 mg), (c, d) MoS<sub>2</sub>/rGO-325 (1.36 mg), (e, f) MoS<sub>2</sub>/rGO-250 (1.28 mg), and (g, h) MoS<sub>3</sub>/rGO-intermediate hybrid material (0.88 mg). Panels (a), (c) and (e) follow same legend as panel (g).

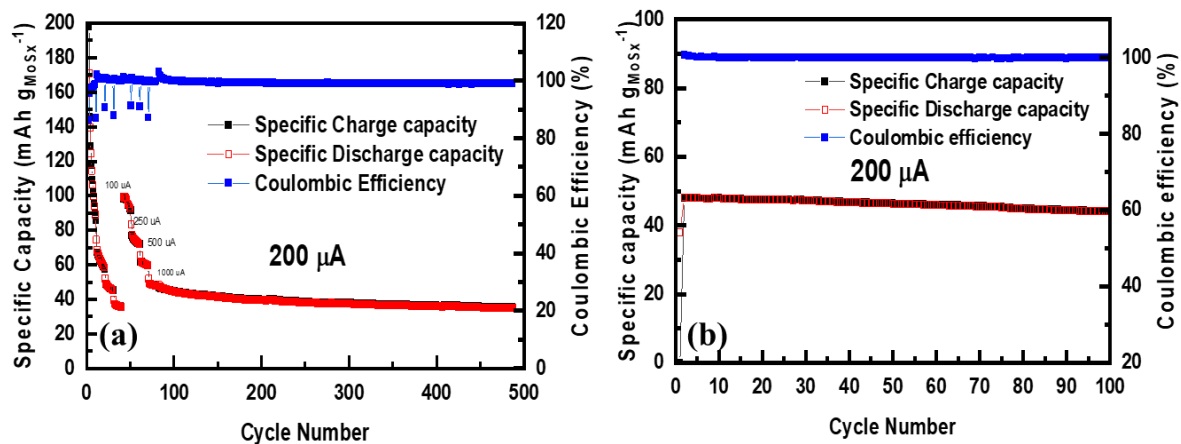


**Figure A.13.** The cycle stability of Zn-ion battery half cells with the cathode made of (a) MoS<sub>2</sub>/rGO-250 (2.16 mg) and (b) MoS<sub>3</sub>/rGO-intermediate (0.88 mg). The charge/discharge was carried out at 0.25 – 1.30 V vs Zn<sup>2+</sup>/Zn.

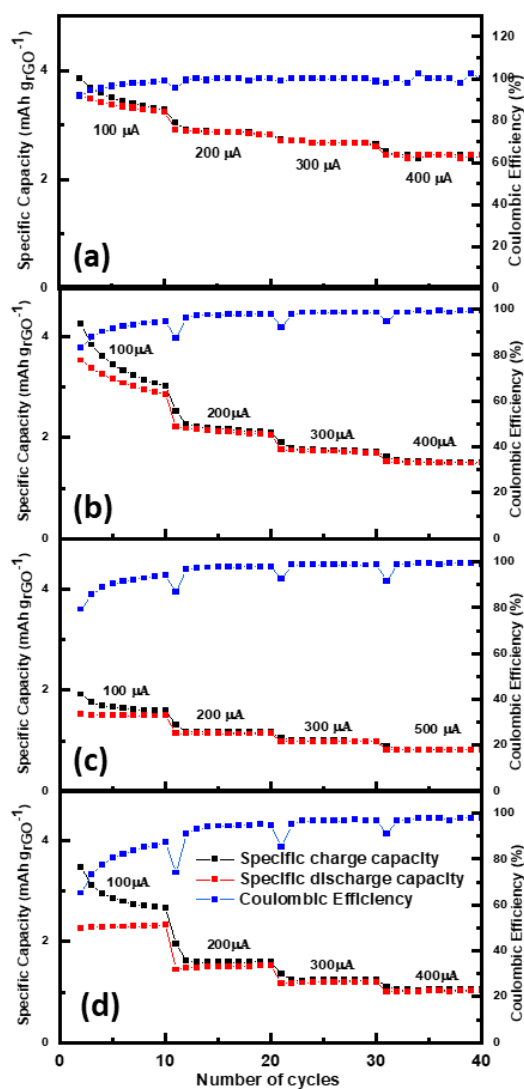


**Figure A.14.** Rate performance test of Zn ion battery half cells with the cathode made of (a) control rGO-600 (1.38 mg) (b) control rGO-325 (2.0 mg) (c) control sample-250 (0.90 mg) (d) control rGO-intermediate (1.50 mg). Panels (a), (b) and (c) follow same legend as panel (d).





## Appendix B - Supplementary Information for Chapter 4

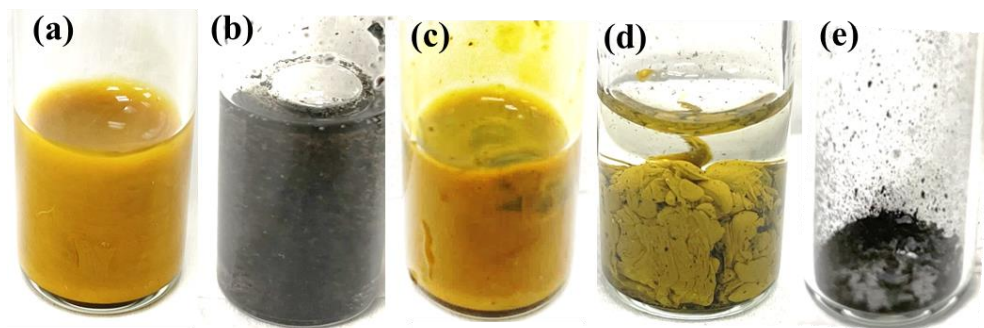


**Figure B.1.** The optical images of the homogeneous aqueous suspensions (in DI water) of (a)  $V_2O_5$  NRs, (b) GO precursor and (c)  $V_2O_5$  NRs and GO mixture. (d) The optical image of a gel-like precipitate after adding divalent cations (such as  $Zn^{2+}$  or  $Mn^{2+}$ ) into the mixed suspension of  $V_2O_5$  NRs and GO during the coprecipitation process. (e) The optical image of the dried co-precipitated hybrids, i.e., M- $V_2O_5$  NR/GO.

**Table B.1.** Measured zeta potential values of  $V_2O_5$  NRs and control GO precursors

Samples	Measure Zeta potential (mV)
$V_2O_5$ NRs	-32.16
Control GO	-31.55

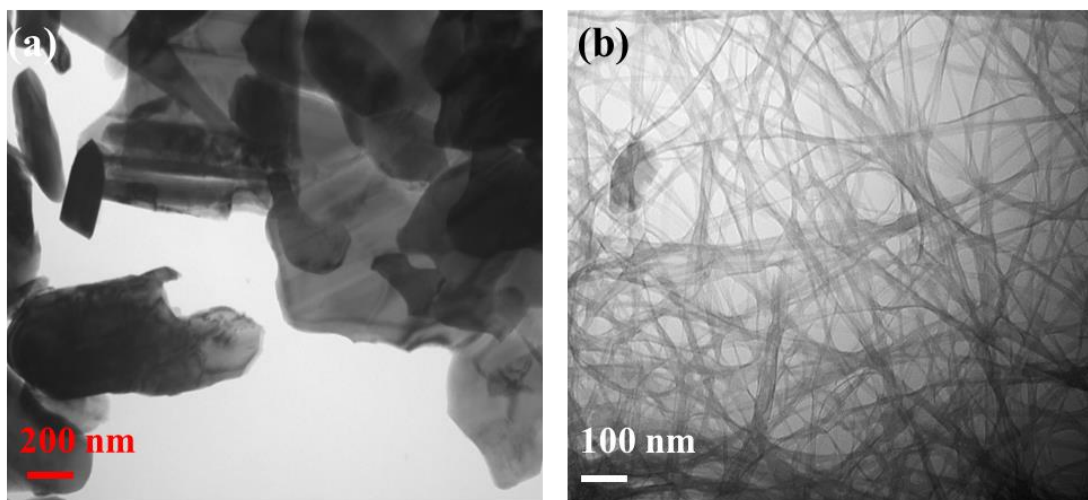


**Figure B.2.** TEM images of (a) bulk V<sub>2</sub>O<sub>5</sub> and (b) as-exfoliated V<sub>2</sub>O<sub>5</sub> nanoribbons.

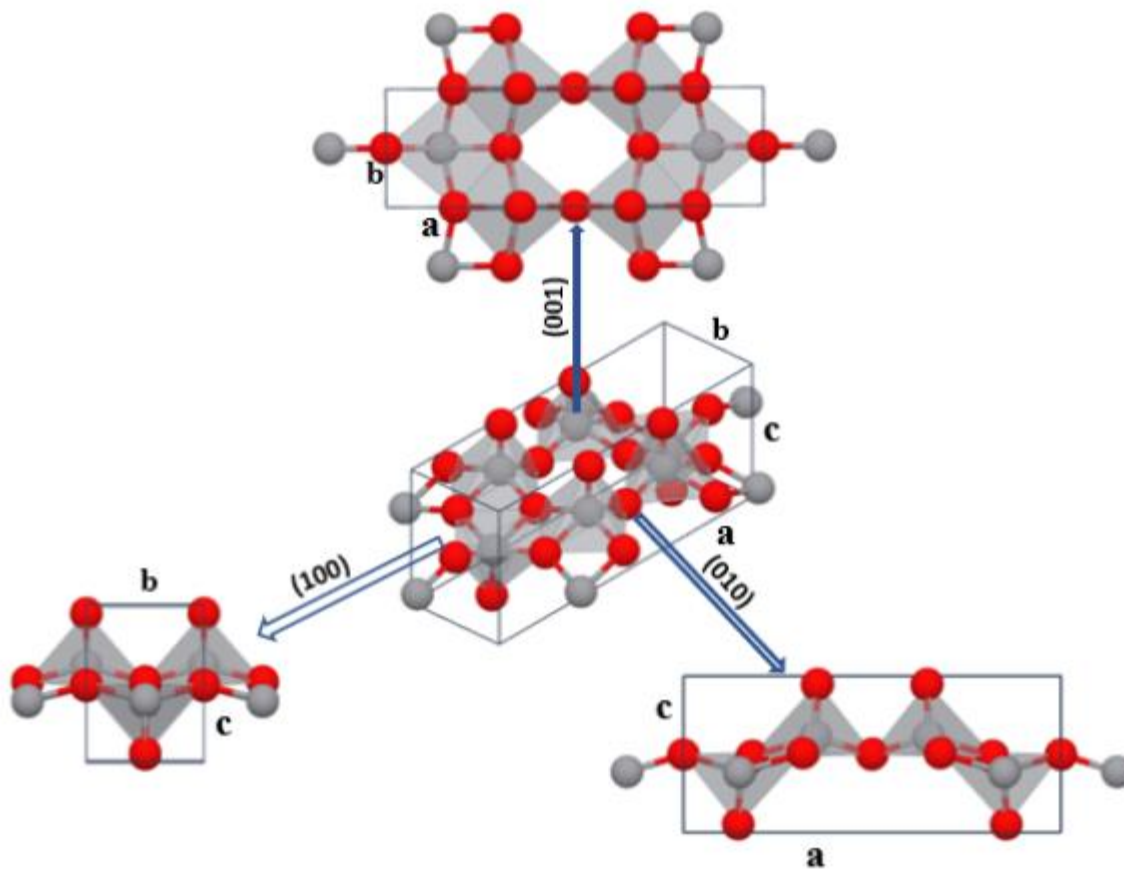


**Figure B.3.** The three-dimensional representation of the unit cell of orthorhombic  $\alpha$ - $V_2O_5$  with  $a = 11.516 \text{ \AA}$ ,  $b = 3.566 \text{ \AA}$ ,  $c = 4.373 \text{ \AA}$  and all angles between the lattice vectors of  $90^\circ$  (based on the standard pattern of JCPDS:41-1426). The atomic structures were rendered with the open web-access tool provided by “The Materials Project” at: <https://materialsproject.org>.

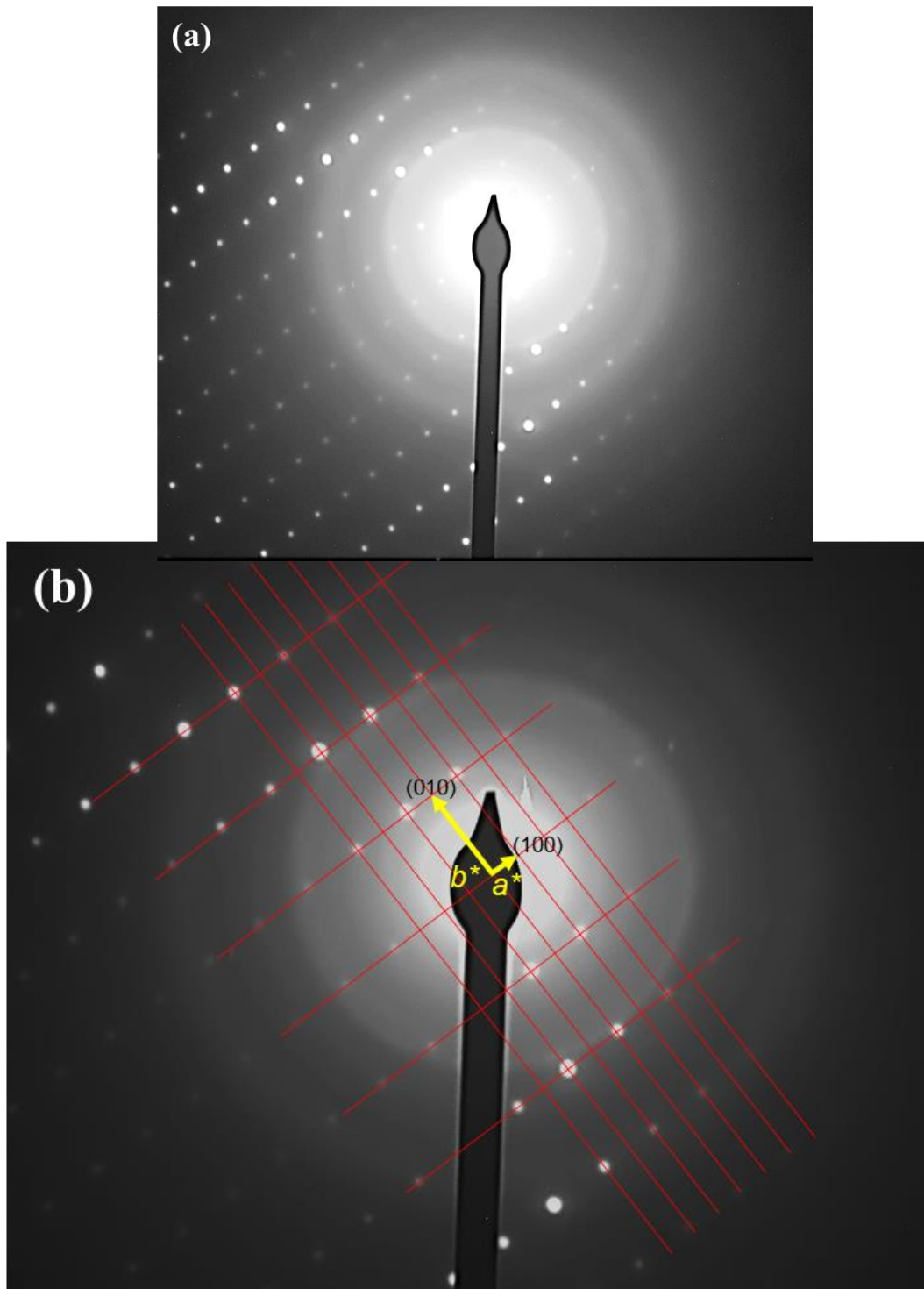


**Figure B.4.** (a) The raw image of the Selected Area Electron Diffraction (SAED) pattern of the  $V_2O_5$  nanoribbon marked in Figure 2(b). (b) The enlarged area near (000) to illustrate that the SAED pattern matches the rectangular lattice of the (001) plane of orthorhombic  $\alpha$ - $V_2O_5$  crystal, with the electron beam perpendicular to the (001) plane.

## SAED Analysis

Figure S4(a) shows the raw SAED pattern. These sharp diffraction spots present a well-defined rectangular reciprocal lattice. For better view of the diffraction spots, Figure S4(b) shows the enlarged SAED image around the primary (000) spot. It is clear that all diffraction spots fall on the rectangular lattice (illustrated with the red lines) that is consistent with the orthorhombic  $\alpha$ - $V_2O_5$  crystal structure with  $a = 11.516 \text{ \AA}$ ,  $b = 3.566 \text{ \AA}$  and  $c = 4.373 \text{ \AA}$  (based on JCPDS: 41-1426) as shown in Figure S3. Since the electron beam in the SAED measurement is perpendicular to the (001) crystal plane, all diffraction spots can be indexed as (hk0) in the reciprocal space. The two primary reciprocal lattice points (100) and (010) are labelled in Figure S4(b). The yellow arrows represent the corresponding reciprocal vector  $\mathbf{a}^*$  and  $\mathbf{b}^*$  of the orthorhombic  $\alpha$ - $V_2O_5$  crystals. The vector  $\mathbf{c}^*$  is perpendicular to the image plane. The real-space crystal lattice and their orientation relative to the  $V_2O_5$  nanoribbon are illustrated in Figure 4.2(d). The ratio of the magnitude of the reciprocal lattice is  $|\mathbf{b}^*|/|\mathbf{a}^*| = 3.23$ , which exactly matches the inverse ratio of the corresponding real-space lattice, i.e.,  $|a|/|b| = 3.23$ . This validates that the SAED pattern is attributed to electron diffraction from the orthorhombic  $\alpha$ - $V_2O_5$  crystal with the electron beam perpendicular to the (001) plane.

The indices of other diffraction spots (hk0) can be easily extended from the two primary lattice points (100) and (010). To avoid making the figure too crowded, they are not shown in Figure S4(b). Interestingly, the SAED pattern shows systematic variation in the intensity of the (hk0) spots, with some spots, such as (200), (020), (400), (040), (110), (220), (310), (130), etc., appearing as bright spots while others, such as (100), (010), (300), (030), (120), (210), etc., shown as dark spots. These are due to the variation of the form factors associated with the large unit cell of the orthorhombic  $\alpha$ - $V_2O_5$  crystals at the respective (hk0) spots, which are consistent with the JCPDS: 41-1426 standard.

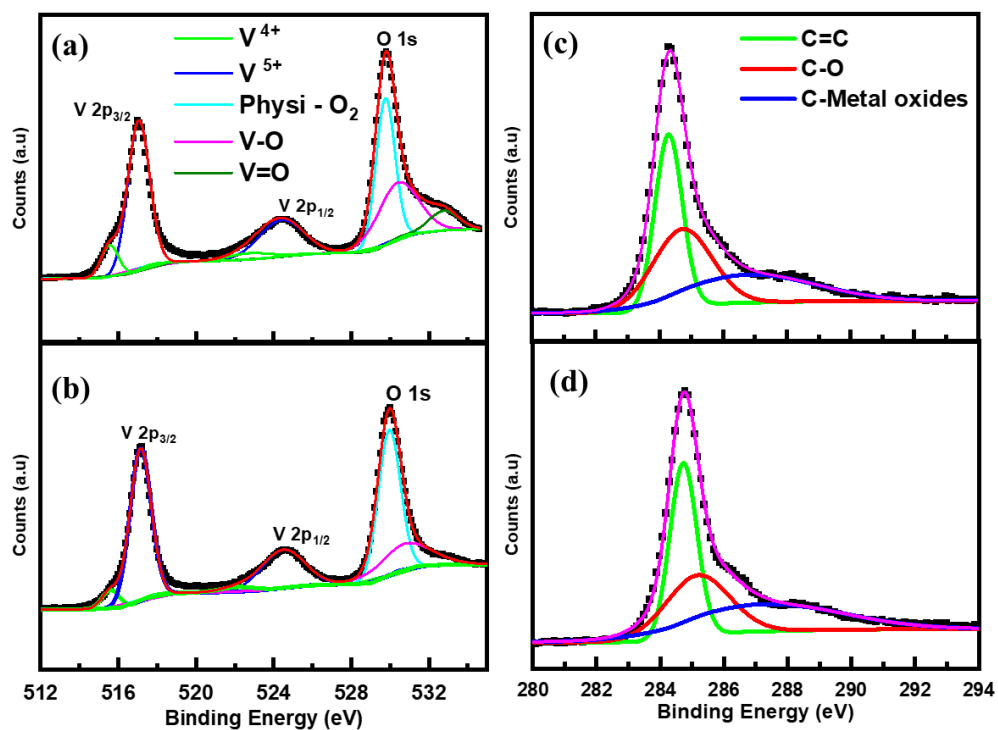


**Figure B.5.** The XPS spectra of V2p (512 – 528 eV) and O 1s (528 – 535 eV) of (a) V<sub>2</sub>O<sub>5</sub> NRs and (b) bulk V<sub>2</sub>O<sub>5</sub> powder. The C 1s XPS spectra of (c) Zn-V<sub>2</sub>O<sub>5</sub> NR/rGO and (d) (Mn+Zn)-V<sub>2</sub>O<sub>5</sub> NR/rGO.

**Table B.2.** XPS analysis of V<sub>2</sub>O<sub>5</sub> NRs and V<sub>2</sub>O<sub>5</sub> NR/rGO hybrids

Elements	Bulk V <sub>2</sub> O <sub>5</sub>	V <sub>2</sub> O <sub>5</sub> NRs	Zn-V <sub>2</sub> O <sub>5</sub> NR/rGO	(Mn+Zn)-V <sub>2</sub> O <sub>5</sub> NR/rGO		
<b>Peak Position in BE (eV)</b>						
V <sup>4+</sup> 2p <sub>3/2</sub> (eV)	515.60 (+/-0.04)	515.55 (+/- 0.02)	515.84 (+/-0.006)	515.92 (+/-0.024)		
V <sup>4+</sup> 2p <sub>1/2</sub> (eV)	522.15 (+/- 0.001)	522.75 (+/- 0.024)	522.71(+/-0.001)	522.74 (+/-0.001)		
V <sup>5+</sup> 2p <sub>3/2</sub> (eV)	517.14 (+/- 0.005)	517.04 (+/- 0.006)	517.36(+/-0.007)	517.27 (+/-0.007)		
V <sup>5+</sup> 2p <sub>1/2</sub> (eV)	524.50(+/-0.03)	524.50 (+/-0.03)	524.67(+/-0.03)	524.64(+/-0.04)		
V-O 1s (eV)	530.71 (+/-0.12)	530.38 (+/-0.01)	531.12 (+/-0.14)	530.56(+/-0.01)		
V=O 1s (eV)	-	532.75 (+/- 0.02)	533.26(+/-0.17)	532.99 (+/-0.11)		
<b>Atomic percentage (%)</b>						
Atomic % of V as V <sup>4+</sup>	8.90	14.57	12.30	17.30		
Atomic % of V as V <sup>5+</sup>	91.10	85.43	87.7	82.72		
Atomic % of Mn as Mn <sup>n+</sup> :	-	-	-	Mn <sup>2+</sup> : 9.21 %	Mn <sup>3+</sup> : 41.50%	Mn <sup>4+</sup> : 49.29 %
V <sup>4+</sup> / V <sup>5+</sup>	0.10	0.17	0.14	0.21		
V:O	1:2.7	1:3.13	1:3.77	1:3.58		
V:Zn			1:0.21	1:0.06		
V:Mn	-	-	-	1:0.07		
Elemental Formula	V <sub>2</sub> O <sub>5.4</sub>	V <sub>2</sub> O <sub>6.26</sub>	Zn <sub>0.42</sub> V <sub>2</sub> O <sub>7.54</sub>	Zn <sub>0.12</sub> Mn <sub>0.14</sub> V <sub>2</sub> O <sub>7.16</sub>		

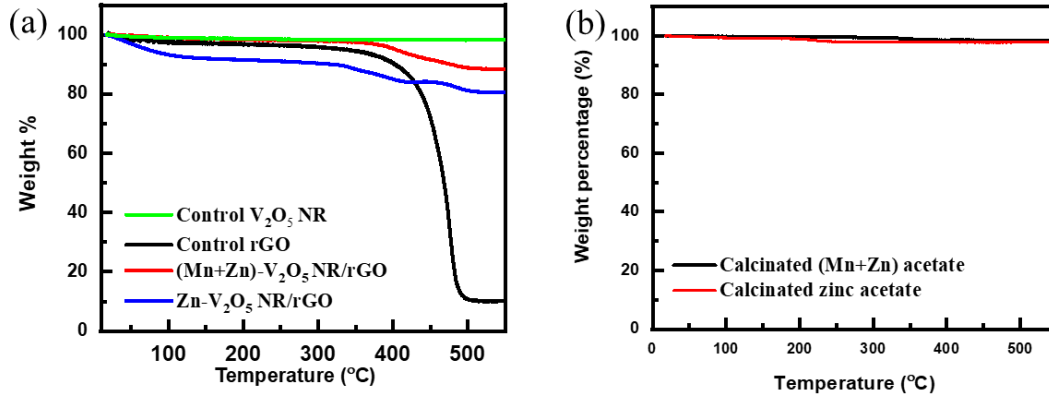


**Figure B.6.** (a) Thermogravimetric Analysis of various hybrid materials and control samples. (b) TGA plots of control samples (calcinated Zinc Acetate – red; calcinated mixture of Manganese acetate and Zinc acetate – black).

### TGA derivation based on Figure B.6:

- ❖ There is negligible weight loss by V<sub>2</sub>O<sub>5</sub>, ZnO and MnO upto 550 °C.
- ❖ Weight loss of the sample upto 550 °C = Wt loss by V<sub>2</sub>O<sub>5</sub> + Wt loss by rGO + Wt loss by ZnO/MnO

$$= (\text{Wt\% of V}_2\text{O}_5) * 0\% + (\text{Wt\% of rGO}) * 89.84\% + 0\%$$

$$= (\text{Wt\% of rGO}) * 89.84\%$$

#### Zn-V<sub>2</sub>O<sub>5</sub> NR/rGO

- 19.46 % = (Wt% of rGO) \* 89.84%
- Wt % of rGO = 21.66 %
- Wt% of Zn-V<sub>2</sub>O<sub>5</sub> NR = 100% - (Wt% of rGO) = 78.34%

#### (Mn+Zn)-V<sub>2</sub>O<sub>5</sub> NR/rGO

- 11.66% = (Wt% of rGO) \* 89.84%
- Wt% of rGO = 12.98%
- Wt% of (Mn+Zn)-V<sub>2</sub>O<sub>5</sub> NR = 100% - (Wt% of rGO) = 87.02%

**Table B.3.** Weight percentage of M-V<sub>2</sub>O<sub>5</sub> in divalent metal ion coprecipitated M-V<sub>2</sub>O<sub>5</sub> NR/rGO hybrids, control V<sub>2</sub>O<sub>5</sub> NR and control rGO samples calculated based on TGA plots in Figure B.6.

<b>Sample</b>	<b>Wt% of samples at 550 °C</b>	<b>Wt% of M-V<sub>2</sub>O<sub>5</sub></b>	<b>Wt% of rGO</b>
<b>Zn-V<sub>2</sub>O<sub>5</sub> NR/rGO</b>	80.54	78.34	21.66
<b>(Mn+Zn)-V<sub>2</sub>O<sub>5</sub> NR/rGO</b>	88.34	87.02	12.98
<b>Control rGO</b>	10.16	-	-
<b>Control V<sub>2</sub>O<sub>5</sub> NR</b>	100	-	-

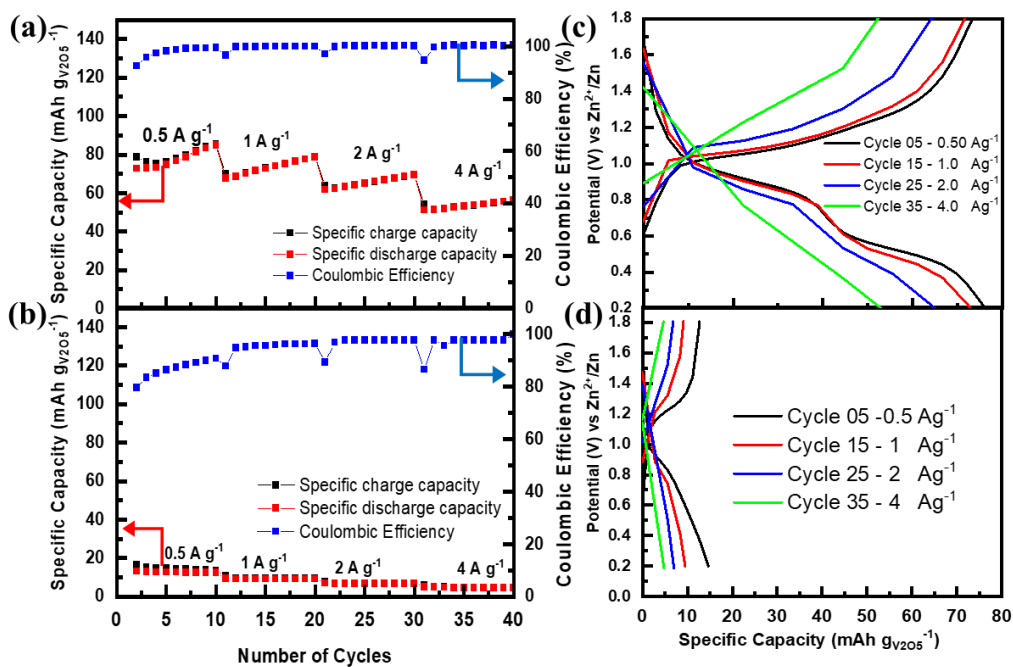


**Figure B.7.** The rate-performance behavior of AZIB at different current densities with the cathode material of ( $V_2O_5$  NRs and (b) bulk  $V_2O_5$  powder. Galvanostatic charge-discharge profiles of (c)  $V_2O_5$  NRs and (d) bulk  $V_2O_5$  powder at different current densities (0.5  $A g^{-1}$ , 1.0  $A g^{-1}$ , 2.0  $A g^{-1}$ , 4.0  $A g^{-1}$ ). All the above tests are performed in the potential window of 0.20-1.80 V.

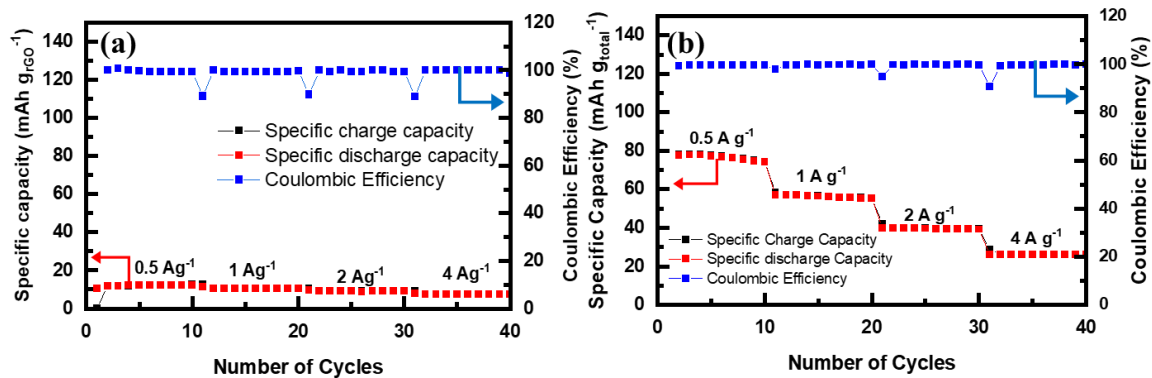


**Figure B.8.** Rate-performance behavior of AZIBs in the potential window of 0.20-1.80 V at different current densities with (a) control rGO and (b) physically mixed V<sub>2</sub>O<sub>5</sub> NR and rGO without the incorporation of divalent metal cations.

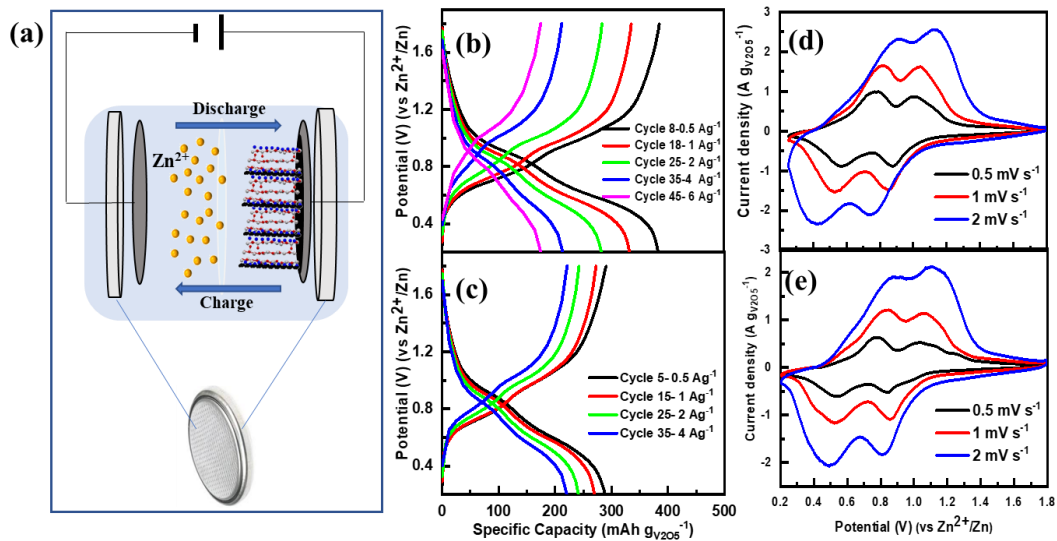


**Figure B.9.** (a) Schematic illustration of the Zn<sup>2+</sup> ion transport during the charge - discharge processes in AZIB with a Zn metal anode and a cathode made of V<sub>2</sub>O<sub>5</sub> NR/rGO hybrids. Galvanostatic charge discharge profiles and CV curves in the potential window of 0.20 – 1.80 V; (b, d) with Zn-V<sub>2</sub>O<sub>5</sub> NR/rGO cathode and (c, e) with (Mn+Zn)-V<sub>2</sub>O<sub>5</sub> NR/rGO.

## Appendix C - Supplementary information for Chapter 5

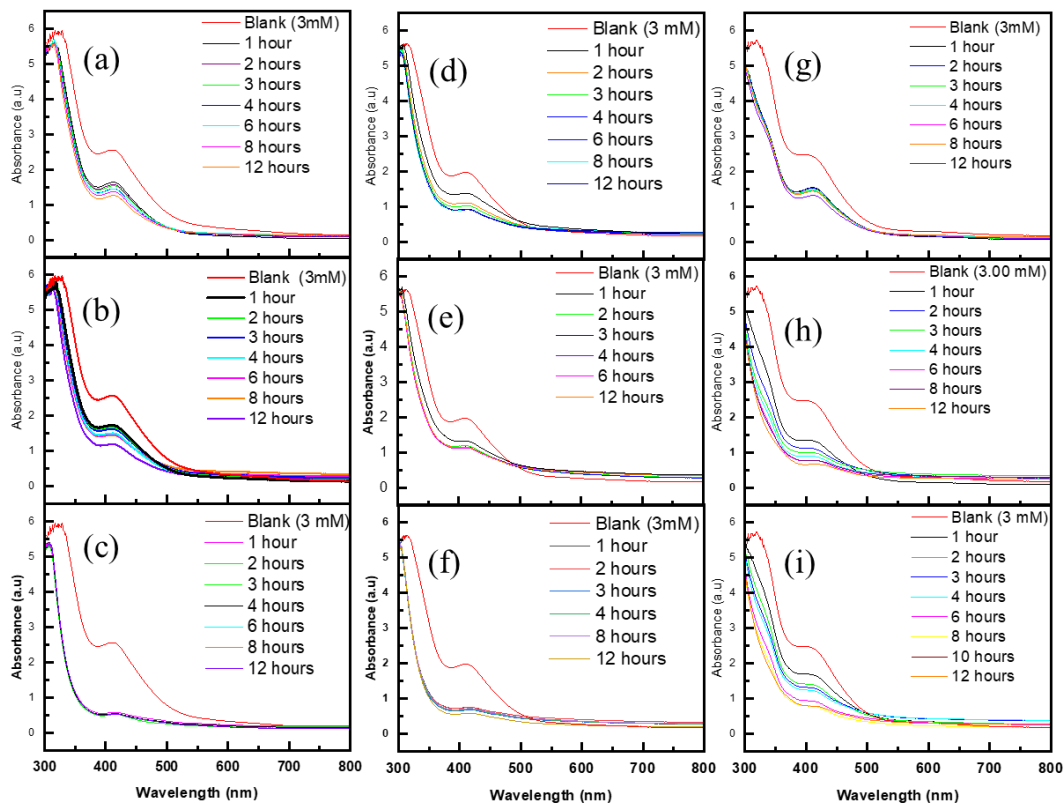


**Figure C.1.** Systematic analysis of lithium polysulfide adsorption capacities of MoS<sub>2</sub>/rGO-600(a, d, g); MoS<sub>2</sub>/rGO-250 (b, e, h); and MoS<sub>3</sub>/rGO-intermediate (c, f, i) electrocatalysts. Time-dependent UV-Visible absorbance measurements of the 3.0 mL of 3.0 mM Lithium polysulfide solutions in 1:1 DOL/DME solvent, (a-c) Li<sub>2</sub>S<sub>8</sub>, (d-f) Li<sub>2</sub>S<sub>6</sub>, (g-i) Li<sub>2</sub>S<sub>4</sub> before (red curve) and after adding 5 mg/mL electrocatalysts samples. Measurement was done for 12 hours at a constant interval of every one hour after stirring for 40 minutes and resting for 20 minutes.

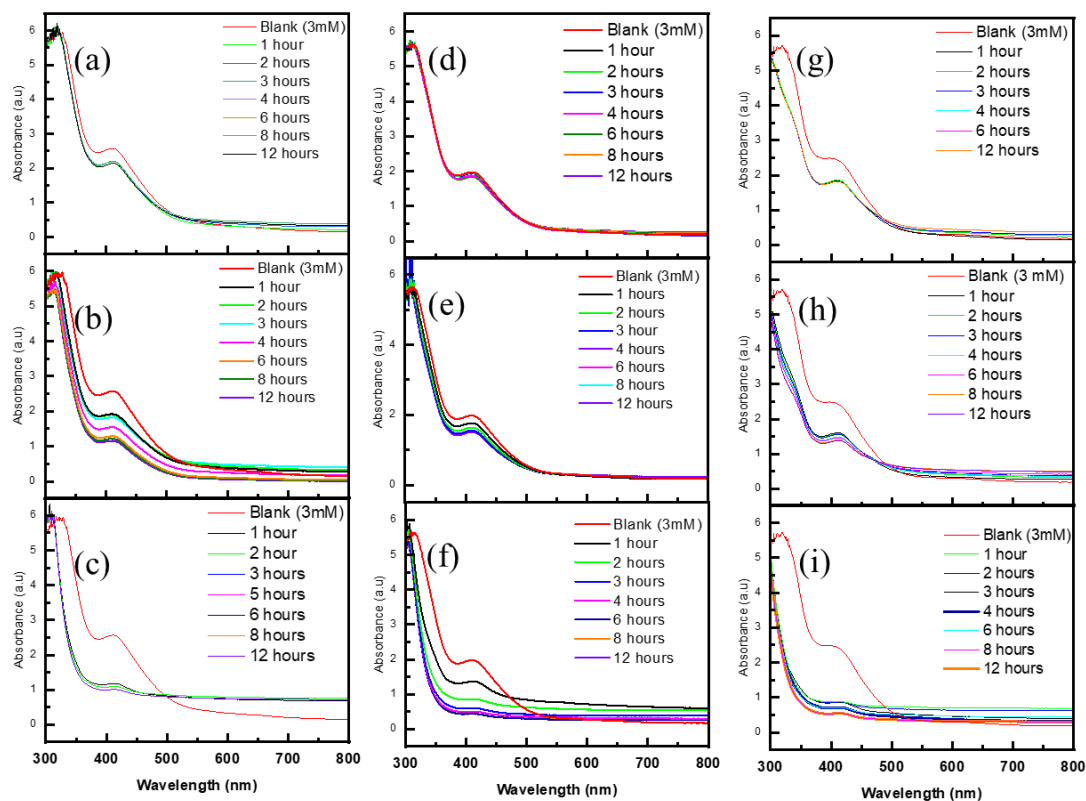


**Figure C.2.** Systematic analysis of lithium polysulfide adsorption capacities of MW-rGO-600(a, d, g); MW-rGO-250 (b, e, h); and MW-rGO-intermediate (c, f, i) electrocatalysts. Time-dependent UV-Visible absorbance measurements of the 3.0 mL of 3.0 mM Lithium polysulfide solutions in 1:1 DOL/DME solvent (a-c)  $\text{Li}_2\text{S}_8$ , (d-f)  $\text{Li}_2\text{S}_6$ , (g-i)  $\text{Li}_2\text{S}_4$  before (red curve) and after adding 5 mg/mL electrocatalysts samples. Measurement was done for 12 hours at a constant interval of every one hour after stirring for 40 minutes and resting for 20 minutes.

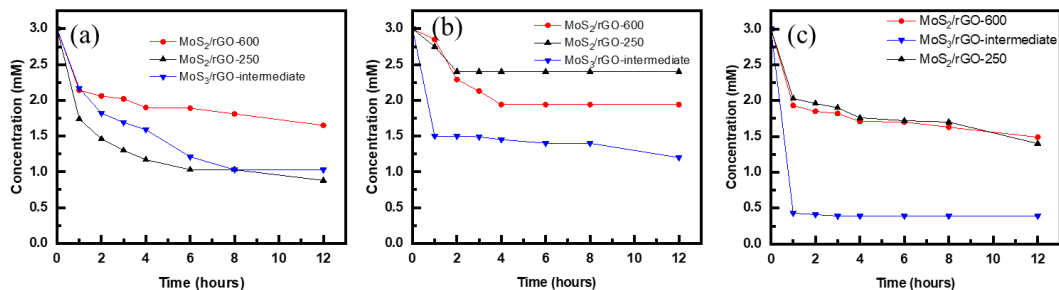


**Figure C.3.** Analysis of time vs concentration of lithium polysulfide solutions after adding various MoS<sub>2</sub>/rGO hybrid electrocatalysts based on the absorbance measured in Figure C.1. (MoS<sub>2</sub>/rGO-600 – Red curve; MoS<sub>2</sub>/rGO-250 – Black curve; MoS<sub>3</sub>/rGO-intermediate – Blue curve). (a) Li<sub>2</sub>S<sub>4</sub>, (b) Li<sub>2</sub>S<sub>6</sub>, (c) Li<sub>2</sub>S<sub>8</sub>.

**Table C.1.** Adsorption capacities of MoS<sub>2</sub> electrocatalysts after the deduction of the adsorption capacities of control rGO from the adsorption capacities of MoS<sub>2</sub>/rGO based on the formula described below. The weight percentages were taken from the elemental analysis of MoS<sub>2</sub>/rGO shown in table A.3.

Sample	Wt% of MoS <sub>2</sub>	Wt% of rGO	Adsorption capacity of MoS <sub>2</sub> /rGO (mmoles/g) (Ads <sub>total</sub> )			Adsorption capacity of Control rGO (mmoles/g) (Ads <sub>rGO</sub> )			Adsorption Capacity (mmoles /g <sub>MoS<sub>2</sub></sub> ) (Li <sub>2</sub> S <sub>4</sub> )	Adsorption Capacity (mmoles /g <sub>MoS<sub>2</sub></sub> ) (Li <sub>2</sub> S <sub>6</sub> )	Adsorption Capacity (mmoles /g <sub>MoS<sub>2</sub></sub> ) (Li <sub>2</sub> S <sub>8</sub> )
			Li <sub>2</sub> S <sub>4</sub>	Li <sub>2</sub> S <sub>6</sub>	Li <sub>2</sub> S <sub>8</sub>	Li <sub>2</sub> S <sub>4</sub>	Li <sub>2</sub> S <sub>6</sub>	Li <sub>2</sub> S <sub>8</sub>			
MoS <sub>2</sub> /rGO-600	78.4	21.6	0.20	0.25	0.24	0.12	0.041	0.097	0.22	0.27	0.28
MoS <sub>2</sub> /rGO-250	74.8	25.2	0.32	0.18	0.24	0.13	0.14	0.24	0.38	0.19	0.20
MoS <sub>3</sub> /rGO As synth	68.4	31.6	0.26	0.30	0.38	0.46	0.45	0.36	0.16	0.21	0.39

Formula for the calculation of adsorption capacities of MoS<sub>2</sub> in electrocatalysts:

$$\frac{\text{Ads.}_{\text{MoS}_2}}{M_{\text{total}} * \text{Wt\% of MoS}_2} = \frac{\text{Ads.}_{\text{total}} - (\text{Ads.}_{\text{rGO}} * \text{Wt\% of rGO} * M_{\text{total}})}{M_{\text{rGO}} * M_{\text{total}} * \text{Wt\% of MoS}_2}$$

